Thin films for applications in generation and storage of electrical energy

A thesis submitted in partial fulfillment of the requirements
for the degree of Doctor of Philosphy (PhD) in Engineering Science

By Chellda EXANTUS

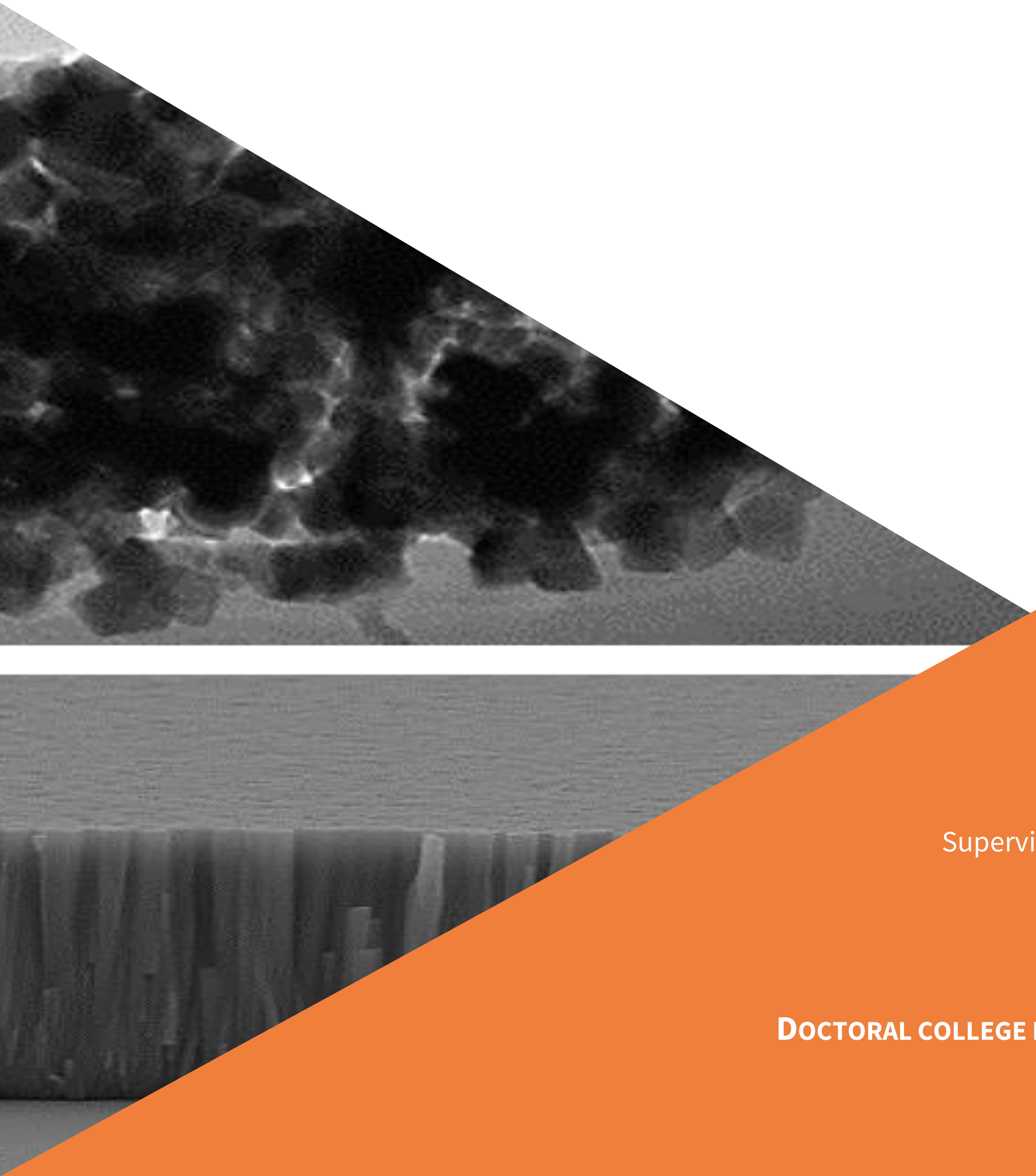

Supervisor: Nathalie JOB

DOCTORAL COLLEGE IN CHEMICAL ENGINEERING

DECEMBER 2020

Thin films for applications in generation and storage of electrical energy

Chellda EXANTUS

Supervisor

Pr. Nathalie JOB

UR Chemical Engineering ULiège - NCE, ULiège

Members of the jury

Pr. Benoît HEINRICHS, President	UR Chemical Engineering ULiège – NCE, ULiège
Dr. Natacha KRINS	LCMCP, Sorbonne University, Paris (France)
Dr. Kévin NADAUD	GREMAN UMR 7347 University of Tours, Tours (France)
Dr. David ESKENAZI	Prayon s.a., Engis
Pr. Bénédicte VERTRUYEN	UR CESAM, GREENMAT, ULiège
Dr. Christelle ALIE	UR Chemical Engineering ULiège – NCE, ULiège

Remerciements

Ce travail de thèse n’aurait pas pu être réalisé sans la contribution de nombreuses personnes, merci à vous.

J’adresse de sincères remerciements au Pr. Nathalie Job, pour sa grande implication dans la direction de cette thèse, son écoute, sa sincérité, sa disponibilité et surtout son optimisme. Ses encouragements ont été un réel soutien lors des moments difficiles de cette thèse.

J’adresse mes remerciements à Dimitri Liquet, un manager à l’écoute, riche en conseils, et qui a su gérer les difficultés rencontrées lors de ce projet sans y laisser trop de cheveux ;-).

Je remercie Alain Germeau et David Eskenazi, de Prayon s.a., pour leur présence, leur soutien et leurs conseils tout au long de ce projet.

Je remercie également les chercheurs NCE du projet en commençant par Dr. Christelle Alié pour son travail sur la partie « nanogénérateurs ». Je la remercie aussi chaleureusement pour son travail de relecture du manuscrit. Je suis reconnaissante envers Cédric Calberg pour les différents échanges et les dépôts des couches d’électrolytes polymères. J’adresse mes remerciements au Dr. Dorra Dallel pour son travail sur le spray et l’optimisation des dépôts de couches de cathodes mais aussi ses conseils depuis mon arrivée au laboratoire NCE.

J’adresse un remerciement tout particulier au Dr. Carlos Alberto Pàez, dit Beto, devenu bien plus qu’un collègue, pour son travail sur la partie « cathodes », pour sa bonne humeur, son optimisme, ses blagues, ses idées farfelues, mais surtout les conseils depuis mon arrivée au laboratoire NCE.

Je tiens à remercier l’ensemble des membres du jury pour leur évaluation de ce travail : Natacha Krins, Maître de Conférence à Sorbonne Université (Paris), Kévin Nadaud, Maître de Conférence à l’Université de Tours, David Eskenazi, senior research scientist chez Prayon s.a., Bénédicte Vertruyen, Professeure au département de chimie de l’Université de Liège, Christelle Alié, chercheuse senior au département de chemical engineering de l’Université de Liège et Benoît Heinrichs, Professeur au département de chemical engineering de l’Université de Liège.

Aucune caractérisation des nanogénérateurs n’aurait pu être possible sans le laboratoire du GREMAN. Merci au Pr. Guylaine Poulin-Vittrant pour son accueil et au Dr. Kévin Nadaud, de l’Université de Tours, pour les échanges au cours du projet sur la partie montage et caractérisation des nanogénérateurs.

Mes remerciements vont aussi aux membres du laboratoire GreenMat de l’ULiège, notamment la Pr. Bénédicte Vertruyen pour la formation à la DRX et sa confiance, Dr. Catherine Henrist pour la formation ESEM et les échanges, ainsi que le Dr. Pierre Colson pour l’utilisation de l’AFM et les bonbons à la violette. La formation et les conseils du Pr. Philipe Compère, du laboratoire de Morphologie Ultrastructurale de l’ULiège, concernant l’EDX ont également été précieux.

J’adresse également mes remerciements aux membres du CERM de l’ULiège, Charlotte, Martine, Valérie, Charlène, Fabiana, Philip, Raphael et Jérémie pour leur accueil ainsi que l’accès aux mesures de DLS, et la caractérisation par TEM.

Merci à Dirk Poelman Professeur au Lumilab de l’Université de Gand de nous avoir permis de réaliser les mesures de photoluminescence de nos matériaux.

Mes remerciements vont également à Korina et Jérôme, pour le soutien mutuel tout au long de ce projet, les discussions, les gâteaux, et tous les moments passés et à venir.

Je souhaite à présent remercier l’équipe « carbone », les présents et anciens, pour tous les échanges, leur disponibilité, et pour avoir répondu à mes nombreuses questions toutes ces années : Marie-Laure, Anthony, Alexandre, Vaios, Giuseppe, Joe, Aleksandra et Fabien.

Mes remerciements vont aussi à l’ensemble du Département de Chemical Engineering. En particulier, merci à Martine, Maria-Rosa et Marlène pour tout le travail administratif, pour leur bonne humeur, pour les différents évènements organisés. Merci à vous, Artium, Carlitos, Céline, Cédric, Polina, Carmenita, Tristan, Julien, Nicolas, Rémi, Antoine, Paul. À vous tous, je vous souhaite le meilleur pour la suite.

Ces quelques lignes sont pour ma mère, mes frères et ma sœur qui m’ont soutenue, encouragée, écoutée, conseillée tout au long de ces études. Un grand merci à Mathieu, qui m’a supportée tout au long de ces études. Je le remercie pour son aide, ses conseils, son soutien et sa motivation.

Résumé

La thèse porte sur le développement de couches minces d'oxydes métalliques par procédé sol-gel, pour des applications diverses. Elle s'inscrit dans le contexte global du projet européen EnSO (Energy for Smart Objects), financé par l'Electronic Components and Systems for European Leadership Joint Undertaking (ECSEL-JTI), en collaboration avec le H2020 Framework Programme (H2020/2014-2020) de l'Union européenne et les autorités nationales. Le projet visait au développement de microsources autonomes d'énergie, comprenant à la fois un système de récupération de l'énergie et un système de stockage. Dans la mesure où le laboratoire NCE de l'ULiège a été impliqué dans le développement des deux parties, et suite à une réorientation générale du projet à mi-parcours, la candidate a été amenée à travailler sur deux types de matériaux différents. La thèse se présente donc en deux parties distinctes.

La première partie porte sur l'optimisation d'un procédé de croissance de nanofils d'oxyde de zinc (ZnO), utilisables comme matériau dans un microgénérateur piézoélectrique, en vue de développement industriel. L'objectif a été de mettre au point un procédé de synthèse des nanofils sur substrat, avec des vitesses de croissance compatibles pour une mise à l'échelle industrielle (minimum 20 $nm.min^{-1}$). Un procédé de synthèse mixte comprenant (i) l'ensemencement du substrat par des nanocristaux de ZnO suivi (ii) de la croissance en milieu liquide a été mis au point. L'étude des différentes étapes du procédé ainsi que de la cinétique de croissance des nanofils a permis d'optimiser les conditions de dépôt et d'obtenir une croissance compatible avec l'échelle industrielle (70 $nm.min^{-1}$). En combinant les résultats avec ceux obtenus par d'autres chercheurs du projet, il a été possible d'obtenir des matériaux utilisables pour la fabrication de nanogénérateurs piézoélectriques, comme le montrent les caractérisations après montage, en collaboration avec le laboratoire Greman (Tours). Les nanofils ont également été testé comme photocatalyseur pour la décomposition potentielle de polluants dans l'eau, ce qui montre la diversité des applications possibles.

La deuxième partie porte sur l'optimisation de couches poreuses de matériaux d'électrode positive de batterie Li-métal *via* l'utilisation du $Li_7La_3Zr_2O_{12}$ (LLZO), un conducteur ionique nanostructuré, synthétisé par voie sol-gel. L'objectif final du projet, réalisé essentiellement en collaboration avec Prayon s.a. et le CEA-Leti (Grenoble), était d'aboutir à des microbatteries Li-métal/LCO tout solide. Le but de cette partie de la thèse, qui se base sur le travail d'un autre chercheur du laboratoire NCE, a été d'améliorer la conductivité ionique des couches d'électrodes positives en remplissant leur porosité de LLZO. Des couches hybrides LCO-LLZO conservant les propriétés électrochimiques du matériau actif d'électrode ont été préparées, et les caractérisations effectuées en ajoutant un électrolyte liquide montrent que le LCO ne subit aucune altération en présence de LLZO. Enfin, des résultats préliminaires encourageants ont été obtenus en remplaçant l'électrolyte liquide par un électrolyte solide polymère (Gel Polymer Electrolyte) développé au NCE : l'ajout de LLZO à l'électrode de LCO a permis d'obtenir une microbatterie qui cycle de manière stable à une vitesse de 1C.

Mots clés : nanofils de ZnO, nanogénérateur, couches minces, $LiCoO_2$, LLZO, microbatteries solide.

Abstract

The PhD was focused on the development of metal oxides thin films using sol-gel process, for various applications. It is part of the overall context of the European EnSO (Energy for Smart Objects) project, funded by the Electronic Components and Systems for European Leadership Joint Undertaking (ECSEL-JTI), in collaboration with the European Union's H2020 Framework Programme (H2020/2014-2020) and national authorities. The project aimed at developing autonomous micro energy sources, including both an energy harvesting system and a storage system. As the ULiège NCE laboratory was involved in the development of both parts, and following a general reorientation of the project at mid-term, the candidate was led to work on two different types of materials. This PhD thesis is thus presented in two distinct parts.

The first part concerns the optimisation of a process for the growth of zinc oxide nanowires (ZnO NWs) for piezoelectric nanogenerator application. The objective was to develop a process for the synthesis of NWs on a substrate, with a growth rate compatible for industrial scale-up (minimum 20 nm min^{-1}). A combined process including (i) the deposition of a seed layer made of ZnO crystallites followed by (ii) ZnO NW growth using wet chemistry was developed at the NCE laboratory. The study of the different steps of the process, as well as the growth kinetics of the NWs, made it possible to optimise the conditions of deposition and to obtain a growth speed compatible with industrial scale (70 nm min^{-1}). By combining the results with those obtained by other researchers in the project, it was possible to obtain materials that can be used for the manufacture of piezoelectric nanogenerators, as shown by the characterisations after assembly, in collaboration with the Greman laboratory (Tours).

The NWs were also characterised as photocatalysts for the potential decomposition of pollutants in water, thus showing the diversity of possible applications.

The second part focuses on the optimisation of porous layers for positive electrodes of Li-metal batteries. Optimisation was based on the use of $Li_7La_3Zr_2O_{12}$ (LLZO), an ionic conductor synthesised by sol-gel process, as nanostructured solid electrolyte within the electrode. The final objective of the project, carried out mainly in collaboration with Prayon s.a. and CEA-Leti (Grenoble), was to produce solid-state Li-metal/LCO microbatteries. The aim of the thesis, which is based on the work of another researcher from the NCE laboratory, was to improve the ionic conductivity of the positive electrode layers by filling their porosity with the nanostructured LLZO. Hybrid LCO-LLZO layers preserving the electrochemical properties of the active electrode material were prepared and the characterisations carried out by adding a liquid electrolyte showed that the LCO does not undergo any alteration in the presence of LLZO. Finally, preliminary encouraging results were obtained when replacing the liquid electrolyte with the gel polymer electrolyte (GPE) developed at NCE: the addition of LLZO to the LCO electrode resulted in a microbattery that is stable when cycling at 1C.

Keywords: ZnO nanowires, nanogenerator, thin films, $LiCoO_2$, LLZO, solid-state microbattery.

Table of contents

General introduction

Context of the thesis

The development of the wearable electronic technologies such as wireless sensors networks (WSN) based equipment is evolving quickly. The WSN technologies enable ultra-fast and reliable communication as well as data transfer. This field of research has attracted much attention of researchers and industry experts in the areas of industrial automation [1], health care, internet-of-things (IoT) [2], *etc.* IoT, is a concept where everyday objects will be able to communicate together *via* internet to enhance their efficiency upon use; it is nowadays gaining more and more attention within the electronics industry. As an example, Figure 1 shows dynamic cryptogram for bank card developed by Gemalto in order to reinforce payment security.

Figure 1. Gemalto dynamic cryptogram developed for BNP.

All these “smart objects” have to be autonomous, easy to use and handle, as small as possible, robust and long lasting with a long operating lifetime. The key component for all electronic systems is the energy supplier: how to harvest, store and use energy? To answer this question, it is necessary to combine different devices: (i) an energy harvester, which is able to capture energy from the environment and, possibly, transform it into electrical energy, (ii) a storage system, able to keep this energy available for a sufficient long time and (iii) electronics for energy management upon storage and use.

In this context, the Energy for Smart Object project (EnSO) [3] was accepted for financing within the Electronic Components and Systems for European Leadership Joint Undertaking (ECSEL-JTI), in collaboration with the European Union's H2020 Framework Programme (H2020/2014-2020) and National Authorities. The project was managed by ST Microelectronics in collaboration between 35 European partners, among which (i) 8 academic research partners, (ii) 5 supply chain companies, (iii) 4 integrated device manufacturers and

(iv) 15 end-users. It started in 2016 and was focusing on providing Autonomous Micro Energy Sources (AMES) to end-users. AMES would at least consist of three elements:

(i) An energy harvester, *i.e.* a nano energy generator, which converts energy from the environment into electricity;
(ii) A battery as micro energy storage system;
(iii) A battery management system.

Within this framework, the Nanomaterials, Catalysis and Electrochemistry (NCE) laboratory of the University of Liège was involved (i) in the development of materials to be integrated in energy harvesters, in collaboration with the Greman laboratory in Tours (France) and (ii) in the development of layers of active materials for microbatteries as energy storage systems, in collaboration with Prayon s.a. and the Commissariat à l'Energie Atomique et aux Energies Alternatives (CEA-Leti), located in Grenoble (France). Throughout the years, 3 post-doctoral researchers, 2 research engineers and 2 PhD students were involved in the research performed at the NCE laboratory in the framework of the EnSO project.

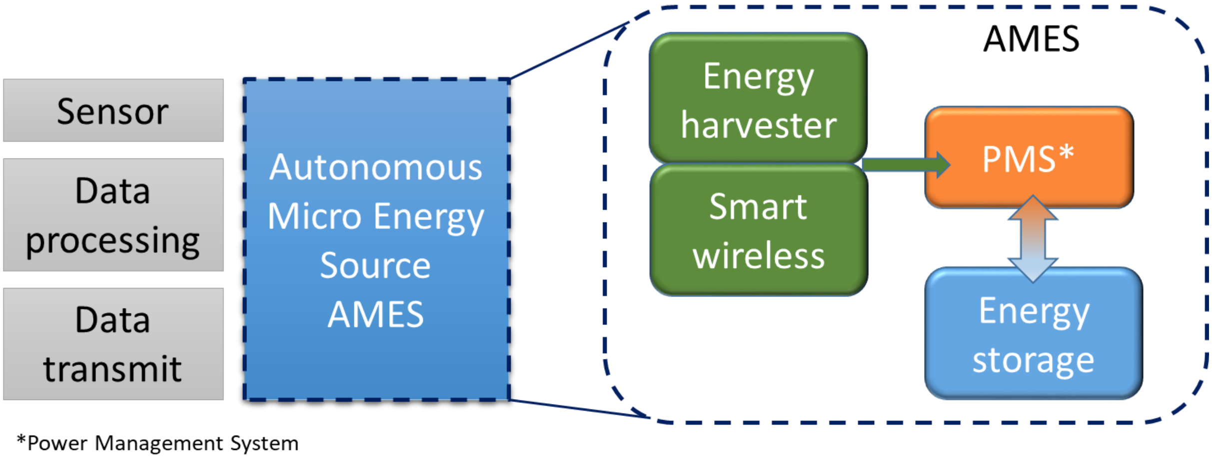

Figure 2. Scheme of an AMES using energy harvester.

Energy harvesters

The development of energy harvesters was focused on the use of a piezoelectric system. The global objective was to develop a piezoelectric nanogenerator (Figure 3) based on zinc oxide nanowires (ZnO NWs), in collaboration with the Greman laboratory. The latter had already developed a strong expertise on such energy harvesters [4, 5]. While the NCE was in charge of developing a ZnO NW synthesis process compatible with scale-up, the Greman laboratory dedicated the effort to the encapsulation of the ZnO NWs into complete piezoelectric devices and to their characterisation (electrical response to mechanical solicitation).

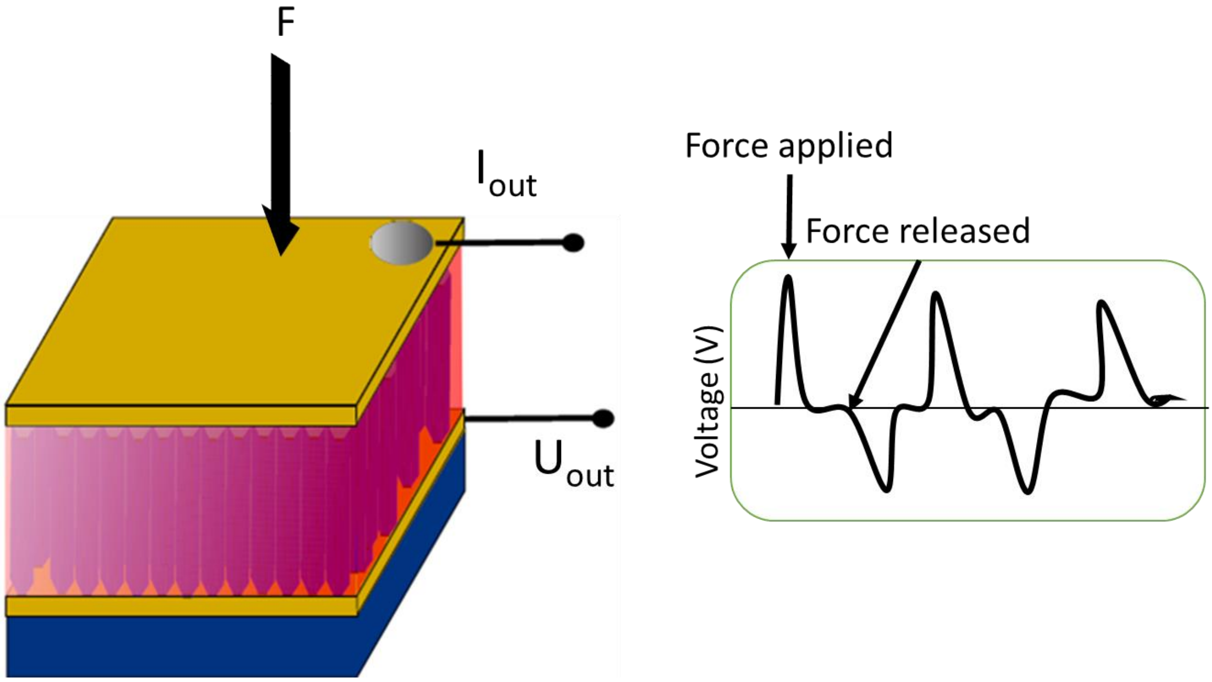

Figure 3. Principle of piezoelectric nanogenerator.

Piezoelectric materials such as ZnO NWs exhibit an induced voltage under applied stress (Figure 3). According to the EnSO project specifications, high crystalline quality ZnO NWs should be synthesised using a low temperature process (< 400 °C) so that the NWs can ultimately be deposited onto flexible organic substrates. In addition, the developed process needs to be suitable for large-scale manufacturing, meaning that the growth speed of the NWs should reach 20 nm min^{-1} while keeping the process as simple as possible. Finally, the obtained micrometric layer should be composed of well-aligned and well-crystallised NWs, able to power a Li-metal microbattery system by providing a power of the order of 1 μW cm^{-2} at a voltage of 4.2 V.

The growth of ZnO NWs usually requires the pre-deposition of a seed layer onto which NWs are grown [6–8]. In that perspective, sol-gel processes were used and optimised to develop both the seed layer and the NWs. Two researchers of the NCE laboratory were involved in the research program: one PhD student (Chellda Exantus) and one senior researcher (Dr Christelle Alié). Thus, the results presented here are a part of the global research program performed at the NCE laboratory during the project. Since both researchers worked in parallel, results obtained by one could fed the other’s work part, and results are thus much intricate. For that reason, it was necessary to include in this manuscript some of the experiments and results obtained by the senior researcher in order to understand the evolution of the research program and to show the outcome of the project. Throughout the thesis manuscript, the respective contributions of the PhD student and the senior researcher were highlighted at best.

Microbatteries

Regarding microbatteries, the NCE laboratory was in charge of developing two components for Li-metal systems: $LiCoO_2$ (LCO) electrodes and solid electrolyte, either full Solid-State Electrolyte (SSE) or Gel Polymer Electrolyte (GPE). Both layers had to be deposited *via* spray-coating, in order to replace the costly Physical Vapor Deposition (PVD) processes used by the initial leader of the project, ST Microelectronics. The final objective was to build a full-solid Li-metal microbattery with high energy density, using spray-coating for the deposition of the positive electrode material and the electrolyte. According to the objectives of the EnSO project, the battery should be rechargeable, display a long-life time (> 10 years), and reach a capacity of 3 mAh.

The development of the lithium metal microbatteries was made in collaboration with the CEA-Leti laboratory, as they already had developed materials for thin film batteries, and with Prayon s.a., from the supply chain. Indeed, the NCE laboratory expertise on microbatteries had been previously developed within the framework of a large project co-financed by Wallonia and Prayon s.a. [9]. During that previous project, a senior researcher of the NCE laboratory, Dr Carlos Páez, had developed a low-cost process for the deposition of thin layers of lithium cobalt oxide (LCO) cathode material for Li metal microbatteries [10]. This process uses spray-coating and allows the deposition of 10-µm thick LCO layer. The final battery, assembled in coin-cell with liquid electrolyte in-between Li metal anode and LCO cathode, displayed a capacity of 1 mAh. The challenge here was to replace the liquid electrolyte by an SSE (Lithium Phosphorous Oxynitride, LiPON) or a GPE, in order to get rid of the volatile, flammable liquid electrolyte incompatible with the final application in (flexible) microbatteries. The main issue is the porosity in the cathode coating (~50-60%): while liquid electrolyte easily enters the porosity and allows for easy ion transport through the whole electrode thickness, GPE or SSE are much harder to use since they are normally deposited on top of the electrode. The migration of the lithium ions is thus hindered, which leads to the decrease of the ionic conductivity, and a drop of the battery capacity. It was thus necessary to modify the LCO deposition process so as to include a solid electrolyte within the pore texture of the electrode material layer. In addition, the rugosity of the LCO layer was originally too high for SSE deposition; it had thus to be improved to be compatible with LiPON. Ultimately, the modified LCO layer was to be combined with an SSE or a GPE, and embedded in a full solid-state battery.

Figure 4. Example of microbattery developed during EnSO project.

At the beginning of the EnSO project, research on microbatteries was essentially conducted by two senior researchers of the NCE laboratory: Dr Carlos Páez for the development of modified LCO coatings onto substrates provided by the CEA, and Cédric Calberg for the deposition of GPE onto the electrodes. However, after 2 years, the EnSO project was reorganised and it was decided to reduce the resources allocated to the development of the piezoelectric nanogenerators in order to reinforce the microbattery topic. For that reason, Chellda Exantus joined the microbattery team, and contributed to the development of the modified LCO layer using sol-gel processes.

Even though the subject seems *a priori* quite different from that of the ZnO NWs for piezoelectric generator, it lies on the same competences and techniques. In both cases, the goal was to manufacture thin solid films of materials using sol-gel processes and deposition techniques, and to characterise them by physico-chemical and electrochemical techniques. The apparent constraint of subject change, in the middle of the thesis, was thus an opportunity to develop similar ideas and methods in two different environments.

Objectives of the thesis

As explained above, this thesis was part of a large European project dealing with the manufacturing of complete Autonomous Micro Energy Sources (AMES). The general goal of the thesis was to contribute to the development of AMES by designing innovative techniques to prepare thin layers of materials onto a substrate. The general requirement was that the methods used could be transferred to industrial scale; they had to be cheap, easy to handle, fast, reproducible and require as less energy as possible. Material preparation was thus performed by sol-gel techniques, and the processes were studied so that the required post-treatment temperatures, necessary whatever the material considered, were as low as possible.

As the project evolved throughout the years, two distinct topics with their own goals were studied:

- The optimisation of ZnO NW preparation, including the seeding and the growth steps, in order to obtain NW arrays that could be used in piezoelectric nanogenerators;
- The modification of $LiCoO_2$ (LCO) coatings so that they could be used as cathode layers in full solid-state microbatteries.

Structure of the thesis

The thesis is divided into two main parts. The first one, including Chapters 1 to 3, deals with the development of the ZnO NW manufacturing process and their use in practical applications. The second one, corresponding to Chapters 4 and 5, reports the contribution to the modification of the LCO cathode layers in Li-metal microbatteries, and their combination with a GPE.

In **Chapter 1**, we report a simple process to manufacture a homogeneous arrangement of flat ended hexagonal ZnO NWs, well aligned along the c-axis through a chemical bath deposition (CBD) method. The process developed needed to be suitable for large-scale manufacturing (*i.e.* minimum 20 nm min^{-1} growth speed), and to provide a micrometric layer of well-aligned NWs. In order to meet this expectation, a previously published synthesis method [11, 12] was optimised for growing the ZnO NWs. Before growth, a uniform ZnO seed layer was deposited on the substrate by combining a simple low-cost sol-gel process and a spin-coating technique. The obtained materials were observed by environmental scanning electron microscopy (ESEM) to measure the NW length and diameter. This allowed to study the NW growth kinetics in order to identify the critical process variables, *i.e.* those that have an impact on the synthesis process.

In **Chapter 2**, an original seed method using dip-coating was developed in order to orientate the growth of ZnO crystals. Indeed, the seed layer characteristics (crystallinity, orientation, thickness) has a strong influence on the NW growth. The cleaning of the substrate, the deposition method and the subsequent thermal treatment were studied to determine their impact on the seed quality and, further, on the length, diameter and orientation of the final NWs obtained by CBD. In parallel to the seed study, the senior researcher involved in the topic, Dr Christelle Alié, worked on the optimisation of the NW growth in order to obtain, *in fine*, separate and well-aligned NWs.

In **Chapter 3**, the work was focused on the use of the obtained NWs in two applications. First, in collaboration with the Greman laboratory, ZnO NWs were implemented into piezoelectric nanogenerators. This application requires the use of well-aligned NWs without crystalline defects (vacancies, interstitials elements), which is very difficult by CBD process. The presence of these defects generates free electrons that can mask the piezoelectric charges and thus reduce the performance of the NG [13, 14]. To point out the impact of the research on a global scale, the chapter thus also summarises the parallel work of the senior researcher (Dr Christelle Alié), aiming at decreasing the concentration of defects and improving the nanogenerator performances. Second, as the NCE laboratory also works on photocatalysts for water depollution, a first trial of ZnO NWs as photocatalyst was performed: the catalytic activity of ZnO NWs deposited on glass for the photoctalytic degradation of hydrogen peroxide was evaluated. Both examples point towards the necessity to control at best the NW growth so as to obtain structures compatible with the final chosen application.

Switching from ZnO NWs to microbatteries, **Chapter 4** was dedicated to the synthesis and characterisation of low temperature cubic $Li_7La_3Zr_2O_{12}$ (LLZO), and its insertion into the LCO cathode coating. Indeed, in order to obtain Li^+-conducting LCO layers, it is necessary to fill the layer porosity (~50-60%) with a solid electrolyte to finally be able to build an all solid-state battery. LLZO nanoparticles could be obtained and mixed with the LCO suspension before electrode deposition by spray-coating, following the electrode development performed by Dr Carlos Páez within the EnSO project. Different LLZO amounts were added, and the mixture stability upon cycling in a battery configuration was assessed, still using liquid electrolyte. This step was necessary to make sure that no side-reaction could occur between the two electrode components.

Finally, in **Chapter 5**, the optimised cathode material containing LCO and LLZO was combined with a Gel Polymer Electrolyte developed at the NCE laboratory by Cédric Calberg. It was possible to characterise the full solid-state battery and show the impact of LLZO on the final performances upon cycling.

References

1. D. Christin, P. S. Mogre, M. Hollick, Survey on Wireless Sensor Network Technologies for Industrial Automation: The Security and Quality of Service Perspectives. *Futur. Internet* **2**, 96–125 (2010).
2. N. Khalil, M. R. Abid, D. Benhaddou, M. Gerndt, in *IEEE ISSNIP 2014 - 2014 IEEE 9th International Conference on Intelligent Sensors, Sensor Networks and Information Processing, Conference Proceedings* (2014), pp. 1–6.
3. Energy for Smart Objects (EnSO), EnSO, http://www.enso-ecsel.eu, grant agreement n° 692482, 2016-2020.
4. K. Nadaud, F. Morini, A. S. Dahiya, C. Justeau, S. Boubenia, K. P. Rajeev, D. Alquier, G. Poulin-Vittrant, Double buffer circuit for the characterization of piezoelectric nanogenerators based on ZnO nanowires. *Appl. Phys. Lett.* **112**, 1–6 (2018).
5. A. S. Dahiya, F. Morini, S. Boubenia, K. Nadaud, D. Alquier, G. Poulin-Vittrant, Organic/Inorganic hybrid stretchable piezoelectric nanogenerators for self-powered wearable electronics. *Adv. Mater. Technol.* **3**, 1–11 (2018).
6. Y. H. Kang, C. G. Choi, Y. S. Kim, J. K. Kim, Influence of seed layers on the vertical growth of ZnO nanowires. *Mater. Lett.* **63**, 679–682 (2009).
7. J. Song, S. Lim, Effect of seed layer on the growth of ZnO nanorods. *J. Phys. Chem. C*. **111**, 596–600 (2007).
8. L. E. Greene, M. Law, D. H. Tan, M. Montano, J. Goldberger, G. Somorjai, P. Yang, General route to vertical ZnO nanowire arrays using textured ZnO seeds. *Nano Lett.* **5**, 1231–1236 (2005).
9. Programmes d'Excellence en Partenariat Public Privé – PHOSPHAGEL: "Synthèse par procédé sol-gel de matériaux pour microbatteries en couches minces". Grant No. 0917013, 2009 - 2015.
10. C. A. Páez Martínez, C. Exantus, D. Dallel, C. Alié, C. Calberg, D. Liquet, D. Eskenazi, F. Deschamps, N. Job, B. Heinrichs, Water-based paintable $LiCoO_2$ microelectrodes: a high-rate Li-ion battery free of conductive and binder additives. *Adv. Mater. Technol.* **4**, 1–12 (2019).
11. M. Kokotov, A. Biller, G. Hodes, Reproducible chemical bath deposition of ZnO by a one-step method: The importance of “contaminants” in nucleation. *Chem. Mater.* **20**, 4542–4544 (2008).

12. M. Kokotov, G. Hodes, Reliable chemical bath deposition of ZnO films with controllable morphology from ethanolamine-based solutions using $KMnO_4$ substrate activation. *J. Mater. Chem.* **19**, 3847–3854 (2009).
13. S. Xu, Z. L. Wang, One-dimensional ZnO nanostructures: Solution growth and functional properties. *Nano Res.* **4**, 1013–1098 (2011).
14. D. A. Scrymgeour, J. W. P. Hsu, Correlated piezoelectric and electrical properties in individual ZnO nanorods. *Nano Lett.* **9**, 2204–2209 (2008).

Chapter 1. Kinetic optimisation of zinc oxide nanowire growth

1.1 Introduction

The scavenging of ambient energy for its subsequent exploitation has become a hot research topic in the last few years [1–7]. Energy harvesting relies on a transduction force that converts the ambient mechanical energy into electricity. This mechanical energy can have different forms such as vibrations, random motions or noise, and one of the most common transduction method takes advantage of the piezoelectric effect [8]. A piezoelectric material has the peculiarity of creating an inherent electric field when strained (direct piezoelectric effect). There are several well-known piezoelectric materials [8, 9] with a broad range of applications (*e.g.* AlN, lead zirconate titanate (PZT), ZnO, quartz, *etc.*). However, among them, ZnO has become very popular in material science over the past few years because of its wide variety of nanostructures and its dual property of being both a semiconducting and a piezoelectric material [10]. One of the most useful nanostructures that can be utilised to generate energy is the nanowire (NW). The piezoelectric properties of ZnO are linked to its crystalline asymmetry, which leads to a change in the position of atoms during deformation, and induces the appearance of an electrical dipole along the nanowire. The semiconductor property of ZnO contributes to the formation of a low current electrical potential, and allows the supply of microbattery storage systems.

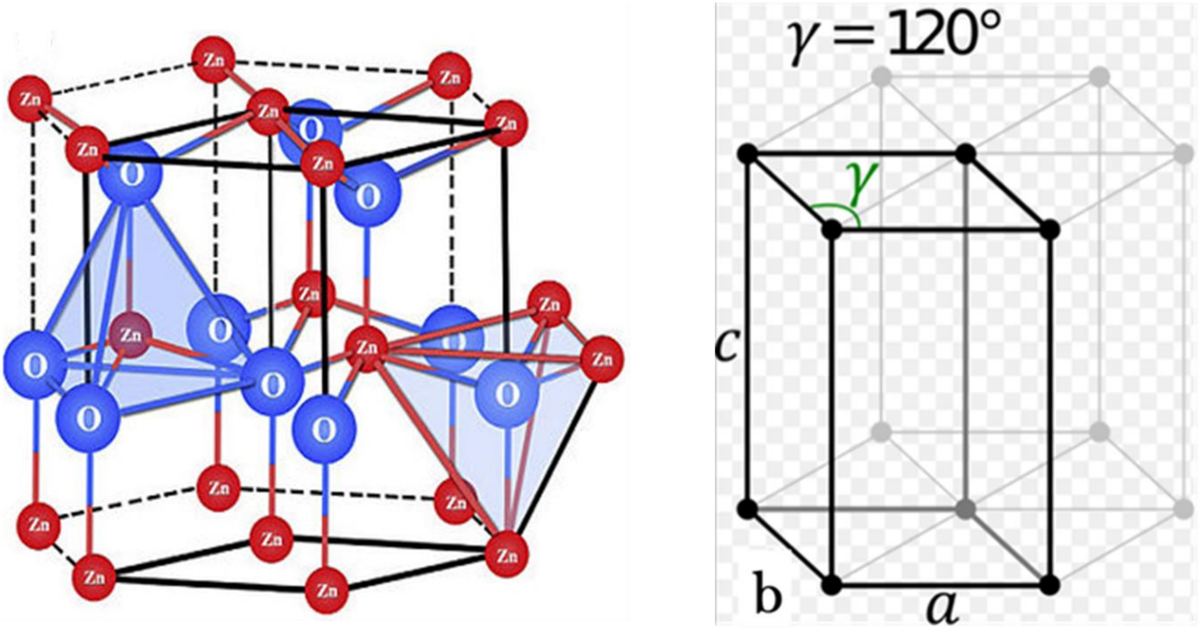

Figure 1.1. Preferential growth of ZnO NWs along 002 axis (c-axis). Reproduced from [11].

In order to limit the recombination of piezoelectric charges between NWs, it is required that the NWs are well aligned along the c-axis (002) (Figure 1.1) [11]. Hinchet *et al.*, showed that thin and long hexagonal flat ended shape NWs improve the piezoelectric performances [12, 13].

In the literature, one can find numerous bottom-up approaches to grow ZnO nanostructures, such as vapor-solid and vapor-liquid-solid processes (vacuum processes consisting in the reaction of precursors in a vapor phase and their deposition on a substrate surface) or electrochemical deposition (process that uses oxidation and reduction of one material onto the surface of another material through an electric current) [14–17]. However, these methods require high temperatures (400-700 °C) and low pressures (10-20 Pa), conductive substrates, or acid-resistant environments that make them difficult to be integrated into standard fabrication processes and future flexible electronics. In order to make the growth process of ZnO nanostructures more energy efficient and cost-effective, the temperature of the process should ideally be reduced below 100 °C. Hence, the chemical bath deposition (CBD) of ZnO is attractive and widespread due to its simplicity and environmentally friendly conditions. The CBD works on the principle of the controlled nucleation of the desired compound from a solution of its constituents, followed by a growth of the nucleus on a substrate and the formation of thin films.

To grow ZnO NWs, a crystalline material with similar crystallographic lattice constants ($a = b = 0.325$ nm; $c = 0.520$ nm) is the best choice in order to obtain aligned and high-quality NWs

[18]. Thus, NWs can be grown directly by using materials such as gold (a = b = c = 0.408 nm), wurtzite gallium nitride (a = b = 0.319 nm; c = 0.518 nm), sapphire (a = b = 0.480; c = 1.310 nm), where vertical growth only is observed. Another way to grow ZnO NWs is the deposition of a layer of zinc oxide nanoparticles using ZnO or zinc acetate, called seed layer, before the growth of ZnO NWs. This layer allows the deposition of ZnO NWs on a wide range of substrates, as the growth and proper orientation of the NWs are triggered by the seed nanoparticles [18–21]. The quality of the seed layer, offering adequate nucleation sites for ZnO growth, is a key factor for obtaining well-oriented and homogeneous NWs arrays [22, 23].

The classical solution-based CBD synthesis leads to epitaxial growth of ZnO nanostructures in aqueous solution in the presence of zinc nitrate and hexamethylenetetramine (hexamine) as precursor materials at temperatures lower than 100 °C. The major drawback in the CBD method is the slowness of the growth process: in some cases, reaching the appropriate length for the ZnO (a few µm) requires a time of about 10-30 h (growth rate between 2-7 nm min^{-1}) and the substrates must be placed into fresh growth solutions repeatedly [24]. The very large extent of homogeneous nucleation (formation of ZnO in the solution) in comparison with heterogeneous nucleation or heteronucleation (formation of ZnO on the seeded substrate) is the main reason for this problem [25]. Heterogeneous nucleation leads to the consumption of the precursor materials necessary to grow ZnO NWs on the substrate. The result of the homogeneous nucleation is ZnO settlement at the bottom of the solution container which leads to a loss of the majority of the precursor materials and reduction of the NW growth.

Several methods have been suggested in order to increase the growth rate of ZnO NWs grown by CBD. It is possible to reduce the time needed to grow NWs by using a microwave-assisted solution-based method; this aims at accelerating the crystal growth *via* a rapid increase of the precursor solution temperature [26]. The main disadvantage of the microwave-assisted CBD method is that it increases both the heterogeneous and the homogeneous process rates and, thus, the loss of the precursor materials would be faster as well. Another method implemented for increasing the ZnO NWs growth rate is called the preferential growth [27]. This method involves the addition of ammonium hydroxide and polyethylenimine (PEI) to the precursor solution. In the presence of both PEI and ammonium hydroxide, formation of ZnO in the bulk solution can be effectively prevented while ZnO wires still grow on the seeded substrate at a reasonably high rate. Furthermore, PEI preferentially adsorbs onto ZnO NWs lateral faces, thus inhibiting radial growth in favour of axial growth. This results in longer and thinner NWs, a morphology that is favourable for high piezoelectric performances [28, 29]. Kokotov *et al.* deposited ZnO NWs using an amino acid-induced self-assembly strategy [25]. The substrate was activated by a simple potassium permanganate solution treatment that forms Mn-(hydroxy)-oxide deposits on the surface; these deposits act as an efficient seed layer. In small vials (10 mL), 5 µm long NWs could be grown in 40 min *(i.e.* 125 nm min^{-1}), which is very fast compared to most processes [30].

The objective is to grow well aligned and separated NWs with an aspect ratio (Length/Diameter) higher than 50, with a flat ended hexagonal shape.

Here we report a simple process to manufacture a homogeneous arrangement of flat ended hexagonal ZnO NWs, well aligned along the c-axis through a chemical bath deposition (CBD) method. The process developed in the present work needs to be suitable for large-scale manufacturing (*i.e.* minimum 20 nm min^{-1} growth speed), and to provide a micrometric layer of well-aligned NWs. To that aim, Kokotov's synthesis process [31, 32] was optimised for growing the ZnO NWs. Before the CBD, a uniform ZnO seed layer was first prepared on the substrate by combining a simple low-cost sol-gel process and a spin-coating technique. A ZnO seed layer was preferred to permanganate activation of the substrate, as the latter technique leads to NWs arrays with poor homogeneity over large substrate. To ensure a suitable growth speed, a kinetic study was completed by controlling the parameters that have an impact on the synthesis and coating process. Finally, the obtained materials were characterised by environmental scanning electron microscopy (ESEM) to measure length and diameter.

1.2 Experimental

The de-ionised (DI) water used in all experiments was prepared in a Purelab Flex purification system (Elga LabWater) and had a resistivity of 18.2 MΩ cm. ZnO NWs were grown by chemical bath deposition (CBD) onto glass microscope slides (Superior Marienfeld) according to the following procedures.

1.2.1 Reproduction of growth procedure from Kokotov et al. [25]

All substrates were first cleaned by sonication in an RBS T105 detergent solution (20 min) and rinsed by dipping the substrate in deionised water (20 min), acetone (20 min) and ethanol (20 min). They were then dried in air for 30 min at 60 °C.

Two preparations of the seed layer were studied. The first procedure consisted in the activation of the substrate by dipping the substrates 30 min at 85 °C into a 0.5 mol L^{-1} solution of potassium permanganate ($KMnO_4$, ≥ 99.0%, Sigma Aldrich) into which 50 µL of n-butanol (≥ 99.0%, Sigma Aldrich) per 20 mL of the permanganate solution were added (as a reducing agent for the $KMnO_4$). Permanganate-treated substrates were extensively rinsed in DI water (the vials containing the samples were filled with DI, which was then poured out, and this was repeated for a total of 10 rinses) and then sonicated 5-10 min in DI water in an ultrasonic bath [31]. The second procedure consisted in the preparation of a solution in ethanol of zinc acetate dihydrate ($Zn(CH_3COO)_2.2H_2O$, Sigma Aldrich, 99.9%) with a concentration of 5×10^{-3} mol L^{-1}. 1 mL of the solution was deposited onto a clean microscope slide substrate *via* the spin-coating technique. The spin coating was performed at 2000 rpm for 30 s; the whole process was repeated 5 times. Finally, calcination at 350 °C for 20 min was performed in order to decompose zinc acetate into ZnO nanocrystals which would act as nucleation sites for the subsequent growth of ZnO NWs.

After the ZnO seed layer deposition, ZnO NWs were grown by CBD. According to Kokotov *et al.* [31, 32], growth solutions were prepared using the following freshly prepared aqueous solutions: 1.0 mol L^{-1} zinc sulphate heptahydrate ($ZnSO_4.7H_2O$, 99%, Sigma Aldrich), 4.0 mol L^{-1} ammonium hydroxide (ammonium hydroxide water solution, NH_4OH, 25-30 wt.% as ammonia (NH_3), Emsure, Merck) and 50% v/v ethanolamine (2-aminoethanol, ≥ 98%, Sigma Aldrich). As the ammonium hydroxide concentration varies when reagent bottles are gradually consumed, the ammonium hydroxide solution was systematically titrated before the synthesis. The final growth solution was prepared from the stock solutions in a 160 mL polypropylene vial, by sequential addition of 13 mL of zinc salt solution, 19.5 mL of ammonia solution and 26 mL of ethanolamine solution to DI water, giving the following final concentrations: 0.1 mol L^{-1} Zn^{2+}, 0.6 mol L^{-1} NH_4OH and 1.7 mol L^{-1} ethanolamine. The amount of water was chosen so that the total volume of growth solution was 130 mL. The final pH was typically 11.1 ± 0.2. During growth, the ZnO particles formed in solution (homogeneous nucleation) can settle on the substrate. That is the reason why, immediately after preparation of the solution, the substrate was introduced inclined from vertical with the seeded side facing downwards. The reaction vial was closed and placed in an oil bath at 90 °C for 2 h. After growth, the substrate was removed from the solution, immediately rinsed with DI water to remove loose ZnO precipitates and any residual reactant from the surface, and dried in air at room temperature for 24 h. After growth, the diameter and length of the NWs were measured from environmental scanning electron microscopy (ESEM-FEG XL30 Philips, Esprit 1.9 software) images.

1.2.2 Modification of the growth procedure from Kokotov et al. [25]

The ZnO NWs growth procedure was optimised for scaling-up by simplifying the preparation of the growth solution: the $ZnSO_4$ powder (3.74 g) was directly dissolved into 19.5 mL of 4.0 mol L^{-1} NH_4OH solution. The previous solution and 13 mL of ethanolamine were added to 97.5 mL of DI water. The growth solution (130 mL) was prepared in a 160 mL polypropylene vial, giving the following final concentrations: 0.1 mol L^{-1} Zn^{2+}, 0.6 mol L^{-1} NH_4OH and 1.7 mol L^{-1} ethanolamine (Figure 1.2). The solution was vigorously stirred until the pH stabilised at ~11.1 ± 0.2 (10 min). The substrate was introduced inclined from vertical to prevent particles which might form in the solution from settling on the downward-facing seeded side of the substrate. The reaction vial was closed and placed in an oil bath at 90 °C for 2 h. After growth, the substrate was treated as for the non-optimised process. The process was repeated 10 times in order to evaluate the reproducibility of the optimised process.

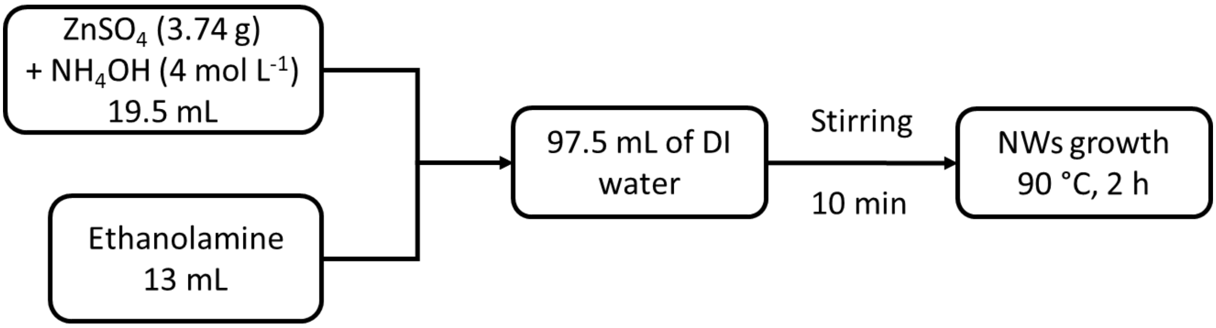

Figure 1.2. Simplified process diagram for the synthesis of ZnO NWs.

During ZnO NWs growth, a combined pH and temperature probe was introduced into the growth solution and temperature and the pH was monitored every 5 min. The monitoring was done for 6 samples. Moreover, photographs of the device (vial + substrate) were taken to follow the visual evolution of the solution after 30 min, 60 min, 90 min and 120 min.

After growth, the diameter and length of the NWs were measured from environmental scanning electron microscopy (ESEM-FEG XL30 Philips, Esprit 1.9 software) images.

1.2.3 Growth kinetics study

The growth rate of the NWs throughout the synthesis has been established by a kinetics study consisting in two different experiments. The first experiment consisted in the determination of the NWs growth speed all along the synthesis (Exp A1). To do so, four syntheses were done in parallel with one substrate in each solution coming from the same growth stock solution; the latter was prepared according to the modified growth procedure from section 1.2.2. The syntheses were started at the same time and stopped at different times: 30 min, 60 min, 90 min and 120 min. At the end of each synthesis, the solution was introduced into an ice bath in order to stop the homogeneous growth process, and the substrates were removed, washed with DI water and dried at room temperature. The growth solution was filtrated through filter paper (VWR grade 474 quantitative filter paper) using Büchner filtration apparatus and 5 mL of the filtrated solution were analysed by Induced Coupled Plasma Mass Spectroscopy (ICP-MS, Thermo Scientific iCAP 6500) to evaluate the quantity of zinc remaining in solution. ICP-MS is a mass spectrometer that uses a plasma to ionise the samples and detects quantitative trace of elements. The substrates were weighed after seeding, after growth, and after the homogenous ZnO was removed from the upward facing side of the substrates by cleaning it with a cotton swab moistened with 0.1 mol L^{-1} HCl solution. The solid recovered on the filter was dried and weighed as well.

The second experiment (Exp B1a) consisted in the introduction of four slides in the same bath and their removal at 30 min, 60 min, 90 min, 120 min, while another slide was introduced in the reactive vial at the same time. To obtain additional results for intermediate times, four substrates were introduced at the same time in one chemical bath and were withdrawn at 15 min, 30 min (control sample), 45 min, 60 min (control sample) while another substrate was introduced in the reactive vial at the same time (Exp B1b). Thus, in these experiments, four glass slides were always present in the growth solution as substrates. Directly after removal, the substrates were cleaned with DI water, and dried at room temperature. The substrates were weighed after seeding, after growth, and after the homogenous ZnO was removed from the upward facing side of the substrates. Diameter and length of the NWs were measured from environmental scanning electron microscopy (ESEM-FEG XL30 Philips, Esprit 1.9 software) images. To assess the reproducibility, the two experiments (Exp A1 and B1) were repeated a second time (Exp A2 and B2).

1.2.4 Optimisation of the NW growth process from the kinetics study

The results from temperature monitoring and kinetics study (see results and discussion section) led to further optimisation of the growth procedure. In order to reach faster the growth temperature, water was preheated before adding the reactants. The water was preheated at 40 °C, 60 °C, 70 °C and 80 °C, before the reactants were added. The $ZnSO_4$ powder (3.74 g) was directly dissolved into 19.5 mL of 4.0 $mol\,L^{-1}$ NH_4OH solution. The previous solution and 13 mL of ethanolamine were added to 97.5 mL of preheated DI water. The growth solution (130 mL) was prepared in a 160 mL polypropylene vial, giving the following final concentrations: 0.1 $mol\,L^{-1}$ Zn^{2+}, 0.6 $mol\,L^{-1}$ NH_4OH and 1.7 $mol\,L^{-1}$ ethanolamine. The solution was vigorously stirred until the pH stabilised at ~11.1 ± 0.2 (10 min). One substrate was introduced inclined from vertical to prevent particles from settling on the downward-facing seeded side of the substrate. The reaction vial was closed and placed in an oil bath (90 °C) until the temperature inside the growth solution was stable at 80 °C. At the end of the experiment, the slide was washed with DI water and dried at room temperature. The morphology of the ZnO NWs was characterised by environmental scanning electron microscopy (ESEM-FEG XL30 Philips, Esprit 1.9 software) and the length and the diameter of the NWs were measured.

1.2.5 Homogeneity of the temperature

Note that preliminary experiments including a magnetic stirrer in the reaction vessel, using a special sample holder, were also performed so that the growth solution was mixed during the process. Although encouraging results were obtained (*i.e.* better orientation of the NWs), the subject change at mid-term of the thesis made it impossible to continue the experiments and obtain a consistent dataset. Further trials should be performed to assess the impact of stirring on the NW quality.

Three different heating systems were studied. In System A, an oil bath was heated by a PID controller to 90 °C on a hot plate with the temperature probe placed into the oil (Figure 1.3a). The reaction vessel was then placed into the preheated oil. Contrarily, in System B, the temperature probe was placed directly into the reaction vessel instead of into the preheated oil bath (Figure 1.3b). System C was homemade: it consisted of building a dual-wall system made of two propylene vials where water is heated at 90 °C and circulates constantly (Figure 1.3c). A thermometer was added in the growth solution to monitor the temperature evolution.

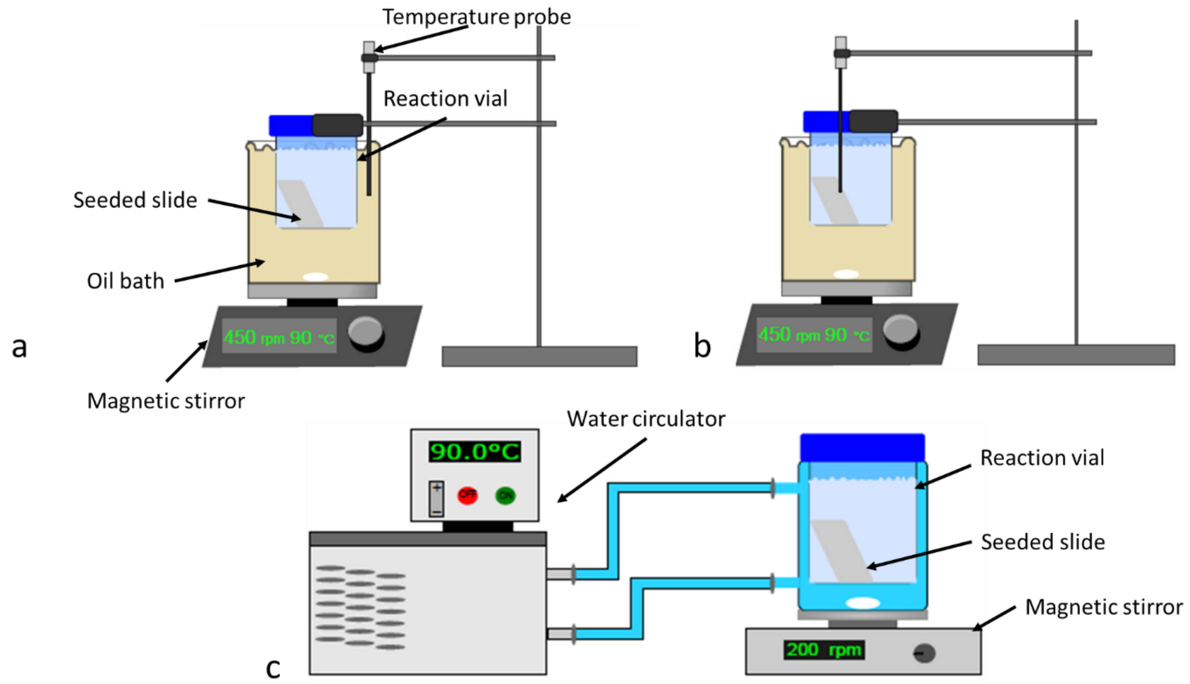

Figure 1.3. Different heating systems studied. (a) A system: oil bath heated by a PID controller to 90 °C on a hot plate with the temperature probe placed into the oil; (b) B system: oil bath heated by PID controller to 90 °C on a hot plate with the temperature probe placed directly into the reaction vessel; (c) C system: dual-wall system made of two propylene vials where water is heated at 90 °C and circulates constantly.

1.3 Results and discussion

1.3.1 Reproduction of growth procedure from Kokotov *et al.* [25]

Two different seeding procedures were studied in order to reproduce the initial procedure and adapt it to achieve the objectives of the project, which is to grow a homogeneous arrangement of flat ended hexagonal ZnO NWs, well aligned along the c-axis, at a growth rate faster than 20 nm min^{-1}. The first procedure, *via* the activation of the glass substrate, consisted in immersing the glass slide into a $KMnO_4$ solution followed by repeated rinsing. The extensive rinsing is important to prevent nucleation of ZnO in the bulk of the deposition solution from Mn-containing particles detached from the treated substrate. The activation allows facile nucleation due to adsorption of Zn species on the hydrated manganese oxide nuclei [31]. The second procedure consisted in the deposition of a solution of zinc acetate, dissolved in ethanol, onto a glass substrate using spin-coating. After calcination, ZnO nuclei are formed onto the surface which will later give rise to ZnO NWs. The two procedures were then followed by the growth of NWs using the CBD method, and these NWs were characterised by ESEM.

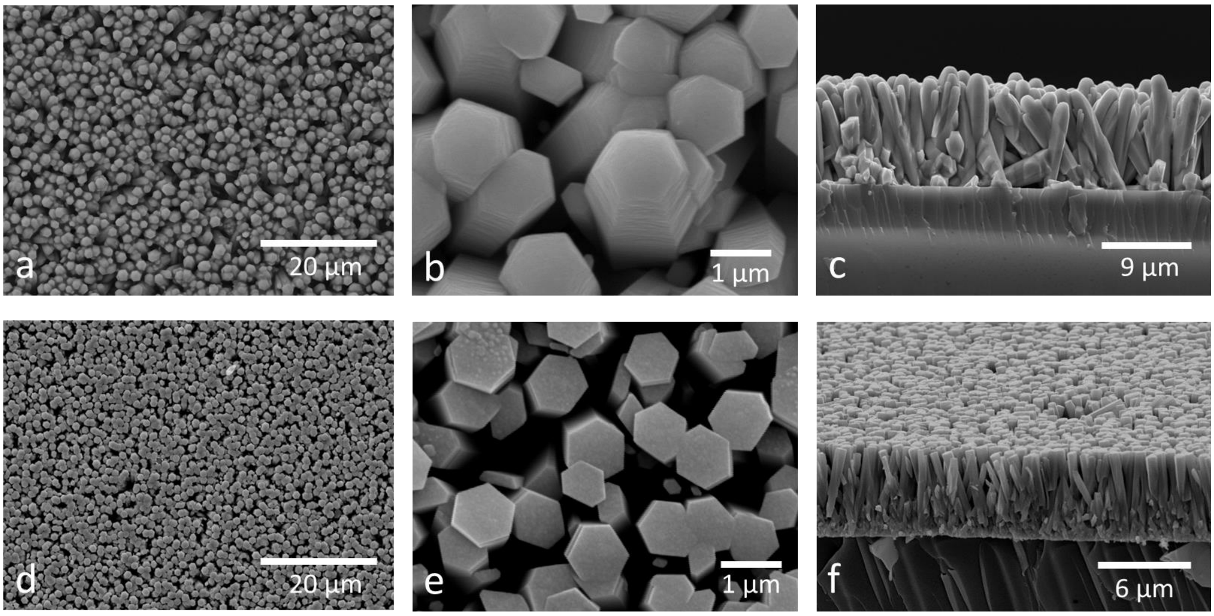

Figure 1.4. ESEM images of NWs grown with $KMnO_4$ activation: (a) general view, (b) top view and (c) side view. NWs grown with ZnO seed layer: (d) general view, (e) top view and (f) side view.

Figure 1.4a shows NWs grown on the substrate activated with $KMnO_4$. The deposit is not uniform in terms of NWs density all over the substrate. This procedure leads to pencil tip ended NWs whose length and diameter are respectively 11 µm and 1.2 µm (Figure 1.4b and Figure 1.4c). The procedure using a ZnO seed layer leads to a more homogeneous growth and density as shown in Figure 1.4d. The NWs show a length of 7 µm and a diameter of 0.8 µm (Figure 1.4e and Figure 1.4f). The seed layer method is thus preferred to the substrate activation as it leads to a homogeneous arrangement of flat ended hexagonal ZnO NWs, well aligned perpendicular to the substrate.

1.3.2 Simplification of the growth procedure from Kokotov *et al.* [25]

As explained in 1.3.1, using a seed layer leads to hexagonal-shaped flat ended NWs whose length and diameter are respectively 7 µm and 0.8 µm (Figure 1.5a and Figure 1.5b).

A first modification consisted in dissolving all the reactant directly in the final amount of water. The results show inhomogeneous growth of the NWs (Figure 1.5c and Figure 1.1d): NWs are oriented in any direction and do not show the expected hexagonal flat ended shape.

In the simplified process, zinc sulphate was first dissolved in the ammonium hydroxide solution. The direct dissolution of zinc precursor in ammonium hydroxide leads to the formation of stable species $[Zn(NH_3)_4]^{z+}$, which will lead to the ZnO precursor, $Zn(OH)_2$, when the growth solution is heated at 90 °C [32]. Two solutions were added to water so that the total volume of the solution was 130 mL: the first solution contained the complexed zinc and the second solution was pure ethanolamine. After combination, the mixture was stirred until pH was stabilised and heated for growth. The NWs obtained after growth with the simplified process are well formed with hexagonal flat ended shape and they are oriented perpendicular to the substrate as shown in Figure 1.5e and Figure 1.5f. They show a diameter of ~0.8 µm and a length of ~6 µm, values which are close to those of the growth procedure from Kokotov *et al.* [25]. The optimised procedure leads to homogeneous NWs and allows to save 50-60% of preparation time (at laboratory scale) in the preparation of the growth solution.

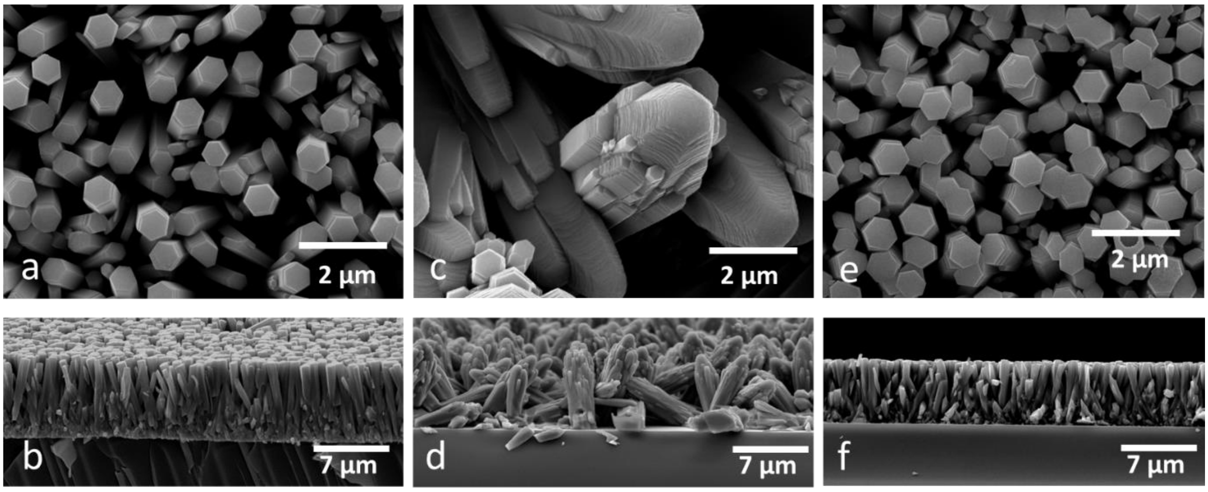

Figure 1.5. ESEM pictures of the NWs obtained by different procedures. (a) and (b): top and side view of initial procedure; (c) and (d): top and side view with first modified procedure; (e) and (f): top and side view with simplified procedure.

The reproducibility of the growth process has been studied for the simplified procedure. The synthesis was fully reproduced 10 times and the morphology of the NWs obtained after growth was characterised. The two graphs in Figure 1.6a and Figure 1.6b respectively show the length and the diameter of the NWs for each distinct synthesis. The average diameter on Figure 1.5b is about 0.95 ± 0.15 µm. Even if the diameter varies from 0.75 µm to 1.12 µm, six measurements out of ten are within the standard deviation (blue frame). The average length is about 6.5 µm ± 0.5 µm and seven measurements out of ten are in the standard deviation.

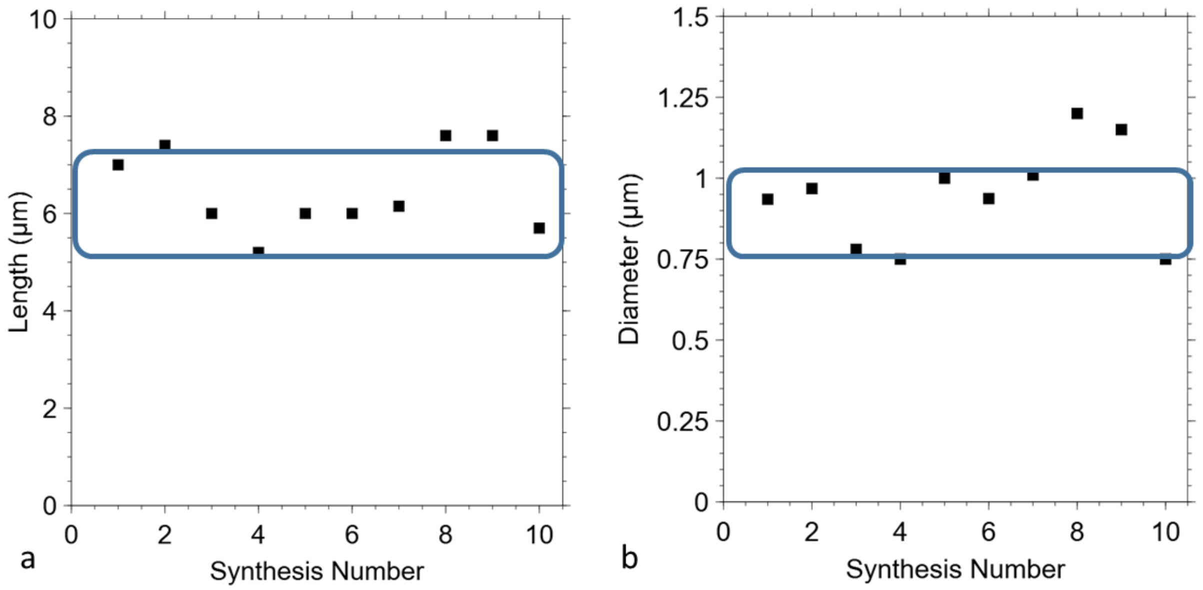

Figure 1.6. Synthesis reproducibility in terms of (a) length and (b) diameter of the NWs**.**

1.3.3 Growth kinetics study

1.3.3.1 Study of the growth process

The visual aspect and evolution of the solution was observed during the whole growth and linked to the pH and temperature monitoring. The temperature in the growth solution stabilises at ~80 °C while the temperature of the oil bath is set at 90 °C. The temperature and pH values were stable from 50 min to the end of the synthesis. During the growth of the NWs, four steps can be observed, as shown in Figure 1.7:

(i) Between 15 and 30 min, the microscope slide is becoming opaque, which is an indication of growth on the substrate (heteronucleation process), while the solution remains clear (Figure 1.7a).

(ii) Between 30 and 60 min, besides the growth on the substrate, the solution becomes opaque, due to the formation of ZnO in solution (homogeneous nucleation – Figure 1.7b).

(iii) Between 60 and 90 min, the homogeneous ZnO precipitates at the bottom of the vial (Figure 1.7c).

(iv) Between 90 and 120 min, the solution becomes clear again and the microscope slide is coated with the NWs (opaque slide - Figure 1.7d).

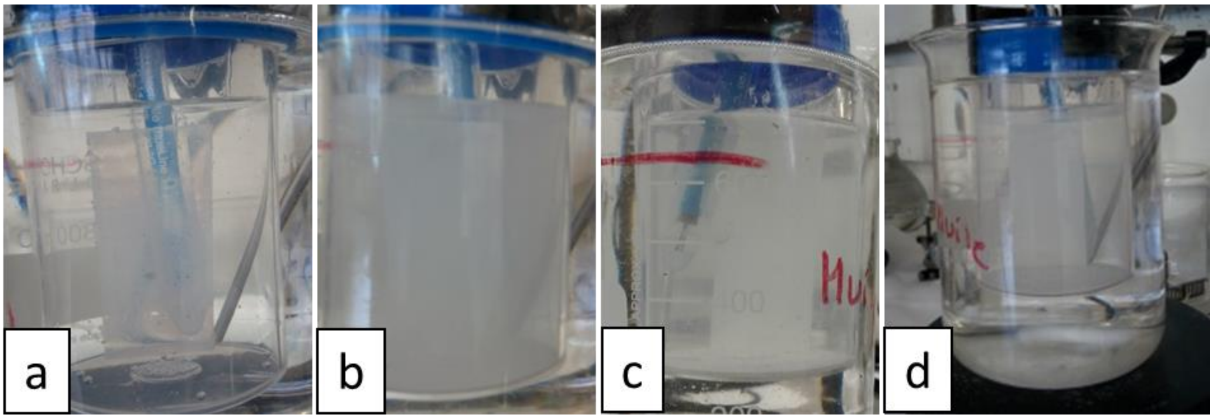

Figure 1.7. Pictures showing the evolution of the synthesis solution after (a) 30 min, (b) 60 min, (c) 90 min and (d) 120 min.

In order to monitor the reaction medium during ZnO nanowire growth, a combined pH and temperature probe was introduced in the vial. Temperature and pH were recorded every 5 min for six different syntheses (Figure 1.8a and Figure 1.8b). The growth solution does not reach the set temperature; the growth is thus occurring at 80 °C instead of 90 °C. The pH decreases when the temperature increases. The temperature and pH values are stable from 50 min to the end of the synthesis. The graphs in Figure 1.8c and Figure 1.8d show the temperature and pH variance. The variance measures the dispersion of the values of a variable; the variance (ν) of a set of *n* equally likely values can be written as:

$$v = \frac{\sum(X_i - \bar{X})^2}{n} \tag{1}$$

where X_i is the ith value of variable X, $\bar{X}$ is the mean of the values of this variable, and *n* the total number of values. In other words, the variance is defined as the average of the squared differences from the mean.

From one synthesis to another, one observes a large temperature and pH variation from the beginning of the syntheses to 45-50 min heating. This variation of temperature is probably due to the regulation of the heating plates, or the level of liquid in the pH probe. After numerous experiments, it was finally found that the maximum temperature reached in the solution depended more on the liquid level of KCl solution inside the pH probe than on other parameters (completely filled probe or ¾ filled already induced measurable differences). The KCl solution partly evaporated during the 2 h of the experiment and we did not fill the probe for each new experiment, which we should have done.

The pH decrease observed is not due to an OH^- consumption: it is linked to the temperature variation, as shown in Figure 1.8e: this figure reports the evolution of pH values of a NH_4OH

solution (prepared with pH = 11.2 at room temperature) placed in the oil bath at 90 °C while its temperature increases, then decreases when stopping the bath heating.

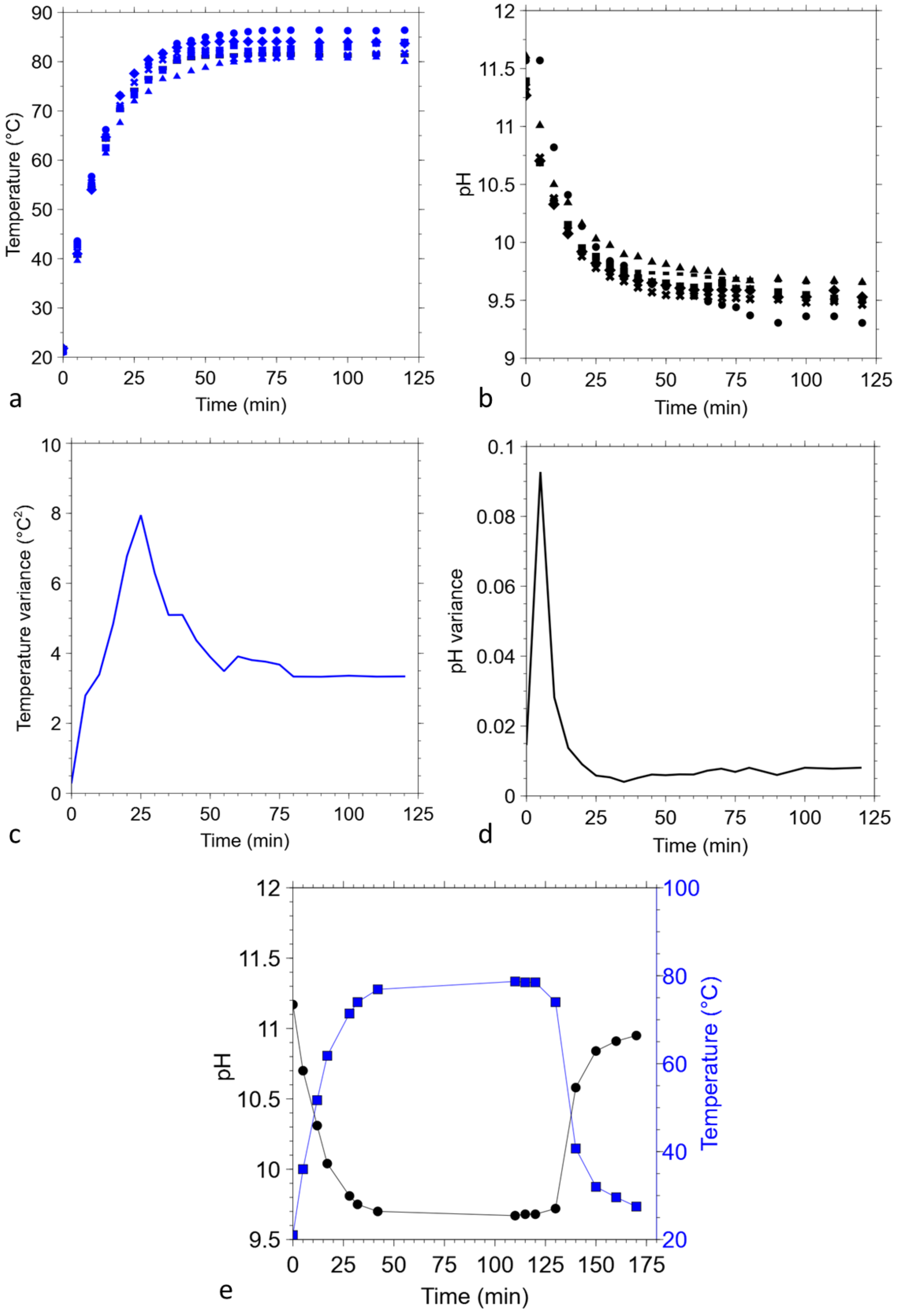

Figure 1.8. (a) Temperature monitoring and (b) pH monitoring, (c) temperature variance and (d) pH variance, (e) monitoring of temperature (■) and pH (●) of the NH$_4$OH solution.

According to Richardson *et al.* [32], the mixing of $ZnSO_4$ and NH_4OH precursors leads to the formation of prevalent stable species $[Zn(NH_3)_4]^{z+}$ at pH = 11 (25 °C). The speciation plots (extracted from Richardson *et al.* [32]) shown in Figure 1.9a indicate that the increased solubility is due to the formation of the zinc tetra-amine complex, $Zn(NH_3)_4^{2+}$, as the prevalent species is Zn(II) in that pH range (clear solution). When the solution is heated up, the pH range where $Zn(NH_3)_4^{2+}$ is stable shrinks and is shifted to lower pH values (pH = 7 to 9). According to Figure 1.9b, a decrease of Zn(II) solubility at pH = 11 is observed when the solution is slowly heated from room temperature to 80 °C. At pH = 11, one of the prevalent species is $Zn(OH)_2$, which precipitates. The solution can remain near equilibrium (clear) by depositing ZnO onto the pre-existing seeds that were produced on the substrate (heteronucleation). This explains the opacity of the slide on Figure 1.7a, while the solution remains clear. The formation of a white precipitate when the solution gets close to 80 °C (30-60 min growth in our case) is due to the rapid decrease of solubility of Zn(II) species, which leads to transition reaction from $[Zn(NH_3)_4]^{z+}$ to $Zn(OH)_2$. This decrease in solubility leads to a supersaturation large enough to initiate the nucleation of epitaxial ZnO on the substrate and to precipitate ZnO particles in solution. This homogeneous nucleation process can limit the growth of ZnO NWs due to fast reactant consumption [32].

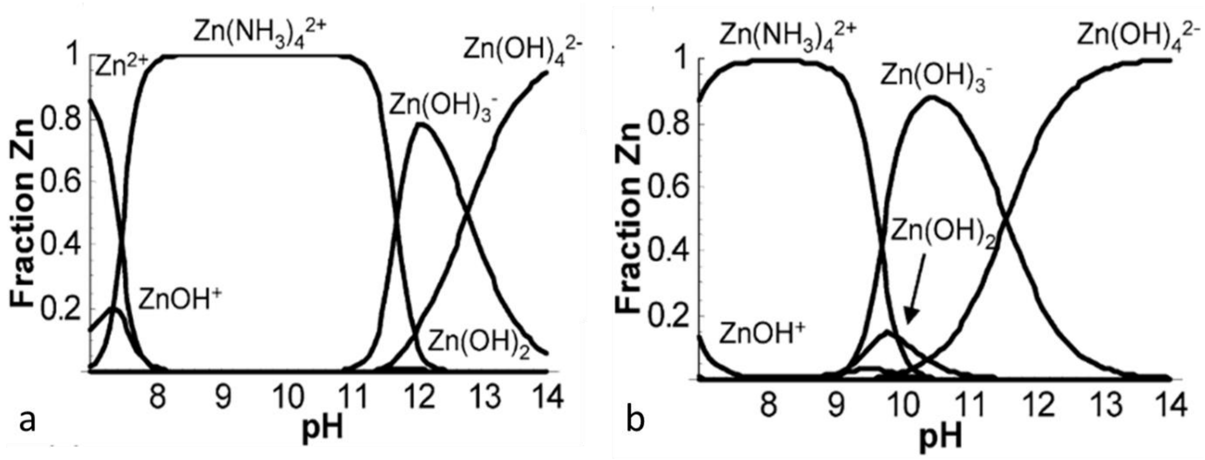

Figure 1.9. Speciation in an aqueous solution of dissolved Zn(II) *vs.* pH (a) at 25°C and (b) at 90 °C. Reprinted from reference [32].

In order to complete the study of the growth process, the distribution of the Zn (II) species was determined after different synthesis times (Exp A1). The time spans were chosen according to the visual aspect of the solution observed in Figure 1.7. Four syntheses have been done in parallel. They were started simultaneously and stopped after different times (Exp A1): 30 min, 60 min, 90 min and 120 min. At the end of each synthesis, the reaction vial was introduced into an ice bath to stop the homogeneous growth process. The growth solution was filtrated using Büchner filtration.

The proportion of zinc on the glass substrate (homogeneous and NWs), in solution and on the filter was evaluated. During growth, ZnO can be formed on the seeded side of the glass substrate (NWs), on the unseeded side of the glass substrate (settling of homogeneous ZnO from the solution), and in solution; the latter phenomenon leads to the formation of a white precipitate (homogeneous ZnO) that mostly settles at the bottom of the reaction vessel and is recovered by filtration.

The substrates were weighed after seeding, after growth, and after the ZnO particles due to homogeneous nucleation were removed from the unseeded upward-facing side of the substrates. The quantity of zinc in solution was evaluated by ICP measurements. The precipitate was weighed in order to evaluate the quantity of homogeneous ZnO formed in solution during growth process.

The percentage of zinc under the different forms was evaluated from the initial quantity of zinc added in the solution before growth. Table 1.1 shows the time evolution of the percentage of NWs grown on the seeded side of the slides, the percentage of homogenous ZnO settling on the upward facing side of the slides, the percentage of the filtered ZnO and the percentage remaining in solution. An increase of the percentage of the NWs and of the homogeneous ZnO deposited on the slide with time is observed (Table 1.1).

Table 1.1. Evolution of the percentage of different ZnO forms during growth.

Time (min)	**% ZnO NWs (on slide)**	**% ZnO homogeneous (on slide)**	**% ZnO filtered homogeneous (in solution)**	**% ZnO in solution**
30	0.6	0.0	0	100
60	3.0	0.7	21	85
90	5.0	2.0	30	66
120	7.0	3.0	15	80

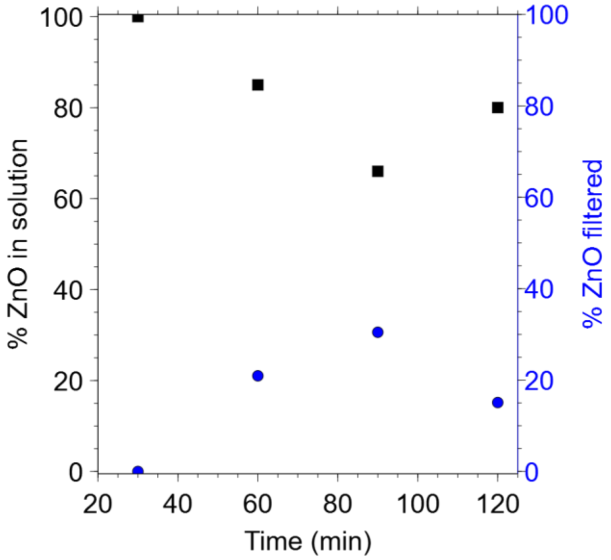

Figure 1.10. Evolution of ZnO during growth. (■) Percentage of ZnO in solution, (●) percentage of ZnO collected *via* Büchner filtration.

Figure 1.10 shows the (mass) percentage of ZnO in the solution and the percentage of homogeneous ZnO material collected *via* Büchner filtration during growth as a function of time. From the beginning of the growth to ~90 min, the percentage of ZnO in solution decreases to 60% while the percentage of precipitated homogeneous ZnO increases to 30%. At 90 min, the tendency is reversed: the fraction of solid ZnO decreases while that in solution increases. This situation is probably due to the dissolution of homogeneous ZnO material. Shaojing Bu *et al.* [33], showed that the growth of ZnO NWs can be described based on the chemical equilibrium of dissolution-regrowth in solution [34, 35]. The thermodynamic equilibrium for $ZnO_{(s)}$-H_2O system can be represented by:

$$ZnO_{(s)} + (n-1)H_2O \leftrightarrow Zn(OH)_n{}^{z-n}{}_{(aq)} + (n-2)H^+ \quad (2)$$

Figure 1.10 suggests that, at equilibrium, the dissolution of ZnO and growth of NWs occur simultaneously. The presence of $ZnO_{(s)}$ in the alkaline environment moves the equilibrium of Equation 2 to the right because of the lower concentration of $Zn(OH)_2{}^{z-n}{}_{(aq)}$ observed after 90 min of growth.

This first study has shown that the visual aspect of the solution during growth and the growth solution temperature evolution are linked. When the temperature is close to 80 °C, the growth of the nanowires starts. During synthesis, a competition with the ZnO formed in solution limits the growth of NWs on the substrate. Moreover, it has been shown (Figure 1.10) that the growth of NWs is based on a dissolution-regrowth equilibrium at the end of the growth procedure when the reactants get depleted.

1.3.3.2 Kinetics study

A kinetic study was performed in order to follow the evolution of the NW morphology and determine their speed growth throughout the growth process. The NW growth speed was determined from length and diameter measurements on ESEM images. In Exp A1, four syntheses were done in parallel with one substrate in each solution coming from the same growth stock solution prepared according to the modified growth procedure from section 1.2.2.

The ESEM pictures in Figure 1.11 show the evolution of the NW morphology at different times. The NW length and diameter are reported in Table 1.2. The ESEM top view at 30 min growth (Figure 1.11a) shows that the morphology of the NWs is not defined (rough surface). The ESEM side view (Figure 1.11b) shows that the NWs are not oriented along the c axis. At 60 min growth, the hexagonal morphology starts to be visible. At the root of the NWs, the growth of NWs which are not oriented perpendicularly to the substrate seems hampered by the well-oriented ones (Figure 1.11d). From 90 min growth on, the hexagonal flat-ended shape of the NWs is visible (Figure 1.11e and Figure 1.11g).

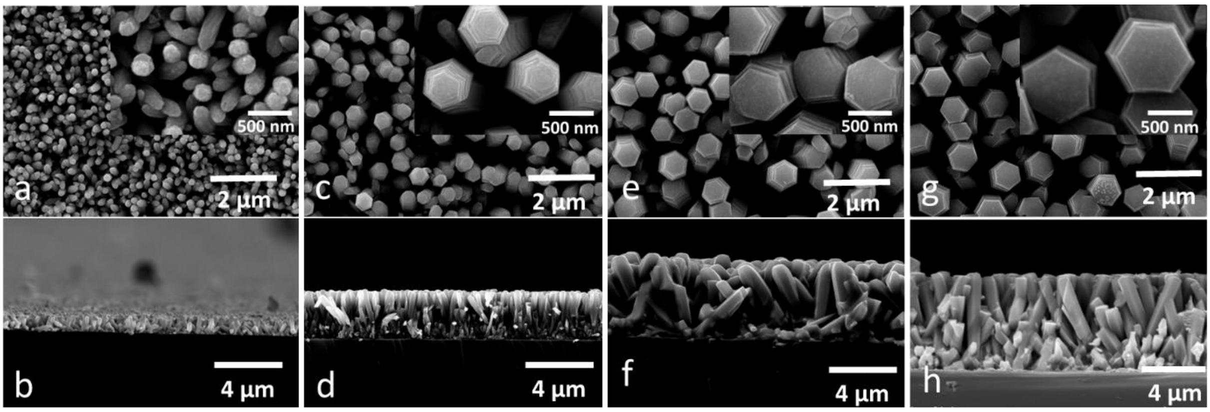

Figure 1.11. ESEM images of the evolution of ZnO NWs during growth process with inserted zoom of NWs. 30 min (a) top view and (b) side view; 60 min (c) top view and (d) side view; 90 min (e) top view and (f) side view; 120 min (g) top view and (h) side view.

According to Table 1.2, the length and diameter of the NWs increase with time. From the values obtained, it is then possible to evaluate the length and diameter growth speed using

Equations 3 and 4, where Lt_i and Lt_{i+1} are the average NW length and Dt_i^2 and Dt_{i+1}^2 the surface area at times t_i and t_{i+1}.

$$Length\ growth\ speed = \frac{L_{ti+1} - L_{ti}}{ti_{+1} - ti} \tag{3}$$

$$Diameter\ growth\ speed = \frac{{D_{ti+1}}^2 - {D_{ti}}^2}{4(ti_{+1} - ti)} \tag{4}$$

Table 1.2. Length and diameter obtained after different growth times for Exp A1.

Time (min)	Length (μm)	Diameter (μm)
30	0.9	0.24
60	2.9	0.68
90	4.7	0.73
120	6.0	0.95

The graph in Figure 1.12 has been plotted using Equation 2 for the y-axis and the middle time between two measurements were used for the x-axis. The graph shows the length growth speed (nm min^{-1}) and the diameter growth speed (nm min^{-1}) as a function of time.

Between 0 and 45 min, the trend line shows an increase of the length and diameter speed growth. In accordance with the temperature monitoring during this period (increase of temperature up to 80 °C on Figure 1.8 a), the $Zn(OH)_2$ species concentration increases at the expense of Zn(II), which leads to the formation of ZnO NWs on the seeded substrate. From 30 min on, the homogeneous nucleation in solution begins. The two growth processes (homogeneous in solution and heterogeneous on the substrate) occur simultaneously. During the second phase (45-70 min), the diameter and length growth speed tend to decrease due to the large consumption of the reactants. This large consumption leads to an increase of the concentration of homogeneous ZnO in solution (opacity of the solution). The diameter growth speed then tends to increase again from ~70 min on. The increase of the diameter growth speed could be explained by the dissolution-reprecipitation of ZnO confirmed by results shown in Table 1.1 and Figure 1.10. From the ESEM top views at 90 and 120 min (Figure 1.11c and Figure 1.11d), it can be assumed that the dissolution-reprecipitation leads to the formation of the hexagonal flat-ended NWs. ZnO that dissolves back probably originates from homogeneous ZnO formed in solution as Table 1.1 shows that, after 90 min, the amount of homogeneous ZnO decreases and the amount of Zn (II) species in solution increases. These Zn (II) free species can precipitate back onto the existing NWs, further increasing their size and, in particular, their diameter, as shown by the results gathered in Table 1.2.

One of the objectives of this project was to reach a minimum length growth speed of 20 nm min^{-1} in order to obtain as fast as possible long nanowires and to have a process suitable for large-scale manufacturing. This experiment shows that it is possible to reach a maximum length growth close to 70 nm min^{-1}, and a maximum diameter growth speed of 3×10^{-3} µm² min^{-1}. Throughout the growth process, the length growth speed thus exceeds the target.

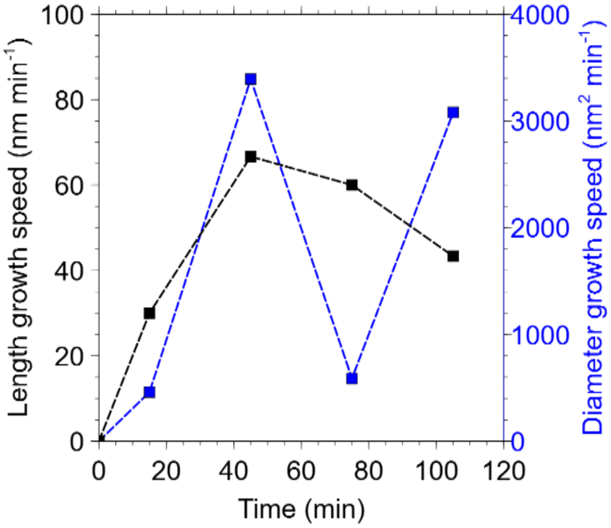

Figure 1.12. (■) Length growth speed and (🟦) diameter growth speed *vs.* time.

The second experiment consisted in introducing four slides in the same bath and to withdraw them successively, at 30 min, 60 min, 90 min and 120 min, while another substrate slide was introduced in the reactive vial at the same time (Exp B1a). To obtain additional results for intermediate times, four substrates were introduced at the same time in one additional chemical bath and were withdrawn at 15 min, 30 min (control sample), 45 min, 60 min (control sample) while another substrate was introduced in the reactive vial at the same time (Exp B1b).

The removed slides were rinsed with deionised water, dried at room temperature and characterised by ESEM.

Figure 1.13 shows the ESEM images of the compiled slides from Exp B1a and B1b which have been withdrawn from the chemical bath at 15, 30, 45, 60, 90 and 120 min. After 15 min, the growth of the ZnO NWs has not started yet, as shown in Figure 1.13a; that is the reason why no side view is shown. The ESEM images on Figure 1.13b show that the ZnO NWs are visible after 30 min. The hexagonal and flat ended shape is not well defined yet, and the side view on Figure 1.13c shows that the nanowires are growing in all directions. After 45 min growth, the nanowires start to get the hexagonal structure with a pencil-like tip (Figure 1.13d). The side view shows that the nanowires are still not well organised (Figure 1.13e). In Figure 1.13f and g the hexagonal shape of the nanowires is more pronounced.

The top views on Figure 1.13h and j show that the flat ended shape is well defined after 90 min and 120 min respectively; furthermore, the side views on Figure 1.13i and Figure 1.13k show that the growth of badly oriented NWs stops when they meet other NWs. Only the well oriented NWs (along the c axis, perpendicular to the substrate) can continue growing without being stopped. The inserts in the top views show that the hexagonal shape appears between 60 and 90 min of growth, which is in accordance with Exp A1.

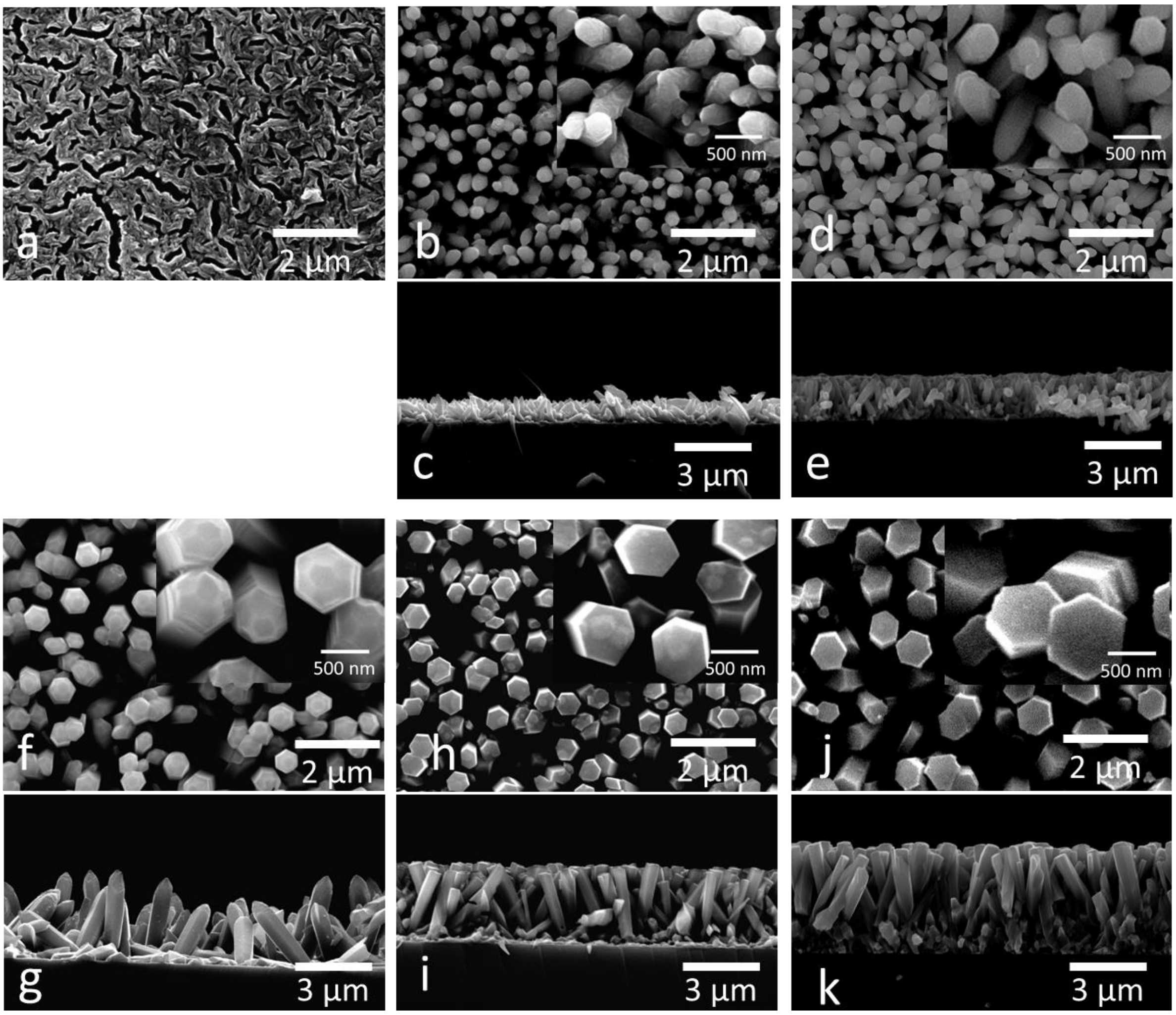

Figure 1.13. ESEM images of the evolution of ZnO NWs during growth process of Exp B1a and B1b. Slide withdrawn at 15 min: (a) top view (NWs are not visible on side view with ESEM). Slide withdrawn at 30 min: (b) top view and (c) side view. Slide withdrawn at 45 min: (d) top view and (e) side view. Slide withdrawn at 60 min: (f) top view and (g) side

view. Slide withdrawn at 90 min: (h) top view and (i) side view. Slide withdrawn at 120 min: (j) top view and (k) side view.

The length and diameter values of the removed slides are reported in Table 1.3. Compared to Exp A1, the values at 120 min are smaller. This difference in size (length and diameter) is probably due to a faster consumption of the reactants in presence of four substrates in solution instead of one. It may also be explained by the frequent opening of the vial (for removing and introducing substrates), which inevitably decreases the temperature.

Table 1.3. Length and diameter obtained after removing the slides at different growth time.

	EXP B1a		**EXP B1b**	
Time (min)	Length (µm)	Diameter (µm)	Length (µm)	Diameter (µm)
15	-[a]	-[a]	0.00	0.00
30	0.91	0.33	0.90	0.32
45	-[a]	-[a]	2.50	0.60
60	3.25	0.63	3.30	0.62
90	3.56	0.65	-[a]	-[a]
120	3.70	0.88	-[a]	-[a]

-[a] Experiment not performed.

As mentioned above, new slides were inserted while others were removed from the solution at 15, 30, 45, 60, and 90 min. Those inserted slides thus spent 105 min (Figure 1.14a top view and Figure 1.14b side view), 90 min (Figure 1.14c top view and Figure 1.14d side view), 75 min (Figure 1.14e), 60 min (Figure 1.14f) and 30 min Figure 1.14g) in the growth solution, respectively. The slides inserted at 15 and 30 min (respectively 105 and 90 min in solution) led to NWs with a length of ~3 µm and a diameter of ~300 nm (Table 1.4), which is the same size range as observed for NWs growing for around 60 min on substrates introduced from the beginning of the reaction (Table 1.3). According to these results, it is thus possible to grow NWs when the seeded substrates are introduced between 15 and 30 min, *i.e.* when the temperature of the solution gets close to 80 °C.

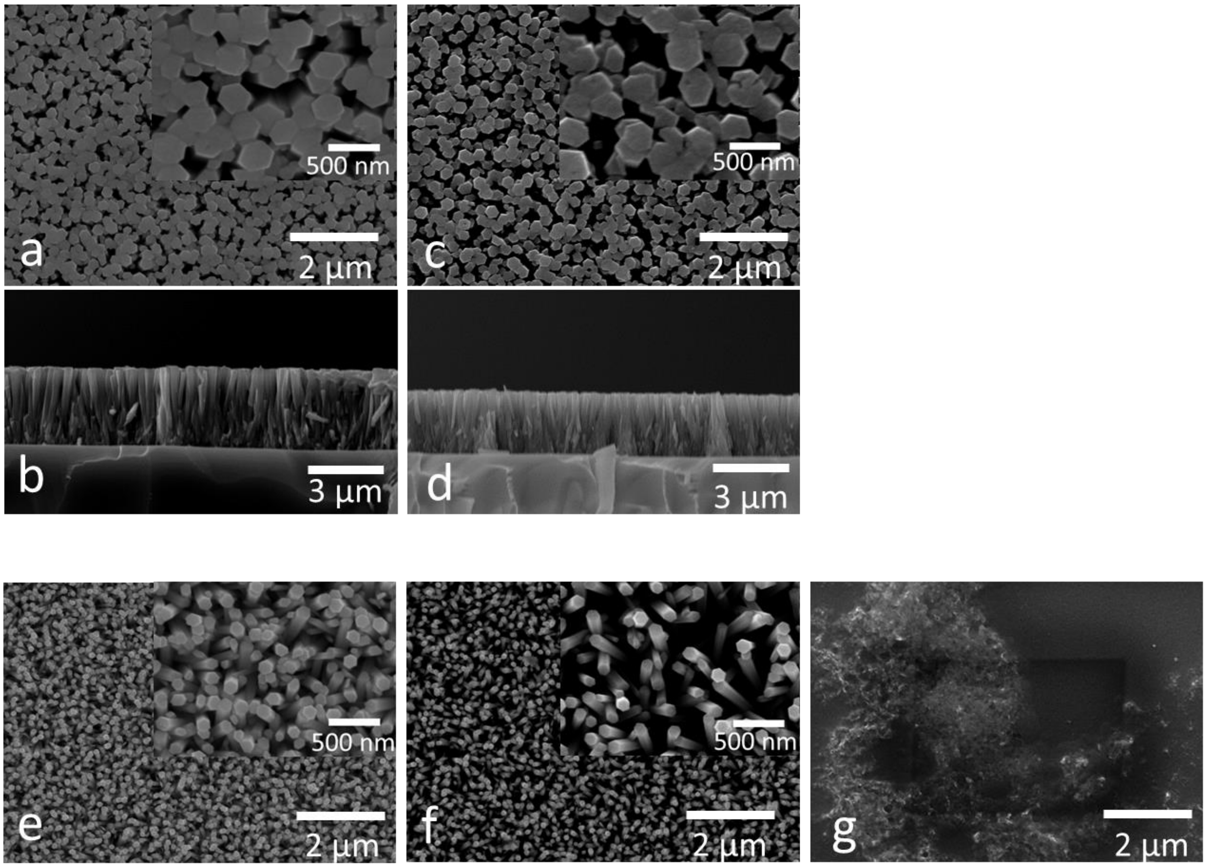

Figure 1.14. ESEM images of the growth of NWs. Slide inserted after 15 min: (a) top view and (b) side view. Slide inserted after 30 min: (c) top view and (d) side view. Slide inserted after 45 min: (e) top view. Slide inserted after 60 min: (f) (top view). Slide inserted after 90 min: (g) top view. NWs are too small to be seen on side view with ESEM for slides inserted after 45, 60 and 90 min.

Moreover, with 105 and 90 min growth time (Figure 1.14a and Figure 1.14c), the hexagonal morphology of the NWs is similar to that of the NWs after 120 min growth (Figure 1.13j and Figure 1.13k). The diameter of the NWs decreases when the slides are inserted after 45 min or more. Starting from 45 min to the end of the experiment, which corresponds to growth times shorter than 75 min, the introduced slides led to NWs with a diameter of around 100 nm, and whose length was too small to be evaluated from ESEM micrographs. This phenomenon is much certainly linked to the fast consumption of reactants by the heteronucleation and the homogeneous nucleation occurring between 30 and 60 min, as explained before (section 1.3.3.1, Table 1.1).

Table 1.4. Length and diameter of the NWs obtained after the insertion of slides at different growth time.

	Exp B1a		**Exp B1b**	
Time (min)	Length (µm)	Diameter (µm)	Length (µm)	Diameter (µm)
15	-[a]	-[a]	3.2	0.32
30	2.5	0.26	2.0	0.20
45	-[a]	-[a]	-[b]	0.13
60	-[b]	0.12	-[b]	0.10
90	-[b]	-[b]	-[a]	-[a]

-[a] Experiment not performed. -[b] Not measurable.

In this experiment, a maximum speed growth of 40 nm min^{-1} was reached, with a maximum of growth rate observed between 30 and 60 min. The growth speed target for industrial application is thus achieved even if, in this case (multi-substrate), the growth speed is lower than that obtained in Exp A1 (one substrate). This is due to the introduction of four slides (Exp B1) in the same growth volume as for one (Exp A1): the consumption of reactants is faster and there is competition of NWs growth between substrates.

Experiment A1 and B1 were repeated to assess the reproducibility.

1.3.3.3 Reproducibility of the kinetic study

The Exp A1 was repeated and the reaction was stopped at 30, 60, 120 min in order to check its reproducibility. Table 1.5 gathers the length and diameter measured for experiment A2. The length and diameter reported are similar to those obtained in Exp A1 (Table 1.2) after 30 and 120 min. In Exp A2, the length and diameter values are reproducible at the beginning and at the end of the NWs growth period but more scattered during the growth period where; this period corresponds to competition between homogeneous and heterogeneous ZnO nucleation and growth and could be more sensitive to very small modifications of the reaction conditions.

Table 1.5. Length and diameter obtained after different growth times for Exp A2.

Time (min)	**Length (µm)**	**Diameter (µm)**
30	1.0	0.28
60	1.7	0.60
120	7.0	0.98

Table 1.6. Length and diameter obtain after removing the slides at different growth time.

	Exp B2a		**Exp B2b**	
Time (min)	Length (µm)	Diameter (µm)	Length (µm)	Diameter (µm)
15	-[a]	-[a]	0.00	0.00
30	1.50	0.53	1.03	0.20
45	-[a]	-[a]	1.60	0.36
60	2.4	0.75	2.00	0.36
90	6.0	0.90	-[a]	-[a]
120	4.0	0.70	-[a]	-[a]

-[a] Experiment not performed.

When the Exp B1 were reproduced, some scattering was observed in the values of the length and diameter of the NWs, probably due to the variation of the bath temperature. In the Exp B2, the insertion and withdrawal of slides at different time during growth led to non-reproducible values of length and diameter (Table 1.6) as the repeated opening of the reaction vessel induces temperature variations and thus disturbances of the nucleation-growth process at the origin of the nanowire growth. However, the length and diameter obtained after 120 min, when the growth solution has become clear again, is reproducible even if intermediate sizes are not.

Those two experiments (Exp B1 and B2) have shown that the target growth rate is reached with this synthesis procedure. Also, the NW synthesis *via* CBD is very sensitive to temperature variations; it is thus preferable to grow ZnO NWs in a batch process to limit temperature variation.

1.3.4 Optimisation from the kinetic study

The results from temperature monitoring and kinetics study (sections 1.3.3.1 and 1.3.3.2) led to further optimisation of the growth procedure. First, these studies have shown that the growth of NWs is very sensitive to temperature variations. Second, it was observed that it was possible to grow NWs on substrates introduced 15 min after the immersion of the growth solution in the oil bath, *i.e.* when the growth solution has reached a temperature of around 60 °C (Table 1.4 and Figure 1.8). It has been previously shown that the temperature in the chemical bath reaches approximately 80 °C after heating for 30 min, and additional 20 min are necessary for the temperature to stabilise. In order to reach faster the temperature of maximum growth rate, water was preheated at various temperature levels before adding the reactants.

Here, the 97.5 mL of water needed to reach the final volume where preheated at 40, 60, 70 and 80 °C. The solution of $(Zn(NH_3)_4)^{2+}$ and the ethanolamine solution were added in non-preheated state to avoid the precipitation of the zinc salt. A decrease of 10 °C was noticed for water preheated at 40, 60, 70 °C; a decrease of 20 °C was observed when the water was preheated at 80 °C. After a growth time of 2 h (40 °C), 1 h 40 (60 °C), 1 h 35 (70 °C) and 1 h 30 (80 °C), the slides were then cleaned with DI water, dried at room temperature and characterised by ESEM (Figure 1.15).

For the solutions preheated at 60, 70 or 80 °C, a white precipitate is directly formed when the $(Zn(NH_3)_4)^{2+}$ solution (*i.e.* a mix of zinc sulphate and ammonia in DI water) is added. This happens because, at 60 °C, the homogeneous nucleation has already started, as explained by Richardson *et al.* [32]. Figure 1.16 shows the length and the diameter of NWs as a function of the preheat temperature. When the water is not preheated (25 °C), the NWs reach 6 to 7 µm in length and 0.9 µm in diameter. When water is preheated starting from 40 °C, the length and diameter decrease significantly. This decrease of both parameters (length and diameter) is due to the spontaneous formation of the ZnO precipitate, which drains the zinc precursors from the solution; the NWs growth thus slows down. This experiment shows again that the concentration of precursors remaining in solution has a direct impact on the growth of the ZnO NWs. Preheating the water at temperatures higher than 40 °C leads to a further decrease of the NW size, both in terms of diameter and length.

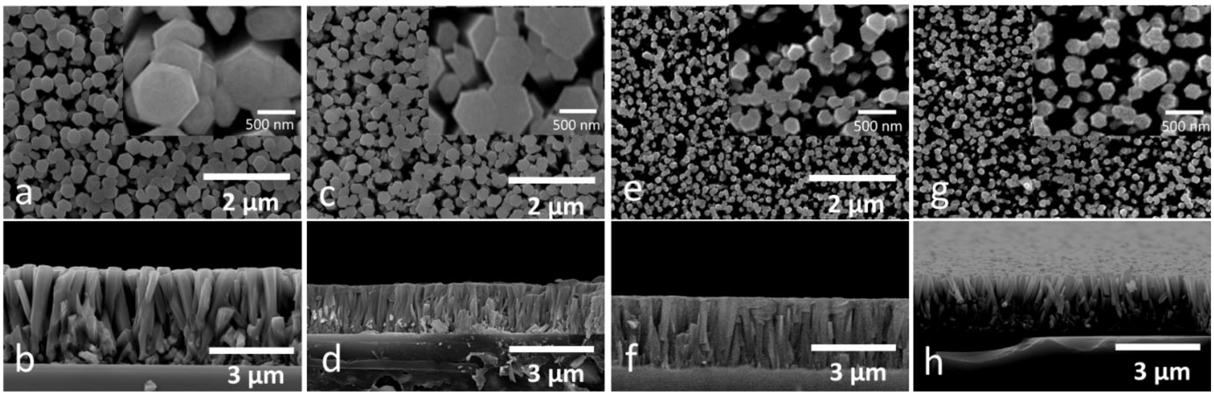

Figure 1.15. ESEM images of the NWs when water is preheated. Preheating at 40°C: (a) top view and (b) side view. Preheating at 60 °C: (c) top view and (d) side view. Preheating at 70 °C: (e) top view and (f) side view. Preheating at 80 °C: (g) top view and (h) side view.

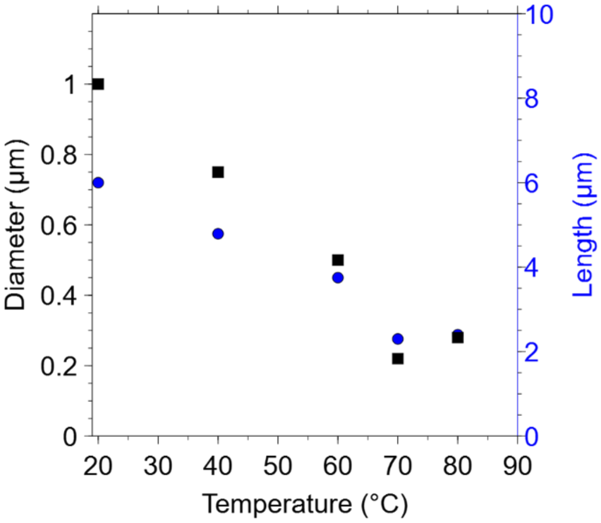

Figure 1.16. Evolution of (■) the diameter and (●) the length of the NWs as a function of the preheating temperature of the water.

1.3.5 Homogeneity of the temperature

In section 1.3.3.1, it was shown that the heating of the solution is not reproducible. As the growth of ZnO NWs is sensitive to temperature variation (see results in section 1.3.3.2), it is necessary to use a reproducible heating system. To this end, three different heating systems were studied. In system A, an oil bath was heated by a PID controller to 90 °C on a hot plate with the temperature probe placed into the oil (Figure 1.3a). The reaction vessel was then placed into the preheated oil. Contrarily, in system B, the temperature probe was placed directly into the reaction vessel instead of into the preheated oil bath (Figure 1.3b). System C was homemade: it consisted of a dual-wall system made of two propylene vials where water is heated at 90 °C and circulates constantly (Figure 1.3c). The temperature was in all cases monitored in order to choose the system with the most reproducible heating. The temperature measurement in Figure 1.17a was monitored for 60 min, to check which system stabilises the fastest. System B takes more time to stabilise compared to systems A and C. Systems A and C follow the same tendency. It has been shown in section 1.3.3 (Figure 1.7) that system A has a variance of 4 °C. To discriminate system C from system A, the temperature monitoring was repeated four times as shown in Figure 1.17b. The temperature is evolving with the same tendency in system C.

Figure 1.17c shows a variance lower than 1 °C after 30 min heating, which is lower than the system A where the variance was around 4 °C after 60 min. System C shows a good heating reproducibility and stabilises faster than system A. System C was thus kept for the following experiment in the next chapters, as reproducible results where obtain from this system.

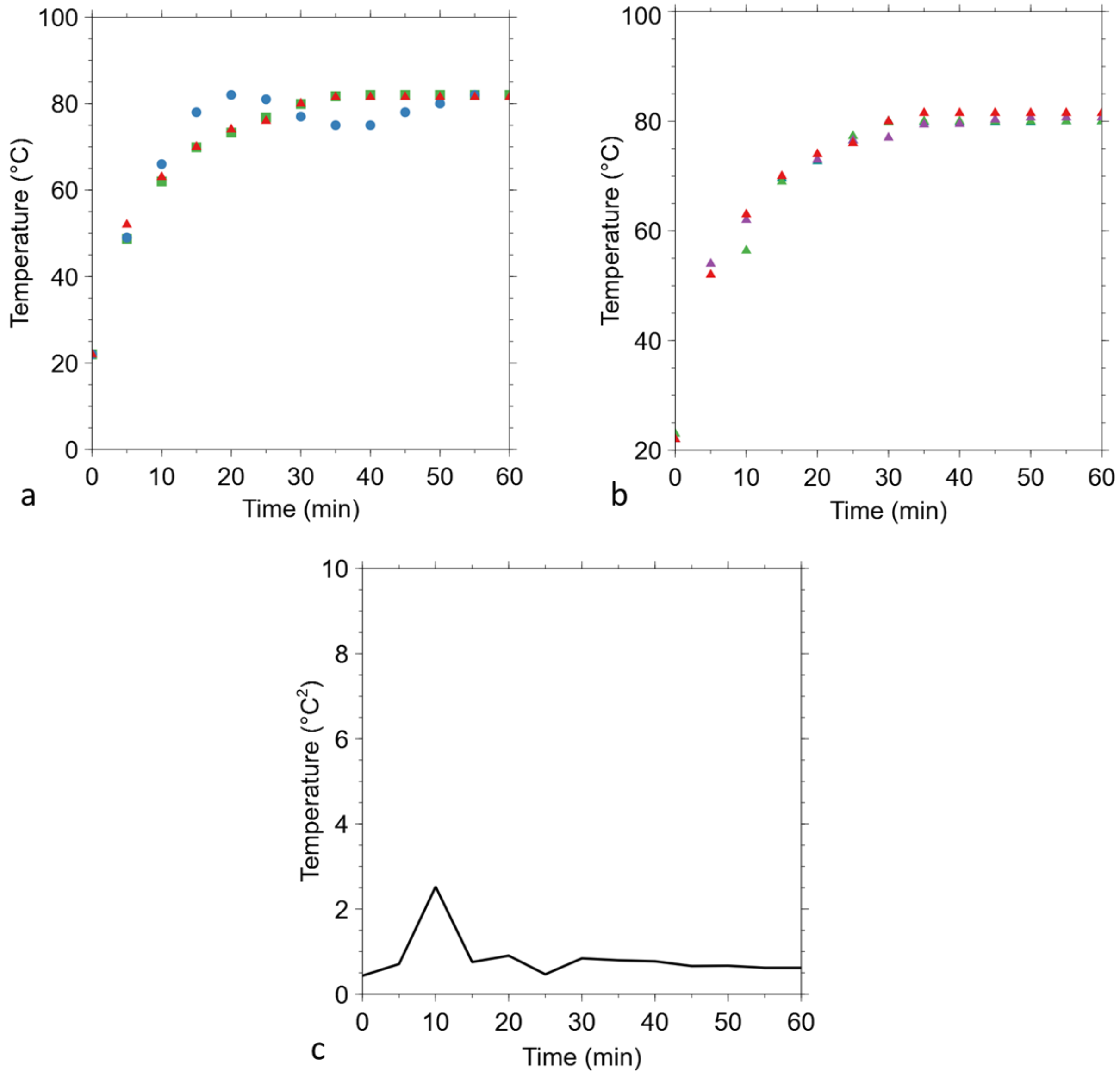

Figure 1.17. (a) Evolution of temperature in the growth solution with the different systems: (■) system A, (●) system B, (▲) system C; (b) System C temperature monitoring for four different synthesis; (c) Temperature variance of system C.

1.4 Conclusion

The objectives here was to grow ZnO NWs for piezoelectric nanogenerator application. To do so, zinc oxide nanowires (NWs) have been grown through a combined process: a seed coating using a sol-gel process followed by growth using chemical bath deposition. The growth process was simplified in order to be suitable for industrial scale up, for which a minimum speed growth of 20 nm min^{-1} is required. The initial mixing process using three solutions of zinc, ammonia and ethanolamine in water was simplified as two solutions by dissolving the zinc salt directly into ammonia. This simplification reduces the number of steps while preserving the morphological properties of the NWs. With this simplified process, it was possible to grow ZnO NWs with length of 6-7 µm and diameter of 0.9 µm diameter in 2 h at 90 °C, in a relatively reproducible way.

The growth mechanism has been linked to the visual aspect of the growth solution. Three growth phases were highlighted. The first phase consisted in ZnO NWs growth on the seeded substrate only. In the second phase, two growth processes are taking place at the same time: ZnO growth is occurring on the substrate and in the solution (homogeneous ZnO). This induces a sharp decrease of the precursors’ concentration which, in turns, leads to the decrease of the growth speed. During this phase, the synthesis process is very sensitive to temperature variations, which suggest that the synthesis should occur in a system that provides very stable reaction conditions. The maximum growth rate was reached at the beginning of this phase. Finally, during the third phase, one observes the dissolution-precipitation of the homogeneous ZnO, *i.e.* previously formed in solution and settling down at the bottom of the vial. The process reached a maximum growth speed of 70 nm min^{-1} which is suitable for large-scale manufacturing, as the target was 20 nm min^{-1}. Moreover, it has been shown that preheating the growth solution leads to a decrease of the NW length and diameter, which is not suitable to obtain long and thin NWs, necessary for piezoelectric applications. Finally, a dual wall heating system was built to replace the oil bath in order to homogeneously heat the growth solution.

However, it was complicated to obtain reproducible, high quality and well aligned NWs. In order to improve the NW quality, work still needs to be done. In particular, studying the cleaning step of the substrate and the seed deposition method to ensure homogeneous NW growth is a key step. The impact of the thermal treatment of the seed layer to improve the NW orientation and growth is, in our opinion, another important factor to be determined. This will be the subject of the next chapter

References

1. K. J. Choi, H. W. Jang, One-dimensional oxide nanostructures as gas-sensing materials: Review and issues. *Sensors* **10**, 4083–4099 (2010).
2. Y. Liu, X. Dong, P. Chen, Biological and chemical sensors based on graphene materials. *Chem. Soc. Rev.* **41**, 2283–2307 (2012).
3. L. Sang, M. Liao, M. Sumiya, A comprehensive review of semiconductor ultraviolet photodetectors: From thin film to one-dimensional nanostructures. *Sensors* **13**, 10482–

10518 (2013).

4. V. J. Babu, S. Vempati, T. Uyar, S. Ramakrishna, Review of one-dimensional and two-dimensional nanostructured materials for hydrogen generation. *Phys. Chem. Chem. Phys.* **17**, 2960–2986 (2015).
5. J. H. Pan, H. Dou, Z. Xiong, C. Xu, J. Ma, X. S. Zhao, Porous photocatalysts for advanced water purifications. *J. Mater. Chem.* **20**, 4512–4528 (2010).
6. M. MacIas-Montero, A. N. Filippin, Z. Saghi, F. J. Aparicio, A. Barranco, J. P. Espinos, F. Frutos, A. R. Gonzalez-Elipe, A. Borras, Vertically aligned hybrid core/shell semiconductor nanowires for photonics applications. *Adv. Funct. Mater.* **23**, 5981–5989 (2013).
7. K. S. Ranjith, R. B. Castillo, M. Sillanpaa, R. T. Rajendra Kumar, Effective shell wall thickness of vertically aligned ZnO-ZnS core-shell nanorod arrays on visible photocatalytic and photo sensing properties. *Appl. Catal. B Environ.* **237**, 128–139 (2018).
8. H. A. Sodano, D. J. Inman, G. Park, A review of power harvesting from vibration using piezoelectric materials. *Shock. Vib.* **36**, 197–205 (2004).
9. X. Wang, Piezoelectric nanogenerators-Harvesting ambient mechanical energy at the nanometer scale. *Nano Energy* **1**, 13–24 (2012).
10. S. Bagga, J. Akhtar, S. Mishra, Synthesis and applications of ZnO nanowire: A review. *AIP Conf. Proc.* **1989** (2018).
11. A. S. Kamble, B. B. Sinha, K. Chung, M. G. Gil, V. Burungale, C. J. Park, J. H. Kim, P. S. Patil, Effect of hydroxide anion generating agents on growth and properties of ZnO nanorod arrays. *Electrochimica Acta*. **149**, 386–393 (2014).
12. C. Xu, P. Shin, L. Cao, D. Gao, Preferential growth of long ZnO nanowire array and its application in dye-sensitized solar cells. *J. Phys. Chem. C.* **114**, 125–129 (2010).
13. R. Hinchet, S. Lee, G. Ardila, L. Montès, M. Mouis, Z. L. Wang, Performance optimization of vertical nanowire-based piezoelectric nanogenerators. *Adv. Funct. Mater*. **24**, 971–977 (2014).
14. L. Liao, D. H. Liu, J. C. Li, C. Liu, Q. Fu, M. S. Ye, Synthesis and Raman analysis of 1D-ZnO nanostructure via vapor phase growth. *Appl. Surf. Sci.* **240**, 175–179 (2005).
15. X. Liu, X. Wu, H. Cao, R. P. H. Chang, Growth mechanism and properties of ZnO nanorods synthesized by plasma-enhanced chemical vapor deposition. *J. Appl. Phys.* **95**, 3141–3147 (2004).
16. V. Khranovskyy, I. Tsiaoussis, L. Hultman, R. Yakimova, Selective homoepitaxial

growth and luminescent properties of ZnO nanopillars. *Nanotechnology* **22** (2011).

17. D. A. Zeze, A. M. Joyce, C. A. Anderson, N. M. D. Brown, Control and mass selection of $C_nH_m^+$ fragments in an inductively coupled pulsed plasma. *Appl. Phys. Lett.* **80**, 22–24 (2002).
18. X. Wang, X. Wang, J. Song, P. Li, J. H. Ryou, R. D. Dupuis, C. J. Summers, Z. L. Wang, Growth of uniformly aligned ZnO nanowire heterojunction arrays on GaN, AlN, and $Al_{0.5}Ga_{0.5}N$ substrates. *J. Am. Chem. Soc.* **127**, 7920–7923 (2005).
19. L. W. Ji, S. M. Peng, J. S. Wu, W. S. Shih, C. Z. Wu, I. T. Tang, Effect of seed layer on the growth of well-aligned ZnO nanowires. *J. Phys. Chem. Solids* **70**, 1359–1362 (2009).
20. B. Nikoobakht, X. Wang, A. Herzing, J. Shi, Scalable synthesis and device integration of self-registered one-dimensional zinc oxide nanostructures and related materials. *Chem. Soc. Rev.* **42**, 342–365 (2013).
21. G. Zhu, Y. Zhou, S. Wang, R. Yang, Y. Ding, X. Wang, Y. Bando, Z. L. Wang, Synthesis of vertically aligned ultra-long ZnO nanowires on heterogeneous substrates with catalyst at the root. *Nanotechnology* **23**, 1–6 (2012).
22. Y. H. Kang, C. G. Choi, Y. S. Kim, J. K. Kim, Influence of seed layers on the vertical growth of ZnO nanowires. *Mater. Lett.* **63**, 679–682 (2009).
23. J. Song, S. Lim, Effect of seed layer on the growth of ZnO nanorods. *J. Phys. Chem. C*. **111**, 596–600 (2007).
24. C. Opoku, A. S. Dahiya, F. Cayrel, G. Poulin-Vittrant, D. Alquier, N. Camara, Fabrication of field-effect transistors and functional nanogenerators using hydrothermally grown ZnO nanowires. *RSC Adv.* **5**, 69925–69931 (2015).
25. M. Kokotov, G. Hodes, Reliable chemical bath deposition of ZnO films with controllable morphology from ethanolamine-based solutions using $KMnO_4$ substrate activation. *J. Mater. Chem.* **19**, 3847–3854 (2009).
26. H. E. Unalan, P. Hiralal, N. Rupesinghe, S. Dalal, W. I. Milne, G. A. J. Amaratunga, Rapid synthesis of aligned zinc oxide nanowires. *Nanotechnology* **19**, 1–6 (2008).
27. M. Ohyama, H. Kozuka, T. Yoko, Sol-gel preparation of ZnO films with extremely preferred orientation along (002) plane from zinc acetate solution. *Thin Solid Films* **306**, 78–85 (1997).
28. Q. Huang, L. Fang, X. Chen, M. Saleem, Effect of polyethyleneimine on the growth of ZnO nanorod arrays and their application in dye-sensitized solar cells. *J. Alloys Compd.* **509**, 9456–9459 (2011).

29. L. E. Greene, B. D. Yuhas, M. Law, D. Zitoun, P. Yang, Solution-grown zinc oxide nanowires. *Inorg. Chem.* **45**, 7535–7543 (2006).
30. S. M. Mahpeykar, J. Koohsorkhi, H. Ghafoori-Fard, Ultra-fast microwave-assisted hydrothermal synthesis of long vertically aligned ZnO nanowires for dye-sensitized solar cell application. *Nanotechnology* **23**, 1–7 (2012).
31. M. Kokotov, S. Bar-Nachum, E. Edri, G. Hodes, Effect of glass dissolution on the solution deposition of ZnO films and its exploitation for deposition of Zn silicates. *J. Am. Chem. Soc.* **132**, 309–314 (2010).
32. J. J. Richardson, F. F. Lange, Controlling low temperature aqueous synthesis of ZnO. *Cryst. Growth Des.* **9**, 2570–2575 (2009).
33. C. Cui, S. Bu, Q. Wang, L. Bai, Growth of ZnO nanowires in aqueous solution by a dissolution-growth mechanism. *J. Nanomater.* **2008**, 1–5 (2008).
34. S. Yamabi, H. Imai, Growth conditions for wurtzite zinc oxide films in aqueous solutions. *J. Mater. Chem.* **12**, 3773–3778 (2002).
35. R. B. Peterson, C. L. Fields, B. A. Gregg, Epitaxial chemical deposition of ZnO nanocolumns from NaOH solutions. *Langmuir* **20**, 5114–5118 (2004).

Chapter 2. Optimisation of the seed layer

2.1 Introduction

The first chapter of this PhD thesis was devoted to the study of ZnO nanowire (NW) growth kinetics. This study determined a NW maximum growth rate of 70 nm min^{-1}. However, it highlighted some reproducibility issues in terms of NW morphology. Since the seed layer influences the NW array, ensuring the homogeneity and reproducibility of the seed layer is an important step to achieve a reproducible NW growth. This chapter will be focused on the study of the seed layer.

According to literature, the quality of the seed layer, offering adequate nucleation sites for ZnO growth, is a key factor for obtaining well-oriented and homogeneous NW arrays [1, 2]. For example, Greene *et al.* [3] coated a seed layer oriented along the c-axis (002 axis); they noticed that, after growth, the well-oriented seed gave rise to (002) ZnO NWs only (Figure 2.1a and Figure 2.1b) whereas a seed layer with a heterogeneous orientation, made from ZnO quantum dots deposited by dip-coating, led to badly oriented NWs (Figure 2.1c and Figure 2.1d).

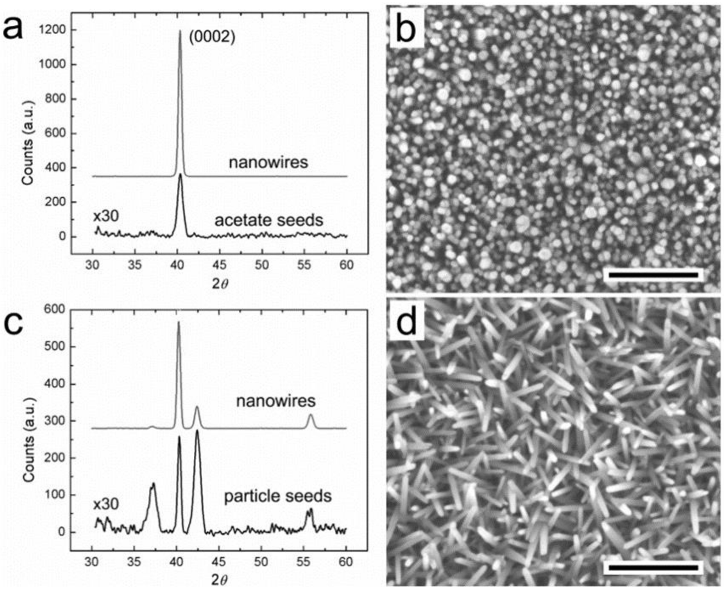

Figure 2.1. Control of ZnO nanowires orientation through the nanoparticle seed. (a) XRD and (b) top view ESEM micrograph of ZnO NWs grown from ZnO oriented nanocrystal seeds formed *in situ* on a silicon surface from the decomposition of a zinc acetate precursor at 350 °C. (c) XRD and (d) top view ESEM micrograph of ZnO NWs grown from ZnO quantum dots (3-4 nm) that were deposited onto silicon by dip-coating. Both ZnO NWs arrays were grown for 30 min. Scale bars on (c) and (d) correspond to 500 nm. Reproduced from reference [3].

Different methods can be used for the preparation of the seed layer. The physical vapor deposition (PVD), such as radio frequency (RF) magnetron sputter-deposition technique, is a first example. Sputtering deposition is a vacuum technique where argon ions accelerated by an electric field hit a target of the desired material, thus ejecting atoms that are sputtered onto a target substrate as a thin layer. However, the cost of the device is too high to be considered as ZnO seed layer deposition technique at industrial scale [1, 4]. As an alternative, the wet coating techniques, such as dip-coating or spin-coating, consist in the deposition of a precursor solution onto the substrate followed by a calcination step at high temperature (> 200 °C) to ensure crystallisation. The wet-coating was preferred in our work for ZnO seed layer deposition because it is a simple, straightforward and low cost equipment as it occurs at ambient atmosphere [5, 6].

Different precursor solutions can be used to form the ZnO seed layer: one can for example use (i) zinc acetate with sodium hydroxide in alcohol, (ii) zinc acetate in alcohol, (iii) zinc acetate and ethanolamine in alcohol, (iv) zinc nitrate and hexamethylenetetramine (HMTA) in water [7–9]. Among these proposals, two different precursor solutions (zinc acetate in ethanol and zinc acetate in ethanol with addition of ethanolamine) were explored in our study for several reasons: (i) their ease of application, (ii) the referred annealing treatment at moderate temperature (350 °C) and, especially, (iii) their ability to further generate a uniform, dense and vertically oriented ZnO NW arrangement with respect to the substrate during the growth by chemical bath deposition (CBD), as mentioned by literature [10].

Many variables can influence the growth of ZnO NWs. Podlogar *et al.* [6] grew ZnO NWs on sapphire and glass substrate, either with or without a seed layer; similar results were obtained on both substrates. More or less separated, randomly oriented prismatic hexagonal ZnO crystals were grown on both substrates without seed layer, while highly oriented ZnO NW film was obtained with a seed layer. According to Ohyama *et al.* [5], the growth of ZnO NWs strongly depends on (i) the seed layer thickness and (ii) the heat treatment applied to the seed layer prior to NW growth. Kang *et al.* [1] showed that a seed layer previously oriented along the c axis (002 axis) would produce nanowires oriented along this axis, as shown in Figure 2.1. As a summary, the NW growth depends on the use of a seed layer. Indeed, the thickness and heat treatment of the seed layer strongly influences the orientation of the ZnO crystallites.

In this work, spin-coating and dip-coating were used to generate the seed layer, and results were compared. With spin-coating, it is possible to control the film thickness by modifying the rotation speed or the viscosity of the precursor solution. However, with the device available in our laboratory, substrates of large size (> 50 cm²) cannot be spun at a sufficiently high speed to obtain thin films; in addition, 2-5% of the volume of the material are effectively deposited onto the substrate, while the remaining 95-98% are lost into the coating bowl. With dip-coating, the film thickness depends on the viscosity of the precursor solution, the rate of solvent evaporation, as well as the angle and speed of substrate withdrawal from the solution [11]. The evaporation rate thus depends on the nature of the solvent. Dip-coating is a commonly used technique in the industry and laboratory, because it requires cheap raw materials and equipment, follows easy steps and because the films obtained are usually homogeneous [12].

In this chapter, we study the spin-coating and dip-coating process for the deposition of the seed layer followed by chemical bath deposition to grow the NWs. The concentration of the precursor solution, the number of layers deposited and the temperature of calcination were studied. The influence of those variables on the NW growth were assessed using profilometry measurement, UV-visible spectroscopy, X-Ray Diffraction and electron microscopy. The synthesis conditions were optimised in order to develop a scalable and low temperature process which opens up the possibility to use a wide range of substrates such as organic flexible substrates.

2.2 Experimental work

The cleaning of the substrates was first optimised in order to ensure a homogeneous deposition on the substrate. Then, two techniques, spin-coating and dip-coating, were studied for the deposition of the seed layer. After selecting the seeding technique, the precursor concentration of the seed solution was optimised. From the results obtained, the number of layers deposited, the thermal pre-treatment and the final calcination step, were studied for the seed deposition method, and their influence on the homogeneity and quality of the ZnO NWs grown was examined.

2.2.1. Cleaning procedure

Before deposition of the seed layer, the substrates were cleaned with RBS T105 detergent solution (20 min) and rinsed by dipping the substrate in deionised water (20 min), acetone (20 min) and ethanol (20 min). As the results showed a heterogeneous deposition of the seed layer when cleaning with detergent (see Section 2.3), the substrates were in the next experiments cleaned with Gardoclean grease remover solution (20 min) and rinsed with deionised water (20 min), acetone (20 min) and ethanol (20 min). They were then dried with under air flow at room temperature. Before deposition, one of the surfaces of the glass slide was covered with adhesive tape protection to ensure the deposition of the seed layer on one side of the glass slide only.

2.2.2. Seed deposition by spin-coating *vs*. dip-coating

2.2.2.1. Seed deposition by spin-coating

The microscope slide substrates (Superior Marienfeld) were first cleaned by sonication in an RBS T105 detergent solution (20 min) and rinsed by dipping the substrate in deionised water (20 min), acetone (20 min) and ethanol (20 min). They were then dried 30 min at 60 °C in air. A solution of zinc acetate dihydrate ($Zn(CH_3COO)_2.2H_2O$, Sigma Aldrich, 99.999%) at in ethanol (concentration: 5×10^{-3} mol L^{-1}) was prepared for the seeding process. The seed layer procedure consisted in the deposition of 1 mL of the solution onto a clean slide substrate *via* spin-coating technique. The spin coating was performed at 2000 rpm for 30 s; the whole process was repeated five times (Figure 2.2a and Figure 2.2b). Finally, calcination at 350 °C for 20 min in air was performed in order to decompose zinc acetate and to form ZnO nanocrystals which would act as nucleation sites for the subsequent growth of ZnO NWs.

After the ZnO seed layer deposition, ZnO NWs were grown by Chemical Bath Deposition (CBD) (see section 2.2.7.1). After growth, the NWs coatings were characterised using environmental scanning electron microscopy (ESEM-FEG XL30 Philips, Esprit 1.9 software). Regarding the poor results obtained using spin-coating (section 2.3.2), the seed study was continued using dip-coating.

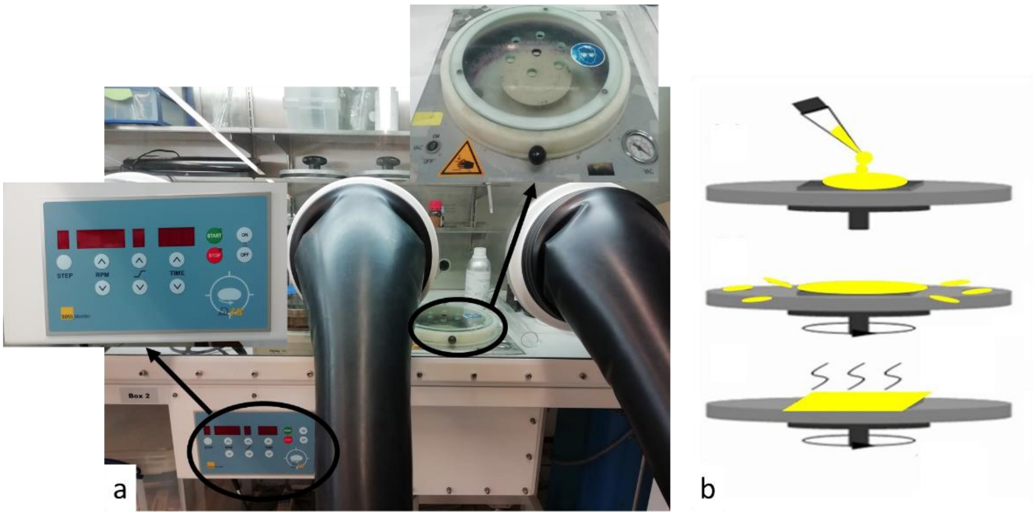

Figure 2.2. (a) Spin-coating device at the NCE laboratory; (b) scheme of the spin-coating principle.

2.2.2.2. Seed deposition by dip-coating

ZnO seed layers were deposited onto clean alkali-free glass slides (Schott AF32 eco) *via* the dip-coating technique. Note that the type of substrate was modified between this section and section 2.2.2.1 because it was then expected to post-treat the seeds by thermal treatment, and Superior Marienfeld glass slides used previously could not withstand temperatures above 350 °C. The substrates were first cleaned with Gardoclean grease remover solution (20 min) and rinsed with deionised water (20 min), acetone (20 min) and ethanol (20 min). They were then dried with under air flow at room temperature. Before deposition, one side of the glass slide was covered with adhesive tape protection to ensure the deposition of the seed layer on one side of the glass slide only. An equimolar solution of 5×10^{-3} mol L^{-1} of zinc acetate dihydrate ($Zn(CH_3COO)_2.2H_2O$, Sigma Aldrich, 99.999%) and ethanolamine (C_2H_7NO, Sigma Aldrich, ≥ 98%) in ethanol was prepared to produce the seed films. Generally, dip coating consists of five-steps, including:

(i) Immersion: at a constant speed, the substrate is dipped into the coating solution.

(ii) Start-up: the substrate remains in the solution for a chosen time, and then it starts to be pulled out.

(iii) Deposition: while the substrate is being pulled out, the thin film coating starts to be deposited on it. The thickness of the coating is directly dependent on the speed by which the substrate is being pulled out. The slower the pull, the thinner the coating layer.

(iv) Drainage: in this step, excess liquid is drained from the substrate surface.

(v) Evaporation: solvent starts to evaporate from the surface of the substrate to form a thin film.

The seed film was prepared by dipping the glass slide in the coating solution and withdrawing it at a rate of 0.2 m min^{-1}, with a start-up time of 30 s. During the withdrawal process, a layer of the precursor solution is entrained with the slide. The liquid is drained by gravitational forces and the solvent evaporates, causing the film deposition (Figure 2.3a and Figure 2.3b). The seeds were then calcined at 350 °C in air for 20 min. After the ZnO seed layer deposition, ZnO NWs were grown by CBD. After ZnO NW growth, the coatings were characterised using environmental scanning electron microscopy (ESEM-FEG XL30 Philips, Esprit 1.9 software).

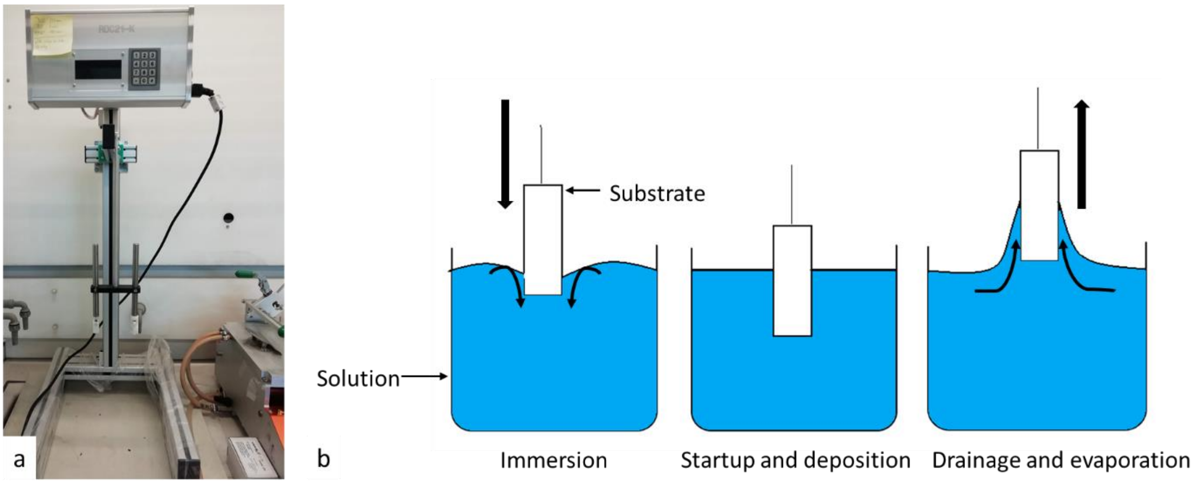

Figure 2.3. (a) Dip-coating installation at the NCE laboratory; (b) scheme of the dip-coating principle.

2.2.3. Influence of $Zn(CH_3COO)_2$ concentration on the seed layer

An equimolar solution of zinc acetate dihydrate ($Zn(CH_3COO)_2.2H_2O$, Sigma Aldrich, 99.999%) and ethanolamine (C_2H_7NO, Sigma Aldrich, ≥ 98%) in ethanol was prepared to produce the seed films. Four concentrations were used: 5×10^{-3} mol L^{-1}, 0.1 mol L^{-1}, 0.25 mol L^{-1} and 0.5 mol L^{-1}. The solutions were heated at 60 ºC for 2 h under stirring and cooled down at room temperature (3 h of natural cooling) in order to obtain a stable and homogeneous colloidal solution. The solution was then deposited onto Gardoclean-cleaned alkali-free glass slides (Schott AF32 eco) *via* the dip-coating technique. The coating was deposited at 0.2 m min^{-1} speed, and then a thermal pre-treatment was performed at 100 °C for 20 min in air, followed by calcination at 650 °C for 20 min in air (Figure 2.4).

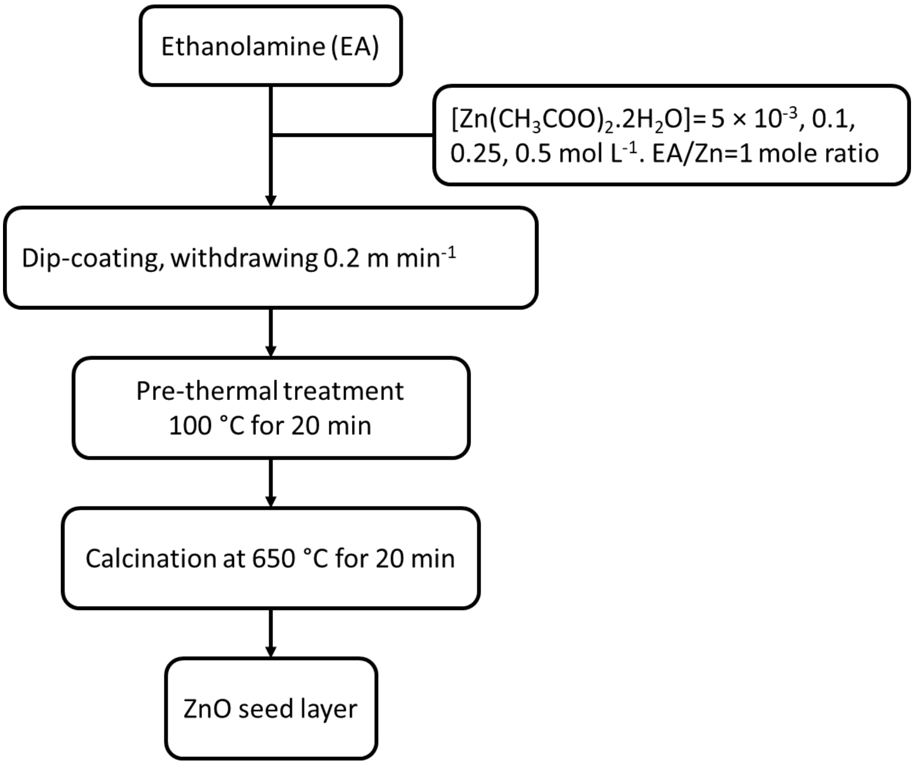

Figure 2.4. Flow chart showing the procedure for preparing ZnO films.

Once the glass slide had been coated with the ZnO seed layer, ZnO NWs were grown by CBD [13, 14] (see section 2.2.7). The orientation of the crystallites of the seed layer was determined using X-ray diffraction on a Siemens D-5000 diffractometer (Cu Kα radiation, 40 kV, 40 mA), and UV-visible spectroscopy on a Thermo Scientific Genesis 10S spectrometer as a complementary technique. The thickness of the seed films was measured by contact profilometry using a Veeco Dektak 8 Stylus Profiler.

2.2.4. Effect of seed layer calcined at different temperature

After the optimisation of the concentration of the seed precursor solution, the next step was to optimise the calcination temperature of the seed layer. An equimolar solution of zinc acetate dihydrate ($Zn(CH_3COO)_2.2H_2O$) and ethanolamine in ethanol was prepared to produce the seed films. The study of the influence of zinc acetate concentration on the seed deposition prompted us to set that variable value at 0.25 mol L^{-1} (see results of section 2.3.3.). This solution was heated at 60 ºC for 2 h under stirring and cooled down to room temperature (3 h of natural cooling), in order to obtain a stable and homogeneous colloidal solution. The solution was then deposited onto the glass substrates by dip-coating. Four different slides were dip-coated and then a thermal pre-treatment was made at 100 °C for 20 min in air, followed by four different calcination treatments: 200, 300, 400 and 650 °C during 20 min in air (Figure 2.5). The seed layer was characterised using contact profilometry, UV-visible and XRD measurement using the same devices as in the previous section. The ZnO NWs were then grown on the seed and characterised as described in section 2.2.7.

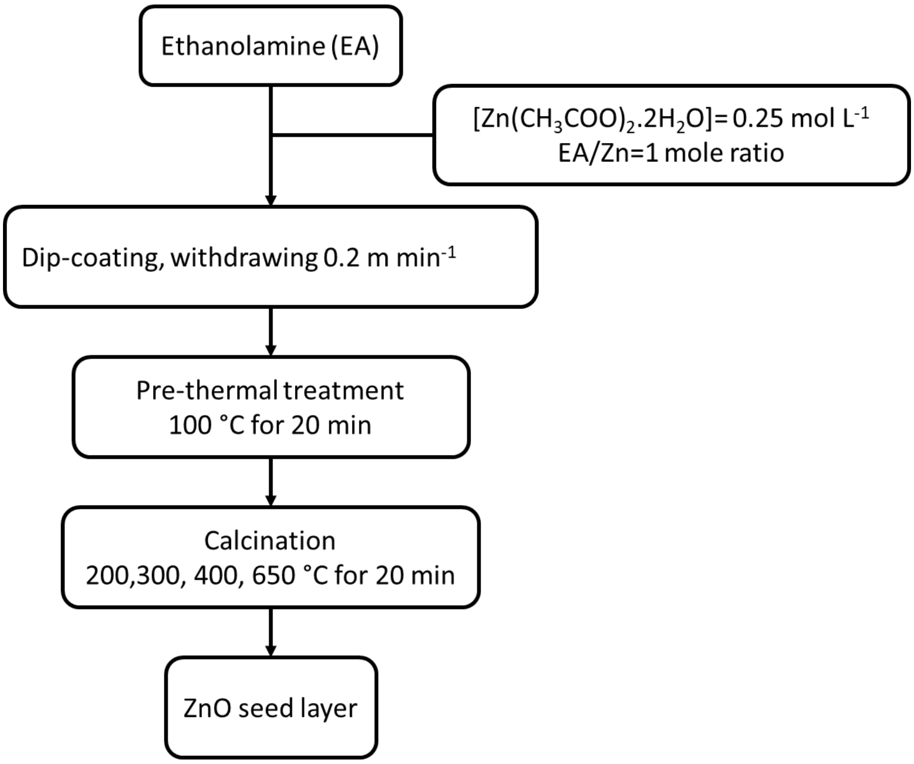

Figure 2.5. Flow chart showing the seed layer calcination step procedure.

2.2.5. Influence of the number of seed layers

The influence of the number of seed layers deposited on the glass slide prior to ZnO NW growth was studied. The seed coatings were made with an equimolar solution of zinc acetate dihydrate ($Zn(CH_3COO)_2.2H_2O$, Sigma Aldrich, 99.999%) and ethanolamine (C_2H_7NO, Sigma Aldrich, ≥ 98%) in ethanol. Three coatings were deposited by the dip-coating method using a precursor solution of 0.25 mol L^{-1}. Two procedures were studied.

The first one consisted in a thermal pre-treatment of the deposited layer at 100 °C for 20 min in air between each coating, followed by a final calcination at 650 °C for 20 min in air. The second one consisted in a double calcination of the deposited layer: the first calcination was done at 350 °C for 20 min in air between each coating, and was followed by a final calcination at 650 °C for 20 min in air (Figure 2.6). The seed layer was then characterised by XRD measurement, UV-visible spectroscopy and profilometry. Finally, the ZnO NWs were grown and characterised as detailed in section 2.2.7.

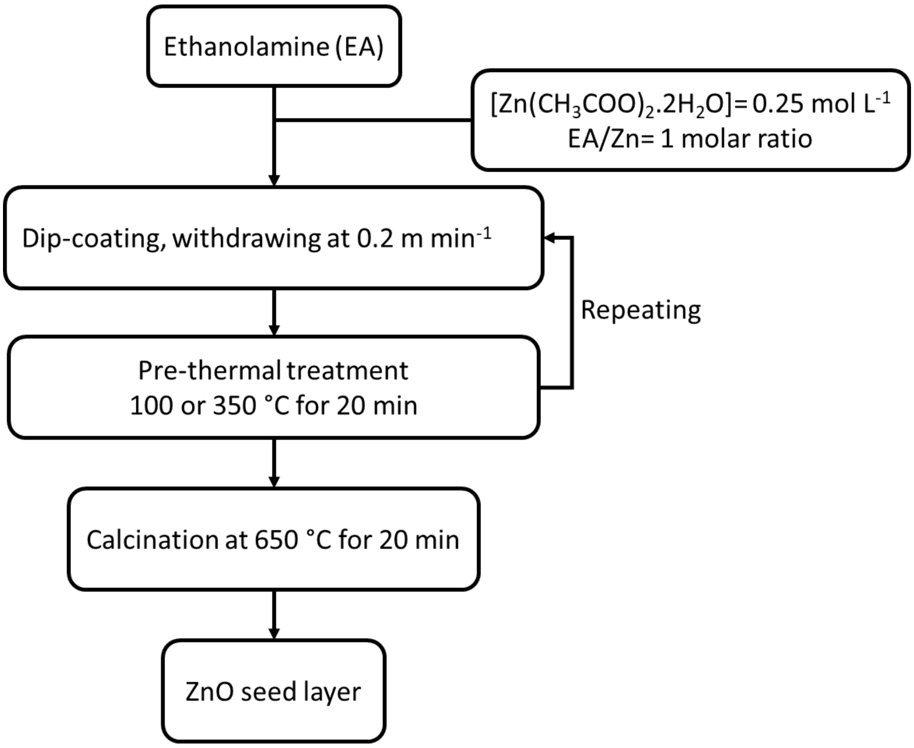

Figure 2.6. Flow chart showing the multi-dip process of the seed layer.

2.2.6. Influence of the calcination procedure of the seed layer

The heating procedure consisting in a double calcination (first at 350 °C, second at 650 °C) presented in section 2.2.5 gave rise to well oriented seed layer (see section 2.3.5). Starting from these results, two additional experiments were performed.

The first experiment consisted in the decrease of the final calcination step from 650 °C down to 350 °C. To do so, one and three deposits were done using an equimolar precursor concentration of zinc acetate and ethanolamine at 0.25 mol L^{-1} with a first calcination of 20 min at 350 °C in air carried out between each deposit, followed by a final calcination step 20 min at 350 °C (Figure 2.7).

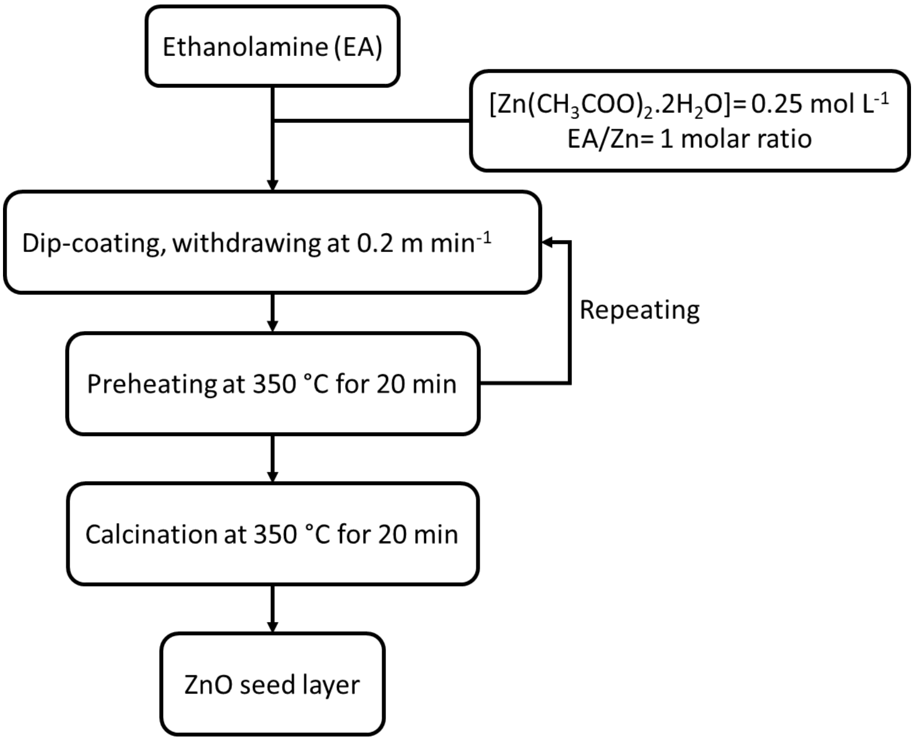

Figure 2.7. Flow chart showing a low temperature process for multiple seed layers.

In the second experiment, the goal was to check if applying a single prolonged heating step at 350 °C gave rise to the same results as a double calcination at 350 °C with intermediate cooling step. In that case, the calcination at 350 °C was carried out for 20, 40, 60 and 80 min after dip-coating of one layer, as presented in Figure 2.8. The seed layers were characterised by XRD measurement and UV-visible, using the same devices as previously. Finally, the ZnO NWs were grown as presented in section 2.2.7.

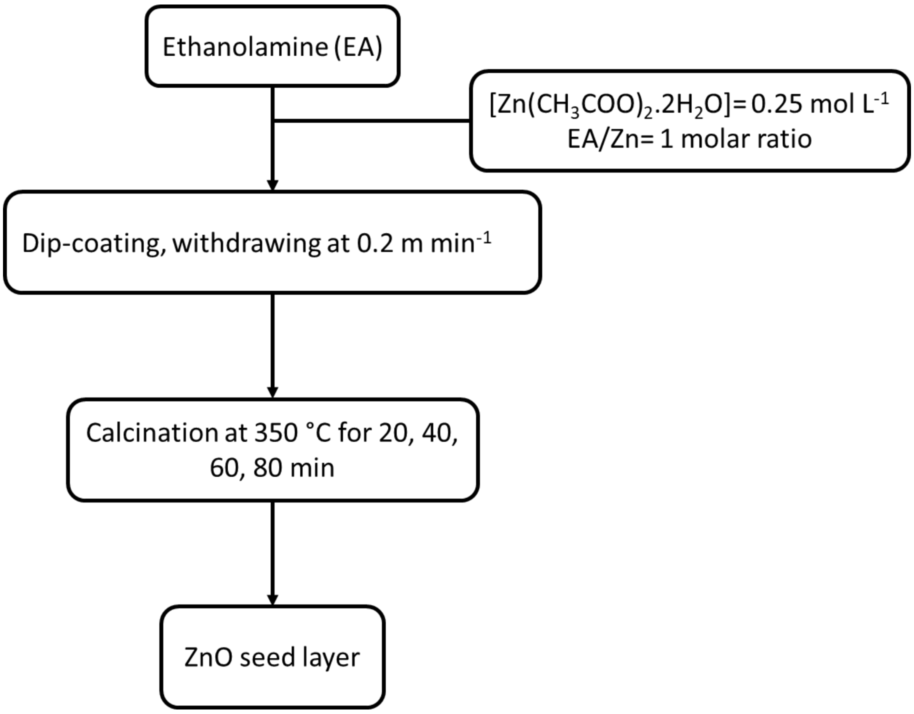

Figure 2.8. Flow chart for the prolonged calcination.

2.2.7. Growth of NWs

2.2.7.1. Optimised growth process using zinc sulphate

After the ZnO seed layer deposition, ZnO NWs were grown by Chemical Bath Deposition (CBD), according to the Kokotov *et al.*[14, 15] optimised process presented in Chapter 1 (section 1.2.2). The zinc sulphate heptahydrate powder (3.74 g, $ZnSO_4.7H_2O$, Sigma Aldrich, 99.9%) was directly dissolved into 19.5 mL of 4.0 mol L^{-1} ammonia solution (NH_4OH, 25-30 wt.% as ammonia (NH_3), Emsure, Merck). The previous solution and 13 mL of ethanolamine (2-aminoethanol, Sigma Aldrich, ≥ 98%) were added to 97.5 mL of deionised (DI) water. The growth solution (130 mL) was prepared in a 160 mL polypropylene vial, giving the following final concentrations: 0.1 mol L^{-1} Zn^{2+}, 0.6 mol L^{-1} NH_4OH and 1.7 mol L^{-1} ethanolamine. The solution was vigorously stirred until the pH stabilised at ~11.1 ± 0.2 (10 min). The substrate was introduced inclined from vertical to prevent particles which might form in the solution from settling on the downward-facing seeded side of the substrate. The reaction vial was closed and placed for 2 h in a dual wall system where water was heated at 90 °C and circulated constantly, as presented in Chapter 1 (section 1.2.5). After growth, the substrate was removed from the solution, immediately rinsed with DI water to remove loose ZnO precipitates and any residual reactant from the surface, and dried in air at room temperature for 24 h. After growth, the NW coatings were characterised using environmental scanning electron microscopy (ESEM-FEG XL30 Philips, Esprit 1.9 software).

2.2.7.2. Modified growth process using zinc nitrate and zinc sulphate

Zinc nitrate hexahydrate ($Zn(NO_3)_2.6H_2O$, Sigma Aldrich, 99.9%) and zinc sulphate heptahydrate ($ZnSO_4.7H_2O$, Sigma Aldrich, 99.9%) powders were directly dissolved into 19.5 mL of 2.7 mol L^{-1} ammonia solution (NH_4OH, 25-30 wt.% as ammonia (NH_3), Emsure, Merck). The previous solution and 13 mL of ethanolamine (2-aminoethanol, Sigma Aldrich, ≥ 98%) were added to 97.5 mL of DI water. The growth solution (130 mL) was prepared in a 160 mL polypropylene vial, giving the following final concentrations: 5×10^{-2} mol L^{-1} Zn^{2+}, 0.4 mol L^{-1} NH_4OH and 1.7 mol L^{-1} ethanolamine. The solution was vigorously stirred until the pH stabilised at 11.2 ± 0.2. The substrate was introduced inclined from vertical to prevent particles which might form in the solution from settling on the downward-facing seeded side of the substrate. The reaction vial was closed and placed for 2 h in an oil bath heated at 90 °C. After growth, the substrate was removed from the solution, immediately rinsed with DI water to remove loose ZnO precipitates and any residual reactant from the surface, and dried in air at room temperature for 24 h. After growth, the coatings were characterised using environmental scanning electron microscopy.

2.3. Results and Discussion

2.3.1. Cleaning procedure

Surface cleaning is an important step to eliminate contaminants originating from manufacturing processes, such as cutting or polishing fluids. Moreover, cleaning the surface leads to coatings as homogeneous as possible and facilitates the reproducibility.

Various ways to clean a surface exist as, for example: (i) plasma reactive species (Ultra Violet and vacuum ultra violet (VUV) emissions, oxygen or hydrogen radicals) [16] which remove contaminants without leaving any residues, (ii) alkaline cleaners (pH = 11) generally combined with heat (*e.g.* saturated solution of KOH at 75 °C), (iii) detergent (soap) cleaner using *e.g.* RBS T105 detergent solution, (iv) solvent cleaning (water, water-alcohol mixture, chlorinated solvents, *etc.*) and (v) ultrasonic cleaning. Among all these techniques, Gardoclean grease remover is widely used for economic reasons to clean glass. As explained in the experimental section, this cleaning is followed by several rinsing steps with water, acetone and ethanol.

We first tried to clean the glass slides with RBS T105 detergent solution; however, when the concentration of the ZnO precursor solution was increased, it was noticed that the seed layer obtained after calcination was very heterogeneous. This is the reason why the cleaning step was changed from RBS T105 to Gardoclean grease remover for the next experiments. Figure 2.9 shows two dip-coated slides which were cleaned either with Gardoclean (Figure 2.9a) or RBS T105 (Figure 2.9b) before dip-coating. The slides were then immersed into the solution for coating, withdrawn and calcined at 350 °C in air. After calcination of the seed layer, the slide cleaned with the grease remover has a better aspect than the slide cleaned with the detergent. The surface of the glass slides looks oily after dip-coating when the detergent is used, which is a sign of poor adhesion of the coating. The cleaning step with the grease remover was preferred to detergent because it leads to a better coating aspect.

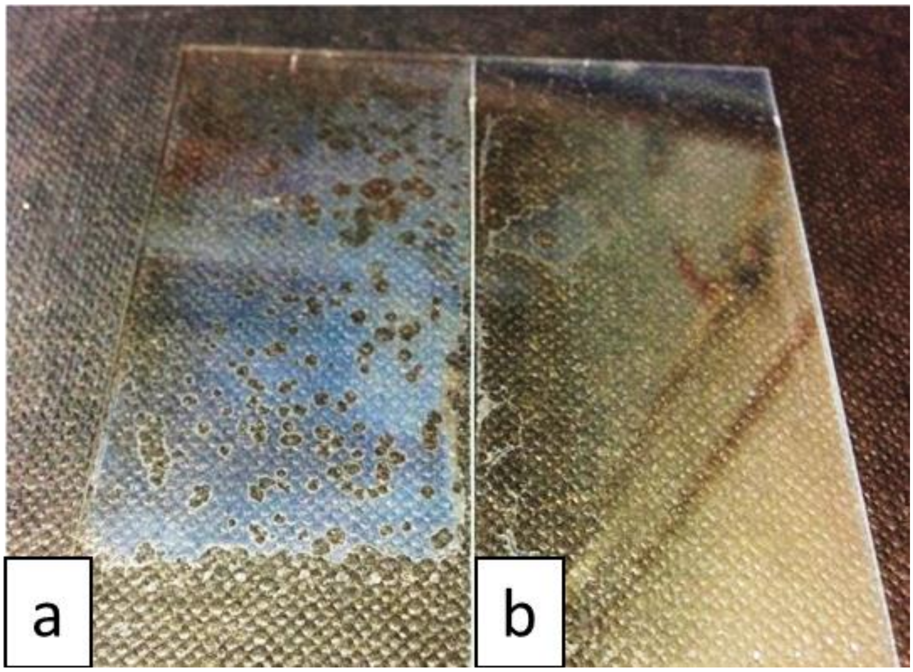

Figure 2.9. Surface preparation before dip-coating. Comparison between (a) Gardoclean grease remover and (b) RBS T105 detergent solution on aspect of seed layer.

2.3.2. Seed layer by spin coating *vs.* dip coating

Spin-coating and dip-coating depositions are commonly used techniques to form thin films. As detailed in the experimental part (section 2.2.2.), the spin-coating technique consists in the application of the precursor solution on the centre of a substrate and its rotation at high speed in order to spread the coating material by centrifugal forces. The dip-coating technique consists in the immersion of a substrate into the coating solution particles and its withdrawal at constant speed. The two techniques were tested with a precursor solution of zinc acetate dihydrate diluted in ethanol (5×10^{-3} mol L^{-1}) for spin-coating, and an equimolar solution of zinc acetate and ethanolamine (5×10^{-3} mol L^{-1}) in ethanol for dip-coating. Mixing zinc acetate dihydrate and ethanolamine in absolute ethanol can produce well-aligned ZnO films [17] and is referenced as providing control of the morphology and particles size of ZnO [18–20]. The addition of ethanolamine is believed to play the role of chelating and stabilising ligands, which would improve the solubility of zinc acetate [18]. Zinc precursor concentrations higher than 5×10^{-3} mol L^{-1} are thus required.

Figure 2.10a shows the seed layer after spin-coating, while Figure 2.10b and Figure 2.10c display ESEM images of NWs grown on the spin-coated seed layer. Figure 2.10d shows ESEM image of NWs grown on the dip-coated seed layer. The “comet-like” shape present in Figure 2.10a and Figure 2.10b is due to the presence of large particles in the precursor solution; those “comets” can be avoided by filtration of the solution prior to coating. Figure 2.10c shows the influence of the seed layer on the NW growth. The characterisation by optical microscope of the seed layer deposited by spin coating (insert in Figure 2.10c) shows non-homogeneous areas. The existing defects on the seed layer shown in the inserted picture are also visible after growth of the NWs (Figure 2.10c). The homogeneity of the solution to deposit is thus essential for the seed homogeneity. In turn, as shown here, the seed layer quality strongly influences the homogeneity of the NWs growth.

According to Figure 2.10d, dip-coating leads to a homogeneous NW array. In this work, dip-coating was preferred to spin-coating, because it was possible to obtain homogeneous seed layer and ZnO NWs without prior filtration of the precursor solution. This is probably due to the fact that the large particles do not cling to the surface and are dragged along by the liquid film when the slide is removed. As this technique is suitable, it was chosen for the remaining work. Nevertheless, with prior filtration of the solution, it is possible that spin-coating would also work; additional experiments would be necessary to verify this.

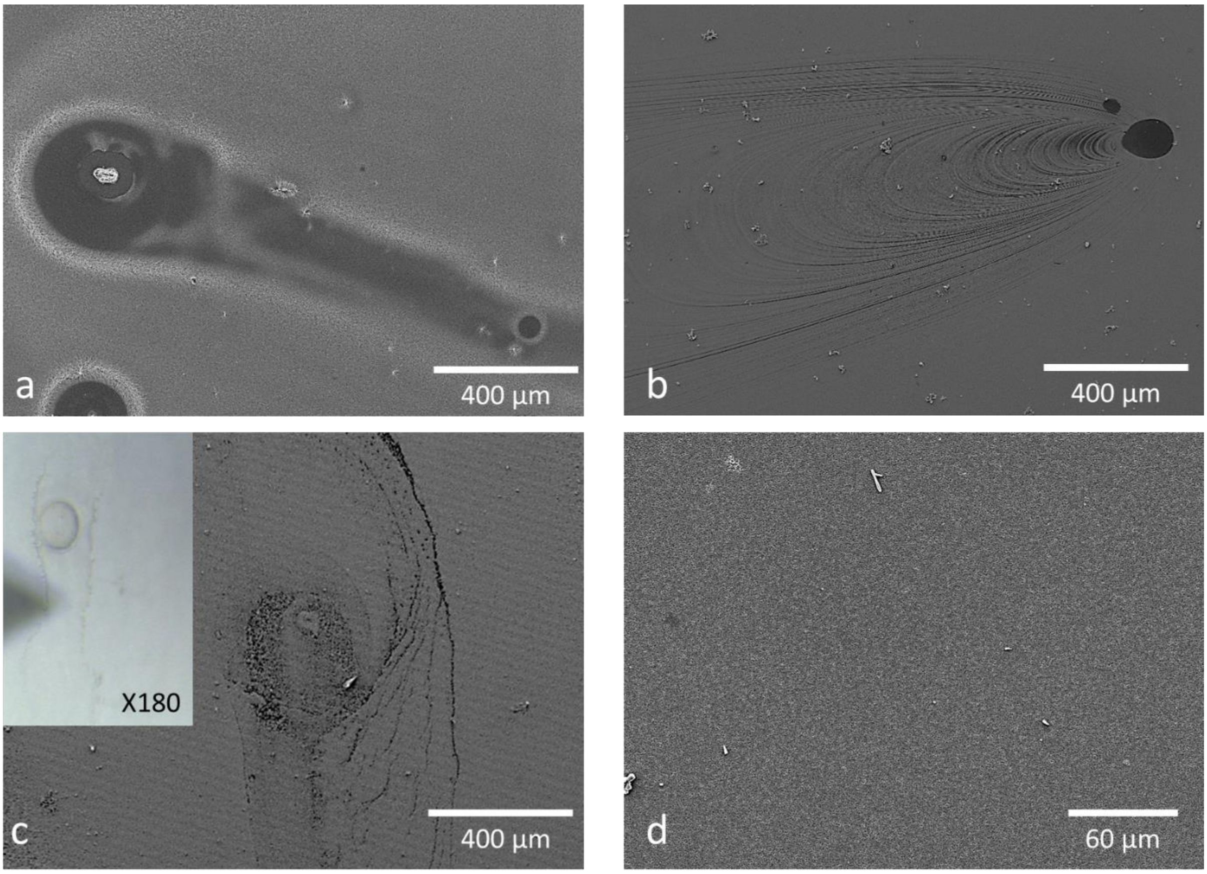

Figure 2.10. ESEM images of seed layer before NW growth: (a) spin-coated seed layer with particles stuck on the surface; (b) image of a “comet” obtained after NWs grow on spin-coated seed; (c) images of the NWs after seeding using spin-coating with insert in showing the seed layer before NW growth; (d) ESEM images of the NWs after growth on a dip-coated seed layer.

2.3.3. Influence of $Zn(CH_3COO)_2$) concentration on the seed layer

In order to determine the influence of the precursor concentration on the orientation of the seed layer, four different concentrations of an equimolar solution of $Zn(CH_3COO)_2.2H_2O$ and ethanolamine have been studied: 5×10^{-3}, 0.1, 0.25 and 0.5 mol L^{-1} (section 2.2.3.). The thickness of the seed layer was evaluated by profilometry. Figure 2.11a shows that the thickness increases with the concentration of the precursor solution. The crystallinity of the ZnO seed layer was evaluated by UV-visible spectroscopy and XRD. The UV-visible and XRD results of the samples prepared using the lowest precursor solution concentration (5×10^{-3} mol L^{-1}) are not shown because no signal could be detected by these characterisation methods. According to Sagar *et al.*[21], the presence of ZnO crystals is characterised by a decrease in transmittance in the UV zone at ~380 nm. In addition, Poelman and Smet [22] have shown that this technique is thickness-dependent. Figure 2.11b shows the UV-visible transmission spectra (wavelength range of 200-500 nm) of ZnO seed layers prepared with different concentrations of precursor solution, after calcination in air at 650 °C. All seed layers exhibit a transmittance higher than 90% in the visible range. Transmittance, however, decreases sharply in the UV region due to the band gap absorption [21]. This decrease gets more and more pronounced as the concentration of $Zn(CH_3COO)_2$ increases; this is due to the thickness increase of the crystalline seed layer [22–24].

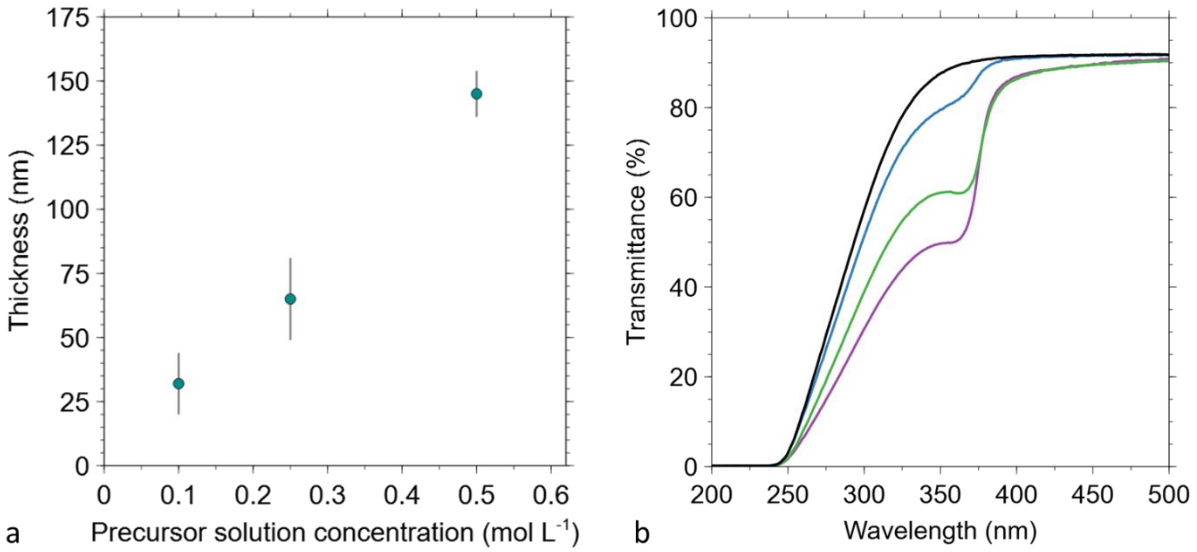

Figure 2.11. (a) ZnO seed layer thickness measurement using profilometry as a function of the precursor solution concentration; (b) UV-visible transmission spectra of ZnO seed layers using various precursor solution concentrations: (▬) substrate; (▬) 0.1 mol L^{-1}; (▬) 0.25 mol L^{-1}; (▬) 0.5 mol L^{-1}.

XRD analysis was carried out to evaluate the crystalline properties of the seed films, with Zn precursor concentration from 5 ×10^{-3} mol L^{-1} to 0.5 mol L^{-1}, and calcined at 650 °C in air. Figure 2.12 shows the XRD spectra between $2\theta = 31°$ and 37° as a function of the $Zn(CH_3COO)_2$ concentration. The intensity of the peaks increases with the concentration of the precursor solution, which could be due to the increase of the film thickness [25]. XRD peaks at 31.6°, 34.3° and 36.1°, corresponding to ZnO (100), (002) and (101) planes respectively [1], were identified for the 0.5 mol L^{-1} seed layer. However, only the (002) peak was observed in the case of the 0.25 mol L^{-1} seed layer, indicating a better orientation of the ZnO seed films (perpendicular to the substrate, see Chapter 1, Figure 1.1). According to Kang *et al.* [1], a well-oriented seed layer should lead to a better orientation of ZnO nanowires along the c-axis.

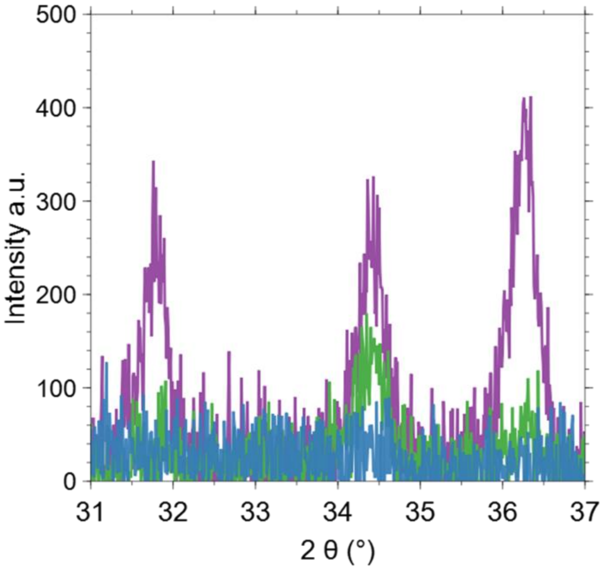

Figure 2.12. XRD spectra of ZnO NWs using precursor solutions with concentration of $Zn(CH_3COO)_2$ equal to (🟦) 0.1 mol L^{-1}, (🟩) 0.25 mol L^{-1} and (🟪) 0.5 mol L^{-1}.

ESEM microscopy was then used to characterise the NWs grown on these different seeds. Figure 2.13 shows top and side views of NWs grown on the seeds obtained with 5×10^{-3} mol L^{-1} (Figure 2.13a and Figure 2.13b), 0.1 mol L^{-1} (Figure 2.13c and Figure 2.13d), 0.25 mol L^{-1} (Figure 2.13 and Figure 2.13f) and 0.5 mol L^{-1} (Figure 2.13g and Figure 2.13h) of $Zn(CH_3COO)_2$ precursor concentrations. Seed solutions with a precursor concentration of 0.1 and 0.5 mol L^{-1} provided thicknesses (NW length) of 5.1 and 5.2 μm, respectively. However, an intermediate concentration of 0.25 mol $L^{-1}$of $Zn(CH_3COO)_2$ produced ZnO NWs with a length of 4.5 μm, and a concentration of 5×10^{-3} mol L^{-1} gave rise to a NW length of 3.7 μm. The high density of the NW does not allow to differentiate which concentration leads to the best orientation. O'Brien *et al.* [26] and Rao *et al.* [27] have shown that the orientation of ZnO seed layers strongly depends on the zinc precursor concentration and deteriorates when the concentration increases from 0.3 to 0.6 mol L^{-1}. The precursor concentration of 0.25 mol L^{-1}, leading to seed layers oriented perpendicular to the c-axis, was chosen in the next sections, devoted to the study of the influence of the seed layer calcination temperature on the morphology of the final ZnO NWs.

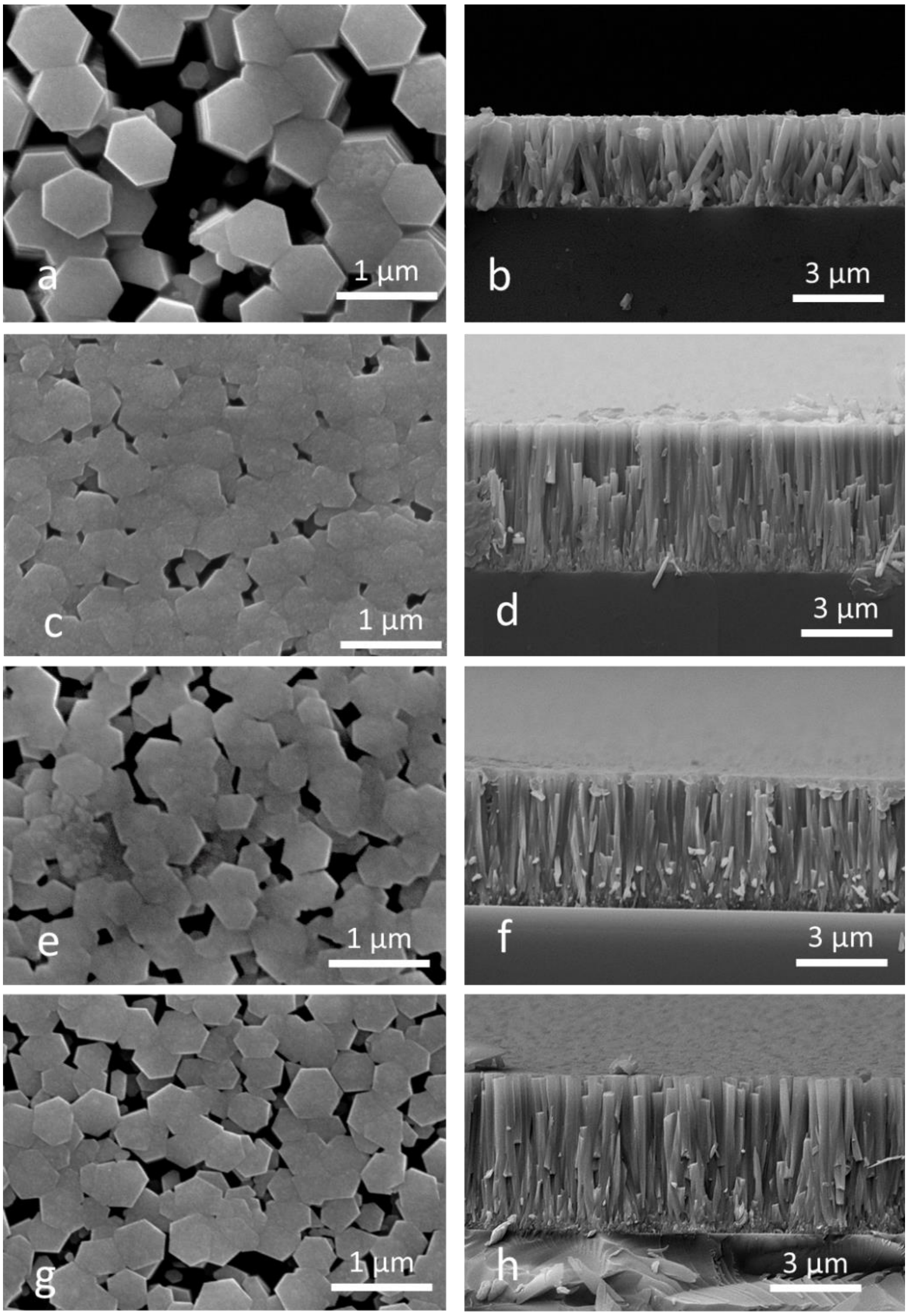

Figure 2.13. ESEM images of ZnO NWs obtained using seed solution with various precursor concentration. (a) Top view and (b) side view obtained for 5×10^{-3} mol L^{-1}; (c) Top view and (d) side view obtained for 0.1 mol L^{-1}; (e) Top view and (f) side view obtained for 0.25 mol L^{-1}; (g) Top view and (h) side view obtained for 0.5 mol L^{-1}.

2.3.4. Influence of the calcination temperature of the seed layer

This section is dedicated to the study of the calcination temperature of the seed layer, as described in section 2.2.4.

The effect of calcination temperature was evaluated for the seed prepared with a $Zn(CH_3COO)_2$ concentration of 0.25 mol L^{-1}. Four temperatures were studied: 200, 300, 400 °C and 650 ºC. As previously described, crystalline ZnO presents a transmission band in UV-visible spectra characterised by a decrease in the transmission signal at a wavelength of 380 nm. Figure 2.14a shows the thickness of the different seed layers after calcination. As the thickness values are close to each other, it has no influence on the UV spectra. Figure 2.14b shows the transmittance spectra of ZnO seed layer calcined at 200, 300, 400 and 650 °C. One observes that transmittance decreases with the increase of the temperature.

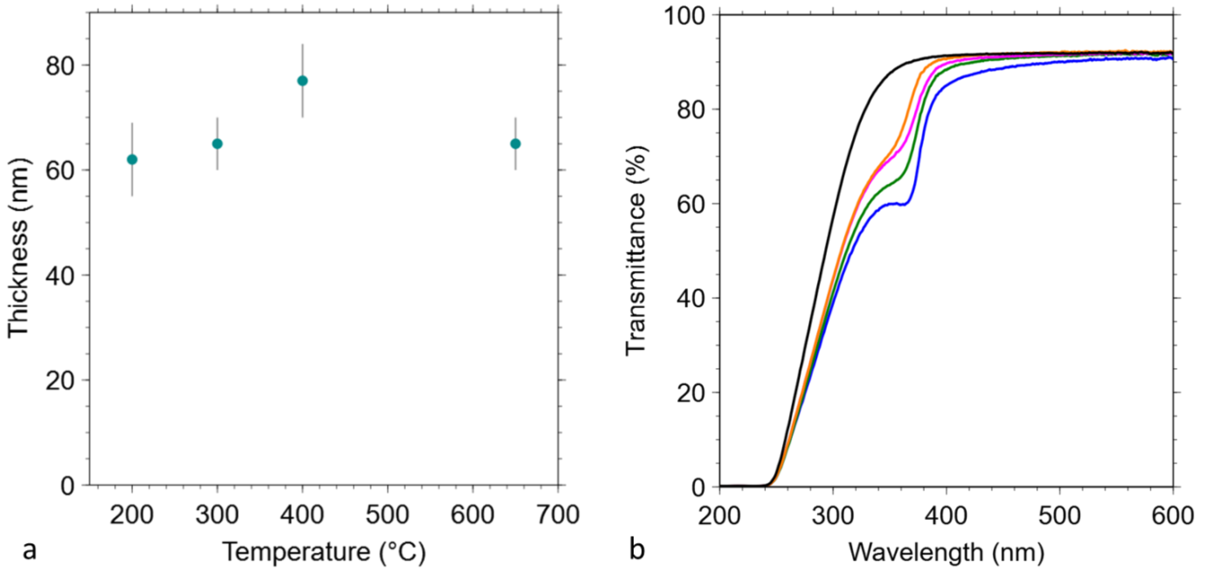

Figure 2.14. (a) Thickness measurements by profilometry and (b) UV-visible transmission spectra of ZnO seed layers calcined at (▬) 200 ºC, (▬) 300 ºC, (▬) 400 ºC and (▬) 650 ºC; (▬) substrate.

The XRD patterns (Figure 2.15) show the evolution of the crystallinity of the seed layer calcined at 200, 300, 400 and 650 °C. Only the (002) peak, corresponding to the desired c-axis orientation, is observed for a calcination temperature of 400 °C. This seed film thus exhibits preferred orientation perpendicular to the substrate surface compared to seed films treated at other calcination temperatures. However, there is an inconsistency in the results when comparing XRD and UV-visible characterisation methods. In XRD, the diffractogram corresponding to a seed calcination at 400 °C exhibits a higher crystallinity than a seed calcination at 650 °C. In UV-visible, a calcination at 650 °C leads to more pronounced absorption by the seed than a calcination at 400 °C, which can be associated with a higher crystallinity of the seed layer [21]. Kim *et al.* have shown that, when the thermal pre-treatment is too high above 300 °C, the vaporisation of the solvents and the thermal decomposition of zinc acetate occur abruptly and simultaneously with crystallisation, disturbing the preferential growth [28]. Here, the thermal decomposition does not take place during the thermal pre-treatment as 100 °C is too low, and the thermal decomposition takes place during the final calcination. Thus, a final calcination at 650 °C could be too high to avoid disturbance of the preferential orientation of the seed.

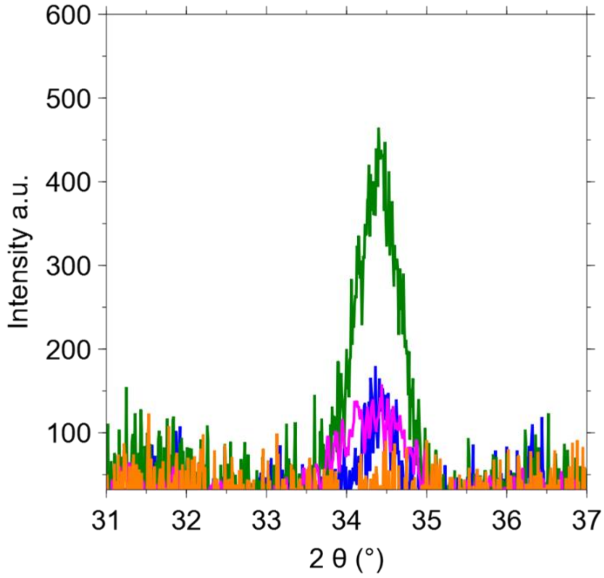

Figure 2.15. XRD diffractogram of ZnO seed layers calcined at (—) 200 ºC, (—) 300 ºC, (—) 400 ºC and (—) 650 ºC.

The calcination temperature process of the seed layer plays a key role in the growth, organisation and orientation of ZnO NWs. It is shown that each deposition process has an upper limit in temperature above which the loss of orientation is observed [5, 29]. This leads to the conclusion that an optimal range of temperature exist; this range certainly depends on the seed synthesis process. For example, using another seed recipe, Kim *et al.*[28] obtained an optimal range of calcination temperature, where preferential crystallisation can occur, between 200 and 300 °C. The impact of the temperature on the NW morphology was observed by environmental scanning electron microscopy. Figure 2.16 shows the top and side views of the synthesised NWs obtained on seed layers calcined at 200, 300, 400 and 650 ºC. The NWs present a diameter of 0.3 µm for a calcination of the seed at 200 °C (Figure 2.16a), a value of 0.4 µm at 300 °C (Figure 2.16b), and a value of 0.5 µm at 650 °C (Figure 2.16d). When the seed is calcined at 400 °C, the NWs are so close to each other that they almost form a continuous film and the diameter could not be evaluated (Figure 2.16c). The diameter of the NWs increases when the calcination temperature increases. This phenomenon was also reported by Ohyama *et al.*[5, 30]

NW length tends to increase with the seed calcination temperature. Seed layers calcined at 200 ºC give rise to slightly less oriented NWs with a length of 2.8 ± 0.05 µm (Figure 2.16e). The samples presented a length of 3.7 ± 0.1 µm at the intermediate temperature of 300 ºC (Figure 2.16f), 3.5 ± 0.1 µm at 400 ºC (Figure 2.16g) and 4 µm ± 0.1 µm at 650 °C (Figure 2.16h).

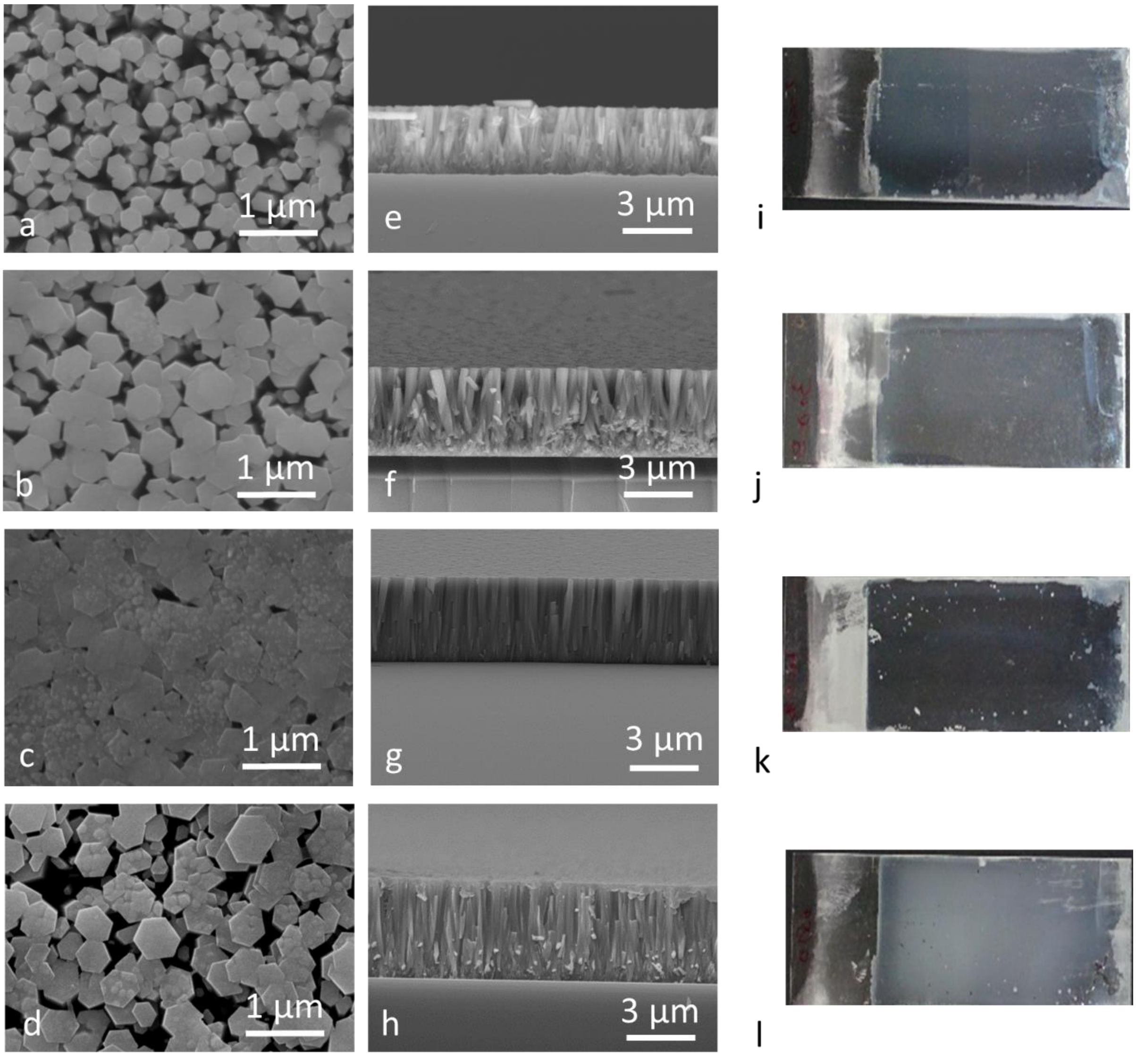

Figure 2.16. ESEM images of ZnO NWs obtained from seed layers calcined at (a) 200 ºC, (b) 300 ºC, (c) 400 °C, (d) 650 ºC (top views) and (e) 200 ºC, (f) 300 ºC, (g) 400 ºC, (h) 650 °C (side views). Pictures of ZnO NW film aspect after growth for seed calcined at (i) 200 °C, (j) 300 °C, (k) 400 °C and (l) 650 °C.

According to Podlogar *et al.*[6], ZnO NWs can grow perpendicular to the substrate even if, close to the seed layer, ZnO NWs grow in all directions (Figure 2.17 random nucleation). When the density of grains in the ZnO seed layer is sufficiently large, NWs growing inclined to the substrate surface collide with each other and their growth is stopped due to impingement with neighbouring NWs, as shown in Figure 2.17 (spatial confinement) [6]. Here, these two growth phases (first, NWs randomly oriented and, second, NWs aligned and perpendicular to the surface) can also be observed. The part at the bottom of the NW array shows rather randomly oriented NWs for all samples except the one calcined at 400 °C as, at the bottom (Figure 2.16g), the NWs adopt the orientation of the seed grain (oriented perpendicular to substrate) on which they grow. The upper region of the NWs array shows the ZnO NWs growing more or less oriented perpendicular to the substrate due to spatial confinement, the better orientation being observed on the seed calcined at 400 °C (Figure 2.16g).

The pictures of the substrates in Figure 2.16 show the NWs film aspect after growth. We can see that a seed layer calcined at 200 °C or 650 °C gives rise to an opaque ZnO NW film, while a transparent ZnO NW film is obtained when the seed layer is calcined at 300 °C and 400 °C. According to Ohyama *et al.*[5], the transparency of the NWs film is linked to the good orientation of the film.

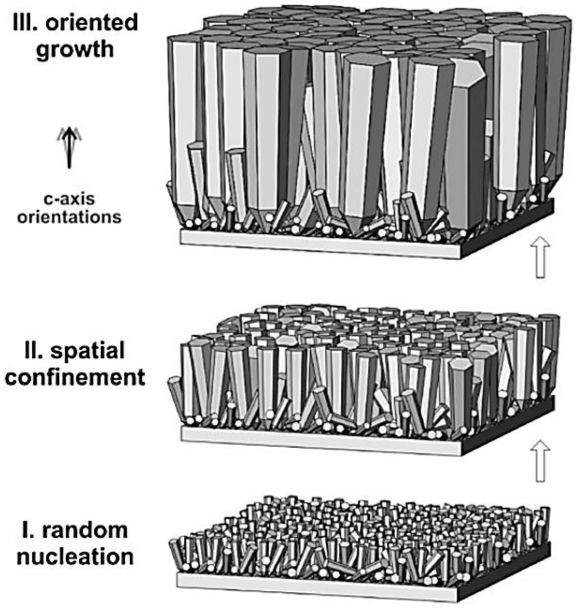

Figure 2.17. Evolution of the NW growth mechanism. Reproduced from reference [6].

2.3.5. Influence of the number of layers

According to Ji *et al.* [4], a thicker seed layer leads to a better orientation and crystallinity of the NWs. The number of layers was thus progressively increased (section 2.2.5) in order to increase the thickness of the seed and, possibly, improve the NW orientation. According to the previous results (section 2.3.3), the precursor solution concentration of 0.25 mol L^{-1} was used to deposit one seed coating with a thermal pre-treatment at 100 °C followed by a calcination at 650 °C and three seed coatings with a thermal pre-treatment at 100 °C of each layer deposited, followed by a final calcination at 650 °C. The seeds were characterised by profilometry, XRD, and UV-visible spectroscopy. Note that the experiments of section 2.3.5 were carried out in parallel with experiments of section 2.3.4 ; therefore, the same calcination temperature as section 2.3.3 was used instead of the optimum temperature determined in section 2.3.4, *i.e.* 400 °C.

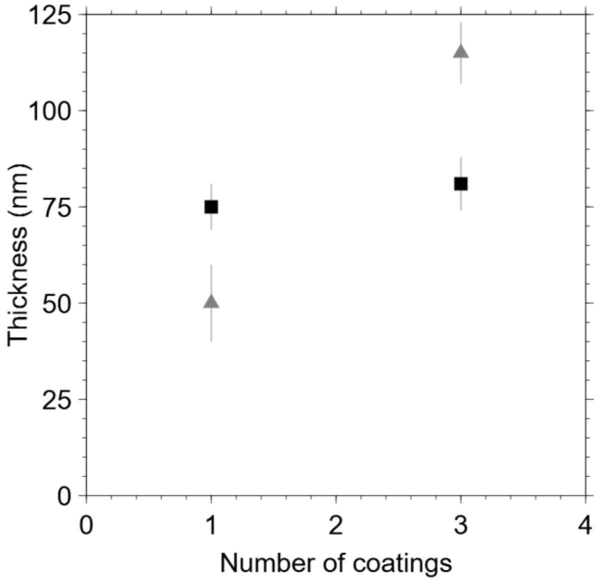

Figure 2.18. Thickness of the seed layer for one and three coatings, pre-treated at (■) 100 °C and (▲) 350 °C followed by a calcination at 650 °C. Measurement performed using profilometry.

Figure 2.18 shows the final seed thickness obtained for one or three successive coatings, thermal pre-treatment of either 100 °C or 350 °C between each deposit and a final treatment at 650 °C. The deposition of one and three layers with a thermal pre-treatment of 100 °C does not lead to an increase of the thickness: both results are included in each other's standard deviation. The optimum thermal pre-treatment and calcination temperature varies with the precursor solution composition. In any case, the intermediate thermal treatment temperature should be higher than the boiling point of ethanol and ethanolamine, and close to the crystallisation temperature of ZnO [28]. According to Greene *et al.* [3], zinc acetate thermally decomposes into ZnO nanoparticles at 200-300 °C. Below that temperature range, it can thus be supposed that the non-crystallised zinc salts of the previous coating dissolve in the precursor solution, when the substrate is introduced for the second coating. The temperature of 100 °C is not sufficient to form an adherent ZnO seed onto the substrate. Therefore, the thermal pre-treatment was increased to 350 °C in order to ensure the total decomposition of zinc acetate and its adhesion onto the substrate. The thickness for one layer deposited is 75 nm for thermal pre-treatment at 100 °C and 50 nm for a pre-treatment at 350 °C (Figure 2.18); this difference is probably due to the evaporation of the acetate precursors at 350 °C when decomposed into ZnO nanoparticles. Thus, calcination at 350 °C between each deposition step leads to an increase of the thickness from 50 nm (one coating) to 115 nm (three coatings). For one layer, the XRD diffractogram in Figure 2.19a shows a thin and intense peak at 2θ = 34.5°, corresponding to the (002) plane, when the pre-treatment is made at 350 °C instead of 100 °C; this indicates a better crystallinity and a preferential orientation perpendicular to the substrate. As the thermal decomposition temperature of zinc acetate is 240 °C, and the crystallisation of the ZnO seed layer begins at about 250 °C, thermally pre-treating at 100 °C is too low to expect a preferential orientation perpendicular to the substrate [28]. When three layers are deposited, the XRD diffractogram in Figure 2.18b shows an intense (002) peak, which again hints at preferential orientation along the c axis (*i.e.* perpendicular to the substrate).

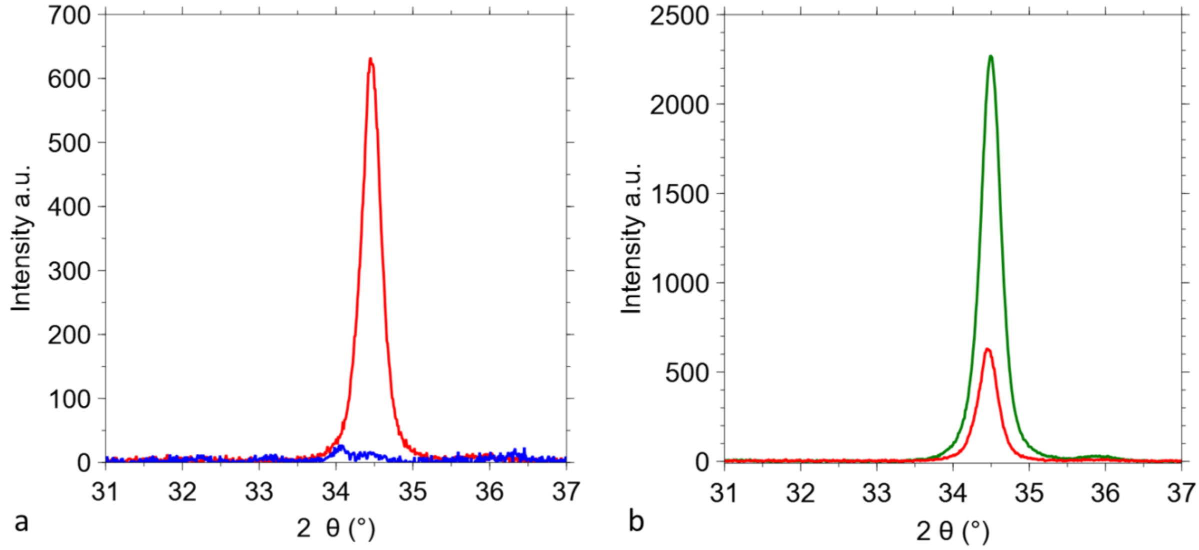

Figure 2.19. (a) Diffractograms comparing two different heating procedures for one coating deposited; coating thermally pre-treated at 100 °C (🟦) or 350 °C (🟥) followed by a final calcination at 650 °C; (b) Diffractogram comparing one coating (🟥) and three coatings (🟩) thermally pre-treated at 350 °C, followed by a calcination at 650 °C.

In the UV-visible characterisation, a higher transmittance is observed for a sample thermally pre-treated at 350 °C than for that pre-treated at 100 °C (Figure 2.20a). As explained before, the UV-visible characterisation is sensitive to both the thickness and the crystallinity of the film. The fact that the thickness of the seed thermally pre-treated at 100 °C is higher could explain why the lower thermal pre-treatment gives rise to more absorption, despite a lower crystallinity.

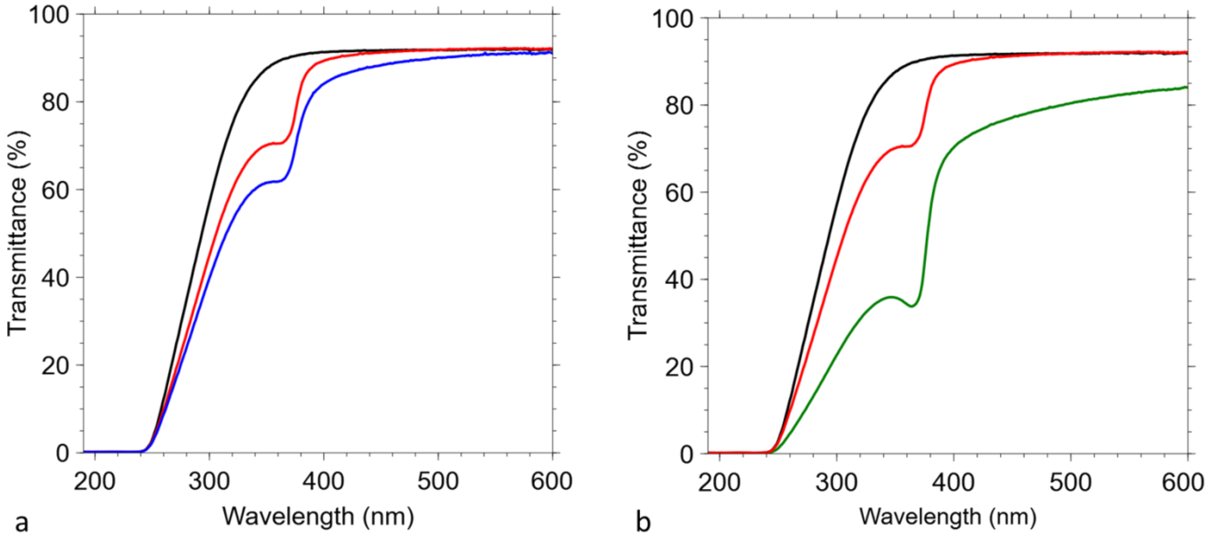

Figure 2.20. UV-visible characterisation of the seed layer on (▬) glass substrate as reference. (a) One coating thermally pre-treated at 100 °C (▬) or 350°C (▬) followed by a final calcination at 650 °C; (b) Comparison of one coating (▬) and three coatings (▬) thermally pre-treated at 350 °C, followed by a calcination at 650 °C.

The UV-visible characterisation shows a higher absorption when three successive coatings instead of one are deposited (Figure 2.20b); results presented concern samples with intermediate heat treatment at 350 °C. This is consistent with other measurement techniques as both thickness (profilometer) and crystallinity (XRD) increase with the number of coatings. To sum up, the results show that an intermediate heat treatment at 350 °C followed by a final calcination at 650 °C made it possible not only to increase the thickness in the case of multiple coating deposition, but also to increase the final seed crystallinity and to obtain a clear preferential orientation along the c-axis.

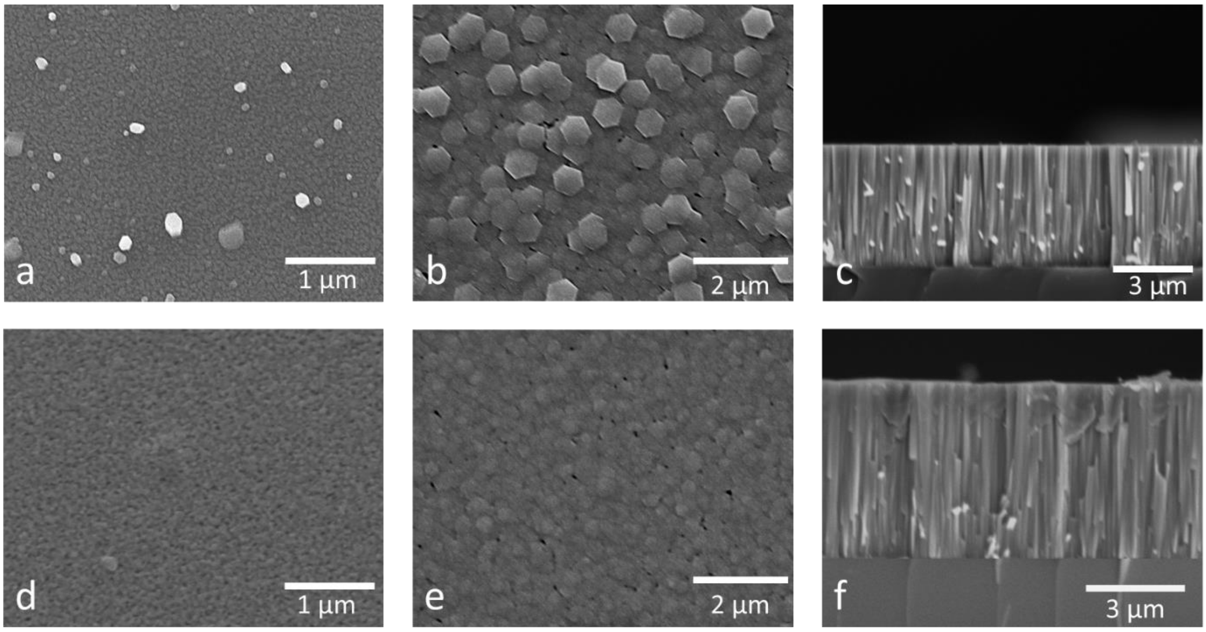

Figure 2.21. ESEM images for seeds made with one layer or three layers. (a) One seed layer with a thermal pre-treatment at 350 °C for 20 min followed by a calcination at 650 °C for 20 min; (b) top view and (c) side view of the NWs obtained after growth; (d) Three seed layers with an intermediate thermal treatment at 350 °C for 20 min between each deposit, followed by a final calcination at 650 °C for 20 min; (e) top view and (f) side view of the NWs obtained after growth.

Figure 2.21a shows one dip-coated seed layer with a thermal pre-treatment of 350 °C for 20 min followed by a calcination at 650 °C for 20 min. The ESEM image shows the aspect of the seed layer, where it is possible to see the ZnO nanoparticles and, in some areas, the beginning of NW growth, emerging from the seed film. Figure 2.21b and Figure 2.21c show the top view and side view of the NWs grown on the seed layer presented in Figure 2.21a. The density of the NWs is significant, their diameter is about 0.6 µm, and their length is 4.5 µm.

In Figure 2.21d, the seed layer with three successive depositions and intermediate heat treatments at 350 °C shows dense nanoparticles on the surface, which leads to dense and close nanowires. Figure 2.21e and Figure 2.21f show the top view and side view of the NWs grown on the seed layer presented in Figure 2.21d. It is difficult to determine whether the NWs have a better orientation or not due to the high density of the material for both one layer and three layers. Due to the high density of NWs for three layers, it is not possible to determine the diameter of the nanowires, while the sample length is about 4.8 µm. By increasing the number of seed layers, the NWs grow in a denser array and it seems that there is no impact on the NW length.

2.3.6. Influence of the calcination procedure on the seed layer

As the objective is to build a low temperature process in order to be able to produce piezoelectric nanogenerators based on ZnO NWs grown on flexible substrates, the next step was to reduce the final calcination temperature (as presented in section 2.2.4). In section 2.3.4, it was shown that a calcination temperature of the seed layer between 300 and 400 °C can lead to well aligned NWs. The following study was about growing ZnO NWs on a seed calcined at a temperature lower than 650 °C. To reduce the process time, the prolonged thermal pre-treatment in one continuous step has been tested. This part of the study consists thus in (i) the deposition of a precursor solution (0.25 mol L^{-1}) by dip-coating, followed by (ii) a continuous calcination at 350 °C, carried out for 20, 40, 60 or 80 min. The deposition of several layers was also studied with an intermediate heat treatment of 20 min at 350 °C between each layer, followed by a final calcination step of 20 min at 350 °C.

In UV-visible, crystalline ZnO exhibits an absorption peak at 380 nm. As presented in Figure 2.22a, modifying the duration of the calcination at 350 °C does not induce any difference in absorption spectra. Figure 2.22b shows the XRD diffractograms of the same seeds: no crystalline peak appears, whatever the duration of the calcination at 350 °C. The fact that the vaporisation of the solvents and the thermal decomposition of zinc acetate occur simultaneously with crystallisation could possibly disturb the preferential growth [28], and lead to badly crystallised samples.

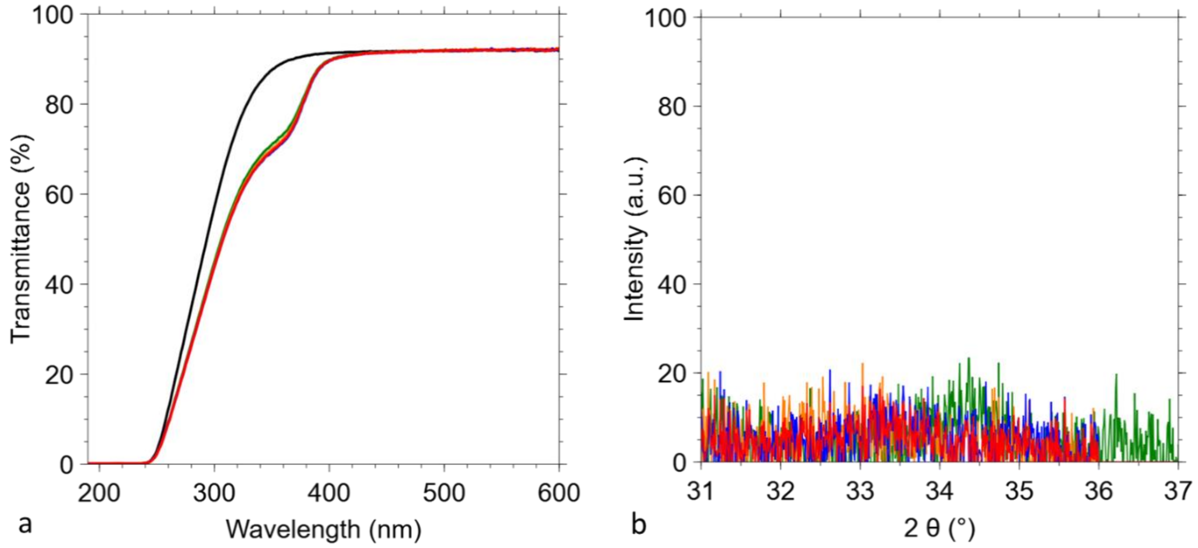

Figure 2.22. (a) UV-visible transmittance of the seed layers on (▬) glass substrate as reference and (b) XRD diffractograms for seeds calcined at 350 °C for different times (▬) 20 min, (▬) 40 min, (▬) 60 min and (▬) 80 min.

As a continuous calcination at 350 °C does not lead to a well-crystallised seed, a second type of thermal treatment was tested. It consisted in two calcination steps at 350 °C for 20 min with a cooling phase in-between. The comparison between the continuous (40 min at 350 °C) and two-step (2 times 20 min at 350 °C) calcination is presented in Figure 2.23a (UV-visible characterisation) and Figure 2.23b (XRD).

In UV-visible, there is no difference between the two types of treatments. UV-visible is a thickness dependant method, the sensitivy of the method regarding thickness is greater in our case. However, X-ray diffraction shows that discontinuous calcination has a strong influence on the crystalline state of the seeding layer. A discontinuous calcination at 350 °C with intermediate cooling to room temperature (20 min + 20 min) exhibits the crystalline peak of preferential orientation along the c-axis (002), while no peak is visible during a continuous calcination at 350 °C (40 min). According to these results, it is necessary to carry out a cooling step to obtain a seed layer oriented along the c axis (002).

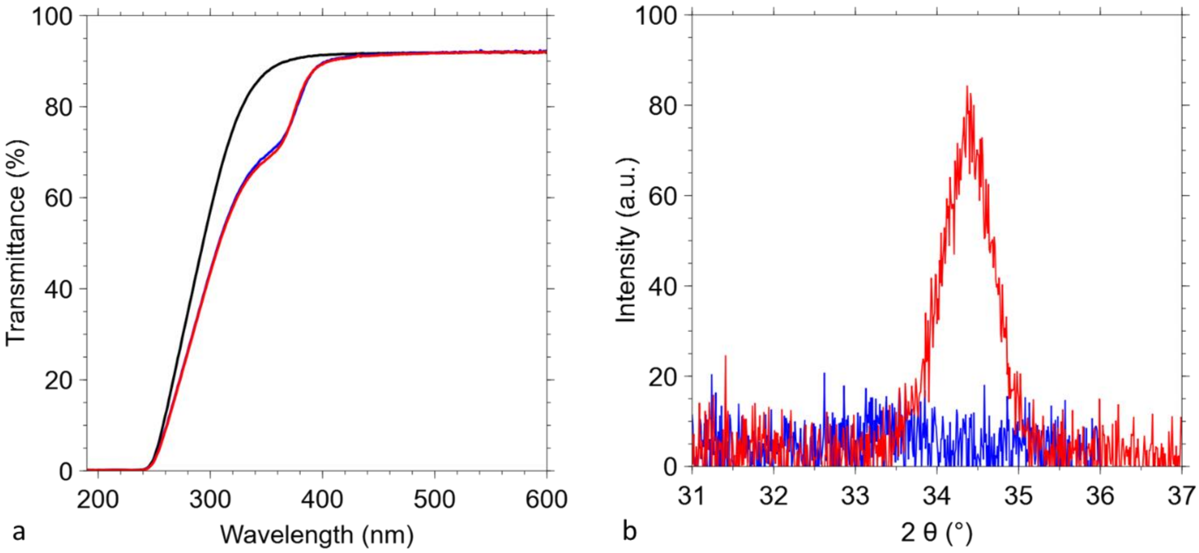

Figure 2.23. (a) UV-visible spectra and (b) XRD diffractogram of on-layer seed after (▬) 40 min continuous heat treatment at 350 °C and (▬) 2 × 20 min of heat treatment at 350 °C with intermediate cooling.

In Figure 2.24, we compare one deposited seed layer with two calcination steps at 350 °C for 20 min and a cooling phase in-between and three deposited seed layers with calcination steps at 350 °C for 20 min between each layer deposited and a final calcination at 350 °C for 20 min. The seed layers were characterised by UV-visible and XRD. The UV-visible characterisation in Figure 2.24a shows a higher absorption when three coatings instead of one are deposited. When three layers are present, the XRD diffractogram in Figure 2.24b shows an intense (002) peak, characteristic of an orientation of the seed layer along the c-axis.

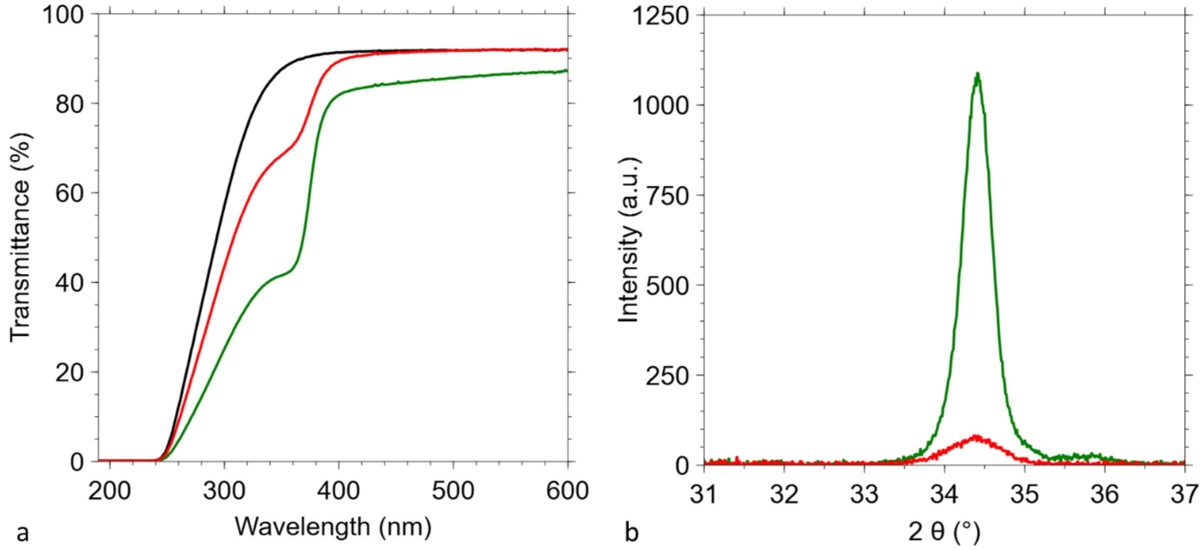

Figure 2.24. (a) UV-visible spectra of the seed for one coating (🟥) and three coatings (🟩) deposited with a calcination procedure of 2 × 20 min at 350 °C with intermediate cooling, substrate as reference (⬛); (b) XRD diffractogram of the seed layer for one coating (🟥) and three coatings (🟩) deposited with a calcination procedure of 2 × 20 min at 350 °C with intermediate cooling.

After characterising the seed layers, growth was achieved on seeds that were heat treated 2 × 20 min at 350 °C with an intermediate cooling. Growth was performed for one and three deposited seed layers. ESEM pictures are shown in Figure 2.25. As the NW layer is dense in each case, it is unfortunately not possible to tell if the nanowires are better oriented in the case of three seed layers, as one would expect because of the better seed orientation (see Figure 2.24).

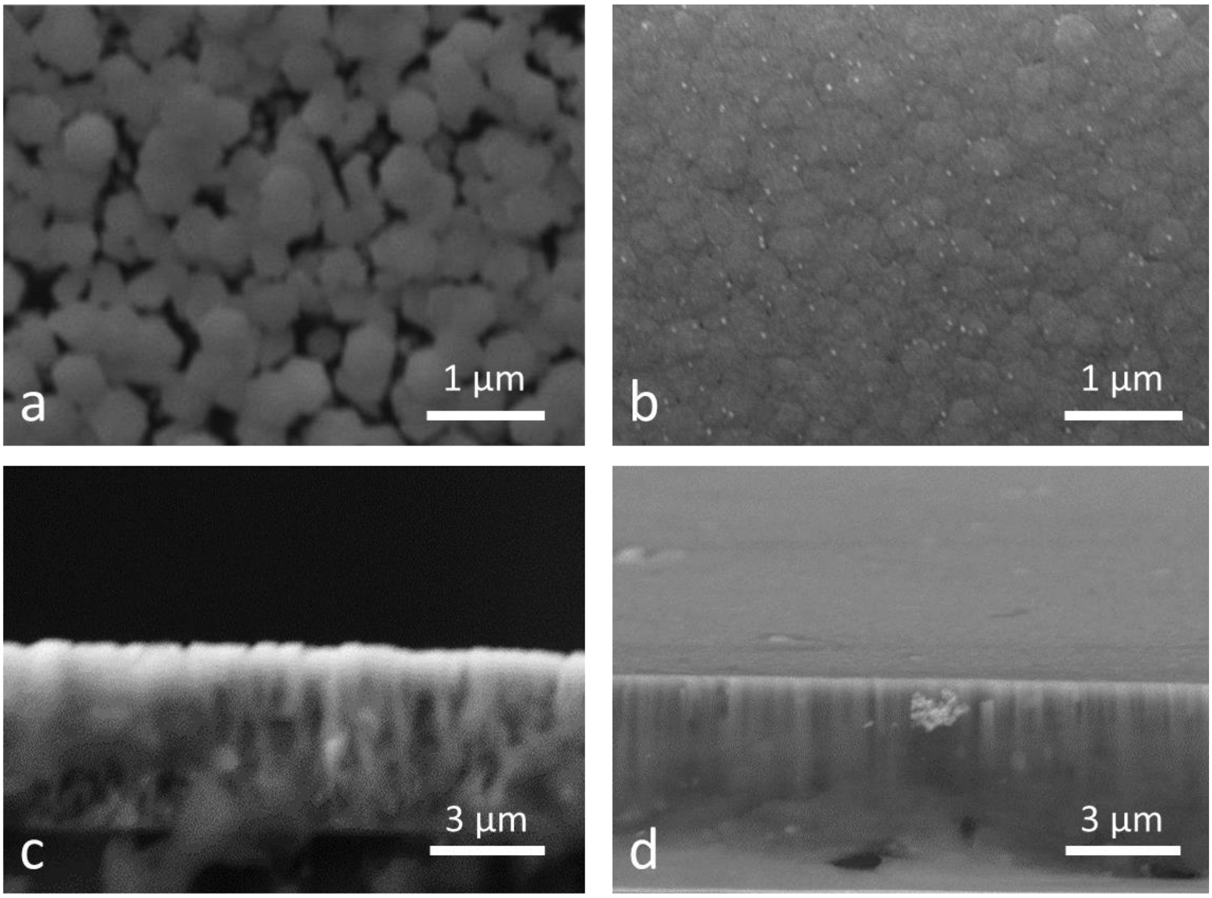

Figure 2.25. ESEM pictures of ZnO NWs grown on seed layers with an intermediate thermal treatment at 350 °C for 20 min, followed by a calcination step at 350 °C for 20 min. (a) Top view and (c) side view of the NWs grown on one seed layer coating; (b) top view and (d) side view of the NWs grown on three successive seed layer coatings.

2.3.7. NW growth process using zinc nitrate and zinc sulphate

The present results highlight the different process variables that impact the seed layer orientation. However, the high density of the NWs obtained under the chosen growth conditions hides the influence of the optimised seed layer on growth. A different growth process has been used to reduce the density of the NWs and thus to see the influence of the optimised seed layer. According to Kokotov *et al.* [13, 31], the growth of the NWs using zinc nitrate as precursor leads to thinner nanowires with a pencil tip shape at the end of the nanowire, while zinc sulphate leads to hexagonal flat-ended NWs. In order to obtain thinner, spaced, flat ended NWs, a growth solution was prepared from a mixture of a zinc nitrate (25%) and zinc sulphate (75%), as detailed in section 2.2.7.2 . This growth solution has been optimised by a researcher from the laboratory within a study parallel to the present work. The use of a mixture of zinc salts optimises the growth of NWs, *i.e.* enables controlling the length, diameter and density of the nanowires. The NWs were grown on the seed layer; this seed layer was prepared using the procedure in section 2.2.6. It can be seen (Figure 2.26) that, with a mixture of zinc precursors, one obtains less dense NWs with smaller diameter (75 nm) and shorter length (3-4 µm). Whatever the number of seed layers (one or three), the NWs are spaced from each other (Figure 2.26). One also observes that the NWs are well oriented along the c-axis, with a slightly better orientation for the three-layer seed (Figure 2.26c and Figure 2.26d). This final result fully confirms the optimisation of the seed layer and its impact on the final ZnO NW morphology.

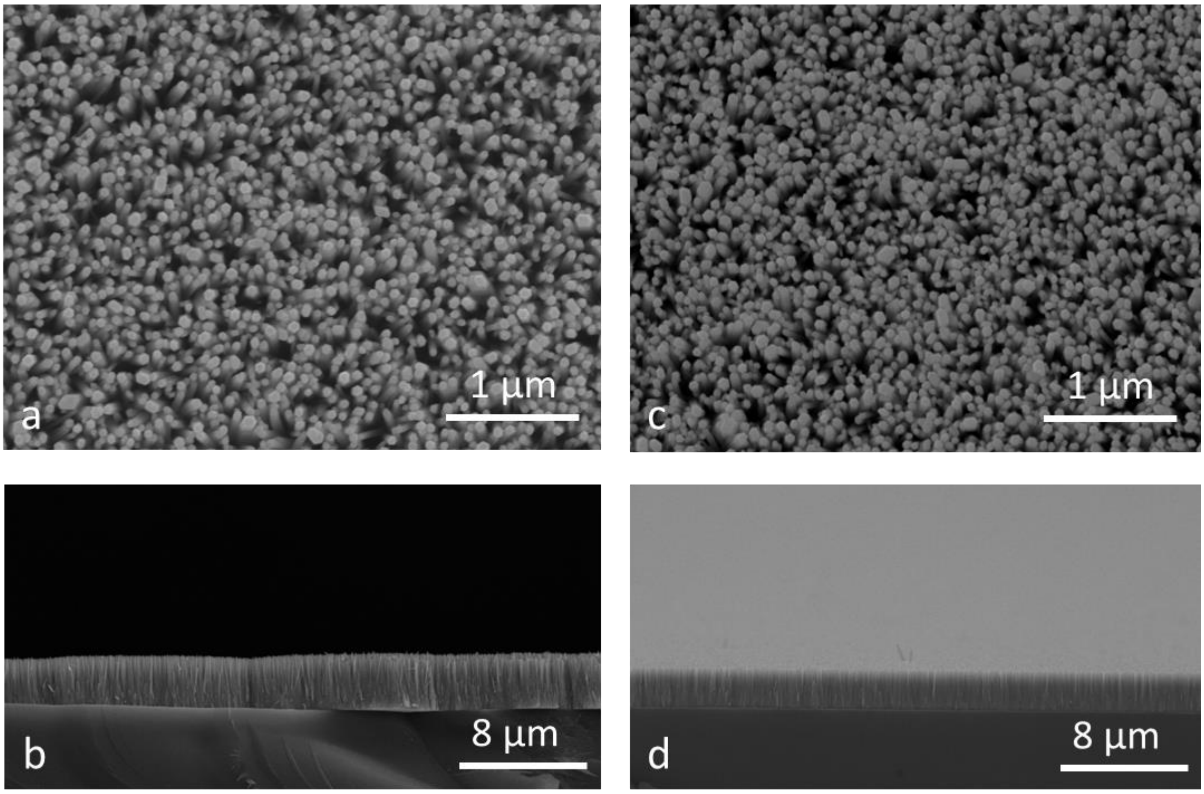

Figure 2.26. ZnO NWs grown using zinc salt mixture (25% zinc nitrate and 75% zinc sulphate), on a seed layer; the seed layer (1 or 3 deposits) was prepared following the procedure of section 2.2.6. Seed layer made of one deposit calcined 2 × 20 min at 350 °C: (a) top view showing the morphology of the NWs and (b) side view. Seed layer made of three deposits calcined 2 × 20 min at 350 °C: (c) top view showing the morphology of the NWs and (d) side view.

2.4. Conclusions

The seed layer of the ZnO NW array has been optimised in order to improve the reproducibility and the homogeneity of the NWs after growth. The deposition method of the seed layer, the precursor solution concentration, as well as the thermal treatment of the seed have been studied. Dip-coating was preferred to spin-coating as deposition technique as it is a low cost, scalable and reproducible method that leads to homogeneous coating.

In this study UV-visible characterisation method was used as an additional technique to XRD measurement to evaluate the crystalline quality of the seed layer. However this technique is thickness sensitive, in our case the influence of the thickness is probably higher. It is therefore preferable to refer to the XRD analysis.

From the results obtained, it is concluded that it is possible to obtain a well oriented seed layer if the deposit is made from an equimolar solution of $Zn(CH_3COO)_2.2H_2O$ and ethanolamine with a concentration of 0.25 mol L^{-1}. It was shown that the heating procedure consisting in a thermal pre-treatment step followed by the calcination of the seed layer has a strong influence on the orientation of the ZnO NWs. On the one hand, an intermediate calcination temperature of the seed at 350 °C instead of 100 °C made it possible to increase the thickness in the case of multilayer deposits by avoiding the redissolution of the precursors. On the other hand, the increase of the temperature of the thermal pre-treatment significantly improves the crystallinity of the layer by converting the precursors into ZnO.

In this study, the results have also shown that a thermal pre-treatment step of the seed, consisting in a step at 350 °C for 20 min, followed by a calcination step of 650 °C leads to a an orientation of the seed layer along the c-axis. This process leads to well-oriented NWs as a seed layer with oriented nanoparticles allows better oriented growth of ZnO NWs. However, 650 °C is too high to consider most flexible supports. So, the next question was whether it was possible or not to decrease the maximum temperature of the thermal treatments. The optimised “low temperature” seed process developed finally consists in (i) the deposition of the ZnO precursors (0.25 mol L^{-1}) by dip coating followed by (ii) two successive calcination steps at 350 °C for 20 min. This process is suitable for several organic substrates used for building flexible nanogenerators, such as *e.g.* Kapton®FN from DuPont™, which is a polyimide material with a maximum thermal stability of 400 °C. The adhesion and homogeneity of ZnO deposits should be characterised when the substrate is modified.

Finally, by combining the optimised seed process and the modified growth process using a solution containing both zinc nitrate and zinc sulphate, as developped by a senior researcher of the NCE laboratory, it was possible to obtain well oriented separate NWs. In the next chapter, the assembly and characterisation of such NW arrays as piezoelectric nanogenerator will be described.

References

1. Y. H. Kang, C. G. Choi, Y. S. Kim, J. K. Kim, Influence of seed layers on the vertical growth of ZnO nanowires. *Mater. Lett.* **63**, 679–682 (2009).
2. J. Song, S. Lim, Effect of seed layer on the growth of ZnO nanorods. *J. Phys. Chem. C*. **111**, 596–600 (2007).
3. L. E. Greene, M. Law, D. H. Tan, M. Montano, J. Goldberger, G. Somorjai, P. Yang, General route to vertical ZnO nanowire arrays using textured ZnO seeds. *Nano Lett.* **5**, 1231–1236 (2005).
4. L. W. Ji, S. M. Peng, J. S. Wu, W. S. Shih, C. Z. Wu, I. T. Tang, Effect of seed layer on the growth of well-aligned ZnO nanowires. *J. Phys. Chem. Solids* **70**, 1359–1362 (2009).
5. M. Ohyama, H. Kozuka, T. Yoko, Sol-gel preparation of ZnO films with extremely preferred orientation along (002) plane from zinc acetate solution. *Thin Solid Films* **306**, 78–85 (1997).
6. M. Podlogar, D. Vengust, J. J. Richardson, M. Strojnik, M. Mazaj, G. Trefalt, N. Daneu, A. Rečnik, S. Bernik, Parametric study of seed-layer formation for low-temperature hydrothermal growth of highly oriented ZnO films on glass substrates. *Phys. Status Solidi A* **210**, 1083–1092 (2013).
7. N. Hoffmann, P. G. Jones, R. Streubel, Intramolecular [3+2] cycloaddition of a nitrilium phosphane ylide complex to the P-phenyl group of a Wittig ylide. *Angew. Chemie - Int. Ed.* **41**, 1186–1188 (2002).
8. S. Baruah, A. E. J. Dutta, Effect of seeded substrates on hydrothermally grown ZnO nanorods. *J. Sol-Gel Sci. Technol.* **50**, 456–464 (2009).
9. J. B. Cui, C. P. Daghlian, U. J. Gibson, R. Püsche, P. Geithner, L. Ley, Low-temperature growth and field emission of ZnO nanowire arrays. *J. Appl. Phys.* **97**, 1–7 (2005).
10. M. T. Spitler, in *Journal of the American Chemical Society*, M. Dekker, Ed. (American Chemical Society, New York and Basel, 2003), vol. 125, pp. 6836–6837.
11. K. Kakaei, M. D. Esrafili, A. Ehsani, in *Graphene surfaces - Particles and catalysts* (Elsevier, Amsterdam, 2019), vol. 27, pp. 303–337.
12. I. A. Neacşu, A. I. Nicoară, O. R. Vasile, B. Ş. Vasile, in *Nanobiomaterials in Hard*

Tissue Engineering: Applications of Nanobiomaterials (Elsevier, Bucarest, 2016), pp. 271–295.

13. M. Kokotov, G. Hodes, Reliable chemical bath deposition of ZnO films with controllable morphology from ethanolamine-based solutions using $KMnO_4$ substrate activation. *J. Mater. Chem.* **19**, 3847–3854 (2009).
14. J. J. Richardson, F. F. Lange, Controlling low temperature aqueous synthesis of ZnO. *Cryst. Growth Des.* **9**, 2570–2575 (2009).
15. M. Kokotov, S. Bar-Nachum, E. Edri, G. Hodes, Effect of glass dissolution on the solution deposition of ZnO films and its exploitation for deposition of Zn silicates. *J. Am. Chem. Soc.* **132**, 309–314 (2010).
16. P. M. Martin, in *Handbook of Deposition Technologies for Films and Coatings*, P. M. Martin, Ed. (Elsevier, Third Edit., 2010), pp. 93–134.
17. S. Guillemin, E. Appert, H. Roussel, B. Doisneau, R. Parize, T. Boudou, G. Bremond, V. Consonni, Controlling the structural properties of single step, dip coated ZnO seed layers for growing perfectly aligned nanowire arrays. *J. Phys. Chem. C.* **119**, 21694–21703 (2015).
18. L. Znaidi, Sol-gel-deposited ZnO thin films: A review. *Mater. Sci. Eng. B* **174**, 18–30 (2010).
19. L. Znaidi, R. L. E. Guennic, C. Sanchez, A. Kanaev, Elaboration of ZnO thin films with preferential orientation. *J. Sol-Gel Sci. Technol.* **26**, 817–821 (2003).
20. L. Znaidi, G. J. A. A. S. Illia, S. Benyahia, C. Sanchez, A. V Kanaev, Oriented ZnO thin films synthesis by sol – gel process for laser application. *Thin Solid Films* **428**, 257–262 (2003).
21. P. Sagar, P. K. Shishodia, R. M. Mehra, H. Okada, A. Wakahara, A. Yoshida, Photoluminescence and absorption in sol-gel-derived ZnO films. *J. Lumin.* **126**, 800–806 (2007).
22. D. Poelman, P. F. Smet, Methods for the determination of the optical constants of thin films from single transmission measurements: a critical review. *J. Phys. D: Appl. Phys.* **36**, 1850–1857 (2003).
23. S. A. Kamaruddin, K. Y. Chan, H. K. Yow, M. Zainizan Sahdan, H. Saim, D. Knipp, Zinc oxide films prepared by sol-gel spin coating technique. *Appl. Phys. A* **104**, 263–268 (2011).
24. S. R, Determination of the thickness and optical constants of amorphous silicon. *J. Phys. E* **16**, 1214 (1983).

25. T. Prasada Rao, M. C. Santhoshkumar, Effect of thickness on structural, optical and electrical properties of nanostructured ZnO thin films by spray pyrolysis. *Appl. Surf. Sci.* **255**, 4579–4584 (2009).
26. S. O. Brien, L. H. K. Koh, G. M. Crean, ZnO thin films prepared by a single step sol – gel process. *Thin Solid Films* **516**, 1391–1395 (2008).
27. J. Rao, R. J. Winfield, L. H. K. Koh, S. O'Brien, G. M. Crean, Patterned transparent zinc oxide films produced by sol-gel embossing. *Phys. Status Solidi A* **205**, 1938–1942 (2008).
28. Y. Kim, W. Tai, S. Shu, Effect of preheating temperature on structural and optical properties of ZnO thin films by sol – gel process. *Thin Solid Films* **491**, 153–160 (2005).
29. J. Lee, K. Ko, B. Park, Electrical and optical properties of ZnO transparent conducting films by the sol – gel method. *J. Cryst. Growth* **247**, 119–125 (2003).
30. M. Ohyama, H. Kozuka, T. Yoko, S. Sakka, Preparation of ZnO films with preferential orientation by sol-gel method. *J. Ceram. Soc. Jpn.* **104**, 296–300 (1996).
31. M. Kokotov, A. Biller, G. Hodes, Reproducible chemical bath deposition of ZnO by a one-step method: The importance of "contaminants" in nucleation. *Chem. Mater.* **20**, 4542–4544 (2008).

Chapter 3. Applications of ZnO nanowires

3.1 Introduction

The first chapter of this thesis was focused on the study of the growth kinetics of the ZnO nanowires (NWs). A combined process consisting in the deposition of a seed layer, followed by the NW growth using chemical bath deposition (CBD), was used to synthesise the NWs. The process reached a maximum growth speed of 70 nm min^{-1}, which is suitable for large-scale manufacturing, as the target was 20 nm min^{-1}. Since it was complicated to obtain high quality, well-aligned NWs in a reproducible manner, the second chapter was devoted to the study of the seed layer deposition and its thermal treatment to obtain homogeneous ZnO NW growth. The results have shown that it was possible to obtain well oriented seed layers, using an equimolar solution of $Zn(CH_3COO)_2.2H_2O$ and ethanolamine at 0.25 mol L^{-1}, followed by two successive calcination steps at 350 °C for 20 min. Finally, the work of a senior researcher of the NCE laboratory made it possible to obtain separate NWs, *via* an optimised growth process using a mix of zinc nitrate and zinc sulphate precursors. The results of the first and second chapters, combined with the parallel work of the senior researcher of the NCE lab active in the same research field in the EnSO project, finally led to well-aligned and separate NWs.

In this chapter, we report two applications of the ZnO NWs developed during this PhD thesis.

The first application consists in the assembly and characterisation of NWs as piezoelectric nanogenerators. The work (section 3.2) deals with the growth of NWs on an appropriate support, the nanogenerator assembly, and the impact of the NW properties on the nanogenerator performances. It must be noted that the reported results were obtained from samples (i) grown on specific substrates sent by the Greman laboratory in Tours (France) in the context of the EnSO project and (ii) prepared and characterised by the senior researcher. The samples were then sent back to the Greman laboratory for assembly and testing as piezoelectric generator. It however could not include the study of the fully optimised NW deposits, since the topic was stopped after two years of research. In fact, the nanogenerators presented here were assembled and characterised while results of Chapter 2 were obtained. The main contribution of the current thesis author lies thus somewhat upstream from that study, *i.e.* in the participation to the growth kinetics and seed optimisation study as described in Chapters 1 and 2. The short report presented here aims at showing where the research ended up, and highlighting the usefulness of the NWs synthesis study, at a global scale.

The second application consists in testing the activity of the NWs for the photocatalytic degradation of various molecules (often pollutants) in water; indeed, one of the main research topics of the NCE laboratory is photocatalysis [1], and ZnO NWs are reported by literature as good materials for that kind of application. Therefore, it was interesting to get an insight into the performance of the obtained NWs for this application. The second part of the Chapter (section 3.3) is thus devoted to the measurement of the photocatalytic activity of ZnO NW arrays for the degradation of H_2O_2. Measurement and analysis were performed in collaboration with another PhD student of the NCE group.

3.2 ZnO NWs as nanogenerators

3.2.1 Introduction

Within the framework of the EnSO project, it was considered to produce piezoelectric nanogenerators (NG) from ZnO NWs. These NGs would use the energy resulting from mechanical stress on the ZnO NWs to convert it into electricity (piezoelectric effect), in order to power Li-metal microbatteries by providing a potential of 4.2 V and a power in the range of 1 μW cm^{-2}. Due to a lack of time, the nanogenerator performances of the NWs previously optimised in Chapter 2 could unfortunately not be tested. This work results from a collaboration with the Greman laboratory (Tours, France). While the NCE laboratory of the ULiège was in charge of synthesising the NW arrays, the Greman laboratory was in charge of the NG set-up and the development of a test bench for the characterisation of NWs as nanogenerators.

The NG consists of four components: (i) the bottom electrode, (ii) the piezoelectric material (ZnO NWs), (iii) an insulating layer and (iv) the top electrode (Figure 3.1). Moreover, wires are attached to the bottom and top electrode of the NG. The bottom electrode is made of a metal that allows the current from the piezoelectric material to pass through. Contrarily to the previous chapters, the substrate used here was made of gold deposited on silicon (Au/Si) by sputtering; those supports were provided directly by the Greman laboratory.

The piezoelectric properties of ZnO NWs is due to their crystalline asymmetry [2], which leads to the change in position of the atoms during deformation, and induces the appearance of an electric dipole along the NW. The semiconducting property of ZnO contributes to the formation of a low electrical potential and allows the power supply of microbattery storage systems. To manufacture the NG, an insulating layer is added around and between the ZnO

NWs as well as between the ZnO and the top electrode. This insulating layer prevents the NWs from touching each other when they are compressed, thus, electrically isolates the NWs from each other. The insulating material also serves as a buffer layer protecting NWs from intimate interaction with the electrode. This also improves the mechanical strength of the NW system. This greatly enhances the NG efficiency as the applied force can then be transferred to all NWs even though they vary in length. Moreover, the insulating layer prevents extrinsic screening due to the top electrode. It means that the insulating polymer layer provides an infinite potential barrier, preventing the induced electrons in the electrodes from “leaking” through the ZnO/metal interface.

Finally, the top electrode is composed of a metal which causes the leakage current through the metal/semiconductor interface and provides extrinsic screening. In case of direct contact between the electrode and the piezoelectric material, weak electrical conduction occurs, which limits the performance of the NG. This contact should therefore be prevented with the insulating layer.

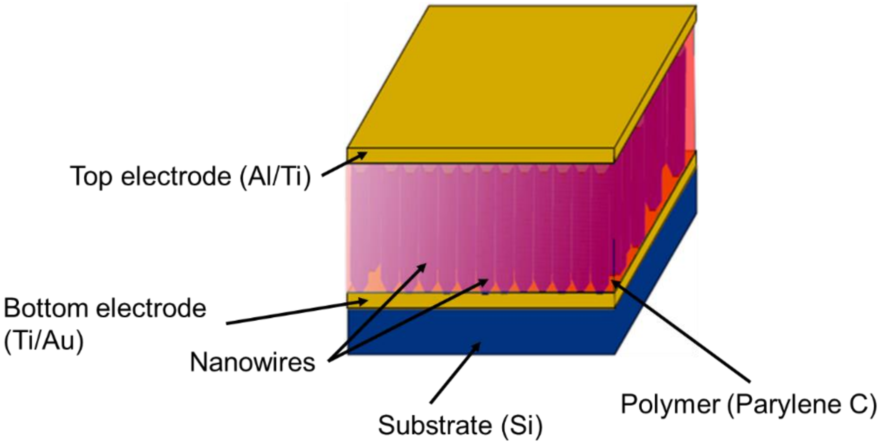

Figure 3.1. Scheme of the configuration of ZnO nanogenerators.

As explained previously, when a mechanical stress is applied onto piezoelectric ZnO NWs, one observes a relative displacement of cations (Zn^{2+}) and anions (O^{2-}) along the direction of strain, which results in the generation of piezopotential, as presented in Figure 3.2. Positive net charges can be assumed at the top of ZnO NWs, with the corresponding negative charges on the top electrode surface. The capacitance associated with the ZnO-Au interface ensures that the bottom electrode is net positive. With these conditions, periodically bending and releasing the NG will generate an alternating voltage that can be detected across a resistive load.

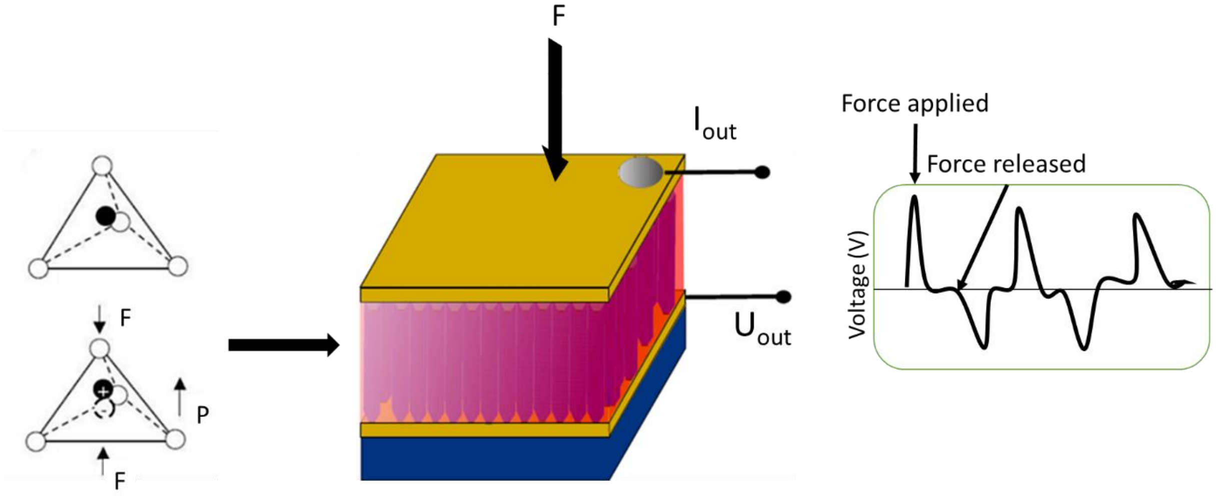

Figure 3.2. Scheme of the working NGs [2].

The performances of the NG depend on the length, diameter and density of the NW arrays. Hinchet *et al.* [3] determined the influence of NW density, length and diameter on the performance of nanogenerators by modelling NW compression. However, this modelling does not take into account the presence of free charges in the NWs which originate from structural defects along the NWs. To measure the influence of the NW density, a ratio parameter R was defined as the NW diameter (D) divided by the core cell (diameter or the NWs + surrounding polymer) width (W), representing the NW density. A ratio $R = 1$ corresponds to a high NW density (4×10^{10} cm^{-2}) and $R = 0.1$ to a low NW density (4×10^{8} cm^{-2}). Figure 3.3a and Figure 3.3b show the computed mechanical energy and electrical energy of the NG core cell as a function of NW density. On the one hand, the results show that low density allows better transfer of the mechanical stress applied to the system to the NWs; that transfer is done through the polymer surrounding the NWs (Figure 3.3a). On the other hand, low density implies less NW to transform mechanical energy into electrical energy (piezoelectric effect). Therefore an optimal ratio R, corresponding to an optimum density of NWs, leads to a maximum of energy (mechanical and electrical) generated [3] (Figure 3.3b).

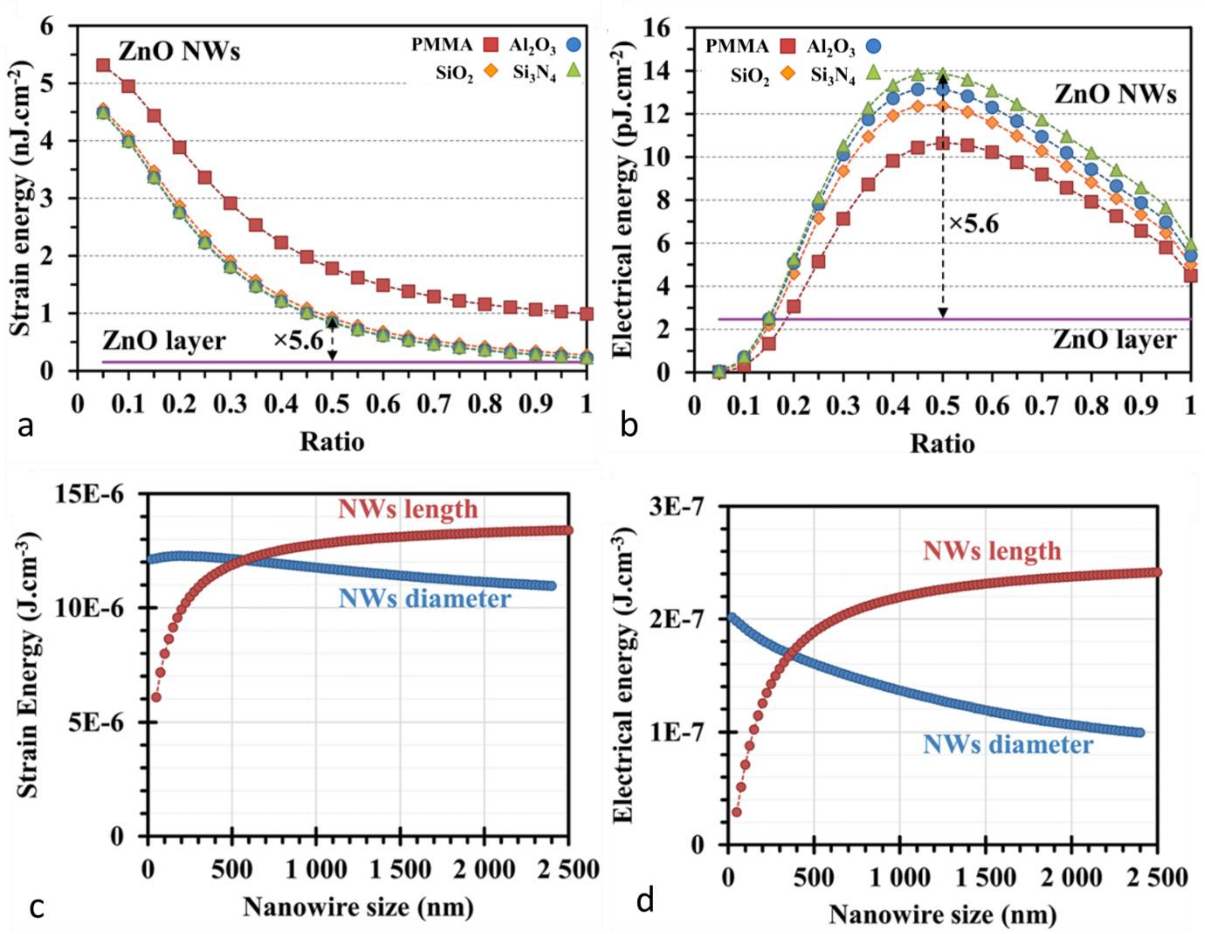

Figure 3.3. Effect of the NW density (in terms of $R = D/W$ ratio) on the NG properties: (a) strain energy, (b) electrical energy of NG core cell using different top insulating materials: PMMA, SiO_2, Al_2O_3, and Si_3N_4. Effect of the length and diameter on the NG properties on (c) strain energy and (d) electrical energy as a function of NW diameter at constant length $L = 600$ nm and as a function of NW length at constant radius $r = 50$ nm. Reproduced from [3].

The aspect ratio of the NWs, defined as the length to diameter ratio, L/D, also has a significant impact on the NG performance, as shown by Hinchet *et al.* [3]. For a given NW length of $L = 600$ nm, the diameter D was increased from 24 to 2400 nm, which led to the decrease of the NW aspect ratio (L/D) from 25 to 0.25. This reduces the density of mechanical energy stored and the electrical energy generated. For a fixed diameter of 50 nm, the NW length was increased from 600 nm to 2500 nm, with a NW aspect ratio increasing from 12 to 50. This increased the density of mechanical energy stored and the electrical energy generated. These results show that a low NW aspect ratio reduces the density of the mechanical energy stored and the electrical energy generated as presented in Figure 3.3c and Figure 3.3d; a high aspect ratio is thus required for efficient NGs.

The intrinsic and extrinsic screenings can also annihilate the electrical performances of NWs. On the one hand, the intrinsic screening is due to structural defects in the crystal, such as oxygen vacancies or the presence of interstitial zinc [4]. These defects generate free charges, *i.e.* positive charges in the case of oxygen vacancies and interstitial zinc. These charges can mask the piezoelectric charges and thus reduce the performance of the NG [5, 6]. The concentration of free charges in the NW is highly dependent on the synthesis, and can even vary from one NW to another in a sample originating from the same synthesis batch. These free charges mask the piezoelectric effect all the more as their concentration is high (Figure 3.4). On the other hand, the extrinsic screening is due to the recombination of piezoelectric charges between NWs when touching each other.

The presence of excess free charge carriers (>10^{18} cm^{-3}) in the material is frequent for NWs grown by CBD [7]. So, despite the interest of ZnO NWs as possible piezoelectric elements in energy harvesters, the excess free charge carriers may completely neutralise the induced piezoelectric potential [8, 9]. It is thus necessary to characterise the structural defects of the NWs to understand the relationship between the NW synthesis process and the obtained NW array properties as NG.

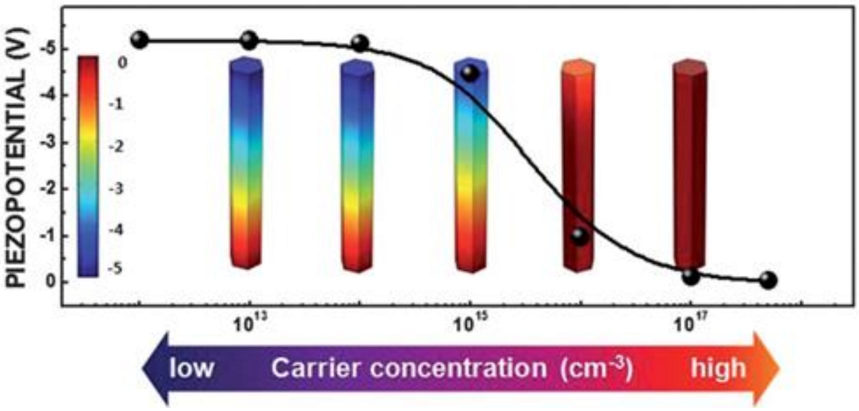

Figure 3.4. Influence of defects on the piezoelectric effect. Reproduced from [4].

Photoluminescence (PL) at room temperature is an excellent characterisation technique to evaluate the amount of structural defects present in the NWs. It consists in exciting an electron in the valence band with a photon whose energy is higher than the energy of the gap to allow its migration to the excited state. When the electron returns to the valence band, it emits a light beam which is detected and allows to obtain an emission spectrum (Figure 3.5). The absolute intensity of emission peaks is proportional to the amount of photoluminescent material on the substrate. Thus, the intensity of the peaks observed in PL increases with the increase in diameter and length of the NWs and with the density of the NWs. The absolute intensity is also a function of the experimental conditions. In case of excess free charge carriers in ZnO NWs due to structural defects, the piezo- electric potential of semiconducting ZnO is generated as a result of competition between piezoelectrically generated ionic charges and the free charges screening them, causing detrimental effect of charges generated from the piezoelectric material [4].

Another factor limiting ZnO NW-based NG performance is the charge leakage across the metal-semiconductor interface in case of direct contact between ZnO NWs and the top electrode [10]. Such limitations have been minimised here by isolation of the ZnO NWs tips from external electrodes using insulating layers [11]. There are various advantages of using NG device prototype where the NWs are completely encapsulated in a polymer. Parylene C was chosen by the Greman as insulating polymer as it allows a conformal deposition with an easily controllable thickness. The Parylene C layer follows the ZnO array roughness and enters the spaces between the ZnO NWs [12].

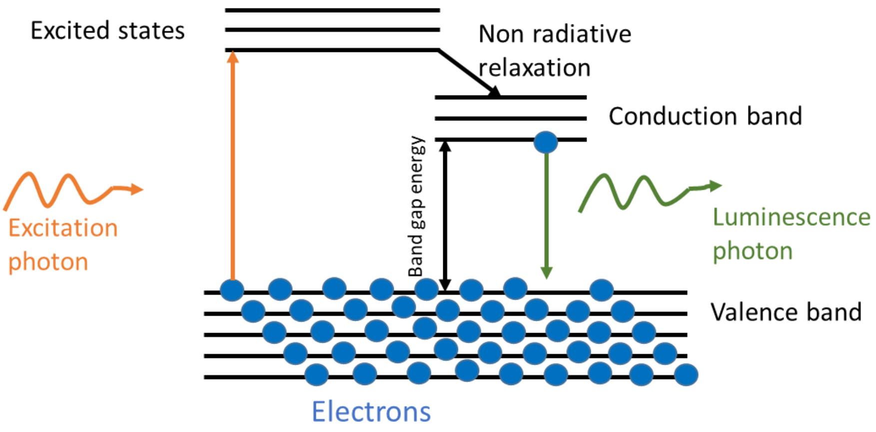

Figure 3.5. Principle of photoluminescence spectroscopy [13].

In this chapter, a mixture of zinc nitrate and zinc sulphate was used in order to optimise the growth of NWs, control the length, diameter and density of the NWs, which are important factors influencing the performance of the NG. Moreover, a work consisting in reducing the structural defects has been done. The silicon substrates coated with gold were provided by the Greman laboratory (Tours, France) and were spin-coated successively with ZnO seed and NWs grew by CBD using a mixture of zinc salts at the NCE laboratory (Chapter 2, section 2.2.7.2). After characterisation of the layers, the substrates were sent back to the Greman laboratory for NG assembly and performance characterisation.

3.2.2 Experimental part

3.2.2.1 ZnO NWs

3.2.2.1.1 Preparation of the substrates

At the Greman laboratory, the substrates (silicon discs) were cleaned sequentially for 10 min in a Piranha solution, rinsed with deionised (DI) water, cleaned with HF/H_2O (50/50) solution, rinsed with DI water and finally dried under a flow of N_2 gas at room temperature. Following the cleaning procedure, a conductive layer of Ti/Au (~100/200 nm thick) was sequentially deposited by a PVD process at room temperature using an Electron Beam Evaporator (Plassys meb 550 S). The Ti layer served as an adhesive layer for the Au layer. The silicon discs were then cut into pieces of 2 cm × 2 cm and sent to ULiège.

3.2.2.1.2 Seed layer deposition

The seed layer was deposited using the spin-coating procedure presented in Chapter 2 (section 2.2.2.1). The Si/Au substrates sent by the Greman laboratory were first cleaned by sonication in an RBS T105 detergent solution (20 min) and rinsed by dipping the substrate in deionised water (20 min), acetone (20 min) and ethanol (20 min). They were then dried 30 min at 60 °C in air.

A solution of zinc acetate dihydrate ($Zn(CH_3COO)_2.2H_2O$, Sigma Aldrich, 99.999%) at 5×10^{-3} mol L^{-1} in ethanol was prepared for the seeding process. The seed layer procedure consisted in the deposition of 1 mL of the solution onto a clean slide substrate *via* the spin-coating technique. The spin coating was performed at 2000 rpm for 30 s; the whole process was repeated five times. Finally, calcination at 350 °C for 20 min in air was performed in order to decompose zinc acetate to form ZnO nanocrystals which would act as nucleation sites for the subsequent growth of ZnO NWs.

3.2.2.1.3 NW growth

The NWs were grown on the seed *via* the modified growth process using zinc nitrate and zinc sulphate presented at the end of Chapter 2 (section 2.2.7.2). Zinc nitrate hexahydrate ($Zn(NO_3)_2.6H_2O$, 98%, Sigma Aldrich) and zinc sulphate heptahydrate powder ($ZnSO_4.7H_2O$, 99.9%, Sigma Aldrich) were directly dissolved into 19.5 mL of 2.7 mol L^{-1} of ammonia solution (NH_4OH, 25-30 wt.% as ammonia (NH_3), Emsure, Merck). The previous solution and 13 mL of ethanolamine (2-aminoethanol, ≥ 98 %, Sigma Aldrich) were added to 97.5 mL of DI water. The growth solution (130 mL) was prepared in a 160 mL polypropylene vial, giving the following final concentrations: 5×10^{-2} mol L^{-1} Zn^{2+}, 0.4 mol L^{-1} NH_4OH and 1.7 mol L^{-1} ethanolamine. The solution was vigorously stirred until the pH stabilised at 11.2 ± 0.2. The substrate was introduced inclined from vertical to prevent particles which might form in the solution from settling on the downward-facing seeded side of the substrate. The reaction vial was closed and placed in an oil bath at 90 °C for 2 h. After growth, the substrate was removed from the solution, immediately rinsed with DI water to remove loose ZnO precipitates and any residual reactant from the surface, and dried in air at room temperature for 24 h. 10 samples, named AuZnO-X (X being the synthesis number), were prepared following the same procedure and characterised.

All samples ZnO NWs were characterised by environmental scanning electron microscope ESEM (ESEM-FEG XL30 Philips, Esprit 1.9 software). Among the ten samples obtained, two were broken into pieces for ESEM side view. Photoluminescence (PL) were performed on all sample using a fluorescence spectrometer (Edinburgh FS920) at Ghent University. The PL measurements were performed at room temperature at 290 nm. The void fraction of the NWs was roughly evaluated from the top view of the ESEM images of the NWs using the diameter and density of the NWs.

3.2.2.2 Nanogenerator assembly

After deposition of the ZnO seed layer and growth of the ZnO NWs (step 1 on Figure 3.6), the eight unbroken substrates were sent to the Greman laboratory for embedding in the nanogenerator (NG) device. To ensure the mechanical robustness of the device, an insulating polymer (Parylene C) was wrapped around the nanowires with a commercially available chemical vapor deposition (CVD) process (step 2 on Figure 3.6). The Parylene C films were formed by vaporising the powdered dimer above 100 ˚C, inducing its sublimation. Then the temperature was increased at approximately 690 ˚C (pyrolysis) to form monomers, to finally polymerise the material on the substrate at room temperature. 1 g of Parylene C leads to an insulating layer of 800-900 nm thickness on the substrate covered with the NWs (2 cm × 2 cm).

After Parylene C deposition, the sample surface was cleaned using oxygen plasma for 10 min. The upper electrode that transmits the external pressure to the NW tips was sequentially deposited by evaporating 400 nm/100 nm thick Al/Ti layers on the top surface of the ZnO NW-polymer using an Electron Beam Evaporator (Plassys meb 550 S) at 10^{-4} Pa (step 3 on Figure 3.6). To complete the device fabrication (step 4 on Figure 3.6), copper wires were bonded to the top and bottom conductive surfaces using silver paste (EPOTEKE4110 A et B - mixture ratio of 10A:1B, 0.1 g: 0.01 g). The device was then encapsulated in PDMS (Polydimethylsiloxane, Sylgard 184) using drop casting. This coating method consists in dropping the solution on the NG and let the drop spread on its own (10 - 15 min) at room temperature. Then, the NG was left for drying at 100 °C under air overnight.

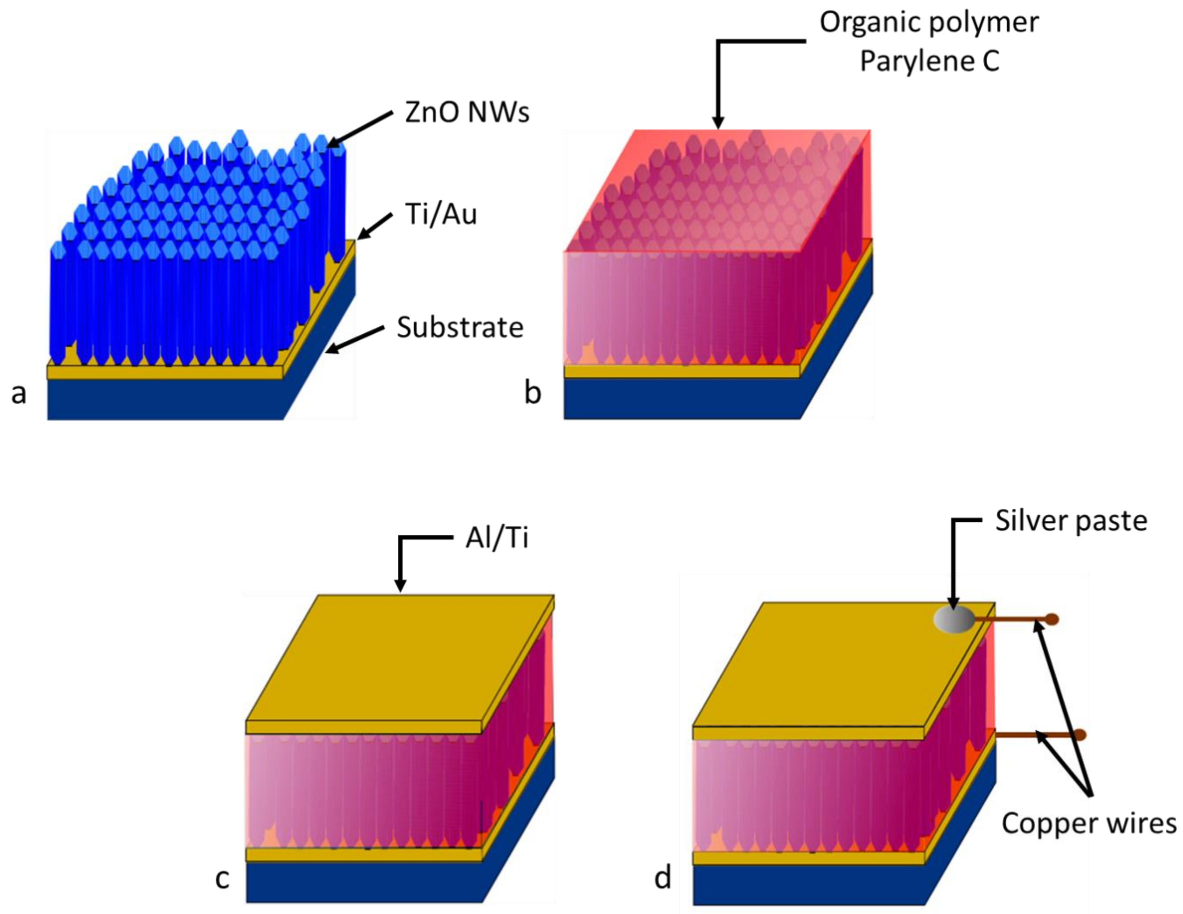

Figure 3.6. Nanogenerator assembly. (a) Step 1: ZnO NWs growth on Ti/Au. (b) Step 2: polymer encapsulation. (c) Step 3: deposition of top metal electrode. (d) Step 4: wire bonding.

3.2.2.3 Nanogenerator characterisation

The ZnO NW based NG devices were characterised to assess their performance at the Greman laboratory. The measurement device consists in a custom-built test bench carefully designed to minimise anomalous signals that can occur apart from piezoelectric effects. The test bench was described previously by Oshman et *al.* [14]. As shown in Figure 3.7, the experimental test bench is a mechanical shaker equipped with an actuator arm made of carbon fibres for strength, rigidity and low weight. The NGs are tested by mechanical stress whose frequency was controlled by the mechanical arm hitting the surface of the NG on a 1 cm² area [14, 15]. The amplitude and frequency (5 Hz) of the shaker are controlled *via* an Agilent 33 250 function generator (A), and an LDS PA100E power amplifier is used to drive the shaker (B); it thus adapts the voltage to the vibrating arm (C) (LDS brand). The electrometer (D) (Keithley 6517B) converts current to voltage visible on the oscilloscope display (E) (Agilent DCS05054A 4-channel oscilloscope). The gateway with coaxial cables (F) (amplifier OPA604) is required to avoid the environmental noise. The whole system is controlled by a computer (G). The actuator arm is attached to the reciprocating shaker platform at one end and a height adjustable screw is inserted through it at the opposite end. To avoid excessive damage to the NGs during testing, the screw tip is also insulated by soft styrene-butadiene rubber.

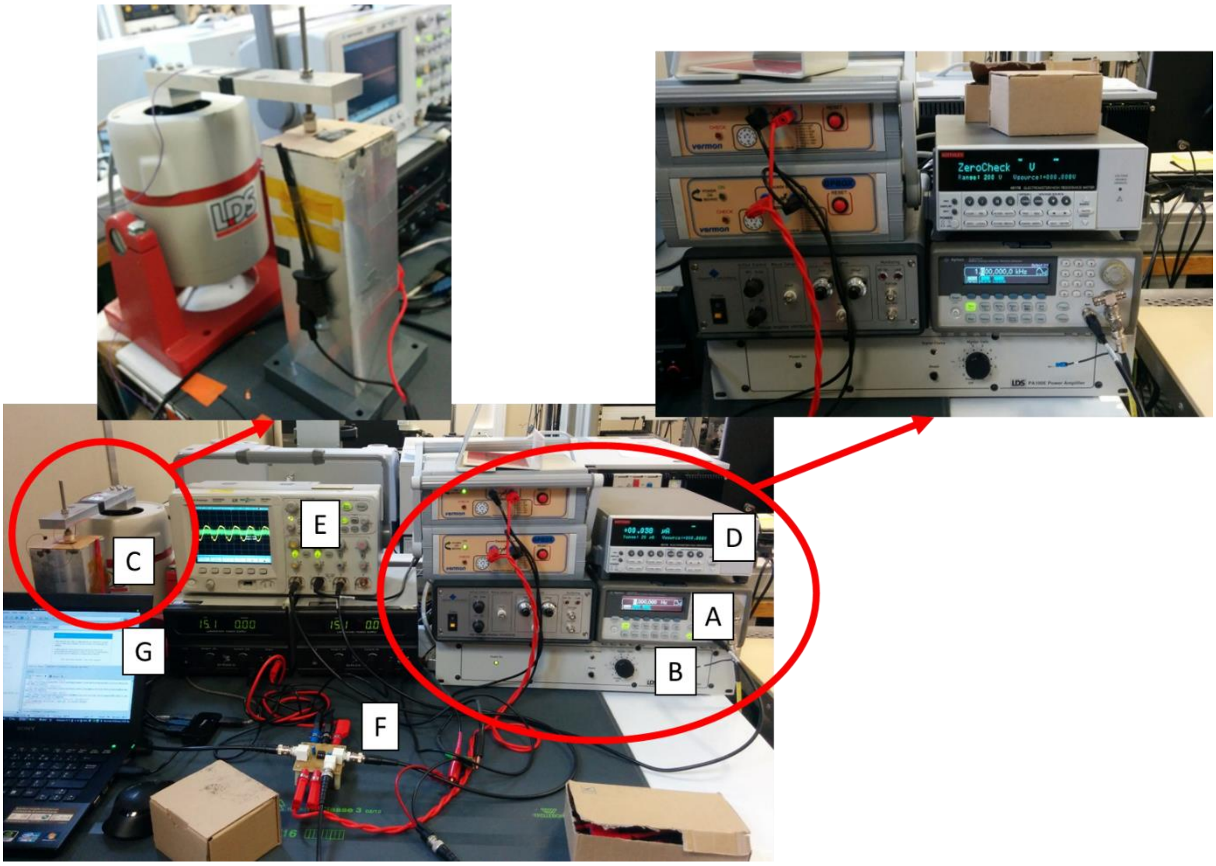

Figure 3.7. Experimental test bench for the characterisation of piezoelectric nanogenerators at the Greman laboratory. (a) Low-frequency generator; (b) high-impedance power amplifier; (c) vibrating arm; (d) electrometer; (e) oscilloscope display; (f) gateway with coaxial cables; (g) computer.

For our experiments, the NGs were firmly fixed onto a solid aluminium block using double sided adhesive tape. The screw tip was positioned over the active region of the NG, without direct contact (Figure 3.8). While the exact forces subjected to the NGs were unknown during testing, a constant output voltage of 1 V was maintained on a commercial lead zirconate titanate ($Pb[Zr_{(x)}Ti_{(1-x)}]O_3$) PZT disc buzzer positioned between two insulating glass plates under the NG. To compress the vertical NWs longitudinally, a uniform pressure was applied to the top surface of the NG (resulting force of 6 N). To assess the impact of resistive loading on the measured NG output characteristics, a series of experiments were conducted, in which the load resistor (R_L) was varied between 0.1 MΩ and 100 MΩ.

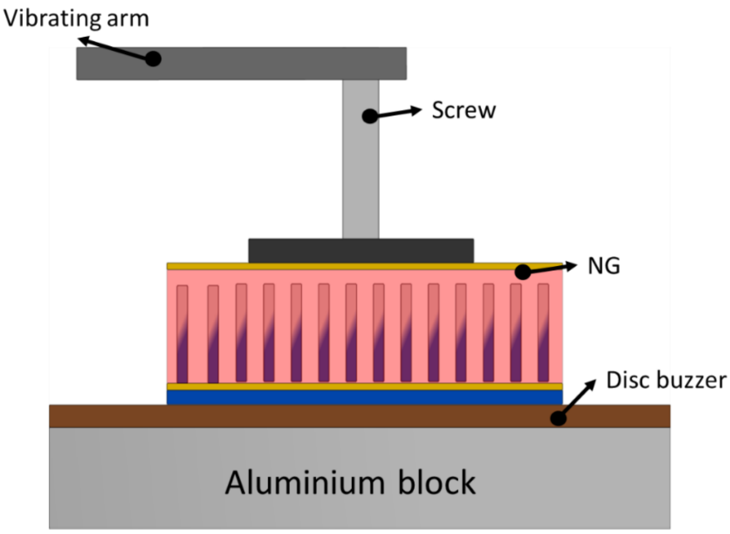

Figure 3.8. Scheme of the set up for ZnO NG testing.

3.2.3 Results and discussion

3.2.3.1 ZnO NW

As explained in the introduction, the aspect ratio, *i.e.* the length to diameter ratio (*L/D*) of the NWs, plays a role in the performances of the NG. The synthesis of ZnO NWs has therefore been optimised to maximise the aspect ratio while maintaining a certain fraction of void between the NWs. To do so, NWs were grown by mixing $Zn(NO_3)_2$ and $Zn(SO_4)$ as ZnO precursors. On the one hand, zinc sulphate enables NWs to be obtained in the shape of a hexagonal prism with a flat top, which is the desired shape, and also improves the verticality of the NWs [16]. Zinc nitrate, on the other hand, makes it possible to obtain longer nanowires with a better aspect ratio and a higher void fraction between the NWs, but the latter are less well oriented and the top of the hexagonal prisms is shaped like the tip of a pencil [16] .

ESEM microscopy was used to characterise the NWs grown on gold substrate, as shown in Figure 3.9a and Figure 3.9b. The NWs displayed a diameter of 0.2 µm and a length of 4 µm. The density was estimated by counting the NWs present on surfaces in various places and was repeated for several images at the same magnification. The number of NWs were reported per unit area of sample. The void fraction estimated from the top view was about 70% and the density was about 1.2×10^9 cm^{-2}.

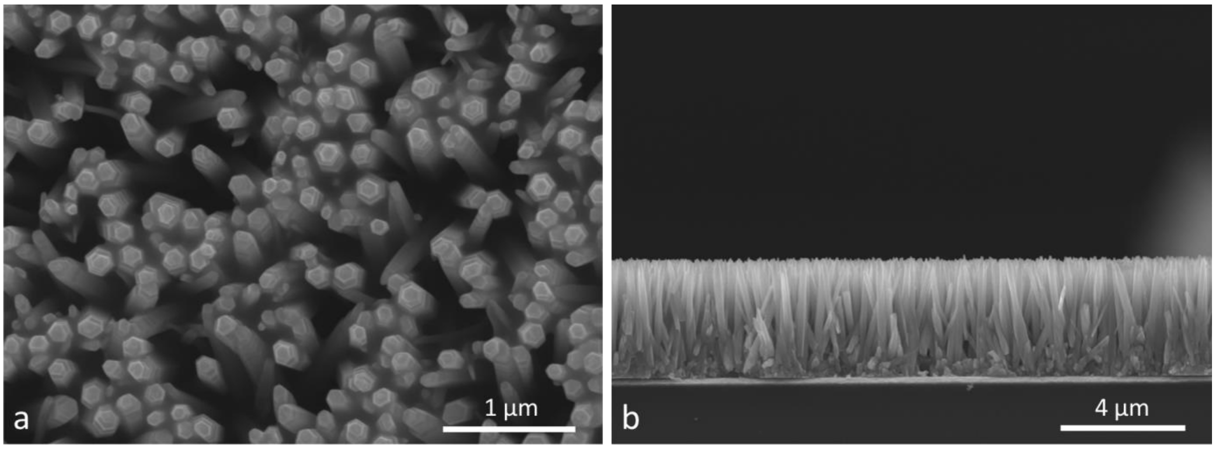

Figure 3.9. ESEM pictures of the NWs grown on gold substrate: (a) top view, (b) side view.

Photoluminescence spectroscopy was performed on the NWs to characterise the structural defects. Figure 3.10 shows the photoluminescence spectrum of four of the ZnO NWs samples obtained; results obtained with the others were similar. The analysis exhibit two peaks: one in the visible area and the second in the UV area. One observes a difference of intensity between the two peaks: the surface of the visible peak is very large compared to the UV peak. The UV emission centred at ~380 nm (3.26 eV) is the characteristic signature of the interband transition between the valence band and the conduction band of the ZnO and corresponds to the band gap (near-band edge emission) [17]. The spectrum in the visible range, *i.e.* the wide peak between 450 and 750 nm with a maximum around 640 nm), corresponds to the presence of crystal defects. These defects can be related to interstitial zinc or oxygen (Zn_i and O_i) [18, 19], or zinc or oxygen vacancies (V_{Zn} and V_O) [20], and tend to form intra-band transitions in the visible which, in PL, corresponds to a low emission [17, 21].

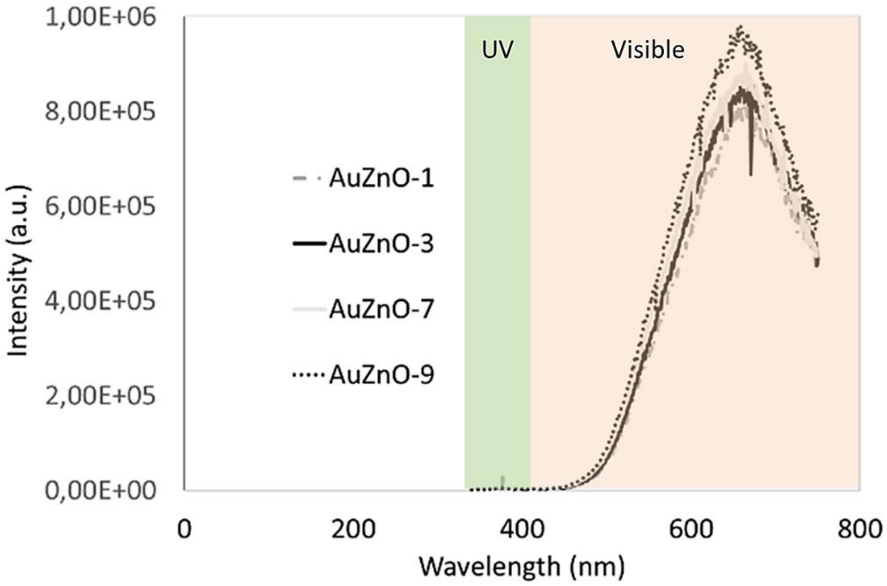

Figure 3.10. Photoluminescence graphs for different ZnO NWs arrays.

A large emission peak of wavelength ≥ 400 nm often observed during wet chemical growth is therefore attributed to defect-induced luminescence and is due to intraband transitions [22]. This peak covers the entire visible region, which explains the white light emission from ZnO NWs. The attribution of these peaks has been the subject of much discussion [23].

One method to qualitatively evaluate the concentration of structural defects in ZnO is to compare the relative intensities of the UV peak and the visible peak. Indeed, if the nanowires exhibit low absorption in the visible range and sharp absorption around 360-380 nm, this indicates good crystallinity and a reduced number of defects in the nanowires [24, 25]. The higher the number of peak intensities, the fewer the structural defects in the NWs. This method also allows to get rid of the effects of the quantity of ZnO on the substrate as well as the changing measurement conditions from one measurement campaign to another. The UV/Vis ratio of the surfaces below the UV and visible peaks is small (Table 3.1). The presence of many structural defects leads to the presence of many free charge carriers that will drastically decrease the piezoelectric potential.

Table 3.1. UV/Vis ratio by photoluminescence for ZnO NWs arrays.

	Ratio UV/Vis
AuZnO-1	1.9×10^{-3}
AuZnO-3	1.8×10^{-3}
AuZnO-7	2.1×10^{-3}
AuZnO-9	1.9×10^{-3}

To obtain efficient NGs, it is thus much probably necessary to reduce the amount of structural defects (repair) or to mask the effect of the associated charges (surface passivation). Hue *et al.* [26] presented oxygen plasma and post-thermal treatment methods in order to reduce structural defects and surface passivation using polymer to mask the free charges of the ZnO NWs. Oxygen plasma contains radical oxygen species O^* that can diffuse through the ZnO bulk to fill the oxygen vacancies [27]. Post-thermal treatment of the ZnO NWs in various atmospheres can also improve the crystal quality. For example, oxygen vacancies could be reduced by calcination of the NWs in air above 200 °C. It is well known that metal oxides surfaces are rich in defects such as oxygen vacancies, which serve as the binding sites for chemical adsorption processes. Surface passivation can eliminate these defects and also makes the surface more chemically inert.

The Greman laboratory showed that a post-thermal treatment at 450 °C can improve the NG performances [15]. The senior researcher involved in the same subject worked thus on the decreasing of the post-thermal treatment temperature, as the final perspective consists in using organic flexible substrate such as Kapton®. The main results, showing structural improvement of the NWs by post-thermal treatment, are briefly described in section 3.2.3.4.

3.2.3.2 NG assembly

The NG assembly can be divided into three parts. First, an arrangement of piezoelectric NWs (ZnO) converts mechanical energy into electrical energy *via* the piezoelectric effect. This is the heart of the device. Second, this NW array is coated by an insulation layer (Parylene C) that (i) increases the mechanical robustness of the NG and (ii) protects the device from electrical leakage and short circuits that could occur due to the unintentional n-type doping of the ZnO (*i.e.* oxygen interstitials generating negative charges). Finally, the upper and lower electrodes are used as collectors of electrical charges.

The Parylene C was chosen by the Greman laboratory among different insulating polymers in a previous PhD work [28]. The Parylene C was chosen for its easy deposition on the surface of the nanowires, good infiltration, and accurate thickness control. Moreover, Parylene C has negligible piezoelectric properties compared to ZnO.

3.2.3.3 NG characterisation

The principle of the nanogenerator characterisation is as follows (Figure 3.11a). Mechanical forces compress the NWs along their c-axis, producing a potential difference along this axis due to the piezoelectric effect. Electrons are forced to flow through the external circuit to compensate for this potential difference. The voltage produced by the compressed NWs leads to the accumulation of charges at the upper and lower electrodes through the external circuit, thereby charging the capacitance and generating a current pulse of the external circuit. A current pulse in the opposite direction occurs when the force is released. To verify that the measured electrical response, whether in voltage or current, corresponds to the piezoelectric effect, the NG is operated in both forward and reverse modes, with the electrical connections to the NG terminals being reversed. If the signal is indeed due to the piezoelectric effect, the profile of the curve should be reversed (Figure 3.11b) by reversing the connections and the reverse curve should be symmetrical to the forward curve.

The frequency-controlled vibrating arm (Figure 3.8) allows the NG to be loaded at a given force and at a given frequency. At the Greman laboratory, performances are classically measured for a force of 6 N applied at a frequency of 5 Hz. Figure 3.11 b shows the measurements of the forward and reverse peak voltage (V_{peak}) (*i.e.* maximum value) obtained when the NWs are compressed. There is indeed inversion but the curve is not perfectly symmetrical. This is due to the measurement system which induces a bias in the response. The Greman test bench has since been improved to overcome this problem.

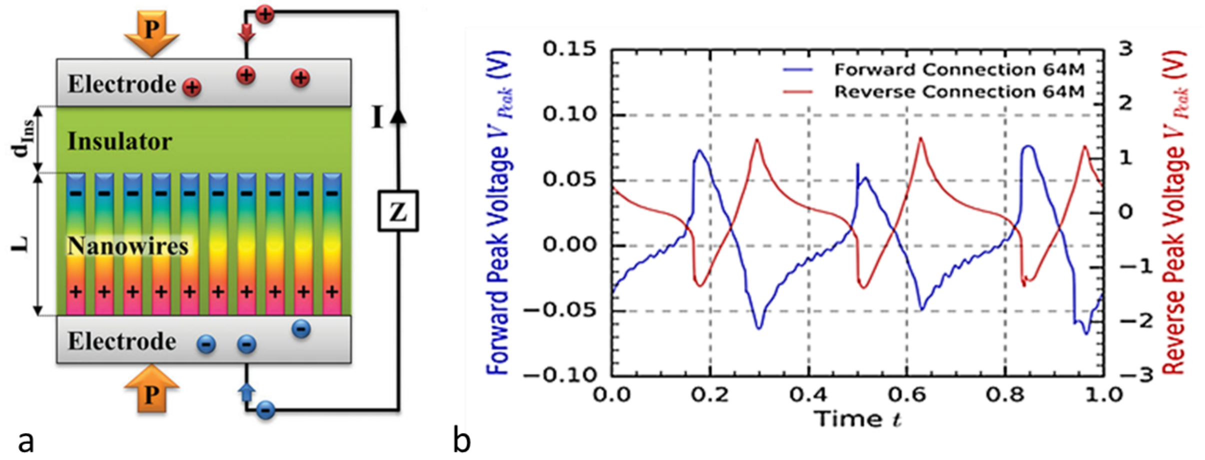

Figure 3.11. (a) Schematic of the NG working as a charged capacitance proportional to the force applied (reproduced from [3]); (b) Measurement of the NG performances of sample AuZnO-1 for a given resistance in forward and reverse modes at Greman laboratory.

According to the Greman laboratory, energy harvesters generally present impedance source into their load circuits and during operation. During the NG characterisation, the load resistance (R_L) is varied, between 0.1 MΩ and 100 MΩ, in order to find the R_L that suits best the resistance of the device. First, different values of peak voltage, V_{Peak}, are obtained by varying the load resistance, as presented in Figure 3.12a. With this method, the open circuit voltage, $V_{oc,}$ is determined at maximum load resistance relevant for the measuring system. Experimental data resulting from the various R_L values can be found in Figure 3.12a. From these results, it can clearly be observed that the output voltages for the device increase with increasing R_L. Figure 3.12b represents the peak power (P_{Peak}) as a function of the varying load resistance. Power is calculated as:

$$P = V \times I \tag{1}$$

where *P* is the power (W), *V* is the voltage (V) and *I* is the current (A).

According to Ohms' law, the current can be calculated as a function of the load resistance *R*:

$$I = \frac{V}{R} \tag{2}$$

A measurement of the P_{Peak} as a function of *R* can thus be obtained from:

$$P = \frac{V^2}{R} \tag{3}$$

By applying Equation 3 to the measured output voltage responses (Figure 3.12a), the P_{Peak} *vs.* R_L variations are shown in Figure 3.12b. From this, the calculated *P* increases with increasing R_L values. The maximum output power (P_{max}) is determined by the maximum of the P_{Peak} *vs.* R_L curve.

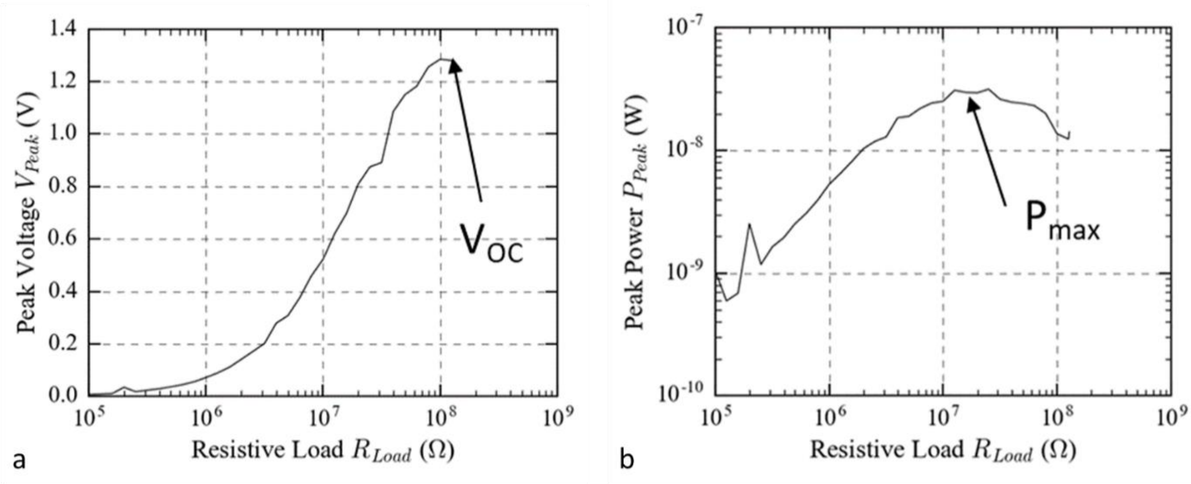

Figure 3.12. (a) Measurement of the maximum open circuit voltage (V_{OC}); (b) measurement of the maximum output power (P_{max}).

Among the eight samples tested, only five showed usable measurements for both $P_{\max}$ and V_{OC}. One sample had short circuits and two samples displayed too low power. Indeed, it was decided to discard NGs whose maximum peak power $P_{\max}$ was lower than 1/10 of the maximum value obtained in the series (45 nW). $P_{\max}$ values between 16 and 45 nW and open circuit voltages from 0.5 to 1.3 V were obtained. On the one hand, the NW synthesis pathway developed in the previous chapters presents advantages such as a growth rate well above the target of 20 nm min^{-1} and a good adhesion of the NWs to the substrate due to the presence of the ZnO seed layer. The power density is evaluated by dividing the maximum power ($P_{\max}$) by the surface area solicited and the thickness of the active layer. On the other hand, the piezoelectric performances are still far from the target of 4.2 V for V_{OC} and from that of 1 µW cm^{-2} for power density. It is very likely that the poor NG performance of the samples may be due to a high concentration of structural defects.

3.2.3.4 Improvement of the NG performances.

Opoku *et al.* [15] (from the Greman laboratory) showed that the thermal post-treatment of the NWs at 450 °C improves the NG performances. However, as the entire synthesis process should allow the use of organic substrates, the thermal post-treatment was performed at a lower temperature, hoping it would be sufficient to repair the NW structural defects. Figure 3.13 shows the photoluminescence spectrum of the NWs before and after post-treatment at 260 °C for 3 h. The spectrum shows that the UV peak increases drastically after thermal post-treatment while the visible peak remains at the same intensity. The UV/Vis ratio increases with the thermal post-treatment (Table 3.2), which means that the concentration of structural defects strongly decreases. This thermal post-treatment improved the NG performances: the maximum power $P_{\max}$ increased from an average value of 37 nW to 121 nW and V_{oc} increased from an average value of 1.1 to 2.3 V (Table 3.2). Results remain however very scattered, maybe due to assembly issues.

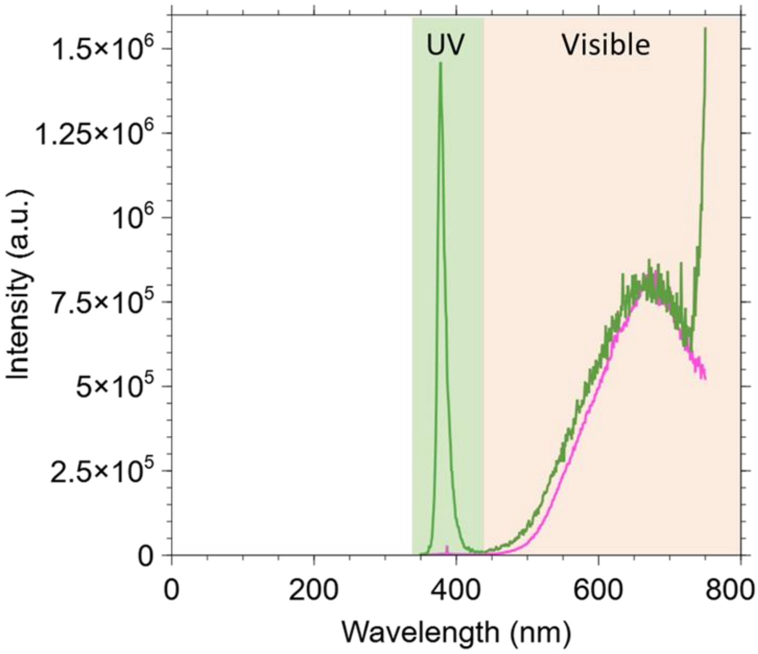

Figure 3.13. Photoluminescence spectrum of the NWs ▬ before and ▬ after post-treatment for sample AuZnO 11-2.

Table 3.2. UV/Vis ratio by photoluminescence and results from NG characterisation for ZnO NWs arrays post-treatment 3h at 260 °C (series AuZnO 11).

	Ratio UV/Vis	**P_{max} (nW)**	**V_{oc} (V)**
AuZnO 11-1	8.8×10^{-2}	36	1.5
AuZnO 11-2	1.2×10^{-1}	42	1.7
AuZnO 11-3	1.5×10^{-1}	discard	discard
AuZnO 11-4	8.4×10^{-2}	discard	discard
AuZnO 11-5	5.2×10^{-2}	286	3.6

3.2.4 Conclusion

In this first application, the ZnO NWs were synthesised using a modified protocol compared to Chapters 1 and 2, and used to build piezoelectric nanogenerators. Several samples of NWs synthesised at ULiège were sent to the Greman laboratory to be assembled as NG and characterised. The NGs were mechanically tested using a vibrating arm which compress the vertical NWs longitudinally. The samples sent for characterisation led to maximum power values between 16 and 45 nW and an open circuit voltage between 0.5 and 1.3 V when a force of 6 N was applied to the sample surface. Those values are too low compared to the targeted values of 4.2 V and 1 µW cm^{-2}. However, applying a thermal post-treatment to the NWs allowed to drastically increase their performance in NG; this was most likely linked to the repair of the structural defects, which initially hampers the piezoelectric effect. Indeed, while the post-treatment allowed to increase the UV/Vis ratio from 10^{-3} to 10^{-1}, an improvement of the maximum power P_{max} from an average value of 37 nW to 121 nW was observed.

These results highlighted that the dimensions (length and diameter) and the density of the nanowires were not the only parameters that influence the NG performances. Indeed, the high concentration of structural defects, such as vacancies or interstitial ions, can decrease the performances of the device, and structural defect repairs allows enhancing the NG performances. This also suggests that it might be possible to improve the NG performances further. As a prospect, the optimised synthesis (seed deposition + NWs growth) presented at the end of the Chapter 2, with and without the thermal post-treatment, should be used to synthesise optimised NWs for NG applications. Other methods such as oxygen plasma treatment [26] on the NWs, or a treatment of the seed layer with H_2O_2 [29] could also reduce the amount of structural defects.

3.3 ZnO NWs as photocatalyst

3.3.1 Introduction

One-dimensional Zinc Oxide Nanowires (ZnO NWs) have attracted a lot of attention during last decade due to their remarkable physical and chemical properties for electronic and optical devices such as chemical sensors, field effect transistors, and nanogenerators, but also for photocatalytic applications. ZnO materials can be used for the degradation of organic compounds, dyes, detergents, and pollutants in nearly neutral solution [30-32]. ZnO nanostructures are efficient photocatalysts in comparison with ZnO bulk materials [33]. Among various nanostructures such as nanowires and nanoneedles, ZnO nano- structures were shown to be good photocatalysts due to their high surface-to-volume ratio [34,35]. In addition, long ZnO nanowires with better photocatalytic activity are ascribed to the increase of surface-to- volume ratio and surface properties such as surface defects and oxygen vacancies [36,37].

As a second example of application, the ZnO NWs were used in the framework of photocatalytic decomposition process. The photocatalytic decomposition of hydrogen peroxide under UV and visible light irradiation was used as a simple method to quantify the photocatalytic activity of the ZnO NWs films. In photocatalysis, electron-hole pairs are generated in the semiconductor through excitation of electrons from the valence band to the conduction band by absorbing light.

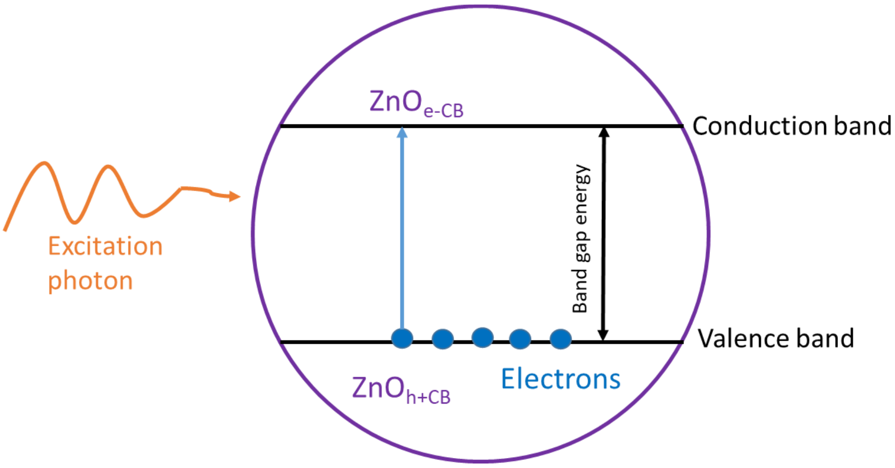

Figure 3.14. Scheme of the mechanism generating reactive species**.**

Under UV-visible light irradiation, the photocatalytic activity of ZnO results from the injection of electrons into the conduction band ($ZnO(e^{-}_{CB})$), which leaves holes in the valence band ($ZnO(h^{+}_{VB})$) as shown in Figure 3.14. These electrons and holes allow the formation of active species such as $O_2^{\bullet}$, $HO_2^{\bullet}$, $OH^{\bullet}$, which are involved in the degradation of various pollutants [38]. H_2O_2 may also be photodecomposed to produce the active species $OH^{\bullet}$. The catalytic activity for the decomposition of H_2O_2 on photocatalyst surfaces under UV-visible light irradiation is commonly used to study the catalytic activity of different semiconductors [39–42]. H_2O_2 decomposition catalysed by ZnO has been evaluated by a simple and inexpensive technique previously developed at the NCE laboratory by Páez *et al.* [43]. The method lies on the observation of O_2 production by gas pressure monitoring (O_2-monitored method) during H_2O_2 decomposition.

Micrometric layers of well-aligned NWs were synthesised by the two-step process consisting in (i) the deposition of a ZnO seed by sol-gel method, using dip-coating, followed by (ii) the growth of ZnO NWs using chemical bath deposition (CBD). Using seed and growth conditions developed in Chapters 2 and 1, respectively, it was possible to obtain NWs oriented along the c-axis. For the seed, an equimolar solution of ethanolamine and zinc acetate in ethanol was prepared and deposited using dip-coating (Chapter 2, section 2.2.4). The seed coating was calcined at different temperatures. ZnO NWs were further grown with the optimised CBD method, consisting in dissolving directly the zinc salt into ammonia (Chapter 1, section 1.1.2). Finally, the NW arrays were tested as photocatalyst for the H_2O_2 degradation in a home-made experimental device.

3.3.2 Experimental work

3.3.2.1 ZnO NWs for the photocatalytic decomposition of H_2O_2

3.3.2.1.1 Seed deposition

ZnO seed layers were deposited onto clean alkali-free glass slides (Schott AF32 eco) *via* the dip-coating technique, as developed in Chapter 2, section 2.2.4. The substrates were first cleaned with Gardoclean grease remover solution (20 min) and rinsed with deionised water (20 min), acetone (20 min) and ethanol (20 min). They were then dried under air flow at room temperature. Before deposition, one side of the glass slide was covered with adhesive tape protection to ensure the deposition of the seed layer only on one side of the glass slide. An equimolar solution of zinc acetate dihydrate ($Zn(CH_3COO)_2.2H_2O$, Sigma Aldrich, 99.999%)) and ethanolamine (2-aminoethanol, ≥ 98%, Sigma Aldrich) in ethanol was prepared to produce the seed films. The concentration of both zinc acetate and ethanolamine was 0.25 mol L^{-1}. This solution was heated at 60 ºC for 2 h under stirring and cooled down at room temperature for 3 h, in order to obtain a stable and homogeneous colloidal solution. The glass substrates were introduced into the solution using dip-coating technique in order to deposit the seed layer. The coating was deposited at 0.2 m min^{-1} speed, and then thermally pre-treated at 100 °C for 20 min, followed by calcination for 20 min at three different temperatures: 200, 300 and 400 °C.

3.3.2.1.2 Growth or ZnO NWs

ZnO NWs were grown by chemical bath deposition (CBD) [44, 45] (see Chapter 1, section 1.1.2). Following the optimised process, the zinc sulphate heptahydrate powder (3.74 g, $ZnSO_4.7H_2O$, Sigma Aldrich, 99.9%) was directly dissolved into 19.5 mL of 4.0 mol L^{-1} ammonia solution (NH_4OH, 25 - 30 wt.% as ammonia (NH_3), Emsure, Merck). The previous solution and 13 mL of ethanolamine (2-aminoethanol, Sigma Aldrich, ≥ 98%) were added to 97.5 mL of DI water. The growth solution (130 mL) was prepared in a 160 mL polypropylene vial, giving the following final concentrations: 0.1 mol L^{-1} Zn^{2+}, 0.6 mol L^{-1} NH_4OH and 1.7

mol L^{-1} ethanolamine. The solution was vigorously stirred until the pH stabilised at ~11.1 ± 0.2 (10 min). The substrate was introduced inclined from vertical to prevent particles which might form in the solution from settling on the downward-facing seeded side of the substrate. The reaction vial was closed and placed in an oil bath at 90 °C for 2 h. At the end of the growth period, the substrates were immediately rinsed with deionised water to remove any residual salt from the surface, and dried in air at room temperature. The morphology of both the ZnO seed layer and the ZnO NWs was observed by ESEM (ESEM XL30 Philips).

3.3.2.2 Measurement of the photocatalytic activity for the decomposition of H_2O_2

The photocatalytic activity of the ZnO NWs grown on seeds treated at different temperatures was determined *via* the degradation of H_2O_2 in aqueous solution by measuring the volume of oxygen produced per time unit at atmospheric pressure. The photoreaction was carried out using a batch reactor with external halogen lamp (300 W, 230 V) powered at 110 V. The emission spectrum of the halogen lamp was measured with a Mini-Spectrometer (Hamamatsu Photonics) (Figure 3.15).

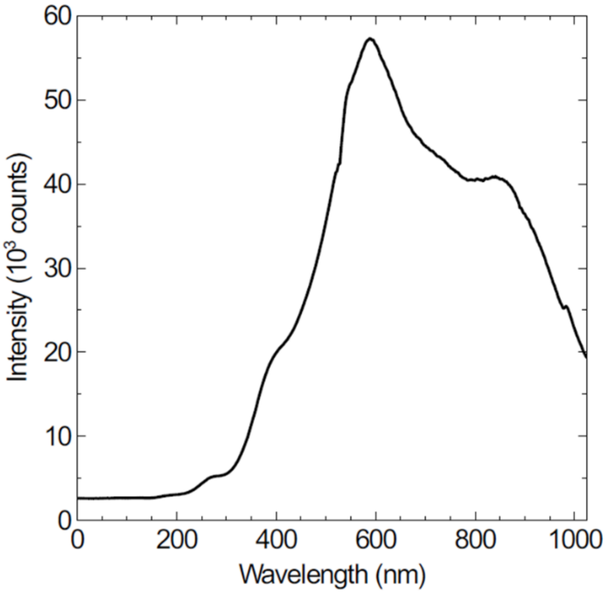

Figure 3.15. Emission spectrum of the halogen lamp used in the photocatalysis experimental setup.

The experimental setup, which was previously described by Páez *et al.* [43], is presented in Figure 3.16. The reactor was however modified to handle a 50 mL solution (initially 100 mL) as the surface covered with NWs is smaller than in the original set-up designed for other samples. Control tests were carried out in the dark in order to check if the degradation of

H_2O_2 occurs in presence of ZnO NWs without any light. Additionally, the degradation rate of H_2O_2 was measured under light irradiation.

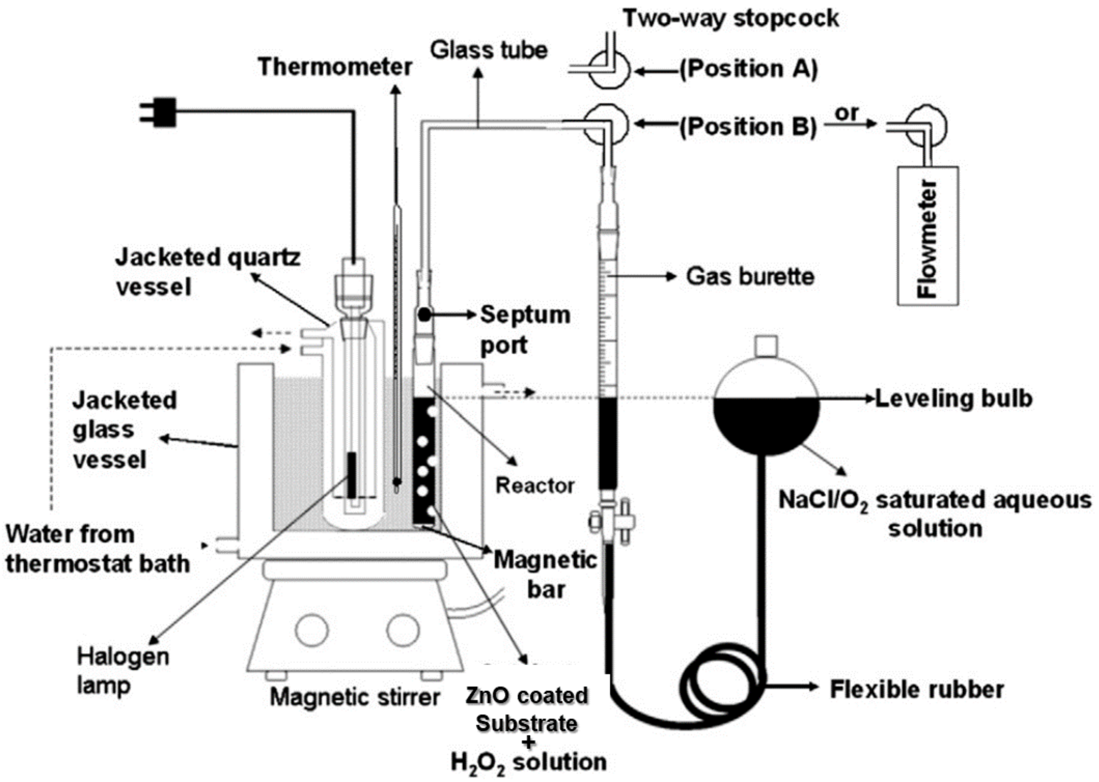

Figure 3.16. Scheme of the experimental set-up for the measurement of the photocatalytic activity toward the decomposition of the H_2O_2. Reprinted from [43].

A typical experiment in the present study took place as follows: (i) the ZnO NW array was cleaned with ethanol and placed in the reactor with 30.6 mL of deionised water; (ii) the reactor was closed with a septum port; (iii) the reactor and the halogen lamp were then placed in a thermostatic bath of DI water with a temperature fixed at 20 °C and stirred for 10 min under magnetic stirring (the pressure in the reactor at the beginning of the reaction was equal to the atmospheric pressure); (iv) 5.4 mL of H_2O_2 solution (30%, Merck) were injected into the deionised water *via* the septum port; (v) the halogen lamp was turned on; (vi) finally, the O_2 pressure was monitored every 10 min for 2 h. The change in H_2O_2 concentration and kinetics rate during photocatalytic run were calculated. The experiment was repeated with ZnO arrays prepared on seeds calcined at various temperature (200, 300 and 400 ºC).

3.3.3 Results and discussion

3.3.3.1 ZnO NWs physical characterisation

The aim of this experiment was to study the impact of the calcination temperature of the seed layer and, indirectly, that of the NW morphology on the photocatalytic properties of the ZnO NWs. The effect of calcination temperature was evaluated for the seed prepared with a $Zn(CH_3COO)_2$ concentration of 0.25 mol L^{-1}. Three temperatures were studied: 200, 300, and 400 ºC. In Chapter 2 (section 2.3.4), the UV-visible characterisation has shown that the absorption intensity increases with the seed calcination temperature, which indicates a higher crystallinity of the seed [46]. Moreover, the XRD pattern have shown only (002) c-axis orientation peak for a calcination temperature at 400 °C, indicating a well-oriented seed layer. This seed film exhibits highly preferred orientation perpendicular to the substrate surface.

The calcination temperature of the seed layer plays a key role in the growth, organisation and orientation of ZnO NWs. The mass of ZnO grown on seeds calcined at 200, 300 and 400 ºC was 20.5, 32.3 and 42.7 mg, respectively. It indicates that the increase of the seed calcination temperature increases the subsequent rate of growth of the NWs. The impact of the temperature on their microstructure was observed by ESEM. Figure 3.17 shows the top views of the synthesised NWs obtained from seed layers calcined at 200 °C (Figure 3.17a), 300 °C (Figure 3.17b) and 400 ºC (Figure 3.17c). Side view images of seed layers calcined at 200 °C, 300 °C and 400 °C are shown in Figure 3.17d, Figure 3.17e and Figure 3.17f, respectively.

Seed layers calcined at 200 ºC give rise to slightly less organised NWs with lower orientation; the measured thickness is 2.8 ± 0.05 μm. This value increased with the seed calcination temperature. The samples displayed a thickness of 3.7 ± 0.1 μm at the intermediate temperature of 300 ºC. However, when the seed was calcined at 400 ºC, the length of the ZnO NWs (3.5 ± 0.1 μm) did not increase compared with the NWs grown on the seed layer calcined at 300 ºC. One can notice that the sample obtained on the seed calcined at 400 ºC presented a very dense organisation with an extremely high orientation, which leads to a continuous film because of the contact between nanowires. This effect is confirmed from the top view in Figure 3.17g and Figure 3.17h, where a closed surface was observed; this indicates that most of the ZnO nanowires are in contact with each other, with no gap in-between. Determining the specific surface area of the NWs using, for instance, nitrogen adsorption-desorption isotherms, would have been a way to evaluate the available surface of the NWs, and quantify the contacts between NWs. However, this measurement could not be performed because the NCE laboratory is not equipped for the measurement of the specific surface area of thin films; the main issue is the too low amount of sample that can be placed in classical adsorption-desorption devices; more advanced measurements techniques would be required to obtain accurate values of the specific surface area.

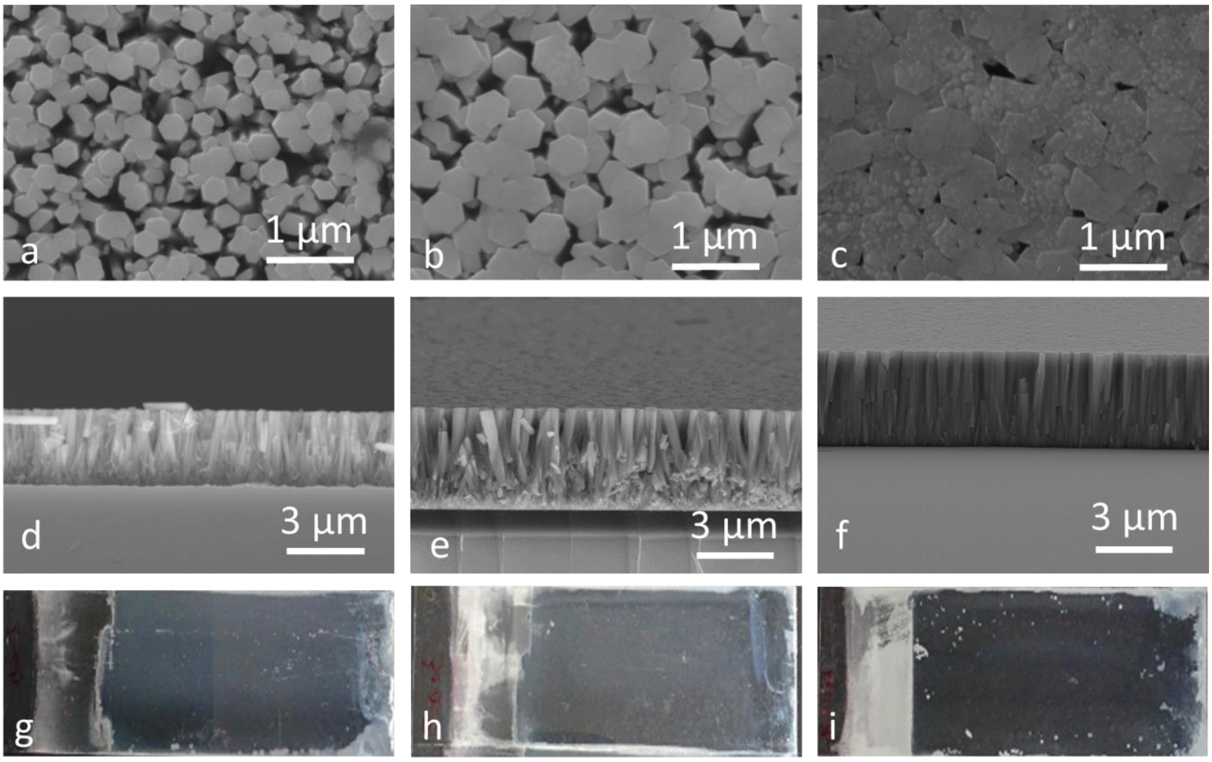

Figure 3.17. ESEM images of ZnO nanowires obtained from seed layers. Top view of the seeds calcined at (a) 200 ºC, (b) 300 ºC and (c) 400 ºC. Side view of the seeds calcined at (d) 200 ºC, (e) 300 ºC and (f) 400 ºC. The pictures show the ZnO NW film aspect after NW growth on seeds calcined at (g) 200 °C, (h) 300 °C and (i) 400 °C.

3.3.3.2 Photocatalytic activity of the ZnO NWS

The photocatalytic activity of the ZnO NWs grown on seed layers calcined at different temperatures was evaluated *via* the degradation of H_2O_2 in aqueous solution by measuring the volume of oxygen produced per time unit at atmospheric pressure. The evolution of H_2O_2 concentration was studied as a function of time under visible light irradiation (Figure 3.18). The evolution of the H_2O_2 concentration during the photocatalytic run was determined from:

$$C = C_0 - 2\,\frac{PV_g}{RTV_L} \tag{4}$$

where C is the concentration of H_2O_2 in the reactor at time t (mol L^{-1}), C_0 is the initial concentration of H_2O_2 (6.18 mol L^{-1}), P is the atmospheric pressure (considered equal to

101.3 kPa), R is the perfect gas constant (8.314 J mol^{-1} K^{-1}), V_L is the total volume of solution in the reactor (0.036 L), T is the room temperature (298 K) and V_g corresponds to the integrated volume of gas liberated at time t (L) at atmospheric pressure. The experiment was performed only once with ZnO NWs deposited on glass slides preliminarily coated with ZnO seed calcined at 200, 300 and 400 ºC.

Rates of H_2O_2 decomposition were evaluated at the reaction temperature (25 ºC) and first-order kinetic law [47, 48] was used to obtain the apparent kinetic constant, k_{app}:

$$\mathrm{r} = k_{app} \cdot \mathrm{C} \left(= -\frac{dC}{dt}\right) \tag{5}$$

Note that, as the kinetic constant depends on quantum yield, incident light intensity, light path, extinction coefficient, and substrate concentration it is more suitable to name it k_{app} [49]. After integration over time in the discontinuous reactor, one obtains:

$$-\ln\left(\frac{C}{C_0}\right) = k_{app} \cdot \mathrm{t} \tag{6}$$

where r is the reaction rate (mol L^{-1} s^{-1}), k_{app} is the apparent first order constant (s^{-1}) and t is the reaction time (s). For each temperature, the initial rate of decomposition of H_2O_2, r_0, was calculated by multiplying k_{app} by the initial concentration, C_0. Additionally, in order to evaluate the efficiency of the ZnO NWs, r_m (mol g^{-1} s^{-1}), *i.e.* the rate of H_2O_2 decomposition per mass unit of ZnO, was calculated:

$$r_m = \frac{V_L}{M} \cdot r_0 \tag{7}$$

where M is the catalyst mass (g), V_L is the total reaction volume (L) and r_0 is the initial rate of H_2O_2 decomposition (mol L^{-1} s^{-1}).

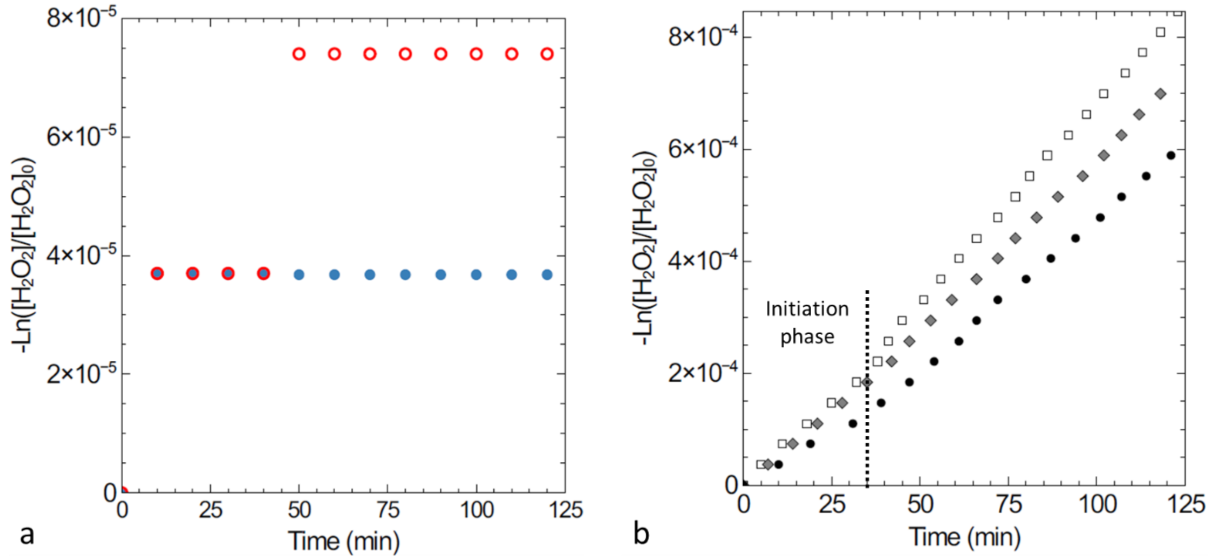

Figure 3.18. (a) Control test of H_2O_2 degradation (●) with ZnO in the dark and (○) without ZnO under light. (b) First-order kinetics linearisation of the H_2O_2 decomposition under light using ZnO NWs grown on ZnO seeds calcined at (●) 200, (◆) 300 and (□) 400 ºC.

Control tests show that no degradation of H_2O_2 was observed in presence of ZnO NWs during the experiments carried out in the dark (Figure 3.18a, blue discs). Additionally, in absence of ZnO NWs, H_2O_2 degradation rate was negligible under only light irradiation (Figure 3.18a, red circles). H_2O_2 was degraded when it was in contact with ZnO NWs under light irradiation. Figure 3.18 shows that the reaction indeed obeys a first order rate law. An initiation period can be observed corresponding to the preheating time of the halogen lamp. This leads to a lower degradation rate and it is characterised by a lower slope in Figure 3.18b.

The apparent first order kinetic constant values (k_{app}) were calculated from the slope of the curve between 35 min and 125 min and were significantly higher when the calcination temperature was increased (Table 3.3). With the k_{app} values, it was then possible to determine the initial rate (r_0); the values chosen were those between 35 min and 50 min as it corresponds to the beginning of the reaction, after the initiation period. For instance, for a calcination temperature of 200, 300 and 400 ºC, r_0 values of 5.16×10^{-7}, 6.13×10^{-7} and 7.18×10^{-7} mmol L^{-1} s^{-1} were obtained, respectively (Table 3.3). Finally, reaction rates were also calculated as a function of the mass of grown ZnO NWs (r_m). The obtained values of r_m decrease when the seed calcination temperature increases and, as a consequence, the NW density increases. This means that, for the H_2O_2 decomposition, and assuming that the activity of the active sites remains identical from sample to sample, the amount and availability of superficial active sites per mass unit of ZnO NWs decreases with the increase of calcination temperature of the seed. The calcination of the seed layer at 200 °C gives rise to separate

NWs with more active surface area exposed than for the continuous NWs film array observed for a calcined seed at 400 °C. This increased accessible surface probably enhances the photocatalytic effect. Combination of these results with an accurate specific surface area measurement would be the best way to confirm this conclusion.

Table 3.3. Kinetic data obtained from the H_2O_2 decomposition over ZnO NWs arrays grown on seeds calcined at 200, 300 and 400 ºC.

Seed calcination temperature (ºC)	**ZnO mass (mg)**	k_{app} **(s^{-1})**	r_0 **(mmol L^{-1} s^{-1})**	r_m **(mmol g^{-1} s^{-1})**
200	20.5	8.35×10^{-8}	5.16×10^{-7}	9.06×10^{-7}
300	32.3	9.93×10^{-8}	6.13×10^{-7}	6.83×10^{-7}
400	42.7	1.16×10^{-7}	7.18×10^{-7}	6.06×10^{-7}

k_{app}: apparent first order constant; r_0: initial rate of decomposition of H_2O_2; r_m: rate of H_2O_2 decomposition by mass unit of ZnO.

To confirm that the first-order is not the result of a mass-transport limited process, it was checked that the gradient of concentration across the reactor was negligible. The calculation was performed assuming that the only transport mechanism was diffusion, *i.e.* that there was no mixing of the solution and no convection. This corresponds to the less favourable case for mass transport from the solution to the catalyst surface. So, mass transport is governed by Fick's law:

$$-j = D\frac{\partial c}{\partial z} \tag{8}$$

where j is the material flow and D is the diffusion coefficient (cm² s^{-1}), which depends only on the temperature.

We consider that the system is a flat plate of 10 cm², immersed in the tube (4 cm in diameter), and that the liquid is not stirred. At the stationary state, the "incoming" and "outgoing" flows on the surface of the substrate must be equal. The "outcoming" flow corresponds to the reaction speed, referred to the unit of surface area of the catalytic plate (in mol cm^{-2} s^{-1}). The "incoming" flow is given by Fick's law. Thus:

$$r = D\frac{\partial c}{\partial z} \tag{9}$$

where r is the reaction rate and D the diffusion coefficient of H_2O_2 in water (~10^{-5} cm² s^{-1}).

Considering that z = L and C = C_0 = 6.18 × 10^{-3} mol cm^{-3}, Equation 9 can be integrated between the surface of the plate (z = 0) and the edge of the tube furthest away (z = L) resulting in:

$$rL = D(C_0 - C_s) \tag{10}$$

where C_s is the concentration of H_2O_2 at the surface of the plate. In other words, the concentration gradient between the plate and the liquid is directly proportional to the reaction speed:

$$r = D\frac{(C_0 - C_s)}{L} \tag{11}$$

It is then possible to evaluate C_s:

$$C_s = C_0 - \frac{rL}{D} \tag{12}$$

With values of C_0 = 6.18 × 10^{-3} mol cm^{-3}, D = 10^{-5} cm^2 s^{-1}, r = r_0 = 3.6 × 10^{-12} mol cm^{-2} s^{-1} and L = 4 cm, one obtains $C_s \sim C_0$. The decrease in concentration is negligible, even in the most extreme case (diffusion only, no agitation). There is therefore no problem of external matter transfer, and the first-order found experimentally is thus related to reaction kinetics, not mass transport in the fluid. It means that variations of reaction rates are representative of the NW catalytic properties.

3.3.4 Conclusion

ZnO NWs prepared on seeds calcined at various temperatures, using techniques developed in Chapters 1 and 2, were tested as possible photocatalyst by using the photocatalytic degradation of H_2O_2 as a test reaction. This first set experiment has shown that the calcination temperature of the ZnO seed layer has an influence in the subsequent growth, organisation and orientation of ZnO NWs. The increase of the calcination temperature of the seed layer leads to a well oriented seed layer (c-axis (002)) with a higher density of NWs. The H_2O_2 degradation rate (expressed in mol L^{-1} s^{-1}) in contact with ZnO NWs under visible light irradiation was significantly higher when the seed calcination temperature was increased. For instance, the best decomposition rate was obtained for a calcination temperature of 400 ºC, with an initial rate of decomposition of H_2O_2 (r_0) value of 7.18 × 10^{-7} mmol L^{-1} s^{-1}. However, when the rate is calculated as function of the ZnO mass deposited, the best result is obtained for a seed layer calcined at 200 °C. This can be explained by the differences of NW density.

When the seed layer is calcined at 200 °C, the NWs are less close to each other than when grown on a seed calcined at 400 °C, as shown in Figure 3.17. This suggest that, if one assumes that the active sites display the same catalytic activity from sample to sample, the photocatalytic activity of ZnO NWs comes not only from the top surface of the material but also from the side surfaces. Note however that the photocatalytic activity of ZnO NWs was only tested once and needs to be reproduced. Moreover, the measurement of the specific area of the NWs is needed to confirm that the photocatalytic activity of the NWs comes from the top and the side surfaces, and not from a modification of the catalytic activity of the active sites.

3.4 Conclusion

In this chapter ZnO nanowires were used to build piezoelectric nanogenerators and as photocatalyst for the degradation of H_2O_2.

The two applications presented here highlighted that the dimensions (length and diameter) and the density of the nanowires were not the only parameters that influence the final performances. Indeed, the high concentration of structural defects such as vacancies or interstitial ions, can decrease the performances of the nanogenerator. A way to improve the NG performances is to decrease the structural defect using the seed deposition process and the NWs growth developed as presented in the previous chapter followed by a post-thermal treatment.

In the case of photocatalysis, the density of NWs has an impact on the reaction rate, which certainly comes from the actual surface in contact with the H_2O_2 solution: indeed, as the calcination seed increases, the voids between the NW decrease, leading to a decrease of the reaction rate per mass unit of ZnO. In order to improve the catalytic activity of the NWs, the catalytic surface area should be increased by decreasing the NW density; however, the total specific surface area of the NW arrays need to be measured to compare the results between each other.

It is then necessary to control the synthesis process of the NWs, which is not obvious. However, we have shown in Chapter 1 and Chapter 2 that the morphology of the NWs could be controlled to some extent. It should thus be possible to adapt the NWs properties to the final application.

References

1. C. Mendoza, N. Emmanuel, C. A. Páez, L. Dreesen, J.-C. M. Monbaliu, B. Heinrichs, Improving continuous flow singlet oxygen photooxygenation reactions with functionalized mesoporous silica nanoparticles. *ChemPhotoChem*. **2**, 890–897 (2018).
2. Z. L. Wang, X. Y. Kong, Y. Ding, P. Gao, W. L. Hughes, R. Yang, Y. Zhang, Semiconducting and piezoelectric oxide nanostructures induced by polar surfaces. *Adv. Funct. Mater.* **14**, 943–956 (2004).
3. R. Hinchet, S. Lee, G. Ardila, L. Montès, M. Mouis, Z. L. Wang, Performance optimization of vertical nanowire-based piezoelectric nanogenerators. *Adv. Funct. Mater.* **24**, 971–977 (2014).
4. J. I. Sohn, S. N. Cha, B. G. Song, S. Lee, S. M. Kim, J. Ku, H. J. Kim, Y. J. Park, B. L. Choi, Z. L. Wang, J. M. Kim, K. Kim, Engineering of efficiency limiting free carriers and an interfacial energy barrier for an enhancing piezoelectric generation. *Energy Environ. Sci.* **6**, 97–104 (2013).
5. S. Xu, Z. L. Wang, One-dimensional ZnO nanostructures: Solution growth and functional properties. *Nano Res.* **4**, 1013–1098 (2011).
6. D. A. Scrymgeour, J. W. P. Hsu, Correlated piezoelectric and electrical properties in individual ZnO nanorods. *Nano Lett.* **9**, 2204–2209 (2008).
7. E. G. Barbagiovanni, V. Strano, G. Franzò, I. Crupi, S. Mirabella, Photoluminescence transient study of surface defects in ZnO nanorods grown by chemical bath deposition. *Appl. Phys. Lett.* **106**, 1–4 (2015).
8. Z. L. Wang, Energy harvesting using piezoelectric nanowires-a correspondence on "Energy harvesting using nanowires?" *Adv. Mater.* **21**, 1311–1315 (2009).
9. B. M. Alexe, S. Senz, M. A. Schubert, D. Hesse, Energy harvesting using nanowires ? *Adv. Mater.* **20**, 4021–4026 (2008).
10. G. Zhu, R. Yang, S. Wang, Z. L. Wang, Flexible high-output nanogenerator based on lateral ZnO nanowire array. *Nano Lett.* **10**, 3151–3155 (2010).
11. G. Zhu, A. C. Wang, Y. Liu, Y. Zhou, Z. L. Wang, Functional electrical stimulation by nanogenerator with 58 V output voltage. *Nano Lett.* **12**, 3086–3090 (2012).
12. A. S. Dahiya, F. Morini, S. Boubenia, K. Nadaud, D. Alquier, G. Poulin-Vittrant, Organic/Inorganic hybrid stretchable piezoelectric nanogenerators for self-powered

wearable electronics. *Adv. Mater. Technol.* **3**, 1–11 (2018).

13. D. R. Baer, S. Thevuthasan, in *Handbook of deposition technologies for films and coatings*, P. M. Martin, Ed. (Third Edit., 2010), pp. 749–864.
14. C. Oshman, C. Opoku, A. S. Dahiya, D. Alquier, N. Camara, G. Poulin-Vittrant, Measurement of spurious voltages in ZnO piezoelectric nanogenerators. *J. Microelectromechanical Syst.* **25**, 533–541 (2016).
15. C. Opoku, A. S. Dahiya, F. Cayrel, G. Poulin-Vittrant, D. Alquier, N. Camara, Fabrication of field-effect transistors and functional nanogenerators using hydrothermally grown ZnO nanowires. *RSC Adv.* **5**, 69925–69931 (2015).
16. M. Kokotov, G. Hodes, Reliable chemical bath deposition of ZnO films with controllable morphology from ethanolamine-based solutions using $KMnO_4$ substrate activation. *J. Mater. Chem.* **19**, 3847–3854 (2009).
17. P. Sagar, P. K. Shishodia, R. M. Mehra, H. Okada, A. Wakahara, A. Yoshida, Photoluminescence and absorption in sol-gel-derived ZnO films. *J. Lumin.* **126**, 800–806 (2007).
18. L. E. Greene, M. Law, J. Goldberger, F. Kim, J. C. Johnson, Y. Zhang, R. J. Saykally, P. Yang, Low-temperature wafer-scale production of ZnO nanowire arrays. *Angew. Chemie - Int. Ed.* **43**, 3031–3034 (2003).
19. Y. Fang, Y. Wang, Y. Wan, Z. Wang, J. Sha, Detailed study on photoluminescence property and growth mechanism of zno nanowire arrays grown by thermal evaporation. *J. Phys. Chem. C* **114**, 12469–12476 (2010).
20. Y. W. Wang, L. D. Zhang, G. Z. Wang, X. S. Peng, Z. Q. Chu, C. H. Liang, Catalytic growth of semiconducting zinc oxide nanowires and their photoluminescence properties. *J. Cryst. Growth* **234**, 171–175 (2002).
21. Y. W. Heo, D. P. Norton, S. J. Pearton, Origin of green luminescence in ZnO thin film grown by molecular-beam epitaxy. *J. Appl. Phys.* **98**, 1–6 (2005).
22. K. H. Tam, C. K. Cheung, Y. H. Leung, A. B. Djurišić, C. C. Ling, C. D. Beling, S. Fung, W. M. Kwok, W. K. Chan, D. L. Phillips, L. Ding, W. K. Ge, Defects in ZnO nanorods prepared by a hydrothermal method. *J. Phys. Chem. B* **110**, 20865–20871 (2006).
23. S. Brahma, J. Huang, C. P. Liu, L. M. Kukreja, S. A. Shivashankar, Low temperature and rapid deposition of ZnO nanorods on Si (100) substrate with tunable optical emissions. *Mater. Chem. Phys.* **140**, 634–642 (2013).
24. H. E. Unalan, P. Hiralal, N. Rupesinghe, S. Dalal, W. I. Milne, G. A. J. Amaratunga,

Rapid synthesis of aligned zinc oxide nanowires. *Nanotechnology* **19**, 1–6 (2008).

25. H. Y. Lin, C. L. Cheng, Y. Y. Chou, L. L. Huang, Y. F. Chen, K. T. Tsen, Enhancement of band gap emission stimulated by defect loss. *Opt. Express* **14**, 2372–2379 (2006).
26. Y. Hu, L. Lin, Y. Zhang, Z. L. Wang, Replacing a Battery by a Nanogenerator with 20 V Output. *Adv. Mater.* **24**, 110–114 (2012).
27. D. A. Gulino, L. A. Kren, T. M. Dever, Isotopic study of oxygen diffusion in silicon dioxide thin films. *Thin Solid Films* **188**, 237–246 (1990).
28. Abhishek Singh DAHIYA, thesis, Université François-Rabelais de Tours (2016).
29. W. Y. Su, J. S. Huang, C. F. Lin, Improving the property of ZnO nanorods using hydrogen peroxide solution. *J. Cryst. Growth* **310**, 2806–2809 (2008).
30. J. Bae, J.B. Han, X.-M. Zhang, M. Wei, X. Duan, Y. Zhang, Z.L. Wang, ZnO nanotubes grown at low temperature using Ga as catalysts and their enhanced photocatalytic activities. *J. Phys. Chem. C* **113** 10379–10383 (2009).
31. X. Cao, H. Zeng, M. Wang, X. Xu, M. Fang, S. Ji, L. Zhang, Large scale fabrication of quasi-aligned ZnO stacking nanoplates. *J. Phys. Chem. C* **112** 5267–5270 (2008).
32. F. Lu, W. Cai, Y. Zhang, ZnO hierarchical micro/nanoarchitectures: solvothermal synthesis and structurally enhanced photocatalytic performance. *Adv. Funct. Mater.* **18** 1047–1056 (2008).
33. Y. Zhang, M.K. Ram, E.K. Stefanakos, D.Y. Goswami, Synthesis, characterization, and applications of ZnO nanowires. *J. Nanomater.* **22** (2012).
34. J.L. Yang, S.J. An, W.I. Park, G.C. Yi, W. Choi, Photocatalysis using ZnO thin films and nanoneedles grown by metal-organic chemical vapor deposition. *Adv. Mater.* **16** 1661–1664 (2004).
35. T.-J. Kuo, C.-N. Lin, C.-L. Kuo, M.H. Huang, Growth of ultralong ZnO nanowires on silicon substrates by vapor transport and their use as recyclable photocatalysts. *Chem. Mater.* **19** 5143–5147 (2007).
36. I. Udom, M.K. Ram, E.K. Stefanakos, A.F. Hepp, D.Y. Goswami, One dimensional-ZnO nanostructures: synthesis, properties and environmental applications. *Mater. Sci. Semicond. Process.* **16** 2070–2083 (2013).
37. Y.-C. Chang, Low temperature growth of ZnO nanowire arrays with enhanced high performance photocatalytic activity and reusability. *Catalysis Communications* **56** 45–49 (2014).
38. D. Rajamanickam, M. Shanthi, Photocatalytic degradation of an organic pollutant by

zinc oxide – solar process. *Arab. J. Chem.* **9**, S1858–S1868 (2016).

39. X. Li, C. Chen, J. Zhao, Mechanism of Photodecomposition of H_2O_2 on TiO_2 Surfaces under Visible Light Irradiation. *Langmuir* **17**, 4118–4122 (2001).
40. T. Hirakawa, Y. Nosaka, Properties of $O_2^{\cdot -}$. formed in TiO_2 aqueous suspensions by photocatalytic reaction and the influence of H_2O_2 and some ions. *Langmuir* **18**, 3247–3254 (2002).
41. H. Goto, Y. Hanada, T. Ohno, M. Matsumura, Quantitative analysis of superoxide ion and hydrogen peroxide produced from molecular oxygen on photoirradiated TiO_2 particles. *J. Catal.* **225**, 223–229 (2004).
42. T. Hirakawa, K. Yawata, Y. Nosaka, Photocatalytic reactivity for $O_2^{\cdot -}$ and $OH^{\cdot}$ radical formation in anatase and rutile TiO_2 suspension as the effect of H_2O_2 addition. *Appl. Catal. A Gen.* **325**, 105–111 (2007).
43. C. A. Páez, D. Y. Liquet, C. Calberg, S. D. Lambert, I. Willems, A. Germeau, J. P. Pirard, B. Heinrichs, Study of photocatalytic decomposition of hydrogen peroxide over ramsdellite-MnO_2 by O_2^- pressure monitoring. *Catal. Commun.* **15**, 132–136 (2011).
44. M. Kokotov, S. Bar-Nachum, E. Edri, G. Hodes, Effect of glass dissolution on the solution deposition of ZnO films and its exploitation for deposition of Zn silicates. *J. Am. Chem. Soc.* **132**, 309–314 (2010).
45. J. J. Richardson, F. F. Lange, Controlling low temperature aqueous synthesis of ZnO. *Cryst. Growth Des.* **9**, 2570–2575 (2009).
46. D. Poelman, P. F. Smet, Methods for the determination of the optical constants of thin films from single transmission measurements: a critical review. *J. Phys. D: Appl. Phys.* **36**, 1850–1857 (2003).
47. I. A. Salem, Catalytic decomposition of H_2O_2 over supported ZnO. *Monatshefte fur Chemie* **131**, 1139–1150 (2000).
48. H. A. Kiwaan, T. M. Atwee, E. A. Azab, A. A. El-Bindary, Efficient photocatalytic degradation of Acid Red 57 using synthesized ZnO nanowires. *J. Chinese Chem. Soc.* **66**, 89–98 (2019).
49. H. Kisch, D. Bahnemann, Best practice in photocatalysis: comparing rates or apparent quantum yields? *J. Phys. Chem. Lett.* **6**, 1907–1910 (2015).

Chapter 4. Optimisation of $LiCoO_2$ cathode material using $Li_7La_3Zr_2O_{12}$

4.1 Introduction

A battery is a device that converts the chemical energy contained in a material into electrical energy, *via* an electrochemical reaction (oxidation-reduction). Rechargeable lithium batteries, are the most widely sold, as they have a high capacity, high charging speed and a long lifespan, particularly in portable electronics. Two types of lithium batteries exist: (i) Li-ion batteries, which uses intercalation materials of Li^+ as negative and positive electrodes; (ii) Li-metal batteries, where lithium metal is used as negative electrode whereas an intercalation material is used at the positive electrode. In the latter case, the oxidation state of Li changes at the negative electrode.

A lithium battery consists of the assembly of three components: the positive electrode, the negative electrode and the electrolyte containing Li^+ ions (Figure 4.1). The two electrodes are isolated from each other by the separator, which is a porous membrane that avoids electrical contact between the electrodes (and therefore internal short-circuits) and allows the transfer of ions [1]. During charging, the two electrodes are connected externally to a generator. The electrons are forced to be released at the positive electrode and move externally to the negative electrode. Simultaneously the lithium ions move in the same direction, but internally from positive to negative electrode, *via* the electrolyte (meaning that the oxidation reaction corresponds to a delithiation of the positive electrode). During discharging, the opposite occurs: the ions move from the negative to the positive electrode in the electrolyte (the reduction corresponds to the lithiation of the positive electrode) [1].

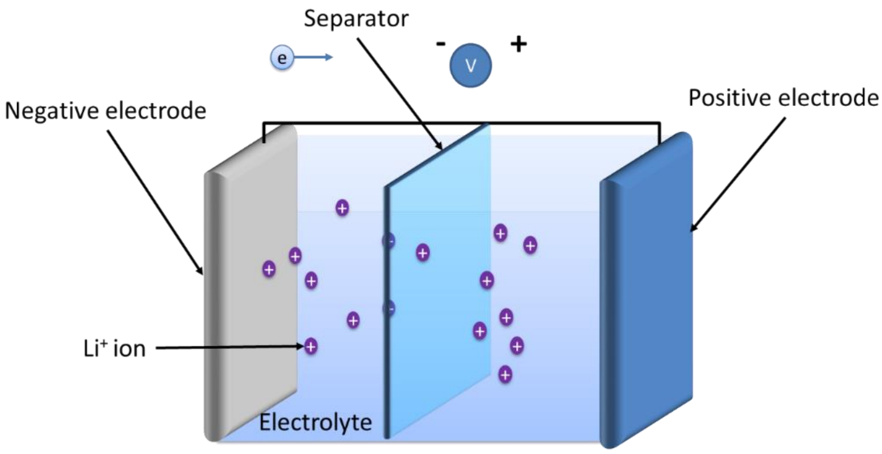

Figure 4.1. General scheme of a lithium battery.

Currently, research is focusing on the miniaturisation and mechanical flexibility of lithium batteries, in order to be integrated into microsystems. For this application, lithium metal is the most commonly used negative electrode. This is due to its very high mass capacity of 3828 mAh g^{-1} and its highly reducing properties which allows high battery voltage to be achieved. However, the high reactivity of lithium metal with oxygen and water forbids any contact with the ambient atmosphere, both when processed and upon use. Those microbatteries are made by successive deposition of layers of cathode material, solid electrolyte and anode material. These devices can be integrated within autonomous micro energy sources, such as micro-sensors or microchips (bank card security); they are also suitable for medical applications, such as biochips. The thickness of the different layers can vary from a few nanometres to several microns, with the total thickness not exceeding ~100 µm. The cycling lifetime and theoretical capacity are key electrochemical properties. The theoretical capacity, represents the amount of electrical charge stored in the battery and can be expressed by the Faraday law (Equation 1):

$$Q = \frac{x\,n\,F}{3600\,S} \text{ (Ah cm}^{-2}\text{)} \qquad (1)$$

where x represents the number of exchanged electrons, n represents the amount of mole of material (mol), F represents the Faraday constant (96400 C mol^{-1}), and S is the electrode area (cm^2). The thickness of the coatings in microbatteries usually do not exceed 10 µm, so that the surface area, and not the mass, is the limiting factor. Unlike conventional batteries, where capacity is expressed per mass unit of LCO present in the electrode, it is thus better for microbatteries to express it as a function of the surface area of electrode (Ah cm^{-2}). The capacity is the product of the discharge (charge) time and the current imposed on the battery. Cycling performance is usually evaluated by the percentage of capacity loss per cycle.

$LiCoO_2$ (LCO), introduced by the group of J. B. Goodenough [2], remains the most commercially successful form of layered transition metal oxide used in positive electrodes (Figure 4.2a). It was originally commercialised by SONY, and this material is still used in the majority of commercial rechargeable lithium batteries. LCO is a very attractive cathode material because of its (relatively) high theoretical specific capacity of 274 mAh g^{-1}, low self-discharge, high discharge voltage and good cycling performance [3–5].

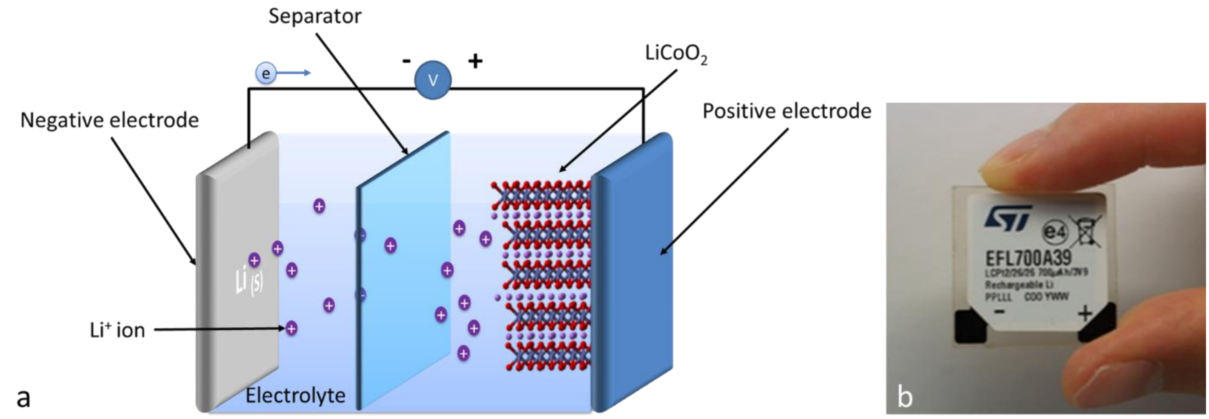

Figure 4.2. (a) Scheme of lithium metal battery; (b) Prototype of microbattery from ST microelectronics.

Lithium metal batteries are not viable due to the instability of a Li metal/liquid electrolyte interface induced by the dendrite growth of lithium. The short circuit of dendrites leads to thermal runaway and a risk of explosion. In order to improve safety, the absence of liquid electrolyte and associated leakage is essential. To that end, the EnSO project aims at the development of lithium solid-state batteries, using solid electrolyte or gel polymer electrolyte (GPE) (Figure 4.2b) instead of a liquid electrolyte.

Previously in the EnSO project, two processes were developed at the Nanomaterials, Catalysis and Electrochemistry (NCE) laboratory of the University of Liège [6] by a senior researcher for the deposition of thin layers of LCO for microbatteries (Figure 4.3). The first one consists in a low-cost water-based process were LCO is ground, calcined at 700 °C and directly introduced into water to be sprayed onto a current collector; the spray is performed while heating the current collector at 80 °C to allow the fast water evaporation. The second one consists in the development of an ethanol-based process, were LCO is ground, calcined and functionalised by an amorphous titanium dioxide (TiO_2) before dispersion into water and spray onto a current collector [7]. According to the obtained results, the addition of TiO_2 first provides a better stability of LCO under high cycling conditions. Second, the TiO_2 acts as a chemical protective agent in order to prevent cobalt dissolution due to the hydrofluoric acid (HF) formed during cycling. Indeed, when the battery is running, the electrolyte decomposes and forms HF *via* the reaction:

$$LiPF_6 + H_2O \rightarrow LiF + POF_3 + 2HF \tag{2}$$

Finally, the TiO_2 introduced into the electrode stabilises the LCO particles in ethanol, which makes it possible to decrease the deposition temperature from 80 °C (when the electrode is processed using water) to 40 °C (using ethanol).

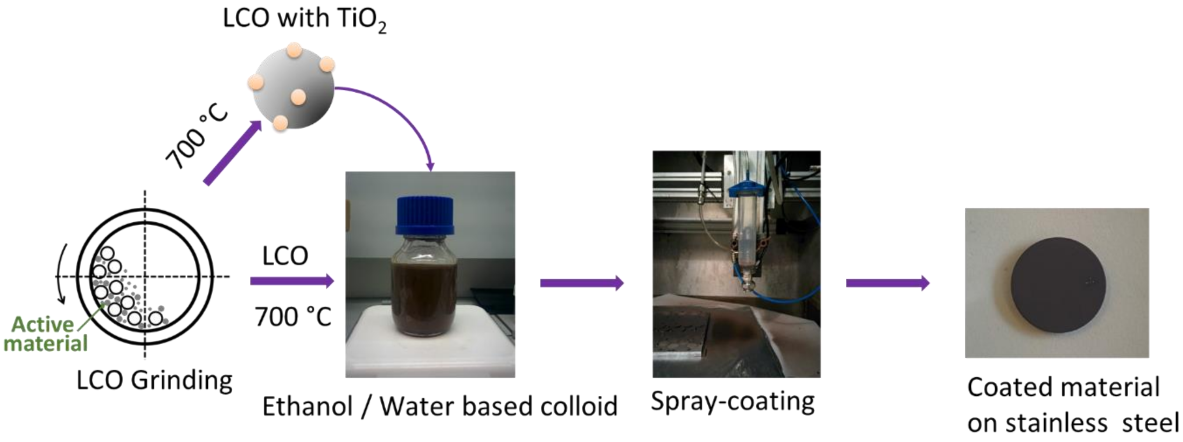

Figure 4.3. Processes previously developed at the NCE laboratory [6, 7].

To sum up, these processes consist in depositing a ~10 µm thick layer of LCO (positive electrode material) using spray-coating without the use of any binder, conductive or dispersant additives. However, the spray-coated deposit showed a roughness between 450 nm and 800 nm, which is too high compared to the industry requirement (< 100 nm), as well as a porosity of 50-60%. The presence of porosity limits the contact between particles and thus the motion of lithium ions within the layer. Therefore, the layer porosity leads to a decrease in the electrochemical performances of the electrode when a solid electrolyte or GPE is used.

In order to improve the ionic conductivity, a nanostructured ion-conductive material can be added to the electrode. In general, oxide materials are believed to be superior to non-oxide materials for reasons of handling and mechanical, chemical, and electrochemical stability [8]. Weppner *et al.* have recently discovered a series of garnet structured solid electrolytes with high lithium ionic conductivities [9–12]. One of these, zirconium-containing lithium garnet ($Li_7La_3Zr_2O_{12}$, LLZO), has received much attention as a next generation solid electrolyte because of its high lithium ionic conductivity at room temperature (2×10^{-4} S cm^{-1}) and sufficient stability against lithium metal [10–12]. Several solid electrolytes, such as lanthanum lithium titanate [13] and sulphide-based glass ceramics [14, 15] display higher lithium ionic conductivities. However, such solid electrolytes are unstable against lithium metal [16]. Therefore, LLZO seems to be the most suitable material for solid-state Li metal batteries.

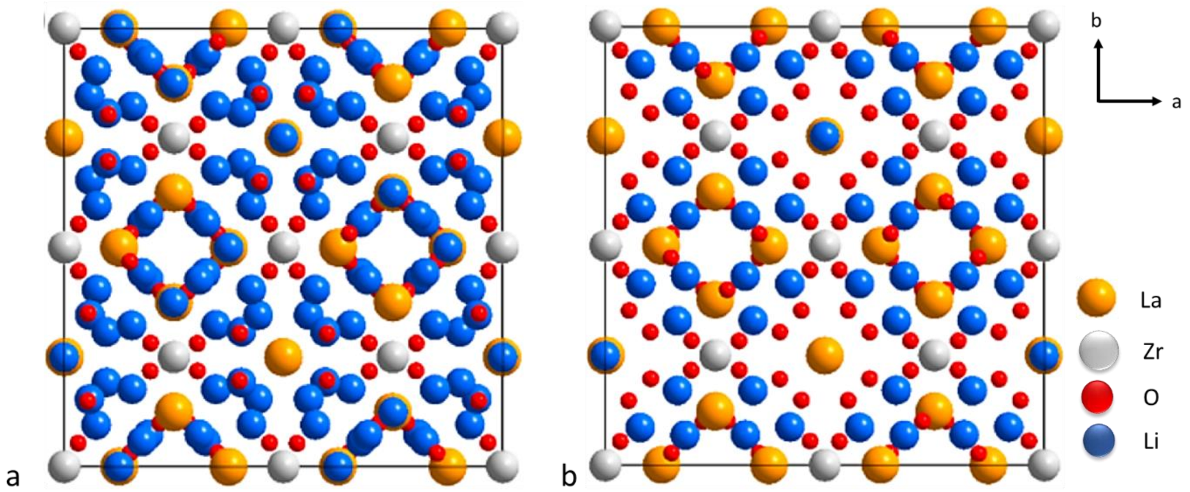

Figure 4.4. (a) Unit cell of HT-cubic LLZO. (b) Unit cell of tetragonal phase LLZO. Reproduced from reference [16].

Three LLZO polymorphs exist. The first is the high-temperature cubic phase (HT-cubic): this crystalline phase gives an ionic conductivity of ~10^{-4} S cm^{-1} at room temperature (Figure 4.4a). However, the HT-cubic phase requires a calcination step at temperatures above 1120 °C, which is too energy consuming and limits the choice of the layer support; furthermore, it is not stable at room temperature [10]. The second polymorph is the tetragonal phase (Figure 4.4b). It can be synthesised at temperatures above 800 °C and displays an ionic conductivity of ~10^{-6} S cm^{-1} [17]. Finally, the development of low-temperature synthesis methods has led to the low-temperature LT-cubic phase. This phase has the same structure as HT-cubic, with a larger crystal lattice and a conductivity of ~10^{-6} S cm^{-1}. The LT-cubic phase is stable at room temperature, and can be synthesised by sol-gel process (≤ 700 °C), using the so-called Pechini method, to obtain nanocrystallites (~25 nm in size) [17]. The Pechini method uses citric acid as a chelating agent, in order to form a homogeneous solution of metal/citrate complexes [18]. Given its synthesis conditions and properties, the LT-cubic phase has been selected in the present work to increase the ion conductivity of the LCO particles in positive electrode layers. The goal of the study was to improve the positive electrode performances, in order to build a solid-state battery using solid electrolyte such as Lithium Phosphorous Oxynitride (LiPON) or GPE.

The main challenge using nanostructured LLZO as ion-conductivity improver was to fill the LCO coating porosity (between 50-60%), without changing the electrochemical properties of LCO, to finally be able to build an all solid-state battery. To do so, nanostructured garnet-LLZO particles were first synthesised using the Pechini method [17, 19]. The obtained LT-cubic phase LLZO was then mixed to the LCO cathode material, and that mix was used in our previously-developed water-based process to prepare positive electrodes. These electrodes were then assembled with separator, a Li metal negative electrode, and the impact of the LLZO presence on the performances of the battery was studied. Note that, as a first step, liquid electrolyte was still added to the system. Ultimately, it will be replaced by GPE or solid electrolyte in a further study (Chapter 5).

4.2 Experimental work

4.2.1 Synthesis and physico-chemical characterisation of LT-cubic LLZO

The LT-cubic LLZO was synthesised by a Pechini sol-gel method using citric acid as organic chelating agent and propanol as surface active agent, as presented by Janani *et al.* [19]. The diagram flow chart in Figure 4.5 shows the LLZO synthesis process. The solutions of lithium nitrate ($LiNO_3$, Sigma Aldrich, 99.99%), lanthanum nitrate ($La(NO_3)_3.6H_2O$, Sigma Aldrich, 99.99%) and zirconium oxynitrate hexahydrate ($ZrO(NO_3)_2.xH_2O$, Sigma Aldrich, 99.99%) were prepared so that the Li:La:Zr ratio was 7:3:2. Two separate cation solutions were first prepared. The first solution contained 0.53 g of $LiNO_3$ (10 wt.% excess was added to compensate Li loss occurring during calcination at 700 °C) [20] and 1.30 g of $La(NO_3)_3.6H_2O$ diluted in 250 mL of deionised water. The second solution contained 0.462 g of $ZrO(NO_3)_2.xH_2O$ and 4.61 g of citric acid (Sigma Aldrich, 99.5%) in a 250 mL of deionised water. The two solutions were then mixed together with 100 mL of isopropanol (2-Propanol, Sigma Aldrich, $\geq$ 99.5%). The mixture was then heated at 60 °C for 45 min under stirring. Finally, the whole solution was put in an oven at 100 °C for gelation and maturation overnight. The obtained gel was heated at 250 °C for 1 h to obtain a brown solid. The solid was then ground manually to form a powder which was successively calcined at 500 °C for 2 h and at 700 °C for 5 h. At the end of the synthesis, 0.8 g of LLZO were obtained and the final white powder was then stored in an inert atmosphere as LLZO is moisture sensistive.

Thermogravimetric measurements were performed after the gel was heated at 250 °C in order to follow the thermal evolution, using a Setaram TG-DSC 111 thermoanalyser. To carry out this analysis, 10 mg of ground gel dried at 250 °C was heated from 20 to 800 °C at a rate of 5 °C min^{-1} in air in a 100 µL platinum crucible. Powders calcined at 500 °C and 700 °C were then characterised by X-ray diffraction (Siemens D5000 Cu Kα radiation) to check their crystalline properties after heat treatment at various temperature.

The particle size distribution of the final powder, after calcination at 700 °C, was obtained using dynamic light scattering (DLS, Delsa Nano C from Beckman Coulter) in ethanol and water. The morphology of the particles was characterised by transmission electronic microscopy (TEM, CM100 Philips). To that aim, a small amount of LLZO powder was dispersed into ethanol; a drop of the suspension was then deposited onto a microgrid (Agar grid hexagonal 200 mesh Copper 3.05 mm, Agar scientific) and dried at room temperature for 2 h to ensure solvent removal.

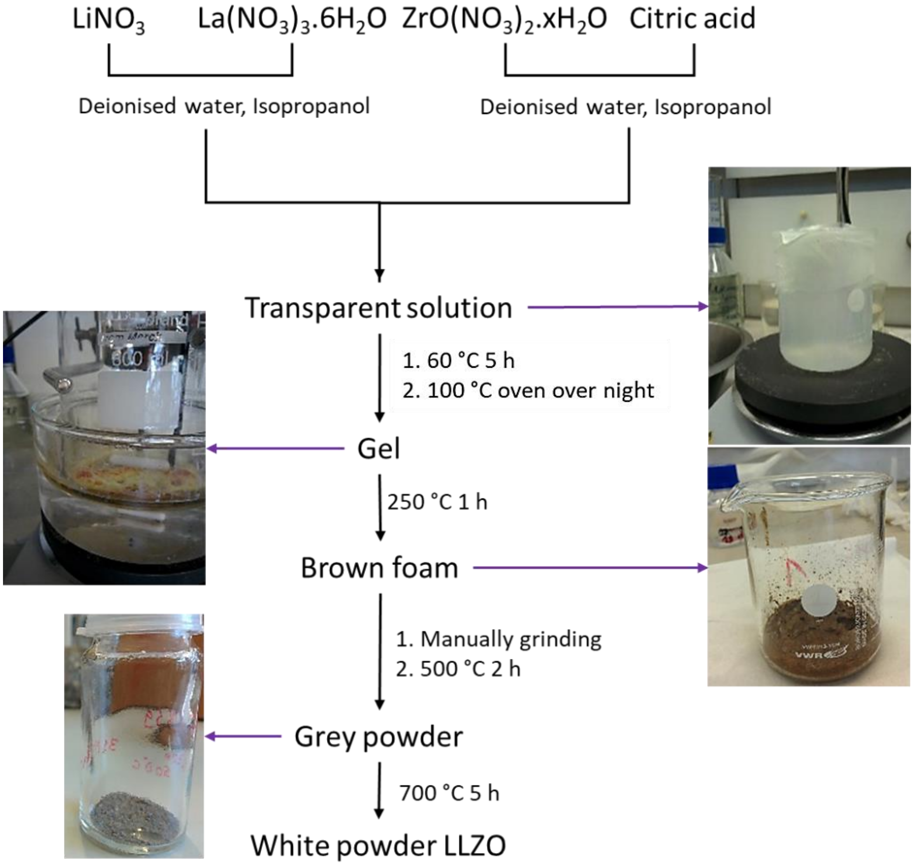

Figure 4.5. Diagram flow chart for the synthesis of LLZO.

4.2.2 Preparation of the LCO suspensions

In order to perform the spray-coating onto the current collector, two suspensions of LCO were prepared: (i) in water and (ii) in ethanol. This was made in order to study the influence of LLZO on the coatings based on the two different processes developed previously at the NCE laboratory.

4.2.2.1 LCO suspension in water

The LCO suspension in water was prepared as presented by Páez *et al.* [6] using a commercial grade LCO. The powder was ground per 6.0 g in a stainless steel jar with 100 g of stainless steel beads (3 mm diameter) using a Fritsch pulverisette 6 planetary mill. The grinding was performed for 20 cycles at 450 rpm for 5 min and 5 min pause by cycle. After grinding, the sample was calcined at 700 °C at a rate of 10 °C min^{-1} under flowing air (0.1 mmol s^{-1}) and the temperature was maintained for 2.5 h. To prepare the suspension, 10.0 g of the obtained powder were then dispersed into 500 mL of deionised water. The suspension was stirred for 90 min, then left in ultrasonicated water bath (42 kHz) for 16 h. The solid in excess was then separated from the suspension after 3 h of decanting. The concentration of the suspension was determined by taking 3 mL from the LCO suspension, which was placed in a vial and dried at 120 °C for 1 h. The vial was weighted before and after introduction of the suspension to determine the weight of the obtained solid. This operation was repeated three times for reproducibility. The solid mass obtained makes it possible to determine the mass concentration of the suspension. The final suspension displayed a final concentration of ~10 g L^{-1}, which was in agreement with the previous work performed at the NCE laboratory [6].

4.2.2.2 LCO suspension in ethanol

The LCO commercial grade powder was ground at 450 rpm and calcined at 700 °C as mentioned before. The LCO powder was then functionalised with ~1.5 wt.% of titanium dioxide (TiO_2) using a process developed and patented previously at the NCE laboratory (results to be published) [7]. To do so, two solutions were prepared at room temperature. The first solution (S1) was obtained by mixing 38 mL of titanium (IV) isopropoxide (Sigma Aldrich, 97% purity) and 206 mL of 2-methoxyethanol (Sigma Aldrich, 99.9%) for 1 h. The second solution (S2) was prepared by adding 5.2 mL of deionised water to 206 mL of 2-methoxyethanol, and mixing for 1 h. Under high stirring (450 rpm), 6 g of the ground and calcined LCO powder was dispersed in methoxyethanol at 60 °C (S3). When the temperature was stable, 1.55 mL of the S1 was added to S3. After 3 h of stirring, 1.55 mL of S2 was added to the previous solution and stirred at 60 °C for 16 h in a closed vial. The solvent was then evaporated using rota evaporation and the resulting LCO functionalised with TiO_2 (labelled LCO_{TiO2}) was dried at 150 °C at 2000 Pa for 16 h.

Finally, the suspension to be used for electrode manufacture was prepared by adding 20 g of the LCO_{TiO2} to 1 L of ethanol. The suspension was first stirred at 450 rpm for 1 h and put into ultrasonicated bath (42 kHz) for 16 h. The solid in excess was then separated from the suspension after 3 h of decanting. The concentration of the suspension was determined by taking 3 mL from the LCO_{TiO2} suspension; these 3 mL were placed in a vial and dried at 120 °C for 1 h. The solid mass was then determined by weighting. This operation was repeated three times for reproducibility. The mass concentration of the suspension was ~10 g L^{-1}.

4.2.3 Electrode Preparation

Stainless steel (SS) 304 disc of 1.88 cm^2 area and 0.5 mm thick were used as supports to deposit the electrode material. This stainless steel disc will constitute the current collector of the positive electrode in the assembled battery.

4.2.3.1 LLZO deposition

Before spraying, the stainless steel discs were weighted and fixed onto a larger support so that they do not move during the spray process. Pure LLZO powder was sprayed onto stainless steel disc in order to test its stability. To do so, 600 mg of the powder were introduced in 30 mL of ethanol and left for 1 h in ultrasonic bath (42 kHz). Then, the 10 g L^{-1} solution was sprayed onto the stainless steel disc heated at 40 °C using a Fuso Seiki Lumina STS-10 spray gun mounted on a robotised arm (Figure 4.6). A circulation pump was used in order to avoid at best the powder precipitation in the spray gun. The discs were weighted before and after deposition to ensure a homogeneous deposition of the LLZO. After deposition, the coatings were then stored in an inert atmosphere as LLZO is moisture sensistive.

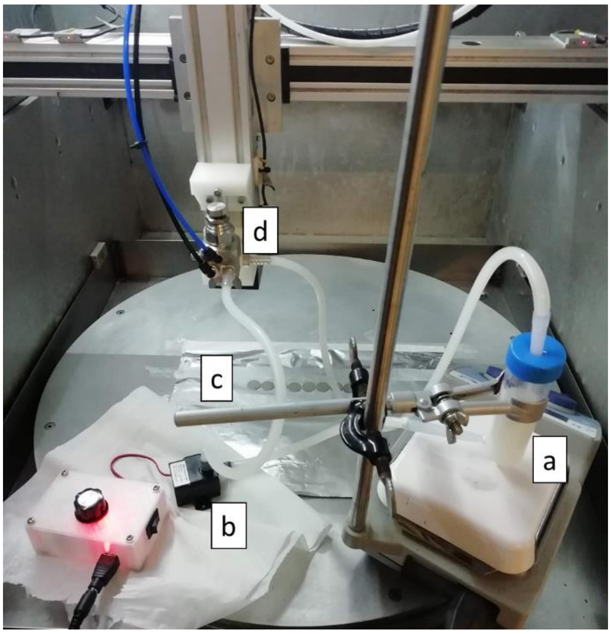

Figure 4.6. Deposition of LLZO using the robotised spray-coater. (a) LLZO suspension in ethanol; (b) Circulation pump; (c) Stainless steel disc; (d) Spray gun.

4.2.3.2 Deposition of LCO and LCO_{TiO2} suspensions

All LCO suspensions were deposited using the set up presented in Figure 4.7. Before spraying, the stainless steel discs were weighted and fixed onto a larger support so that they do not move during the spray process. To spray 10 mg of cathode material (LCO or LCO_{TiO2}) onto the stainless steel disc, 500 mL of the LCO_{TiO2} (or LCO in water) suspension were needed. The suspensions were sprayed onto stainless steel disc heated at 40 °C using a Nordson EFD 781S, spray gun. After spraying the electrodes were heated at 350 °C at 10 °C min^{-1} rate for 1 h.

4.2.3.3 Deposition of LCO_{TiO2} + LLZO suspension

First, the concentration of the suspension was determined by taking 3 mL from the LCO_{TiO2} suspension; these 3 mL were placed in a vial and dried at 120 °C for 1 h. The solid mass was then determined by weighting. This operation was repeated three times for reproducibility. The mass concentration of the suspension was ~9-10 g L^{-1}.

To obtain LCO_{TiO2} + LLZO suspensions with various LLZO content (15, 30, 45 and 60 wt.%), LLZO was added to the LCO_{TiO2} suspension according to Equation 3 and highly stirred for 5-6 h.

$$\frac{m_{LLZO}}{m_{LCO}+m_{LLZO}} x100 = wt.\% \tag{3}$$

The obtained suspensions are labelled LCO_{TiO2} + LLZO 15%, LCO_{TiO2} + LLZO 30%, LCO_{TiO2} + LLZO 45% and LCO_{TiO2} + LLZO 60%. Before spraying, the stainless steel discs were weighted and fixed onto a larger support so that they do not move during the spray process. The suspension under stirring was then sprayed at room temperature onto stainless steel disc in order to obtain 10 mg of active material (LCO_{TiO2}) per disc. The deposition resulted in positive electrode material with 12 samples from each mixed LCO_{TiO2} and LLZO suspension.

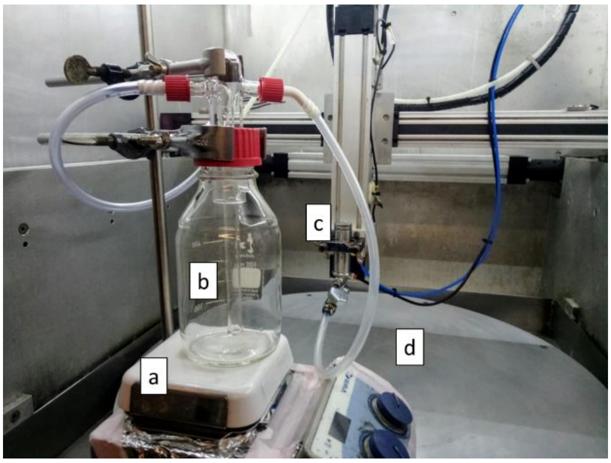

Figure 4.7. Spray coater set-up for the deposition of LCO and LCO_{TiO2} without circulation pump. (a) Magnetic stirrer; (b) 500 mL glass bottle for the suspension; (c) Spray gun; (d) Spray heating plate.

After the cathode material was sprayed, the electrodes were heated at 350 °C at 10 °C min^{-1} rate for 1 h and ready for characterisation. The coatings were characterised by X-ray diffraction and ESEM-EDX (ESEM-FEG XL-30 Philips, Esprit 1.9 software). The open porosity of the film was characterised by Archimedes' method [21] using PEG (average molecular weight 200, Acros Organics, ρ_{PEG} = 1.125 g cm^{-3}) as solvent. The principle of Archimedes' method is to saturate the pores by a liquid (here PEG). Knowing the volume of liquid required to saturate the porous material, its open porosity can be deduced. After the physico-chemical characterisation of the powders/suspensions/electrodes, only the electrodes containing 15% and 30% LLZO were retained for electrochemical characterisation.

4.2.4 Electrochemical characterisation

4.2.4.1 Set-up for LLZO characterisation

The coin cell (CR2032) was set-up in a glove box filled with argon (MBraun 200B). The LLZO coating was introduced into a coin cell (CR2032) where LLZO was at the positive side and lithium foil was at the negative side; the two electrodes were separated with two Celgard 2730 membranes wetted with lithium hexafluorophosphate ($LiPF_6$ in ethylene carbonate/diethylcarbonate, 1:1, w/w, Merck), used as liquid electrolyte (Figure 4.8). A spacer and a spring were added to spread the pressure. Finally, the positive case was added and the coin cell closed using a hydraulic crimper (MSK 110, MTI). The stability of the LLZO was checked using cyclic voltammetry (CV multichannel Bio-Logic VMP3) in the range of 3-4.2 V *vs.* Li^+/Li at 0.1 mV s^{-1} rate (10 cycles) at room temperature. The CV measurements were performed in the same electrochemical window as in the case of a classical LCO/Li battery. During CV, the potential range of the battery was varied at a specific rate, in order to detect any current relative to an electrochemical reaction involving LLZO.

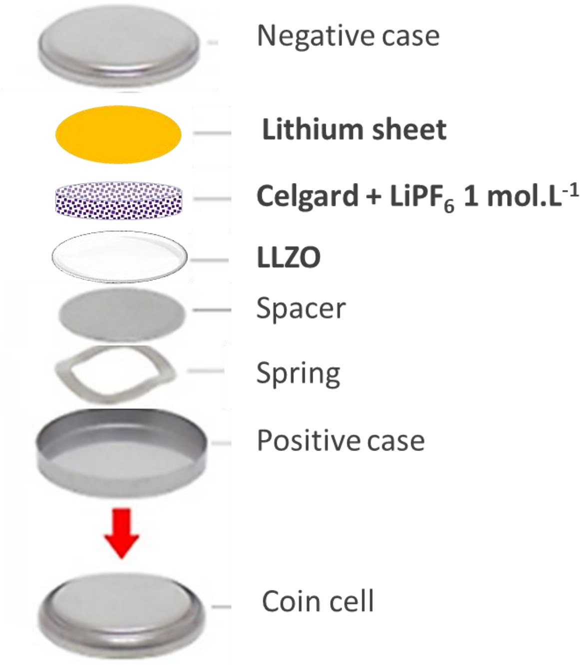

Figure 4.8. LLZO characterisation set-up.

4.2.4.2 LCO characterisation set-up

The LCO and LCO_{TiO2} coatings were included into a coin cell set-up as shown previously. The coin cells were characterised using galvanostatic cycling with potential limitation (GCPL) between 3.0 and 4.2 V *vs*. Li^+/Li at 1, 2, 4, 7, and 10 C rates for five cycles each and a recovering cycling at 1 C for 30 cycles (GCPL on multichannel Bio-Logic VMP3). 1 C corresponds to 1 h of charge and 1 h of discharge and 10 C correspond to 6 min of charge and 6 min of discharge. GCPL is a common technique used to define the capacity of the battery and to check its stability as a function of the number of charge and discharge cycles.

4.2.4.3 LCO_{TiO2} + LLZO characterisation set-up

The two selected coatings (LCO_{TiO2} + LLZO 15% and LCO_{TiO2} + LLZO 30%) were included into a coin cell to determine their electrochemical properties using liquid electrolyte (lithium hexafluorophosphate, $LiPF_6$ in ethylene carbonate/diethylcarbonate, 1:1, w/w, Merck). The set-up of the coin cell is the same as that in section 2.4.1, except that LLZO is replaced by the positive electrode material. The coin cell (CR2032) was set-up in a glove box filled with argon (MBraun 200B). The Li metal foil (negative electrode) and two separators (Celgard 2730 membranes) were introduced into the negative case. Then 80 µL of liquid electrolyte were deposited onto the separators. The mixed LCO_{TiO2} + LLZO 15% or LCO_{TiO2} + LLZO 30% coatings used as cathode material were deposited facing the separators. A spacer and a spring were added to spread the pressure. Finally, the positive case was added and the coin cell was closed using a hydraulic crimper (MSK 110, MTI). Galvanostatic cycling with potential limitation (GCPL) was performed as explained in section 4.2.4.2.

As LCO_{TiO2} + LLZO 30% led to better preliminary results (see section 4.3.4.4), three identical samples of the series (A, B, C) were chosen for further work. The cyclic voltammetry (CV) of LCO_{TiO2} + LLZO 30% were conducted for 10 cycles on sample A using a multichannel Bio-Logic VMP3 at room temperature. The CVs were measured at 0.1 mV s^{-1} scan rate between 3.0 and 4.2 V *vs* Li^+/Li. While sample A was being characterised by CV, GCPL was performed on samples B and C between 3.0 and 4.2 V *vs*. Li^+/Li at 1 C for 100 cycles.

4.3 Results and discussion

4.3.1 Synthesis and physico-chemical characterisation of the LT-cubic LLZO

The synthesis of garnet-like LLZO was performed using a low temperature sol-gel process, and physico-chemical characterisations were done in order to ensure that the low temperature cubic form (LT-cubic LLZO) was indeed obtained. The thermogravimetric analysis (TGA) coupled with a calorimetric measurement (DSC) analysis was performed in air using the gel calcined at 250 °C; the obtained curves up to 800 °C are shown in Figure 4.9. In parallel, the material was characterised by X-ray diffraction after calcination at 500 °C and 700 °C, to check the crystalline properties, as shown in Figure 4.10a. DLS was performed to get an idea of the particle size of the final powder after calcination at 700 °C and results are presented in Figure 4.10b. Finally, transmission electron microscopy (TEM) was used to determine the particle morphology and size of the material calcined at 700 °C: corresponding micrographs are shown in Figure 4.10c.

The TGA (Figure 4.9) allows to follow the weight loss of the sample as a function of temperature (black curve) while the DSC provides information about the exothermicity of the reaction associated with the loss of mass (grey dashed curve). The weight loss between 60 and 160 °C can be attributed to the evaporation of remaining water [19]. The thermogravimetric curve shows (i) two significant mass losses between 300 °C and 700 °C, (ii) three exothermic peaks at 300, 450 and 575 °C, and (iii) one endothermic peak at 725 °C. The first two exothermic peaks between 300 and 450 °C correspond to a 40% mass loss that can be ascribed to the evaporation of reagents. The third exothermic peak between 470 and 600 °C corresponds to a loss of ~20% mass, and is associated with the degradation and oxidation of residual organic compounds. The endothermic peak observed at ~720 °C corresponds to no mass loss and is characteristic of the transition from the low temperature cubic phase of LLZO to the tetragonal phase of LLZO. This transition phase was probably possible because of the close lattice between low temperature LLZO and the tetragonal phase [22].

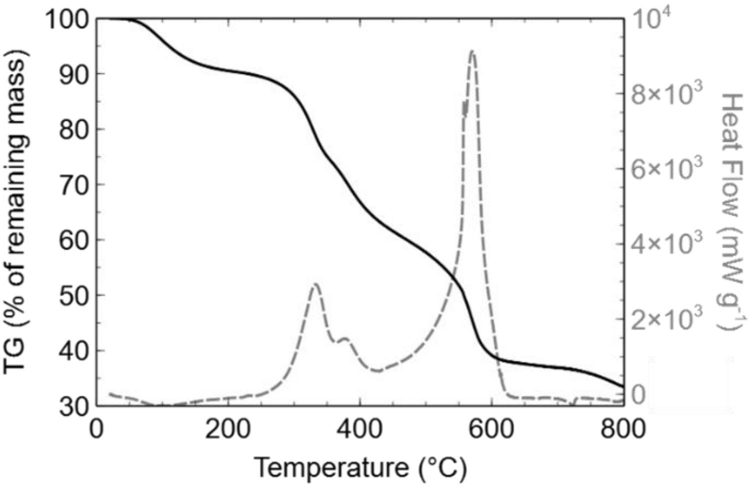

Figure 4.9. TG-DSC analysis performed on the LLZO gel dried at 250 °C. Heat flow (dashed grey curve), TG analysis (black curve).

Garnets are orthosilicates with the general structural formula $A^{II}_3B^{III}_2(SiO_4)_3$, where A and B refer to eight-coordinated and six-coordinated cation sites [23]. The XRD diffractogram in Figure 4.10a shows the influence of the calcination temperature on the different steps of the synthesis. After a calcination at 500 °C in air for 2 h, nanocrystalline pyrochlore ($La_2Zr_2O_7$) is present. At this calcination temperature, the $La_2Zr_2O_7$ is the only crystallographic phase detected [19, 22, 24]. When the gel is calcined at 700 °C, even if trace amounts of $La_2Zr_2O_7$ are still detected, the expected garnet cubic-LLZO phase is formed and matches with typical cubic garnet structure (JCPDS 45-109). The size of the crystallites can be calculated from the full width at half maximum of the peak as [25]:

$$t = \frac{k\ \lambda}{\beta_{1/2}\ cos(\frac{2\theta}{2})} \tag{4}$$

where t is the average crystallite size in the direction perpendicular to the planes (hkl), λ is the incident wavelength, k is a constant (0.89 for spherical particles), θ is the Bragg angle (radians), $\beta_{1/2}$ is the full width at half maximum (radians) [26]. The calculated size of the crystallites was about 20-30 nm, which is confirmed by the TEM images in Figure 4.10c. The DLS has shown that the powder is made of particles of 300-400 nm (Figure 4.10b). As a conclusion, the LLZO powder obtained from the sol-gel method used is made of 350-400 nm particles composed of 20-30 nm cubic crystallites after calcination at 700 °C.

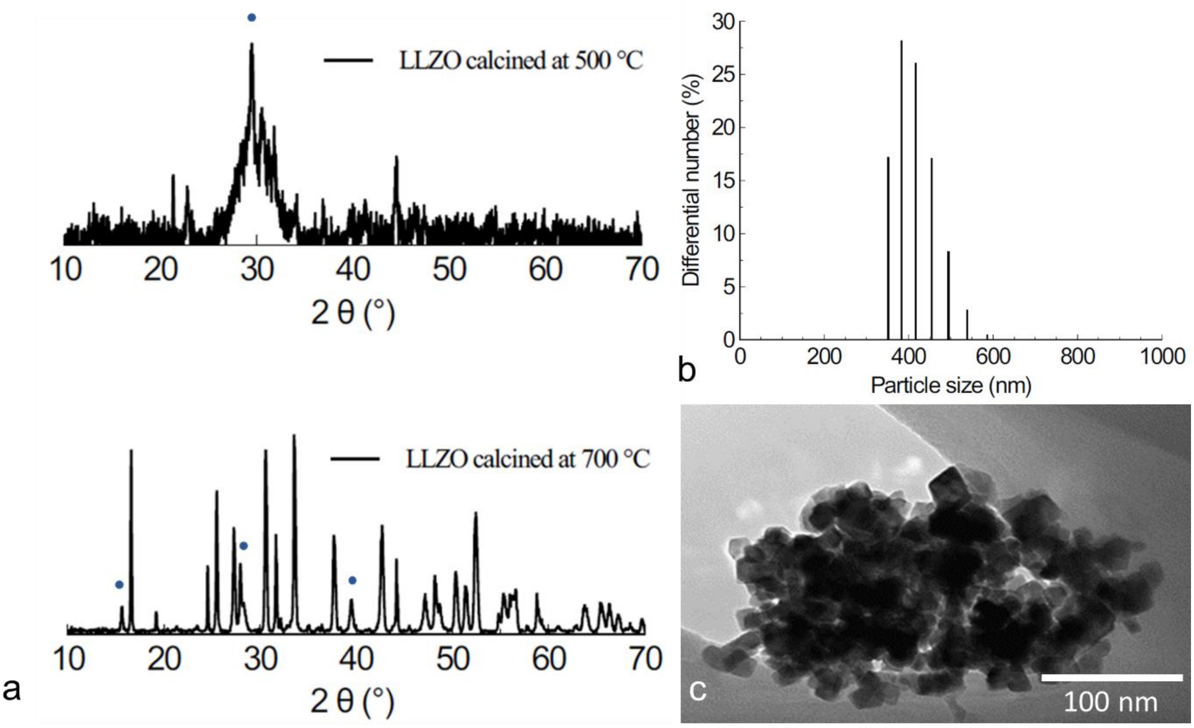

Figure 4.10. (a) XRD analysis of the powder calcined at 500 °C and 700 °C; (●) position of the $La_2Zr_2O_7$ peaks. (b) DLS measurement in ethanol of the LLZO powder after calcination at 700 °C. (c) TEM image of the LLZO powder calcined at 700 °C.

To obtain a better dispersion of the LLZO crystallites, DLS measurement were also performed in water compare with ethanol; results are presented in Figure 4.11a and Figure 4.11b. In the case of measurements in ethanol (Figure 4.11a), the maximum of the peak is located around 400 nm. When water is used (Figure 4.11b), that maximum is shifted to ~200 nm with a smaller disparity of the size of the particles. The LLZO tends thus to dispersed better in water than ethanol and form smaller aggregates. This result suggests that mixing LCO and LLZO in water should lead to a better distribution of the LLZO particles within the electrode coating.

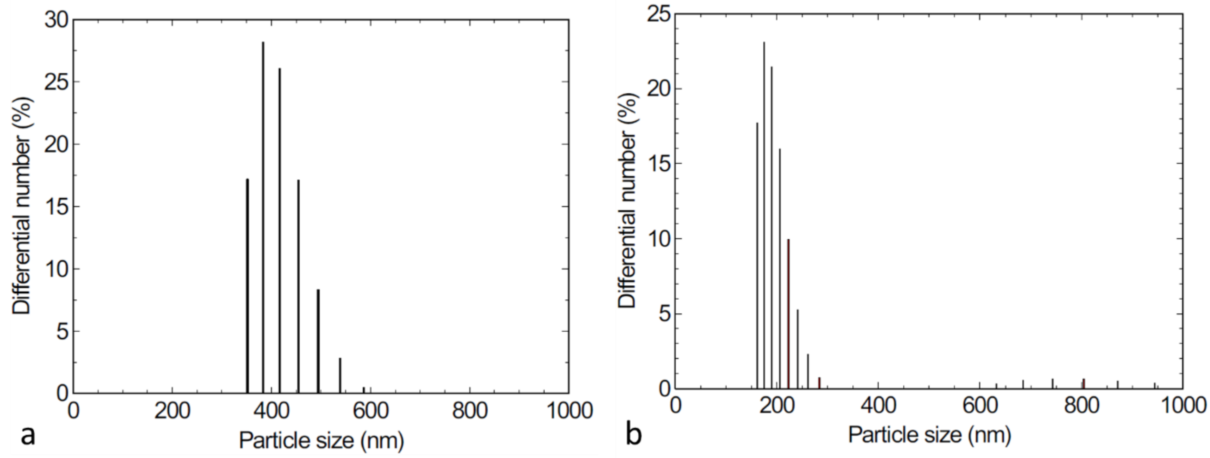

Figure 4.11. LLZO particle size distribution measured by DLS (a) in ethanol and (b) in water.

4.3.2 Preparation of LCO suspensions

4.3.2.1 LCO suspension in water *vs.* LCO_{TiO2} in ethanol

Pure LCO powder was introduced in water, and sprayed onto stainless steel disc heated at 80 °C, to obtain a homogeneous coating. In order to decrease the temperature deposition, LCO was also dispersed in ethanol to perform the coating. To do so, the LCO powder was first functionalised with TiO_2 in order to stabilise the particles in ethanol, improve the ionic conductivity into the cathode film and allow the deposition of a higher amount (5 mg cm^{-2}) of LCO_{TiO2}. Moreover, LCO and TiO_2 simultaneously provide: (i) an open porosity network allowing an excellent impregnation with the liquid electrolyte and low tortuosity, (ii) an adequate packing density developing continuous paths for electron conduction, and (iii) high electrochemical stability. The open porosity of the cathode material was evaluated using Archimedes' method and calculated using Equation 5.

$$P\% = \frac{\frac{m_{\mathrm{PEG}}}{\rho_{\mathrm{PEG}}}}{\frac{m_{\mathrm{PEG}}}{\rho_{\mathrm{PEG}}}+\frac{m_{\mathrm{LCO}}}{\rho_{\mathrm{LCO}}}} \text{ x } 100 \qquad (5)$$

where m_{PEG} correspond to the masse of polyethylene glycol (g), ρ_{PEG} represents the polyethylene glycol density (g cm^{-3}), m_{LCO} is the masse of lithium cobalt dioxide (g), and ρ_{LCO} the lithium cobalt dioxide density (g cm^{-3}). The open porosity of the LCO coating from the suspension in water was 50% and the LCO_{TiO2} coating from the suspension in ethanol was around 55%.

4.3.2.2 Preparation of LCO-LLZO suspension

Different amounts of LLZO were added in the LCO_{TiO2} suspension. The obtained suspensions were sprayed onto the stainless steel disc. During spraying, the spray nozzle was often clogged when using the suspensions with 45 wt.% and 60 wt.% of LLZO, which led to an inhomogeneous coating in both cases (Figure 4.12).

Figure 4.12. Picture showing an example of inhomogeneous deposition of LCO_{TiO2} + LLZO 45% suspension. The same inhomogeneous deposition was obtained for the LCO_{TiO2} + LLZO 60% suspension.

The porosity obtained was 50% for a coating made of LCO_{TiO2} + LLZO 15%, and 40% for a coating made of LCO_{TiO2} + LLZO 30%. The open porosity was about 50% for the coating made of LCO_{TiO2} + LLZO 45% and LCO_{TiO2} + LLZO 60%. Note that the coatings made with 45 wt.% and 60 wt.% of LLZO have been discarded due to the impossibility to obtain homogeneous coatings. No further work was performed on these coatings.

Table 4.1. Open porosity measured using Archimedes' method.

LLZO amount (wt.%)	Open Porosity (%)
0	55
15	50
30	40

4.3.3 Electrode preparation

4.3.3.1 Pure LLZO

The LLZO suspension was deposited directly onto stainless steel disc using spray coating. The LLZO coating were homogeneous as shown in Figure 4.13. The suspension was evenly deposited on the substrates resulting in a mass of 2 ± 0.15 mg on each disc.

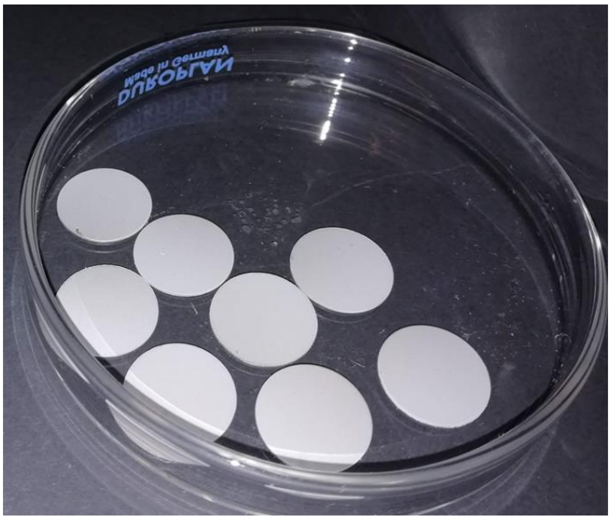

Figure 4.13. Picture showing the LLZO deposited on stainless steel disc.

4.3.3.2 LCO_{TiO2}-LLZO

The LCO_{TiO2}-LLZO suspensions containing 15 wt.% of LLZO and 30 wt.% of LLZO were deposited using spray-coating onto stainless steel disc (Figure 4.14). In each case, the material was evenly deposited on the substrates. In the case of the LCO_{TiO2} + LLZO 15% suspension, a total mass of 11.5 ± 0.2 mg was deposited, which correspond to 9.3 mg LCO_{TiO2} and 1.7 mg LLZO per disc; in the case of the LCO_{TiO2} + LLZO 30% suspension, 15.3 ± 1.0 mg were deposited, which correspond to 10.7 mg of LCO_{TiO2} and 4.6 mg of LLZO per disc.

Figure 4.14. LCO_{TiO2}-LLZO 30% deposited on stainless steel disc.

The coatings were characterised by XRD and ESEM. Figure 4.15 presents the characterisation results for the electrode containing 30 wt.% LLZO; results obtained with 15 wt.% LLZO are quite similar. The diffractogram of the electrode LCO_{TiO2} + LLZO 30% show the presence of LLZO (signal around $2\theta = 15°$) and LCO_{TiO2} (signal at $2\theta = 20°$) (Figure 4.15a).

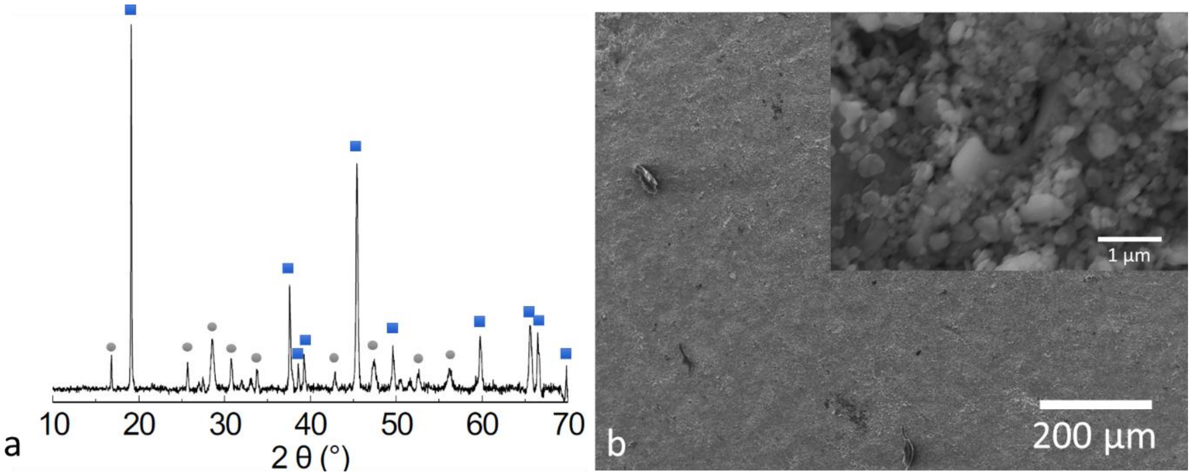

Figure 4.15. LCO$_{\text{TiO2}}$ + LLZO 30% electrode material. (a) XRD diffractogram: peaks corresponding to (■) LCO$_{\text{TiO2}}$ and (●) LLZO; (b) ESEM image with a zoom in the inserted figure.

Characterisation by environmental scanning electron microscopy (ESEM) made it possible to observe the morphology of the layer deposited by spray-coating, as shown in Figure 4.15b. In the inserted picture (Figure 4.15b), one can observe particles of different sizes; however, it is difficult to distinguish the LLZO particles from the LCO$_{\text{TiO2}}$. ESEM technique was coupled to Energy Dispersive X-ray (EDX) analysis to check for the sample chemical homogeneity. In EDX, the impact of electrons on the sample produces X-rays that are characteristic of the elements present in the sample. The analysis can be used to determine the elemental composition of individual points or to map the distribution of elements from the digitised area in the form of an image. However, sensitivity is limited for elements with low atomic number Z; therefore, lithium is not detectable by this technique. Figure 4.16a represents the area which has been scanned. Figure 4.16b-e show the maps obtained by EDX analysis for the different element (Co, O, La, Zr, respectively). Figure 4.16f combines the cartography of all the elements detected.

Since oxygen is present in both LLZO and LCO$_{\text{TiO2}}$, the particles cannot be differentiated from each other using the O cartography. However, lanthanum and zirconium are not present in the same places as cobalt and are therefore representative of the position of the LLZO particles. EDX results show that the distribution of LLZO particles within the layer is homogeneous at the µm scale, meaning that no large aggregates of LCO (without LLZO) or LLZO (without LCO) were detected.

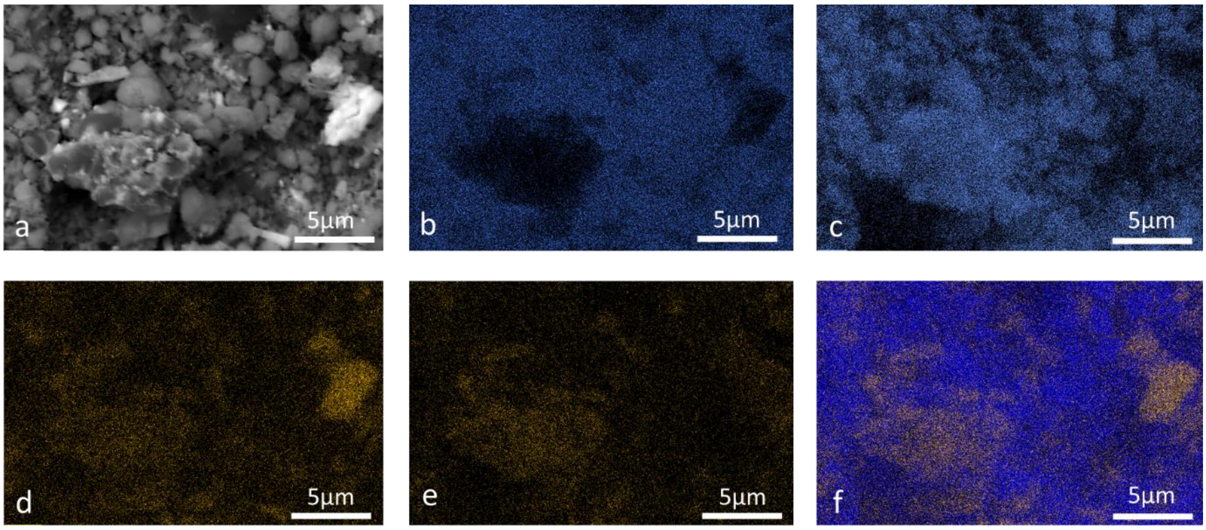

Figure 4.16. EDX mapping of LCO_{TiO2} + LLZO 30% cathode material, (a) ESEM image of the area for mapping, (b) Co mapping, (c) O mapping, (d) La mapping, (e) Zr mapping, (f) combined cartography of Co, O, La and Zr.

4.3.4 Electrochemical measurements

As explained in the introduction, it is better to express the capacity of the microbattery as a function of the surface area of material deposited (mAh cm^{-2}). Here the capacity is represented as a function of the mass of LCO (mAh g^{-1}) and as a function of the surface area coating (mAh cm^{-2}).

4.3.4.1 Characterisation of LLZO

The stability of the LLZO in the chosen voltage window was checked by performing a CV at a scanning rate of 0.1 mV s^{-1} from 3.0 V to 4.2 V *vs*. Li^+/Li; results obtained in the same voltage window with a coating made of LCO_{TiO2} are shown to make sure that the signal obtained with pure LLZO is negligible compared to that of LCO_{TiO2}. Note that the LCO_{TiO2} CV curve will be discussed in the next section. As presented in Figure 4.17a, the LLZO was completely stable in the range of 3.0-4.2 V *vs*. Li^+/Li: indeed, no redox peak is observed in that range for the curve related to pure LLZO (blue curve). Figure 4.17b shows a zoom of the LLZO curve: a signal is visible, but the very low current confirms the stability of the LLZO in this measurement range.

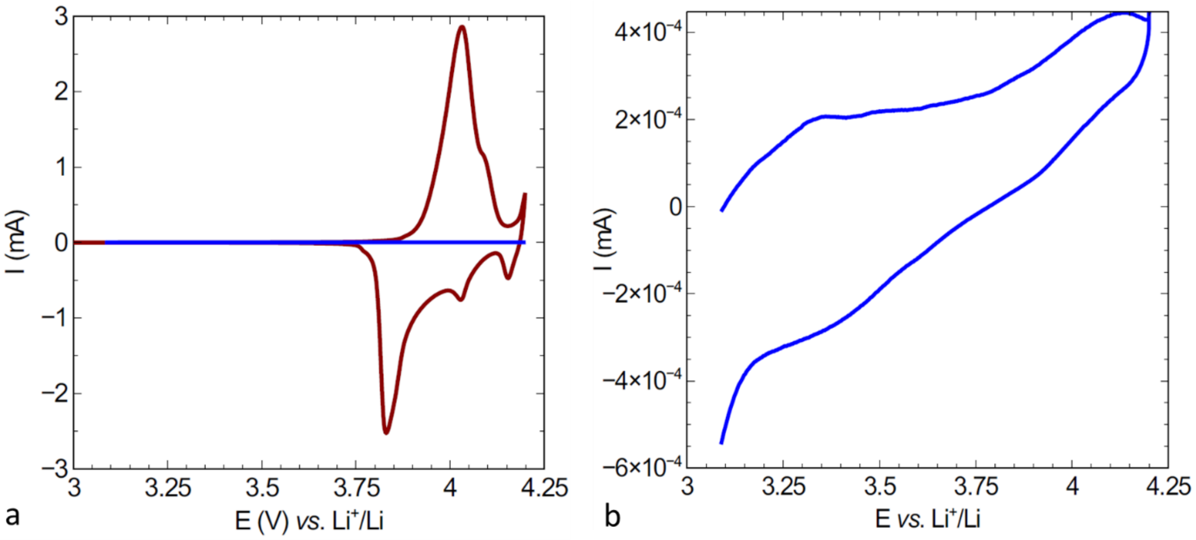

Figure 4.17. Cyclic voltammetry (CV) within the voltage range of 3.0 to 4.2 V *vs*. Li^+/Li at a scanning rate of 0.1 mV s^{-1}. (a) (🟦) LLZO compared to (🟥) LCO_{TiO2}. (b) Zoom of the CV performed on the LLZO coating.

4.3.4.2 Characterisation of LCO coatings prepared in water *vs.* ethanol

Figure 4.18 compares the charge/discharge capacity variation at different cycling rates (5 cycles at 1, 2, 4, 7 and 10 C; then 30 cycles at 1 C for recovery) for the two LCO electrodes prepared using (i) a suspension of LCO in water (Figure 4.18a) and (ii) a suspension of LCO_{TiO2} in ethanol (Figure 4.18b).

In the case of LCO in water, the charge and discharge curves are superimposed and show the same behaviour. The capacity is not stable even at slow rate and tends to decrease with time. After only 5 cycles at 1 C, the system goes to 95% (135 mAh g^{-1}) of its initial capacity, 86% (125 mAh g^{-1}) after 5 cycles at 2 C and 70% (100 mAh g^{-1}) after 5 cycles at 4 C. At higher charge/discharge rates (7 and 10 C) the capacity fades completely. Coming back to 1 C, the system recovers and the capacity decreases continuously while cycling.

In the case of the electrode prepared from LCO_{TiO2} suspension in ethanol (Figure 4.18b), the system is slightly more resilient at high cycling rate (7 and 10 C), but it still loses 96% of its capacity at 10 C. When coming back to 1 C, the obtained electrode seems more stable.

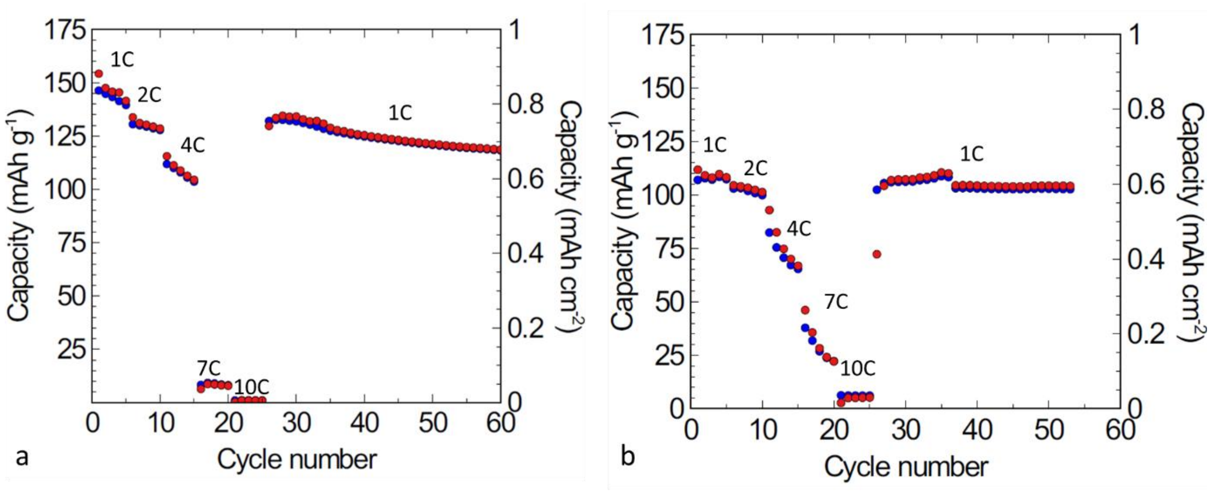

Figure 4.18. (●) Charge and (●) discharge capacity obtained at 1, 2, 4, 7, 10 C (5 cycles each) and at 1 C during 30 additional cycles. Electrodes prepared using a suspension of (a) LCO in water and (b) LCO$_{\mathrm{TiO2}}$ in ethanol. The capacity is represented as a function of the mass of LCO (mAh g^{-1}).

Coating the LCO on the current collector using a suspension in water is an interesting process, because of its ease to prepare the solution to spray. However, the electrode prepared from LCO$_{\mathrm{TiO2}}$ in ethanol shows better performance: even if the battery loses 96% of its capacity at high rate (7 C and 10 C), it shows a good stability over cycling at lower rate (1, 2, 4 C). LCO functionalised with TiO_2 in ethanol will thus be used for the next experiments, where various mass fractions of LLZO were added.

4.3.4.3 Characterisation of LCO$_{\mathrm{TiO2}}$ coatings by cyclic voltammetry

Cyclic voltammograms of LCO$_{\mathrm{TiO2}}$ (1st and 10th cycles) obtained in the range of 3.0 to 4.2 V *vs.* Li$^+$/Li are represented in Figure 4.19a. The 1st cycle shows an oxidation peak at ~4.05 V *vs.* Li$^+$/Li which is shifted at ~3.99 V *vs.* Li$^+$/Li for the 10th cycle. In parallel, the reduction peak at ~3.83 V *vs.* Li$^+$/Li is shifted to ~3.85 V *vs.* Li$^+$/Li. LCO (Figure 4.19b) usually displays a reversible electrochemical potential at 3.93 V *vs.* Li$^+$/Li, which is typical of the hexagonal phase. The shift may be due to a tiny modification of the crystallographic phase by the finctionnalisation of LCO by TiO_2. The diffusion rate of lithium ions and electrons is probably modified by the addition of this amorphous TiO_2 layer on the surface of the LCO, this could also explain the shift observed.

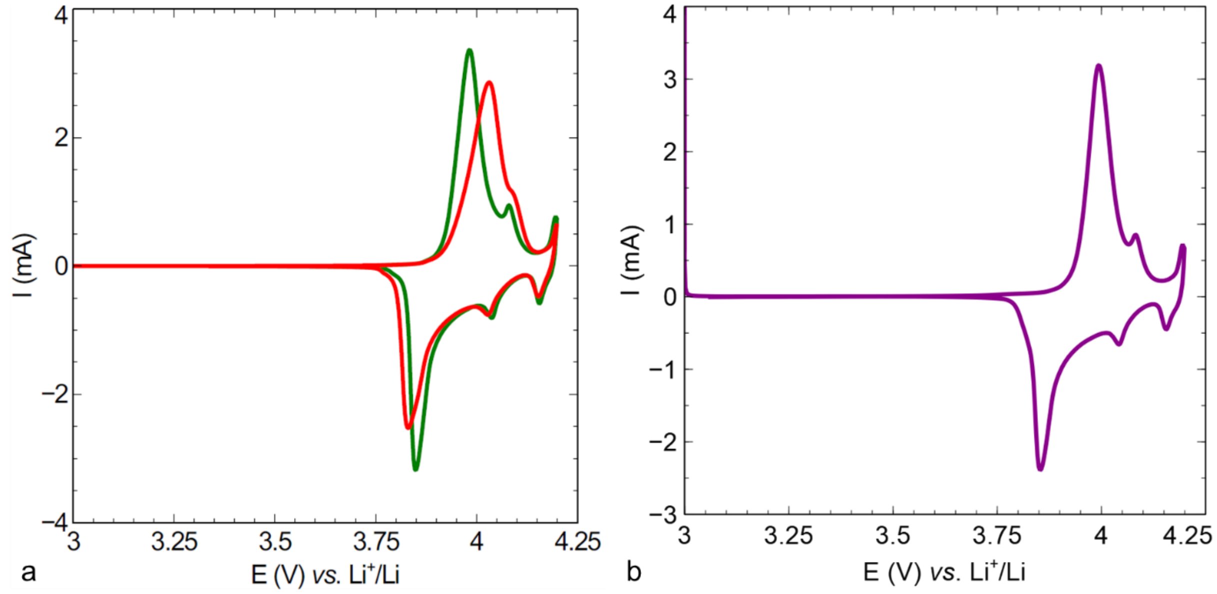

Figure 4.19. Electrochemical characterisation of (a) LCO_{TiO2} (🟥) 1st cycle, (🟩) 10th cycle and (b) LCO non functionnalised by cyclic voltammetry in the voltage range of 3.0 to 4.2 V *vs.* Li^+/Li at scanning rate of 0.1 mV s^{-1}.

4.3.4.4 Characterisation of LCO_{TiO2} + LLZO coatings

Figure 4.20 compares the electrochemical properties of coatings prepared using LCO_{TiO2}, LCO_{TiO2} + LLZO 15% and LCO_{TiO2} + LLZO 30%. Here, the discharge capacity is represented as a function of the number of cycles at rates of 1, 2, 4, 7 and 10 C. All capacities are reported per mass unit of LCO present in the electrode. For the LCO_{TiO2} electrode, when the rate increases to 10 C, the electrode loses all its capacity and recovers at 1 C. When adding 15 wt.% LLZO, the initial capacity of the electrode is slightly lower (115 mAh g^{-1}) than that of the functionalised LCO_{TiO2} alone (130 mAh g^{-1}); the same phenomenon is observed when 30 wt.% of LLZO is added (100 mAh g^{-1}). When 15 wt.% of LLZO is added, the capacity of the battery decreases from 115 mAh g^{-1} to 0 mAh g^{-1} when the cycling rate increases from 1 C to 10 C. When the rate goes back to 1 C, the discharge capacity first varies between 115 mAh g^{-1} and 85 mAh g^{-1} to finally stabilise at 80 mAh g^{-1}. After the stress was applied, the battery that contains 15 wt.% LLZO recovers 70% of its initial capacity, while the battery with LCO_{TiO2} recovers 92%. Interestingly, when 30 wt.% of LLZO is added, the discharge capacity of the battery only decreases to 65% when the cycling rate is increased to 10 C and the system recovers 90% of its initial discharge capacity when going back to 1 C. Adding 30 wt.% of LLZO thus improves the discharge capacity of the battery at high cycling rate.

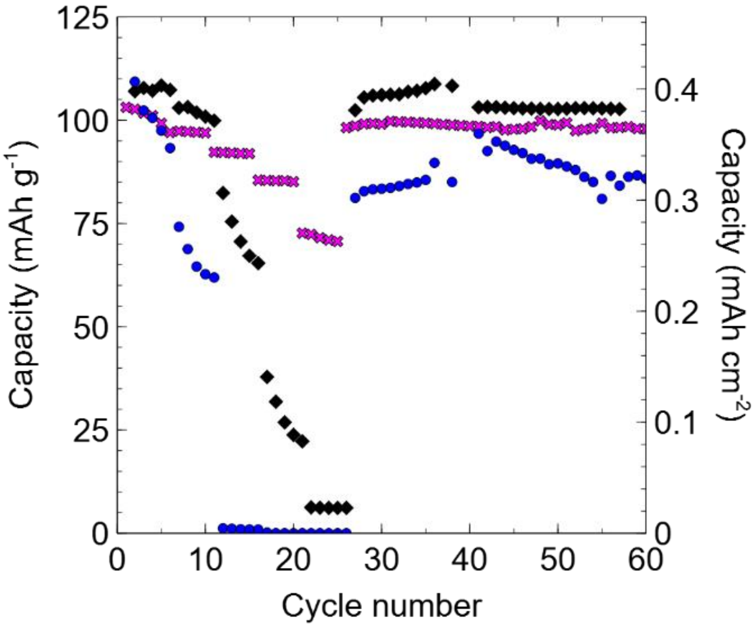

Figure 4.20. Comparison of discharge capacity obtained at rate 1, 2, 4, 7 and 10 C (5 cycles each) and 1C during the last 30 cycles for electrodes without and with LLZO. (◆) LCO_{TiO2}, (●) LCO_{TiO2} + LLZO 15%, (×) LCO_{TiO2} + LLZO 30%. Capacities expressed in mAh g^{-1} are reported per mass unit of LCO present in the electrode.

Figure 4.21 shows the charging and discharging capacity obtained at different cycling rate. Comparing to the discharging curve, which is stable, the charging curve shows high “capacity” after cycling at high rate (7 and 10 C). These values are certainly not related to the disinsertion of Li^+ from the LCO since it is not retrieved during insertion (discharge). The reasons for the discrepancy between charging and discharging could be due to (i) side reactions during charging or (ii) connection issues during the battery assembly, probably leading to small short circuits.

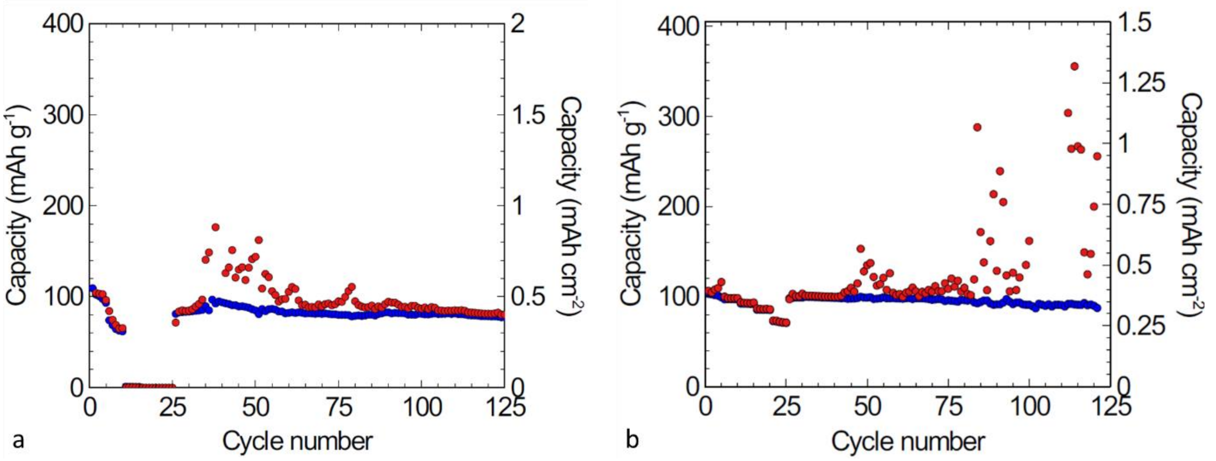

Figure 4.21. (●) Charging and (●) discharging capacity obtained at rate 1, 2, 4, 7 and 10 C (5 cycles each) and 1C during the last 30 cycles. (a) LCO_{TiO2} + LLZO 15%, (b) LCO_{TiO2} + LLZO 30%. Capacities expressed in mAh g^{-1} are reported per mass unit of LCO present in the electrode.

To check for any side reaction during charge and discharge, cyclic voltammetry was performed. Figure 4.22a shows the 1st and 10th voltammetry cycles (CV) of the LCO_{TiO2} + LLZO 30% electrode (sample A) in the voltage range of 3.0 to 4.2 V *vs*. Li^+/Li at a scanning rate of 0.1 mV s^{-1}. For the first cycle, the voltamogram displays oxidation peaks at 3.99, 4.08 and 4.19 V *vs*. Li^+/Li; the corresponding reduction peaks are located at 3.85, 4.03 and 4.15 V *vs*. Li^+/Li. These peaks are characteristic of LCO [6, 27]. For the 10th cycle, the current intensity tends to increase. When the CV is reproduced onto the same sample after GCPL characterisation (Figure 4.22b), the oxidation peaks at 4.15 and 4.19 V are still present and characteristic of LCO. However, the reduction peaks are not clearly discernible. Kim *et al*. [12] suggested that this phenomenon can be explained by the formation of La_2CoO_4 at the LLZO/LCO interface when the composite is calcined. Moreover this curve shape modification may be due to the formation of other oxidised components, such as Li_2CO_3, on the LLZO surface through reaction with remaining water and CO_2 [28, 29]. However, the CV results do not explain the charging issues observed in Figure 4.21. The discrepancy observed between charging and discharging were thus probably due to issues in the battery set-up. These effects, which are quite irregular, are sometimes observed with coin cell assemblies.

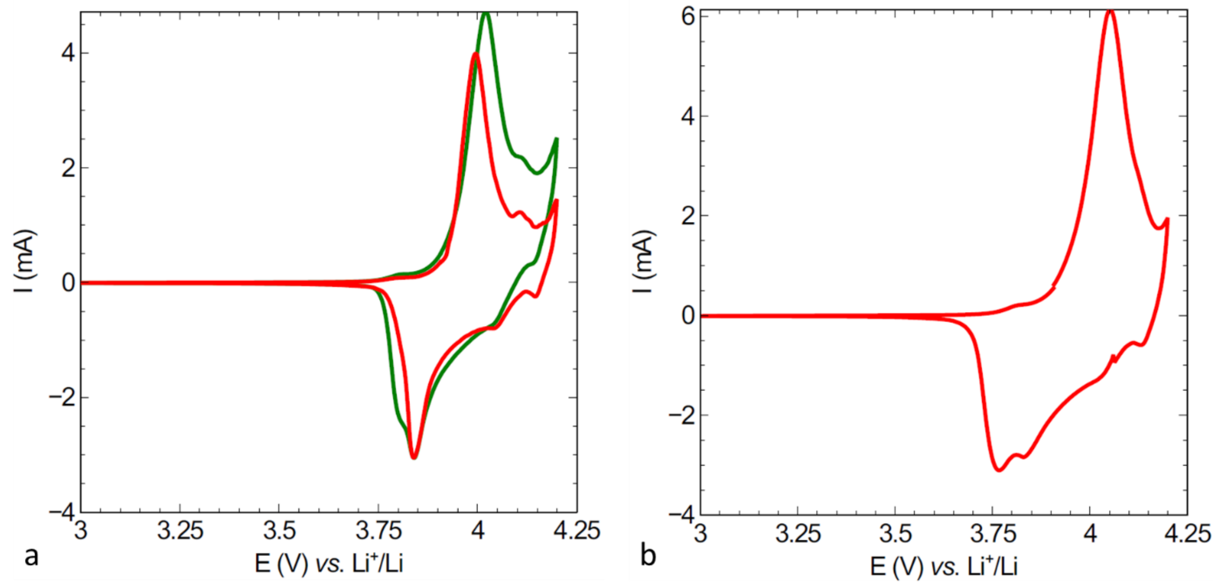

Figure 4.22. Cyclic voltammetry of LCO$_{TiO2}$ + LLZO 30% in the voltage range of 3.0 to 4.2 V *vs.* Li$^+$/Li at scanning rate of 0.1 mV s^{-1}. (a) Sample A, (🟥) 1st cycle and (🟩) 10th cycle; (b) reproduction of CV measurement of sample A after GCPL at different cycling rates.

Sample A was analysed for one cycle of charge/discharge at C/2 (2 h of charging and 2 h of discharging), as presented in Figure 4.23a. The charging curve reaches 4.2 V *vs.* Li$^+$/Li with a capacity of 200 mAh g^{-1}, which is higher than the theoretical capacity of LCO (140 mAh g^{-1}). The discharge of the battery occurs faster than usual, delivering a capacity of ~125 mAh g^{-1} only. In addition, the voltage is not stable. Two other samples, B and C, still prepared using LCO$_{TiO2}$ + LLZO 30%, were analysed for reproducibility; Figure 4.23b and Figure 4.23c show the 1st cycle results for these two additional samples. Sample B (Figure 4.23b) was not able to reach 4.2 V *vs.* Li$^+$/Li during charging, and displays a capacity of ~115 mAh g^{-1}, which is lower than the theoretical value [6]. Sample C charge and discharge curves (Figure 4.23c) are characteristic of Li metal battery. Moreover, the LCO$_{TiO2}$ shows a capacity of ~138 mAh g^{-1} which is really close to the theoretical value. The difference between samples is much probably due to connection issues during the battery assembly, which led to short circuits for sample A. Differences between samples B and C can partly be explained by a slight difference of the mass of material deposited (Table 4.2). All these results show that the building of a battery using these components is not straightforward and can lead to reproducibility issues due to assembly.

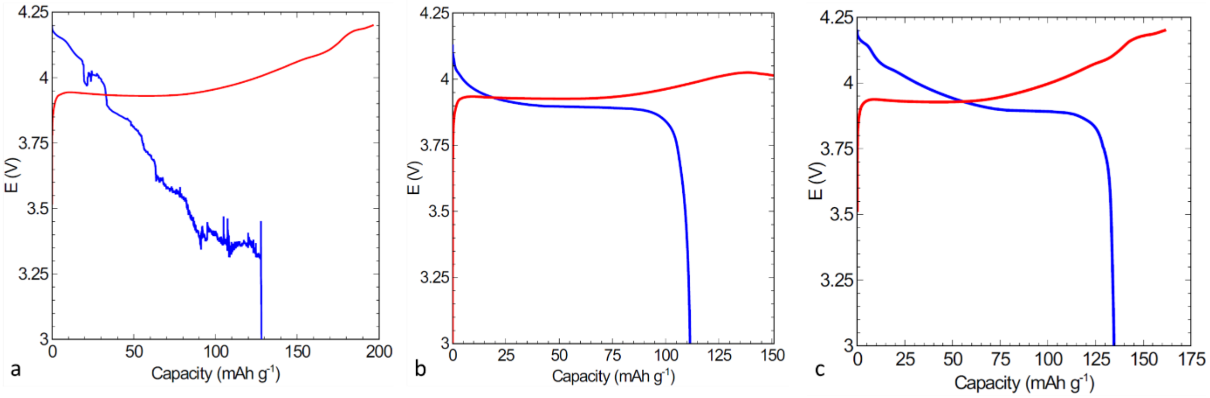

Figure 4.23. Analysis of three LCO_{TiO2} + LLZO 30% coatings by cycling at C/2 (1st cycle): (🟥) charge and (🟦) discharge curves. (a) Sample A, (b) sample B and (c) sample C. All capacities are reported per mass unit of LCO present in the electrode.

Table 4.2. Mass of LCO_{TiO2} + LLZO 30%.

	Sample A	**Sample B**	**Sample C**
LCO_{TiO2}+LLZO 30% (mg)	14.2	15.6	16.7

In order to check the stability of samples B and C, the galvanostatic cycling with potential limit (GCPL) technique was used. Here, the experiment was performed between 3.0 and 4.2 V *vs.* Li^+/Li at 1 C rate for 100 cycles. Figure 4.24a and Figure 4.24b show the graphs obtained with samples B and C, respectively. Sample B shows tiny capacity variation between 90 mAh g^{-1} and ~100 mAh g^{-1} the first 30 cycles. From the 30th to the 70th cycle, the capacity increases up to 125 mAh g^{-1}, to finally decrease down to 100 mAh g^{-1} from the 70th cycle to the end. Sample C shows an important variation between 125 mAh.g^{-1} and 110 mAh g^{-1} during the first 30 cycles. From the 30th cycle to the end, the capacity is decreasing until it reaches ~95 mAh g^{-1}.

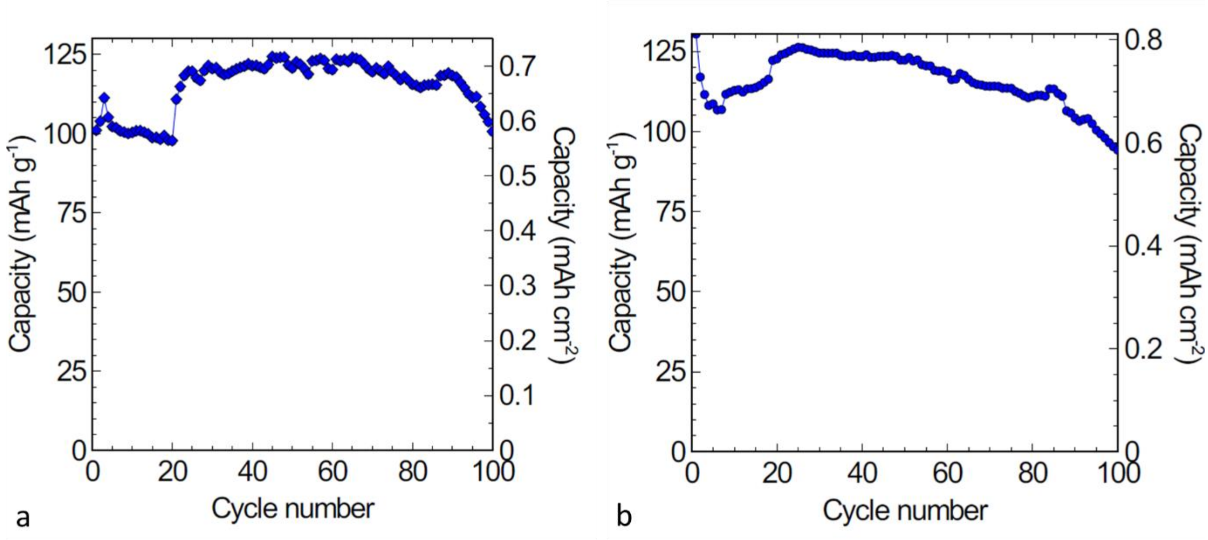

Figure 4.24. Discharge GCPL curves of LCO_{TiO2}+ LLZO 30% electrodes for cycling at 1C between 3.0 and 4.2 V *vs.* Li^+/Li. (a) Sample B; (b) sample C. Capacities expressed in mAh g^{-1} are reported per mass unit of LCO present in the electrode.

The above results show that the electrochemical performances of the LCO_{TiO2}/LLZO cathode material are scattered, probably due to assembly issues. Nevertheless, the characterisation by galvanostatic cycling with potential limit performed at different charge and discharge rates (1 C being the lowest rate and 10 C the highest) showed that adding 30 wt.% LLZO allows to better handle the stress than in the case of a classical LCO_{TiO2} electrode. In some samples, the cycling performance was however low but, in good measurement conditions, the addition of LLZO does not change the electrochemical properties of the LCO_{TiO2} system, as a capacity of ~138 mAh g^{-1} is observed for electrodes with and without LLZO (Figure 4.23c).

4.4 Conclusion

The main objective of this chapter was to improve the performances of LCO electrodes previously developed by a senior researcher of the NCE laboratory, so that the LCO electrode can eventually be used in an all-solid system in combination with a solid or GPE type electrolyte. To do so, the strategy used here was to fill the porosity of the LCO layers (typically 50-60% of the coating volume), with a nanostructured material with good ionic conductivity: LLZO. The goal of the LLZO introduction, was to improve the ionic conductivity of the electrode without changing its electrochemical properties.

For this purpose, garnet-type low-temperature cubic LLZO was synthesised by sol-gel process. Even if XRD analysis showed trace amounts of $La_2Zr_2O_7$, the expected crystalline phase was formed and matched with typical cubic garnet (JCPDS 45-109). The LLZO powder obtained from the sol-gel process displayed 350-400 nm particles made of 20-30 nm cubic crystallites.

Different amounts of cubic LLZO (15, 30, 45, 60 wt.%) were introduced into a suspension of LCO (functionalised with TiO_2 – *i.e.* LCO_{TiO2}) in ethanol. Among these suspensions, only those containing 15 and 30 wt.% were selected because they were stable during spray coating. The open porosity of the LCO_{TiO2} + LLZO 15% and LCO_{TiO2} + LLZO 30% coatings were characterised using Archimedes' method. The open porosity was decreased down to 40% when 30 wt.% of LLZO was added. The LCO_{TiO2} + LLZO 30% coating were characterised using environmental scanning electronic microscopy (ESEM). ESEM showed smooth surface and was coupled with EDX analysis to demonstrate that the LLZO particles seems to be evenly distributed.

Electrochemical characterisation proved hard to reproduce, probably due to battery assembly issues. In some cases, this resulted in very high charging capacities, maybe due to short-circuits, and to scattered results. This shows that the battery assembly is not straightforward and has to be done with caution. However, despite these issues, the electrochemical characterisations have shown that the addition of 30 wt.% of LLZO did not alter the electrochemical properties of LCO, and allowed the cathode system to handle better the stress applied by rapid charge and discharge cycles. LCO + LLZO 30% made it possible to obtain a capacity close to classical Li-ion battery with good cycling stability after 100 cycles. The final goal being to reach a fully solid system, the LCO + LLZO 30% coating will thus be combined with a gel polymer electrolyte developed by a senior researcher of the laboratory. This study is the subject of Chapter 5.

References

1. D. Deng, Li-ion batteries: basics, progress, and challenges. *Energy Sci. Eng.* **3**, 385–418 (2015).
2. K. Mizushima, P. C. Jones, P. J. Wiseman, J. B. Goodenough, Li_xCoO_2 (0 < x ~< 1): A new cathode material for batteries of high energy density. *Solid State Ionics* **3**, 171–174 (1981).

3. J. Graetz, R. Yazami, C. C. Ahn, P. Rez, B. Fultz, in *New trends in intercalation compounds for energy storage*, C. Julien, J. P. Pereira-Ramos, A. Momchilov, Eds. (Springer Science, Dordrecht, 2002), p. 469.

4. A. Du Pasquier, I. Plitz, S. Menocal, G. Amatucci, A comparative study of Li-ion battery, supercapacitor and nonaqueous asymmetric hybrid devices for automotive applications. *J. Power Sources* **115**, 171–178 (2003).

5. N. Nitta, F. Wu, J. T. Lee, G. Yushin, Li-ion battery materials: Present and future. *Mater. Today* **18**, 252–264 (2015).

6. C. A. Páez Martínez, C. Exantus, D. Dallel, C. Alié, C. Calberg, D. Liquet, D. Eskenazi, F. Deschamps, N. Job, B. Heinrichs, Water-based paintable $LiCoO_2$ microelectrodes: a high-rate Li-ion battery free of conductive and binder additives. *Adv. Mater. Technol.* **4**, 1–12 (2019).

7. C. A. Paez, D. Liquet, C. Calberg, B. Heinrichs, C. Alié, Method for the wet deposition of thin films, WO 2016/097396 A1 (2016), pp. 1–4.

8. T. Takahashi, J. Irvine, A. West, in *High conductivity solid ionic conductors*, Takehiko Takahashi (Nagoya), Ed. (World scientific, Aberdeen, 1989), pp. 201–222.

9. V. Thangadurai, W. Weppner, Effect of sintering on the ionic conductivity of garnet-related structure $Li_5La_3Nb_2O_{12}$ and In- and K-doped $Li_5La_3Nb_2O_{12}$. *J. Solid State Chem.* **179**, 974–984 (2006).

10. R. Murugan, V. Thangadurai, W. Weppner, Fast lithium ion conduction in garnet-type $Li_7La_3Zr_2O_{12}$. *Angew. Chemie - Int. Ed.* **46**, 7778–7781 (2007).

11. R. Murugan, V. Thangadurai, W. Weppner, Lithium ion conductivity of Li_{5+x} $Ba_xLa_{3-x}Ta_2O_{12}$ (x∈=∈0-2) with garnet-related structure in dependence of the barium content. *Ionics* **13**, 195–203 (2007).

12. K. H. Kim, Y. Iriyama, K. Yamamoto, S. Kumazaki, T. Asaka, K. Tanabe, C. A. J. Fisher, T. Hirayama, R. Murugan, Z. Ogumi, Characterization of the interface between $LiCoO_2$ and $Li_7La_3Zr_2O_{12}$ in an all-solid-state rechargeable lithium battery. *J. Power Sources* **196**, 764–767 (2011).

13. T. Dixit, A. Bilgaiyan, I. A. Palani, D. Nakamura, T. Okada, V. Singh, Influence of potassium permanganate on the anisotropic growth and enhanced UV emission of ZnO nanostructures using hydrothermal process for optoelectronic applications. *J. Sol-Gel Sci. Technol.* **75**, 693–702 (2015).

14. R. Kanno, M. Murayama, Lithium ionic conductor Thio-LISICON: The Li_2S-GeS_2-P_2S_5. *J. Electrochem. Soc.* **148**, A742–A746 (2001).

15. A. Hayashi, S. Hama, T. Minami, M. Tatsumisago, Formation of superionic crystals from mechanically milled Li_2S-P_2S_5 glasses. *Electrochem. Commun.* **5**, 111–114 (2003).

16. E. Edri, H. Cohen, G. Hodes, Band alignment in partial and complete ZnO/ZnS/CdS/CuSCN extremely thin absorber cells: An X-ray photoelectron spectroscopy study. *ACS Appl. Mater. Interfaces* **5**, 5156–5164 (2013).

17. T. Yang, Z. D. Gordon, Y. Li, C. K. Chan, Nanostructured Garnet-Type Solid Electrolytes for Lithium Batteries: Electrospinning Synthesis of $Li_7La_3Zr_2O_{12}$

Nanowires and Particle Size-Dependent Phase Transformation. *J. Phys. Chem. C*. **119**, 14947–14953 (2015).

18. M. P. Pechini, Pechini method patent, US3330697 (1967), pp. 1–6.

19. N. Janani, S. Ramakumar, L. Dhivya, C. Deviannapoorani, K. Saranya, R. Murugan, Synthesis of cubic $Li_7La_3Zr_2O_{12}$ by modified sol-gel process. *Ionics* **17**, 575–580 (2011).

20. H. Geng, K. Chen, D. Yi, A. Mei, M. Huang, Y. Lin, C. Nan, Formation mechanism of garnet-like $Li_7La_3Zr_2O_{12}$ powder prepared by solid state reaction. *Rare Metal Mater. Eng.* **45**, 612–616 (2016).

21. A. B. Spierings, M. Schneider, R. Eggenberger, Comparison of density measurement techniques for additive manufactured metallic parts. *Rapid Prototyping J.* **17**, 380–386 (2011).

22. I. Kokal, M. Somer, P. H. L. Notten, H. T. Hintzen, Sol-gel synthesis and lithium ion conductivity of $Li_7La_3Zr_2O_{12}$ with garnet-related type structure. *Solid State Ionics* **185**, 42–46 (2011).

23. V. Thangadurai, W. Weppner, $Li_6ALa_2Ta_2O_{12}$ (A=Sr, Ba): Novel garnet-like oxides for fast lithium ion conduction. *Adv. Funct. Mater.* **15**, 107–112 (2005).

24. J. Sakamoto, E. Rangasamy, H. Kim, Y. Kim, J. Wolfenstine, Synthesis of nano-scale fast ion conducting cubic $Li_7La_3Zr_2O_{12}$. *Nanotechnology*. **24**, 1–8 (2013).

25. B. D. Cullity, S. R. Stock, *Elements of X-ray diffraction (Third Edition)* (Prentice-Hall, New York, 2001).

26. A. S. Edelstein, in *Encyclopedia of materials: science and technology (Second Edition),* K. H. J. Buschow, R. W. Cahn, M. C. Flemings, B. Ilschner, E. J. Kramer, S. Mahajan, P. Veyssière, Eds. (Elsevier Ltd, 2001), pp. 5916–5927.

27. B. Garcia, J. Farcy, J. P. Pereira-Ramos, N. Baffier, Electrochemical properties of low temperature crystallized $LiCoO_2$. *J. Electrochem. Soc.* **144**, 1179–1184 (1997).

28. Y. Ren, T. Liu, Y. Shen, Y. Lin, C. W. Nan, Chemical compatibility between garnet-like solid state electrolyte $Li_{6.75}La_3Zr_{1.75}Ta_{0.25}O_{12}$ and major commercial lithium battery cathode materials. *J. Materiomics* **2**, 256–264 (2016).

29. H. Duan, H. Zheng, Y. Zhou, B. Xu, H. Liu, Stability of garnet-type Li ion conductors: An overview. *Solid State Ionics* **318**, 45–53 (2018).

Chapter 5. Combination of the optimised LCO_{TiO2}/LLZO cathode material with GPE electrolyte

5.1. Introduction

Traditional lithium batteries suffer from safety issues because of the use of highly flammable organic liquid electrolyte. Those electrolytes have low thermal stability and low flame point so that it is easy to cause fire accident and explosion in case of leakage [1, 2]. Within this framework, the EnSO project aims at the development of fully solid Li-metal microbatteries, using solid electrolyte or gel polymer electrolyte (GPE). To do so, a process was previously developed at the Nanomaterial Catalysis Electrochemistry (NCE) laboratory of the University of Liège for the deposition of thin film layers of lithium cobalt oxyde (LCO) for microbatteries. This process consists in the deposition of LCO functionnalised with titanium dioxyde (TiO_2), as it provides better stability of the LCO under high cycling conditions. When the LCO positive electrode was deposited using spray-coating, an open porosity of 50-60% was noticed. The presence of porosity limits the contact between particles and thus the flow of lithium ions in the layer. This open porosity is not a problem as long as liquid electrolyte is used, since it usually fills the voids between particles. However, ionic conduction is not that easy in the case a solid electrolyte or GPE is used since one cannot guarantee that its deposition on top of the electrode will lead to good contact between the LCO particles and the electrolyte, leading to a decrease of the electrochemical performances of the battery. A good alternative would be to insert a solid electrolyte within the porosity of the electrode upon electrode manufacturing.

The previous chapter was dealing with the improvement of the positive electrode material developed in the NCE laboratory, *i.e.* lithium cobalt oxide functionnalised with titanium dioxide (LCO_{TiO2}), in order to build a solid state battery. To do so, a solid state electrolyte, lanthanum-lithium-zirconate oxide ($Li_7La_3Zr_2O_{12}$, LLZO), was added to the positive electrode material (30 wt.%). The obtained electrode was characerised in Li-metal battery configuration using a conventional liquid electrolyte. The results have shown interesting properties of the battery when LLZO was added such as cycling at high rate (10 C) while keeping a significant fraction of the LCO original capacity.

The next and last step of the research was to replace the liquid electrolyte by a solid or semi-solid electrolyte. Indeed, the main objective of the EnSO project aims to develop a shapeable and flexible Li-metal microbattery free from leakage issues as presented in Figure 5.1. In the framework of the present study, the introduction of a gel polymer electrolyte, *i.e.* a polymer filled with a liquide electrolyte, was selected.

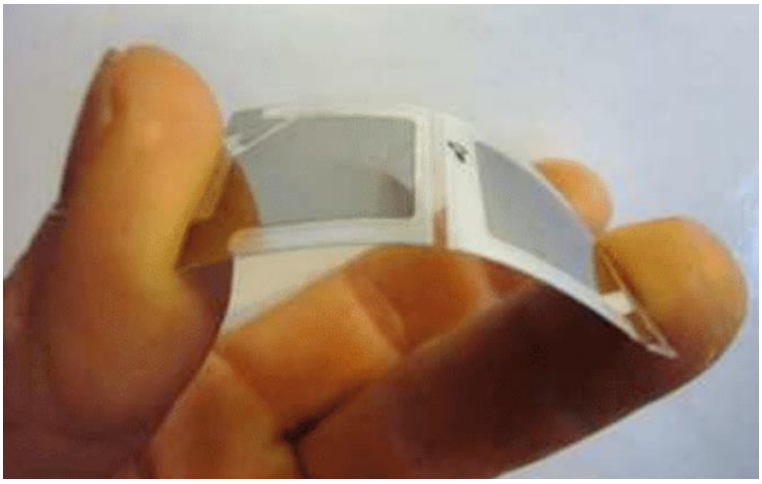

Figure 5.1. EnSO state-of-the-art microbattery on glass substrate.

Various polymer hosts such as polyvinylidene fluoride (PVdF) [3] in conjunction with lithium hexafluorophosphate ($LiPF_6$) as liquid electrolyte have been found to form GPEs with ionic conductivities ranging between 10^{-4} and 10^{-3} S cm^{-1} at 20 °C [4–6]. These values are however low compared to liquid electrolytes (typically, 10^{-1}-10^{-2} S cm^{-1}). The addition of a copolymer such as hexafluoropropylene (HFP) to PVdF have improved the gel properties. Indeed, PVdF-HFP in the gel showed greater solubility for organic solvents and lower crystallinity [4, 7]. Moreover, the addition of ceramic materials such as zeolites ($Na_{12}[Al_{12}Si_{12}O_{48}]$) and alumina ($Al_2O_3$) to gel polymer systems have shown an increase of stability at the lithium metal interface [4, 8]. GPE, a polymer matrix in which the lithium ion conducting organic solution remained trapped, was first demonstrated to be an efficient electrolyte by Feuillade and Perche [3]. Such materials have shown ionic conductivities close to that of the liquid electrolyte (10^{-1}-10^{-2} S cm^{-1}). During the EnSO projet a senior researcher has optimised the GPE system using phyllosilicate clay to increase the stability at the lithium metal interface [10].

The objective in the present chapter was to study the performances of the positive electrode LCO_{TiO2}+LLZO 30 wt.% developped in Chapter 4, with the GPE system reinforced by the senior researcher. The positive electrode was assembled into a coin cell with a Li-metal foil as negative electrode and the optimised GPE as electrolyte and separator. The complete set-up was characterised by cyclic voltammetry (CV), galvanostatic cyclic with potential limitation

(GCPL). The results shows that the positive electrode LCO coating was improved using 30 wt.% LLZO, and was suitable for solid-state microbattery.

5.2. Experimental

5.2.1. Preparation of LCO_{TiO2} and LLZO suspension

As mentioned in Chapter 4 (sections 4.2.2.2 and 4.2.3.3), the LCO_{TiO2} suspension in ethanol was prepared using a commercial grade LCO. The powder was ground per 6.0 g in a stainless steel jar with 100 g of stainless steel beads (3 mm diameter) using a Fritsch pulverisette 6 planetary mill. The grinding was performed for 20 cycles at 450 rpm for 5 min and 5 min pause by cycle. After grinding, the sample was calcined at 700 °C at a rate of 10 °C min^{-1} under flowing air (0.1 mmol s^{-1}) and the temperature was maintained for 2.5 h.

The LCO powder was then functionalised with titanium dioxide (TiO_2, ~1.5 wt.%) using a process developed and patented by a senior researcher of the laboratory [9]. To do so, two solutions were prepared at room temperature. The first solution (S1), was obtained by mixing 38 mL of titanium (IV) isopropoxide (Sigma Aldrich, 97%) and 206 mL of 2-methoxyethanol (Sigma Aldrich, 99.9%) for 1 h. The second solution (S2) was prepared by adding 5.2 mL of deionised water to 206 mL of 2-methoxyethanol; the solution was mixed for 1 h as well. Under high stirring (450 rpm), 6 g of the ground LCO powder was dispersed in methoxyethanol at 60 °C. When the temperature was stable, 1.55 mL of the S1 was added to the suspension. After 3 h of stirring, 1.55 mL of S2 was added to the previous mix and stirred at 60 °C for 16 h in a closed vial. The solvent was then evaporated using rotary evaporator and the resulting LCO functionalised with TiO_2 (LCO_{TiO2}) was further dried at 150 °C at 2000 Pa for 16 h.

5.2.2. Electrode preparation

The chosen current collectors were stainless steel (SS) 304 discs (1.88 cm² area and 0.5 mm thick).

5.2.2.1. LLZO

As presented in Chapter 4 (section 4.2.3.1), pure LLZO powder was sprayed onto stainless steel discs in order to test its stability. To do so, a 10 g L^{-1} solution was sprayed onto the stainless steel discs heated at 40 °C using a Fuso Seiki Lumina STS-10 spray gun mounted on a robotised arm. A circulation pump was used in order to avoid at best the powder precipitation in the spray gun. The discs were weighted before and after deposition to ensure a homogeneous deposition of the LLZO.

5.2.2.2. LCO with LLZO

The positive electrode was prepared by spraying a suspension of LCO_{TiO2} onto a current collector. The suspension was prepared by adding 20 g of the above-obtained LCO_{TiO2} to 1 L of ethanol. The mix was first stirred at 450 rpm for 1 h and left in an ultrasonicated bath for 16 h. The solid excess was then separated from the suspension after 3 h of decanting. The concentration of the resulting suspension was determined by taking 3 mL from the LCO_{TiO2} suspension; these 3 mL were placed in a vial and dried at 120 °C for 1 h. The solid mass was then determined by weighting. This operation was repeated three times for reproducibility. The mass concentration of the suspension was ~10 g L^{-1}.

To spray 10 mg of cathode material (LCO_{TiO2}) on the SS disc, 500 mL of the LCO_{TiO2} suspension were needed. To the LCO_{TiO2} suspension, LLZO powder was added so that the LLZO mass fraction (on dry basis) was 30 wt.%. The suspension was stirred vigorously for 5 h.

Before spraying, the stainless steel discs were weighted and fixed onto a larger support so that they did not move during the spray process. The suspension under stirring was then sprayed at room temperature onto stainless steel discs in order to obtain 10 mg of active material (LCO_{TiO2}) per disc. The deposition resulted in positive electrode material; 12 samples were prepared from the mixed LCO_{TiO2} and LLZO suspension.

After spraying, the electrodes were heated at 350 °C at 10 °C min^{-1} rate under air and the temperature was maintained for 1 h. Samples were then left to cool to room temperature.

5.2.3. Synthesis and deposition of gel polymer electrolyte

The synthesis and deposition of the GPE presented here was performed by a senior researcher of the project. The results of this work have been submitted for publication [10]. The GPE was made of a PVDF-HFP as a polymer, a clay to strengthen the GPE structure, and lithium ions contained in the liquid electrolyte which impregnates the polymer.

First, the selected clay, *i.e.* montmorillonite (Na^+-MMt, Cloisite BYK-Southern Clay products Inc.), was modified by a lithiation process in order to increase its ionic conductivity [11, 12]. The ion-exchanged Li-MMT clays were prepared by cation exchange between the sodium cations of the montmorillonite clay platelets and lithium cations. 30 g of Na-MMT were dispersed in 3 L of distilled water with 60 g of lithium nitrate ($LiNO_3$, Honeywell, > 98%). The solution was stirred for two days at 50 °C in order to exchange the cations and then centrifuged to separate the Li-MMT clay from the supernatant containing the excess ions. To purify the clay, Li-MMt was re-dispersed in distilled water (3 L) and centrifuged once again. The modified clay was then dried under vacuum at 80 °C during one night [13, 14].

Second, lithium bis(fluorosulfonyl)imide (LiFSI, Suzhou Fluolyte Co, > 99%) was dissolved in N-propyl-N-methylpyrrolidinium bis(fluorosulfonyl)imide (PYR13FSI, Solvionic, 99%) with a molar ration of 1.1:1 and homogenised under high stirring for 1 h. Then, the polymer matrix, made of 1.2 g of poly(vinylidene) fluoride-hexafluoropropylene (PVDF-HFP SOLEF 21216, supplied by Solvay) and 1.68 g clay were mixed with 4.8 mL of electrolyte mixture (LiFSI + PYR13FSI) in 90 mL of acetone (VWR, NORMAPUR, > 99.8%).

The GPE was deposited by spray (using a Nordson EFD-781S nozzle mounted on a homemade robot) directly onto LCO_{TiO2} and LCO_{TiO2}/LLZO positive electrode heated at 80 °C. The GPE was deposited by alternating spray deposition and drying steps (20 s). These steps were repeated until a deposited mass of about 40 mg cm^{-2} was achieved, which corresponds to about 80 to 100 deposition steps. At the end of the process, the coatings with GPE were dried under vacuum at 45 °C overnight. The obtained membrane thickness was comprised between 250 and 300 µm.

5.2.4. Characterisation set-up

The electrodes covered by GPE coatings were then introduced into a coin cell for electrochemical characterisation. The coin cells (CR2032) were placed in a glove box filled with argon (MBraun 200B). In order to check for the compatibility with the GPE, LLZO alone was also characterised in the same system.

5.2.4.1. LLZO characterisation set-up

An LLZO coating was included into a coin cell as mentioned in Chapter 4 (section 4.2.4.1). The stability of the LLZO was checked using cyclic voltammetry (CV multichannel Bio-

Logic VMP3) in the range of 3.0-4.2 V *vs.* Li^+/Li at 0.1 mV s^{-1} rate (10 cycles) at room temperature. The CV measurements were performed in the same electrochemical window as in the case of a classical Li metal battery. All measurements were done outside the glovebox.

5.2.4.2. LCO_{TiO2} + LLZO characterisation set-up

The LCO_{TiO2} + 30 wt.% LLZO with the GPE coated on top was at the positive side and lithium foil was at the negative side; no separators were added since the GPE is assumed to play that role. A spacer and a spring were added to spread the pressure. Finally, the positive case was added and the coin cell was closed using a hydraulic crimper (MSK 110, MTI). All measurements were done outside the glovebox.

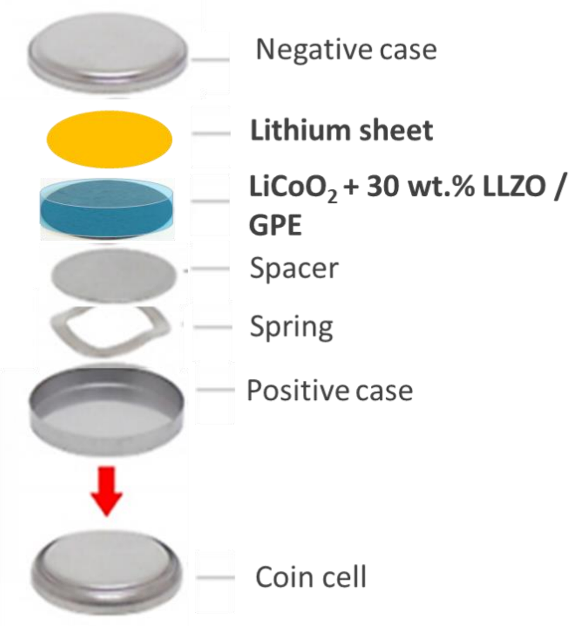

Figure 5.2. Characterisation set-up of LCO_{TiO2} + 30 wt.% LLZO using GPE.

5.2.5. Electrochemical characterisation

The electrochemical characterisations were performed at room temperature, outside the glovebox. Cyclic voltammetry (CV) of LCO_{TiO2} + 30 wt.% LLZO with GPE were conducted for 10 cycles using a multichannel Bio-Logic VMP3 potentiostat. The CVs were measured at 0.1 mV s^{-1} scan rate between 3.0 and 4.2 V *vs* Li^+/Li.

The coin cells were characterised using galvanostatic cycling with potential limitation (GCPL) between 3.0 and 4.2 V *vs.* Li^+/Li at 1 C rates for 100 cycles (GCPL on multichannel Bio-Logic VMP3). 1 C corresponds to 1 h of charge and 1 h of discharge. GCPL is a common technique used to define the capacity of the battery and to check its stability as a function of the number of charge and discharge cycles. Due to temperature variation, the GCPL characterisation was then reproduced into a climate chamber with a temperature fixed at 25 °C.

5.3. Results and discussion

In Chapter 4, the open porosity of the obtained electrodes, with and without LLZO, was measured using the Archimedes' method. The open porosity of pure LCO_{TiO2} coating was about 55%. In the case of the composite containing 30 wt.% of LLZO, the open porosity was decreased down to 40%. Moreover, the electrochemical performances of the mixed cathode material containing 30 wt.% of LLZO allowed the battery system tested with liquid electrolyte to better handle high rate cycling charge and discharge (7C and 10C). This previous result (section 4.3.4.4) encouraged us to characterise the mixed cathode material with GPE. GPE was sprayed directly onto the positive electrode material (LCO_{TiO2} containing 30 wt.% LLZO) and directly included into a coin cell for characterisation as quasi solid-state battery. All capacities are reported per mass unit of LCO present in the electrode. The battery was analysed for one cycle of charge/discharge at C/2 rate between 4.2 and 3.0 V *vs*. Li^+/Li as presented in Figure 5.3a. The charging curve reaches 4.2 V *vs*. Li^+/Li with a capacity of 60 mAh g^{-1}, which is lower than the theoretical capacity of LCO (140 mAh g^{-1}) using liquid electrolyte ($LiPF_6$). The discharging curve reaches 3 V showing a capacity of 80 mAh g^{-1}. The battery was also characterised using cyclic voltammetry (CV) (Figure 5.3b) and galvanostatic cycling with potential limitation (GCPL) (Figure 5.3).

During CV, the potential range of the battery is varied at a specific rate, in order to detect the current of the electrochemical reaction (oxidation/reduction) of the cathode material. Figure 5.3b shows the cyclic voltamogram of the quasi solid state battery measured at 0.1 mV s^{-1} between 3.0 and 4.2 V *vs*. Li^+/Li for 10 cycles. The large oxidation peak from ~3.90 to 4.20 V *vs*. Li^+/Li corresponds to the transition from monoclinic to hexagonal crystalline phase of LCO [15]. This transition phase can be associated to the de-intercalation of lithium from LCO. The maximum current achieved in the first cycle decreases in the following cycles and seems to stabilise starting from the fifth cycle. In the first cycle, three reduction peaks (at 4.05, 3.85 and 3.60 V *vs*. Li^+/Li) can be distinguished. The first two reduction peaks are related to Li^+ insertion into LCO, confirming reversible cycling. The attribution of the third peak is unknown and might be due to side reactions. The oxidation peak at 4.05 V *vs*. Li^+/Li is shifted between the 5th and 10th cycle to an approximately 0.2 V higher potential. The same behaviour is observed for the reduction peaks that are shifted to an approximately 0.01 V higher potential.

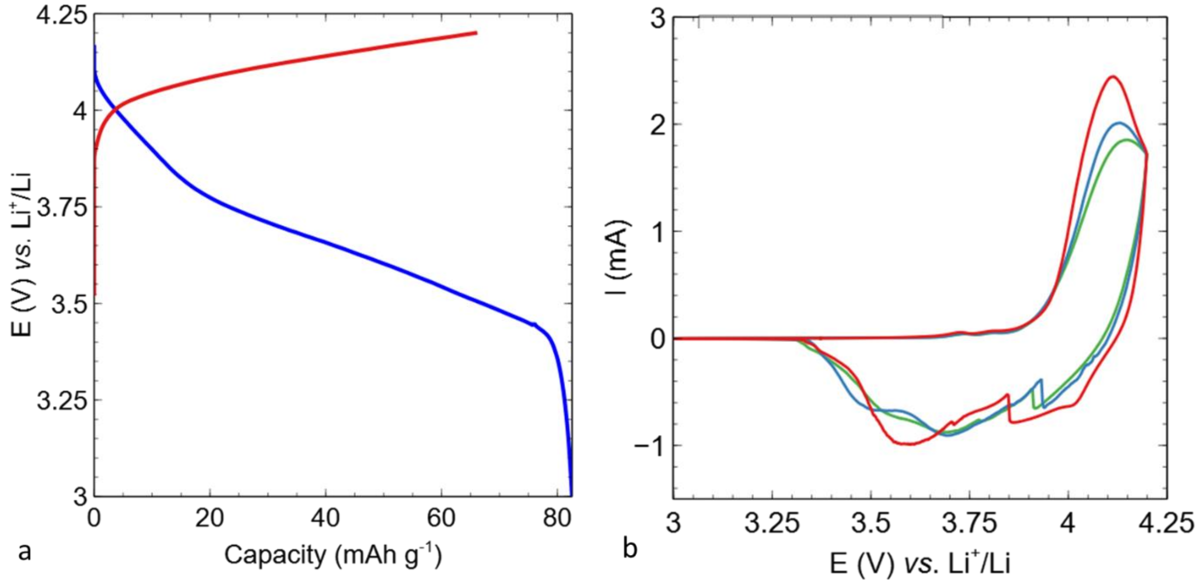

Figure 5.3. Characterisation of Li/GPE/LCO_{TiO2}+LLZO cell. (a) First cycle of (▬) disinsertion and (▬) insertion of Li^+. (b) CV measurements at 0.1 mV s^{-1} between 3.0 and 4.2 V *vs*. Li^+/Li; (▬) 1st cycle, (▬) 5th cycle and (▬) 10th cycle All capacities are reported per mass unit of LCO present in the electrode.

Figure 5.4a and b respectively show the galvanostatic cycling with potential limitation (GCPL) of batteries using LCO_{TiO2} and LCO_{TiO2} + 30 wt.% LLZO as positive electrode material, performed at C-rate between 3.0 and 4.2 V *vs*. Li^+/Li. 100 cycles were performed at room temperature. When LCO_{TiO2} is used with the GPE, the battery loses 90% of its capacity, as shown in Figure 5.4a and last for only 10 cycles. The addition of LLZO drastically improves the performances of the battery. The charging and discharging curves oscillate between 60 mAh g^{-1} and 80 mAh g^{-1} for 100 cycles. Those oscillations can be due to the temperature variation of the room, which is the reason why the experiment was reproduced in a climate chamber at 25 °C, as presented in Figure 5.5.

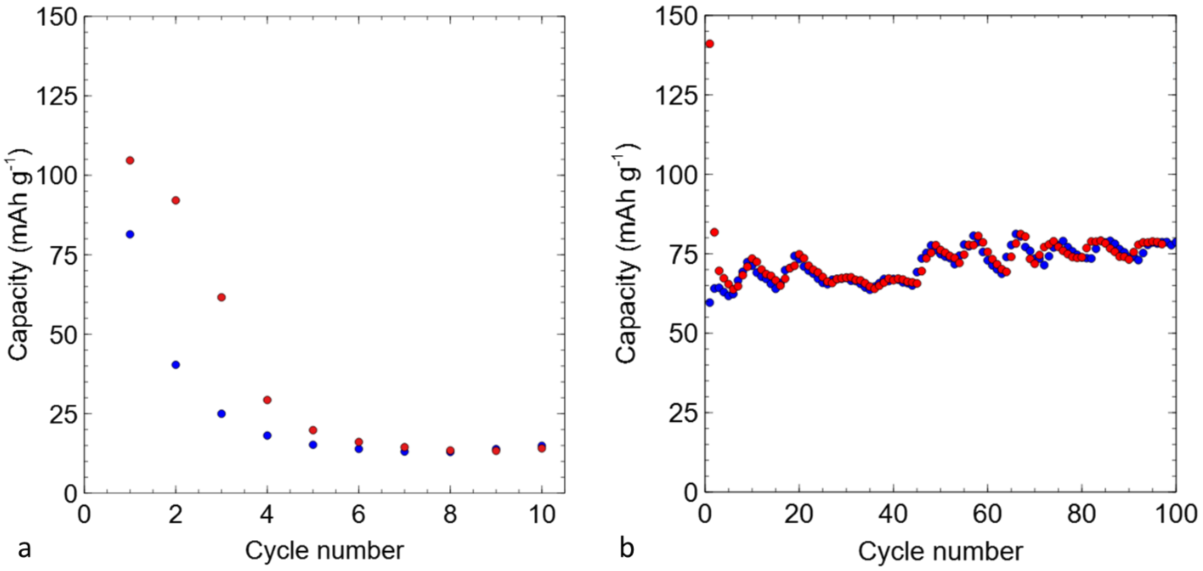

Figure 5.4. GCPL characterisation at 1C between 3.0 and 4.2 V *vs.* Li$^+$/Li at room temperature showing (●) charging and (●) discharging curve. (a) LCO_{TiO2} with GPE as electrolyte; (b) LCO_{TiO2}+ LLZO (30 wt.% LLZO) with GPE as electrolyte. All capacities are reported per mass unit of LCO present in the electrode.

Figure 5.5a presents the galvanostatic cycling of the mixed cathode material (LCO_{TiO2}+ 30 wt.% LLZO) characterised with the GPE in the climate chamber (temperature fixed at 25 °C). Figure 5.5b shows the comparison of that result with those obtained for the mixed cathode material (LCO_{TiO2}+ 30 wt.% LLZO) using liquid electrolyte (results extracted from Chapter 4, section 4.3.4.4.). The initial capacity of the battery with GPE is about 135 mAh g^{-1} and is rather constant over cycling (*i.e.* comprised between 130 and 150 mAh g^{-1} without obvious degradation). However, the charging capacity shows high current leakage over cycles probably due to short-circuits. These short-circuits are probably related to connection issues during the battery assembly as presented in the last chapter, or to internal short-circuits due to the use of GPE as separator. Further experimental improvements should be done to get rid of any contact problems. The results show however that the battery works better when LLZO is added to the LCO_{TiO2} coatings, and that GPE can be used as an electrolyte, as an alternative to the classical liquid one. These results finally demonstrate the feasibility of the LCO+LLZO+GPE concept, which encourage further studies in the same direction.

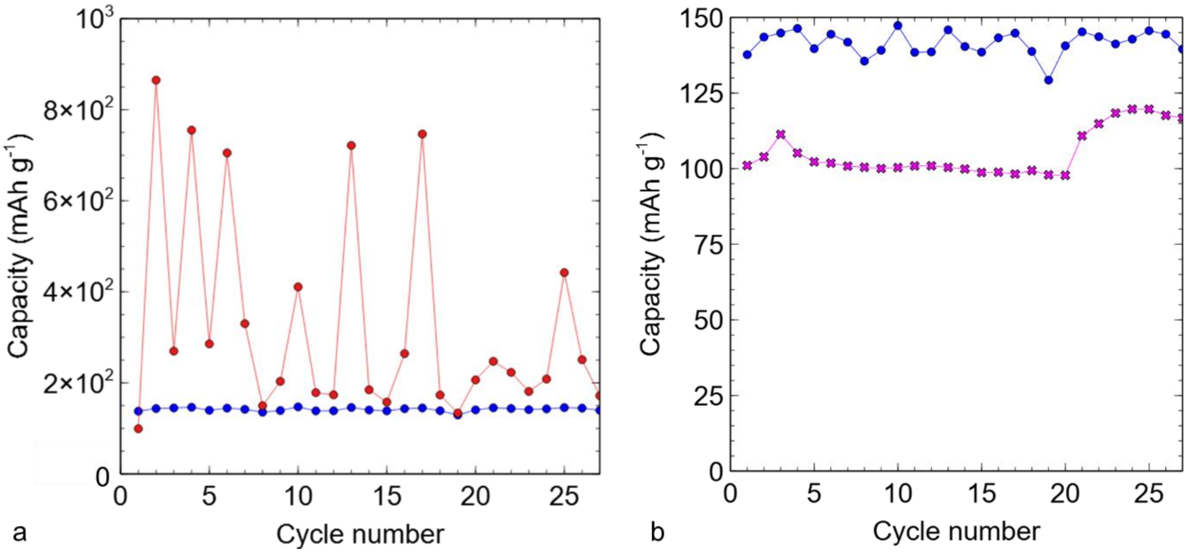

Figure 5.5. Reproduction of GCPL of LCO$_{\mathrm{TiO2}}$ + 30 wt.% LLZO film with GPE, characterised at 1C between 3.0 and 4.2 V *vs.* Li$^+$/Li in climate chamber (25 °C). (a) Figure showing (●) charging and (●) discharging curve; (b) Comparison of discharging curve of LCO$_{\mathrm{TiO2}}$ + LLZO 30% electrodes characterised with (●) GPE and (×) liquid electrolyte (extracted from Chapter 4, section 4.3.4.4). All capacities are reported per mass unit of LCO present in the electrode.

5.4. Conclusion

The main objective of using GPE in the EnSO project was to be able, in the long-term, to build a flexible, full solid-state battery. To do so, a gel polymer electrolyte (GPE) was developed in the NCE laboratory by a senior researcher. In a next step, the use of this GPE in conjunction with the LCO$_{\mathrm{TiO2}}$/LLZO electrodes developed in Chapter 4 was envisaged. So, positive electrodes containing LCO$_{\mathrm{TiO2}}$ mixed with LLZO as ionic conductor were covered with GPE, used as both electrolyte and separator. The electrodes were characterised using metal Li as negative electrode. Experiments were performed in coin cells as a preliminary step towards flexible batteries.

As reference, the GPE was sprayed directly on the LCO$_{\mathrm{TiO2}}$ cathode material (without LLZO); during characterisation, the battery was quickly losing its capacity. This capacity loss was probably due to the 50-60% open porosity within the cathode coating, that were not filled with any electrolyte. On the contrary, the optimised LCO$_{\mathrm{TiO2}}$/LLZO cathode material presented in Chapter 4 have shown interesting properties of the battery system using GPE as electrolyte. The battery with LCO$_{\mathrm{TiO2}}$/LLZO/GPE system displayed performances close to that obtained using liquid electrolyte, as performed in Chapter 4. The addition of LLZO on the cathode coating clearly improves the battery performances; however, high current leakage was observed during charging. Those current leakages are probably due either battery assembly issues and can certainly be solved technically.

As perspective, the battery system must now be tested in a flexible set-up. To that aim, collaboration with laboratories able to produce flexible packaging is currently on tracks and should lead to a final all-solid-state battery with fast charge/discharge rate capability.

References

1. M. Armand, J. M. Tarascon, Building better batteries. *Nature* **45**, 652–657 (2008).
2. W. Li, J. R. Dahn, D. S. Wainwright, Rechargeable lithium batteries with aqueous electrolytes. *Science* **264**, 1115–1118 (1994).
3. G. Feuillade, P. Perche, Ion-conductive macromolecular gels and membranes for solid lithium cells. *J. Appl. Electrochem.* **5**, 63–69 (1975).
4. F. B. Dias, L. Plomp, J. B. J. Veldhuis, Trends in polymer electrolytes for secondary lithium batteries. *J. Power Sources* **88**, 169–191 (2000).
5. K. M. Abraham, M. Alamgir, Room temperature polymer electrolytes and batteries based on them. *Solid State Ionics* **70/71**, 20–26 (1994).
6. K. M. Abraham, M. Alamgir, Ambient temperature rechargeable polymer-electrolyte batteries. *J. Power Sources* **43**, 195–208 (1993).
7. J. P. Voss, S. V. Batty, J. P. Patel, P. V. Wright, Conductivities of poly (ethylene oxide)-alkali salts with aromatic and heterocyclic anions. *Solid State Ionics* **60**, 93–97 (1993).
8. F. Croce, B. Scrosati, Interfacial phenomena in polymer-electrolyte cells: lithium passivation and cycleability. *J. Power Sources* **43**, 9–19 (1993).
9. C. A. Paez, D. Liquet, C. Calberg, B. Heinrichs, C. Alié, Method for the wet deposition of thin films, WO 2016/097396 A1 (2016), pp. 1–4.
10. H. Porthault, C. Calberg, J. Amiran, S. Martin, C. A. Pàez, N. Job, B. Heinrichs, D. Liquet, R. Salot, Development of a new Li metal-gel polymer electrolyte thin flexible battery design operating at room temperature. *J. Power Sources*, submitted for

publication.

11. S. Kim, J. Y. Kang, S. G. Lee, J. R. Lee, S. J. Park, Influence of clay addition on ion conductivity of polymeric electrolyte composites. *Solid State Phenom.* **111**, 155–158 (2006).

12. M. P. Atkins, J. Williams, J. A. Ballantine, J. H. Purnell, Lithiated clays and uses thereof, EP0284397 A1 (1988), pp. 1–18.

13. M. Kerner, N. Plylahan, J. Scheers, P. Johansson, Thermal stability and decomposition of lithium bis(fluorosulfonyl)imide (LiFSI) salts. *RSC Adv.* **6**, 23327–23334 (2016).

14. K. Kubota, T. Nohira, T. Goto, R. Hagiwara, Novel inorganic ionic liquids possessing low melting temperatures and wide electrochemical windows: Binary mixtures of alkali bis(fluorosulfonyl)amides. *Electrochem. Commun.* **10**, 1886–1888 (2008).

15. C. A. Páez Martínez, C. Exantus, D. Dallel, C. Alié, C. Calberg, D. Liquet, D. Eskenazi, F. Deschamps, N. Job, B. Heinrichs, Water-based paintable $LiCoO_2$ microelectrodes: a high-rate Li-ion battery free of conductive and binder additives. *Adv. Mater. Technol.* **4**, 1–12 (2019).

General conclusion and perspectives

The actual market of smart objects, *i.e.* devices interconnected through the Internet, is evolving very fast in multiple fields of application. These smart objects are getting smaller and smaller and include more and more functionalities, whose integration requires energy to keep the systems autonomous. Therefore, the need for Autonomous Micro Energy Sources (AMES) is growing. The development of self-powered systems, comprising both an energy harvester and an energy storage device, can be a way to solve the energy issue. In that perspective, the European EnSO project aimed at developing new AMES to be incorporated in end-users' products.

Among the 35 partners, the NCE laboratory was in charge of (i) the development of piezoelectric materials, *i.e.* zinc oxide nanowires (ZnO NWs), for energy harvester and (ii) the development of components for rechargeable Li-metal microbatteries, *i.e.* $LiCoO_2$-based electrodes and solid electrolyte. Within this framework, the present PhD work was focused on the development of thin films for both applications. Thus, the thesis work was divided into two distinct parts: (i) the study of the growth of ZnO NWs on seeded substrate, followed by an optimisation of the seed layer and (ii) the development of $LiCoO_2$ electrodes comprising an inorganic solid electrolyte (low temperature cubic $Li_7La_3Zr_2O_{12}$, LLZO).

ZnO nanowires for piezoelectric generators

ZnO NWs were grown using a mixed sol-gel process comprising (i) seeding of the substrate with ZnO nanocrystals followed by (ii) growth using chemical bath deposition (CBD). The main goal of the first part was to study the process of the ZnO NW growth in order to achieve a growth rate of 20 nm min^{-1}, compatible with industrial scale-up, and to improve the orientation of the seed layer in order to grow well-aligned individual NWs, perpendicular to the substrate. To do so, the key variables of the CBD process such as the temperature, pH and zinc ion concentration were monitored to (i) highlight their impact on the length and diameter of the NWs and (ii) identify the conditions under which the growth rate was maximum. From that study, detailed in Chapter 1, it was possible to define the maximum growth phase. The maximum growth speed was about 70 nm min^{-1}, which is suitable for a scaling-up of the process. This maximum growth was obtained when the temperature was stabilised at ~80 °C and pH at ~9.5. It was however difficult to obtain reproducible results due to temperature variation from one synthesis to the other. To solve that problem, a dual-wall system where water is heated at 90 °C and circulates constantly was built and tested, which helped decreasing variations. However, it is clear that temperature control is critical in the process. In this work the main objective was to synthesis ZnO NWs in a view of industrial level manufacturing. For the NW growth, we have managed to develop a system where the temperature is controlled homogeneously from one synthesis to the other. As a perspective work, recirculation or stirring device might be an option to homogenise the concentration of reagents in the medium and stabilise the system at its maximum growth. Moreover, a continuous growth process may be an option for possible scaling up of the growth process.

It was also noticed that, in many cases, the obtained NWs were not perpendicular to the substrate, which was certainly due to the heterogeneity of the seed layer, which in Chapter 1 consisted in the deposition of a precursor solution using spin-coating followed by a calcination step at 350 °C (20 min). As the seed layer has a strong influence on the orientation of the NWs, its optimisation was envisaged in Chapter 2. Spin and dip-coating methods were first studied for the deposition of the seed layer. The work carried out has shown that spin-coating does not always result in homogeneous seed layer: in particular, it is certainly necessary to filtrate the seed suspension, which is time-consuming; in addition, spin-coating is not much adapted to large-scale applications. Therefore, dip-coating was further selected in order to improve the quality of the seed layer; further, the impact of thermal post-treatments of the seed on the final ZnO NWs was studied. The use of dip-coating deposition led to a well-oriented and well-crystallised seed layer, perpendicular to substrate surface, when a double calcination at 350 °C (20 min) with cooling in-between was performed. In parallel, the NW growth was optimised by one of the senior researchers of the NCE laboratory (Dr Christelle Alié): a mix of zinc sulfate and zinc nitrate precursors was used, which led to well-oriented and spaced ZnO NWs. Team work made it possible to obtain well aligned and isolated NWs using a low temperature process. As a future work, the optimised NW process should be deposited on a flexible substrate. The homogeneity and adhesion of the coating must be characterised, and the optimised NWs array included into a nanogenerator to be characterised.

In Chapter 3, piezoelectric nanogenerators were built as an example of application. This part, based on the global team work, was performed by the senior researcher of the NCE laboratory involved in the same topic (Dr Christelle Alié) in collaboration with the Greman laboratory in Tours (France). It showed that the defects in the crystalline structure, which are very numerous after the CBD growth process, have a very strong impact on the nanogenerator performance. The next step consisted thus on the reduction of the concentration of the defects in the crystalline structure of the NWs by calcination at 260 °C after growth. This post-treatment led to a maximum power average value of 121 nW instead of 37 nW without post-treatment. It must be pointed out that the results were quite scattered: it is very difficult to obtain reproducible measurements for piezoelectric nanogenerators due to the number of successive steps, from the seed deposition to the piezoelectric generator characterisation. Nevertheless, the results show that the manufacturing of piezoelectric nanogenerators from CBD-grown ZnO NWs is feasible. Due to a lack of time, the NWs obtained with the optimised process were not characterised in terms of defect concentration and the nanogenerators performances were not tested. It would be interesting to test the nanogenerator performances of the optimised seed combined with mixed growth process with and without the post-treatment. In order to improve the results, the reproducibility of the seed layer and the NW growth should be checked. Also, the nanogenerator assembly should be optimised by working on the influence of the thickness of the insulating layer for example.

As one of the major research topics of the NCE laboratory is photocatalysis, a first trial of measurement of the photocatalytic activity of ZnO NWs was also presented in Chapter 3. The photocatalytic activity of ZnO NWs was performed by monitoring the degradation of H_2O_2 as a function of time. The work highlighted that the photocatalyst activity of the samples much probably depends on the accessible surface area of the ZnO NWs, *i.e.* on the array density. This in turn strongly depends on the calcination temperature of the seed layer, which impacts the final diameter and degree of separation of the NWs. Indeed, the reaction rate per gram of ZnO was maximum for seed layers calcined at 200 °C corresponding to final NWs with the lowest apparent density. This shows that the structure of the NWs has to be carefully chosen for the given application.

The different processes developed in this work made it possible to synthesised well-oriented and spaced NWs. However, the CBD growth process does not seem fully adapted to industrial scale as it is not reproducible and gives rise to defect on the crystalline structure. CBD should be compared to other NW low temperature growth processes such as hydrothermal deposition, which consist in the growth of the NWs at a temperature below 100 °C.

Electrodes for Li-metal microbatteries

The second part of the thesis was dedicated to the modification of $LiCoO_2$ (LCO) coatings to develop positive electrodes for all-solid Li-metal microbatteries. LCO coatings on suitable substrates had been previously obtained by a second senior researcher of the NCE laboratory (Dr Carlos Páez) using spray-coating. The porosity of the LCO electrode coating was about

50-60%. This porosity is not a problem as long as liquid electrolyte is used in the battery since the electrolyte impregnates the voids between the LCO particles and allows for easy Li^+ transfer. However, when a solid or gel polymer electrolyte is used, the performances of the microbattery decrease very fast due to a lack of contact between LCO and the electrolyte since, in that case, the electrolyte deposited on top of the coating does not infiltrate the porosity of the layer. The main goal of this second part was to modify the coating, so that it us suitable to build a solid-state microbattery.

In Chapter 4, a nanostructured material, synthesised by a sol-gel method, was chosen in order to increase the performances of the positive electrode material: low temperature cubic $Li_7La_3Zr_2O_{12}$ (LLZO). This material presents a good ionic conductivity (10^{-6} S cm^{-1}). The objective was to prepare nanoparticles about 50-100 nm in size, so that they can be inserted into the porosity of the LCO and increase the performances of the electrode material by increasing the Li^+ conductivity. Different amounts of LLZO were introduced into the LCO suspension before spraying. The mixture of the two materials in ethanol was stable and could be deposited by spray-coating onto the current collector. The electrode coating was characterised by environmental scanning electron microscopy (ESEM) combined with EDX analysis. The images showed that, at the surface of the cathode, the LLZO particles seem to be well-distributed. The LLZO/LCO electrode was then included into a battery set-up and first tested with liquid electrolyte to check that no side-reaction happened and that the presence of LLZO did not alter the LCO properties. The electrochemical characterisation showed that the addition of LLZO had no impact on the electrochemical properties of the LCO, as the capacity of the obtained electrode (~137 mAh g^{-1}) was close to the theoretical value of LCO (140 mAh g^{-1}). Moreover, electrochemical characterisations have shown that the addition of 30 wt.% of LLZO into the LCO suspension enabled the positive electrode material to withstand the stress imposed by rapid charge and discharge cycles. The synthesis of low temperature cubic LLZO needs to be further studied as well as the microstructure (grain size, density) to achieve reproducible material. Moreover, the LLZO is moisture-sensitive, which requires to work in a dry atmosphere. The introduction of the LLZO solid electrolyte powder, into the LCO coating, has improved the electrochemical performances of the positive electrode. However, a deeper understanding of the conduction mechanism of LLZO in the coating using electrochemical impedance spectroscopy is of great importance. Finally, the spray deposition process should be optimised (speed, spraying height) in order to obtain a homogeneous amount of material on the substrate.

Chapter 5 consisted in the next logical step: as the results were quite promising, the positive electrode material was combined with a gel polymer electrolyte (GPE) synthesised by a third senior researcher of the laboratory (Ir. Cédric Calberg). The GPE was deposited on top of the LCO/LLZO electrode with the best composition, as determined in Chapter 4. Results showed that the final electrode could reach a capacity of (100 mAh g^{-1}) with good stability at low cycling rate, and sustain cycling speeds up to 10 C while still keeping 75% of its nominal capacity. This demonstrates that the manufacture of all-solid state microbatteries from the LCO/LLZO coatings presented here is feasible. Note however that some issues were encountered regarding the cell assembly: while the discharge capacity values of the electrodes were normal and stable, very high and erratic charging capacities were recorded. This is certainly due to problems of contacts in the cells that can be corrected by improving the cell assembly process. Note also that, due to time constraints, it was not possible to reproduce the experiments and to correct those technical problems; this will be the next step if the work can be continued. Finally, the LCO/LLZO electrode should be deposited on the substrate from CEA in order to be tested as a microbattery. This modification of substrate may have an influence on the adhesion and, therefore, on the homogeneity of the coating. The deposition procedure should be then studied and adapted in order to obtain a homogeneous coating. Finally, electrochemical characterisation should be performed on the final microbattery set-up to assess its global performance.